Studies for the Loss of Atomic and Molecular Species from Io

William H. Smyth

Atmospheric and Environmental Research, Inc.
840 Memorial Drive
Cambridge, MA 02139-3794

Final Report for the Period of
September 23, 1996 to September 22, 1999

Table of Contents

I. Introduction

The general objective of this project has been to advance our theoretical understanding of Io's atmosphere by studying how various atomic and molecular species are lost from this atmosphere and are distributed near the satellite and in the circumplanetary environment of Jupiter. The project is divided into well-defined studies described for the likely dominant atmospheric gases involving species of the SO_2 family (SO_2, SO, O_2, O, S) and for the trace atmospheric gas, atomic sodium. The relative abundance of the members of the SO_2 family and Na (and its parent, NaX) at the satellite exobase and their relative spatial densities beyond in the extended corona of Io are not well known but will depend upon a number of factors including the upward transport rate of gases from below, the velocity distribution and corresponding escape rate of gases at the exobase, and the operative magnetospheric/solar-photon driven chemistry for the different gases. This question of relative abundance has been pursued in this project.

In order to address this question, we have undertake theoretical modeling studies for the distribution and time variability of these exospheric gases in Io's corona/extended clouds and evaluated the importance of various physical processes that shape their relative abundances and escape rates. Our primary objective is to study near-Io emission observations for O, S, and Na. A secondary objective is to continue the study of various larger-spatial-scale ground-based sodium and spacecraft (Voyager and Galileo) SO_2^+ observations in order to address related issues and to lay the groundwork for larger-spatial-scale O and S observations likely to be obtained in the near future. These studies are of scientific importance in understanding (1) the atmosphere of the satellite, (2) the interactions of the magnetospheric plasma and the atmosphere, (3) the nature and composition of the heavy ion sources for the plasma torus, (4) the impact of these gases on the larger magnetosphere, and (5) the spatial distribution of these gases in the magnetosphere and beyond in the larger solar wind environment.

Near-Io observations for this project were available in four collaborative efforts established with

(1) F. Scherb, of the University of Wisconsin-Madison, who very successfully obtained near-Io synoptic observations of [O I] 6300 Å emission from ground-based facilities over the1990-1998 time interval and continuing in 1999,

(2) G. E. Ballester, of the University of Michigan, who acquired HST cycle IV and cycle V observations for O and S near Io in various UV emission lines,

(3) L. M. Trafton, of the University of Texas, who obtained during the period 1987-1996 ground-based observations for the north-south spatial distribution and spectral line shape of sodium (5890 Å, 5896 Å) emissions near Io, and

(4) N. M. Schneider, of the University of Colorado-Boulder, who obtained in 1987 from ground-based facilities an extensive set of observations for the east-west spatial distribution and spectral line shape of sodium emissions near Io, which exactly overlaps the October 1987 observations of Trafton.

In addition, during the course of this project, two additional collaborations of opportunity were established for new high-spatial-resolution near-Io image observations with

(5) F. L. Roesler, of the University of Wisconsin-Madison, who very successfully obtained with the new STIS (Space Telescope Imaging Spectrometer) instrument on the Hubble Space Telescope (HST) high-resolution (~90 km/pixel) ultraviolet images of Io in several atomic oxygen and sulfur lines and also detection of H Lyman-α emission near the satellite poles, and

(6) M. J. S. Belton, of the National Optical Astronomical Observatory, who as the Team Leader of the Galileo Solid-State Imaging (SSI) instrument very successfully acquired a set of optical high-resolution (~few 10's km/pixel) images of Io while eclipsed by Jupiter's shadow.

These near-Io emissions exhibit time variability and dependence on Io System III longitude and Io east-west location, the nature and cause of which are subjects of investigation in this project.

During the project, different amounts of progress have been made with the six collaborations noted above and appropriate ongoing research has been proposed to continue these investigations. In the Scherb collaboration, the acquisition and reduction of the large ground-based [O I] 6300 Å data set has progressed well, and patterns are finally beginning to emerge regarding the dependence of the oxygen brightness on Io geocentric phase angle and Io System III longitude with plans to write a paper presently being formulated. In the Ballester collaboration, properly reduced data have only recently been received with emphasis placed on understanding the time-dependent changes in species abundances observed during Io eclipse ingress and egress measurements. In the Trafton collaboration, the complete set of north-south sodium observations acquired between 1987 and 1996 was received in the second project year

with a significant third-year expenditure of effort to develop a well ordered, formatted, and valuable data set suitable for modeling. In the Schneider collaboration, only part of the reduced data set for east-west sodium observations has been sent to AER with a critical portion remaining to be received. In the Roesler collaboration, a first paper (Roesler et al. 1999) has been published for the spectacular 1997 HST/STIS observations, and considerable investigations are in progress for both the 1997 and the more recent 1998 HST/STIS observations. In the Belton collaboration, a first exciting paper (Geissler et al. 1999) has been published and more detailed research work to be included in a second paper is in progress. A more detailed summary of the research accomplished in this project is presented in the following sections. Overall the project has made significant progress and, as listed below, has published four papers and recently submitted one paper (all included in the Appendix) and has presented fourteen related papers at scientific meetings.

Papers Published/Submitted in this Project

Geissler, P.E., A.S. McEwen, W. Ip, M.J.S. Belton, T.V. Johnson, W.H. Smyth, and A.P. Ingersoll, Galileo Imaging of Atmospheric Emissions from Io, Science 285, 870-874, 1999.

Roesler, F.L., H.W. Moo, R.J. Oliversen, R.C. Woodward, K.D. Rutherford, F, Scherb, M. McGrath, W.H. Smyth, P.D. Feldman, and D.F. Strobel, Far Ultraviolet Imaging Spectroscopy of Io's with HST/STIS, Science, 283, 353-357, 1999.

Smyth, W.H., Energy Escape Rate of Neutrals from Io and the Implications for Local Magnetospheric Interactions, J. Geophys. Res. 103, 11941-11950, 1998.

Smyth, W.H., and M.R. Combi, Io's sodium exosphere and spatially extended cloud: A consistent flux speed distribution, Icarus 126, 58-77, 1997.

Smyth, W.H. and M.L. Marconi, An Initial Look at the Iogenic SO_2^+ Source during the Galileo Flyby of Io, J. Geophys. Res. 103, 9083-9089, 1998.

Smyth, W.H. and M.L. Marconi, Io's Oxygen Source: Determination from Ground-based Observations and Implications for the Plasma Torus, J. Geophys. Res., submitted 1999.

Project Related Papers Presented at Scientific Meeting

Lisiecki, L., M.C. Wong, and W.H. Smyth, Io's Magnetospheric Interaction: Atmospheric Heating and Neutral Escape, EOS 80, S200, 1999.

Marconi, M.L. and W.H. Smyth, The Iogenic SO_2^+ Source During the Galileo Flyby of Io, BAAS 29, 1002, 1997.

Marconi, M.L. and W.H. Smyth, The Iogenic Neutral Oxygen Source, EOS 79, S200, 1998.

Oliversen, R.J., F. Scherb, F.L. Roesler, J. Corliss, R.C. Woodward, M.E. Freed, O.L. Lupie, and W.H. Smyth, Io [O I] 6300 Å Observations, BAAS 30, 1116, 1998.

Oliversen, R.J., F. Scherb, F.L. Roesler, J. Corliss, R.C. Woodward, M.E. Freed, O.L. Lupie, and W.H. Smyth, Ground-based Io [O I] 6300 Å Observations. Paper presented at the 194th meeting of the American Astronomy Society, Chicago, Illinois, 30 May-June 3, 1999.

Roesler, F.L., F. Scherb, R.C. Woodward, , H.W. Moo, R.J. Oliversen, W.H. Smyth, D.T. Hall, and M. McGrath, STIS Low Spectral Resolution FUV Images of Io, 191st AAS Meeting in Washington, D.C., January 6-10, 1998.

Scherb, F., K. Reutherford, R.C. Woodward and W.H. Smyth, Observations of [O I] 6300 Å Emission from Io's Atmosphere BAAS 28, 1155, 1996.

Scherb, F., K. Reutherford, R.C. Woodward and W.H. Smyth, Observations of [O I] 6300 Å Emission from Io's Atmosphere, presented at the "Magnetospheres of the Outer Planets Meeting" at Boulder, Colorado, March 17-21, 1997.

Scherb, F., R.J. Oliversen, F.L. Roesler, R.C. Woodward, J. Corliss, M. Freed, and, W. Smyth, Recent Ground-Based Observations of [O I] 6300 Å from Io, EOS 79, S200, 1998.

Scherb, F., R.J. Oliversen, M.E. Freed, W.H. Smyth, J. Corliss, R.C. Woodward, P. Morgenthaler, and O.L. Lupie, Ground-based observations of [O I] 6300 Angstrom emission from Io, Paper presented at the "Magnetospheres of the Outer Planets Meeting", Paris, France, 9-14 August, 1999.

Smyth, W.H., Review of the Io Neutral Clouds and Plasma Torus (Invited), Io during the Galileo Era Conference (Flagstaff, AZ, September 22-24, 1997).

Smyth, W.H., Energy Loss Rate of Neutrals from Io and Implications for Io's Atmosphere and Local Magnetospheric Interactions, EOS 79, S200, 1998.

Smyth, W.H. and M.L. Marconi, An Initial Look at the Iogenic Plasma Source During the Galileo Flyby of Io, EOS 77, F436, 1996.

Woodward, R.C., F.L. Roesler, R.J. Oliversen, F. Scherb, H.W. Moos, and W.H. Smyth, Spectrally Dispersed Images of Io in the FUV using STIS, EOS 79, S200, 1998.

II. Studies for Sodium

2.1. Determination of a Consistent Na Flux Speed Distribution at Io's Exobase

Early in the first project year, work was completed on the final publication galley proof for the paper entitled "Io's Sodium Corona and Spatially Extended Cloud: A Consistent Flux Speed Distribution". This paper was written and submitted for publication in the prior NASA project for which this project is a continuation. In this paper (Smyth and Combi 1997, in Appendix A), a consistent Na flux speed distribution at Io's exobase was determined for the incomplete collisional cascade processes in Io's atmosphere from the modeling analysis of three different sodium data sets covering the spatial domain from Io's exobase to ~100 satellite radii (R_{Io}) from Io in the sky-plane. This incomplete collisional cascade source distribution for

sodium, a trace species in Io's atmosphere, has since been used to study the nature of sodium zenocorona at large distances from Jupiter (Wilson et al. 1998) as well as to provide a valuable zeroth-order description for the incomplete collisional cascade source distribution for SO_2 (Smyth and Marconi 1998, see Section III) and O and S (Smyth and Marconi 1999, see Sections IV and VII).

2.2. North-South Sodium Distribution about Io (Trafton Collaboration)

In the 1987 to 1996 time frame, Trafton obtained a data set of just over 100 high-quality sodium D_1 and D_2 line emission observations using a ~1" x 36" Io-centered north-south aligned observing slit. These measurements, recorded at the McDonald Observatory with a reticon focus Coude Spectrometer/CCD, provide a 2-D map (1-D spatially, ~±36 R_{Io} along the slit and 1-D in wavelength) with a spectral resolution of ~30-50 mÅ. The integration time for each measurement (~20 minutes) is short compared to 3.25 hr (one-fourth of the ~13 hr oscillation period of the plasma torus centrifugal symmetry plane about Io's orbital plane). Each 2-D map captures the Doppler-decomposed north-south spatial brightness profile produced by the System III longitude modulation of the Na source at Io and the Na sink spatially about Io. As part of our collaboration with Trafton, the data files for the 2-D maps have been reduced, calibrated and made available to AER on optical disk. The complete set of these reduced sodium emission data was received in late June 1996 during the second project year. In the third project year, these observations have been assessed, addressed regarding corrections and ambiguities, and ordered and output in a common format. The resulting data set provides an excellent resource for modeling. This process has taken a much larger effort than originally anticipated so that modeling analysis efforts have been very minimal. These maps are currently being compared to identify systematic behaviors in the Na brightness distribution as a function of Io geocentric phase and Io System III longitude and also to select observations suitable for modeling analysis.

An example of the 2-D map and its corresponding 1-D brightness profile for one of Trafton's observations is shown in Figure 1a and Figure 1b, respectively. In Figure 1, Io has a geocentric phase angle of 300° and a System III longitude of 231° (well north of the centrifugal symmetry plane of the plasma torus) so that sodium is more depleted to the south by its shorter electron impact ionization lifetime (~1 hr) in the denser plasma torus centrifugal symmetry plane. The shape of the 2-D map will also depend upon Io's source velocity distribution which will determine the repopulation time of the Na atoms north and south of Io (~ several hours, depending on distance and atom speed). The 2-D map can then be inverted to obtain the sodium

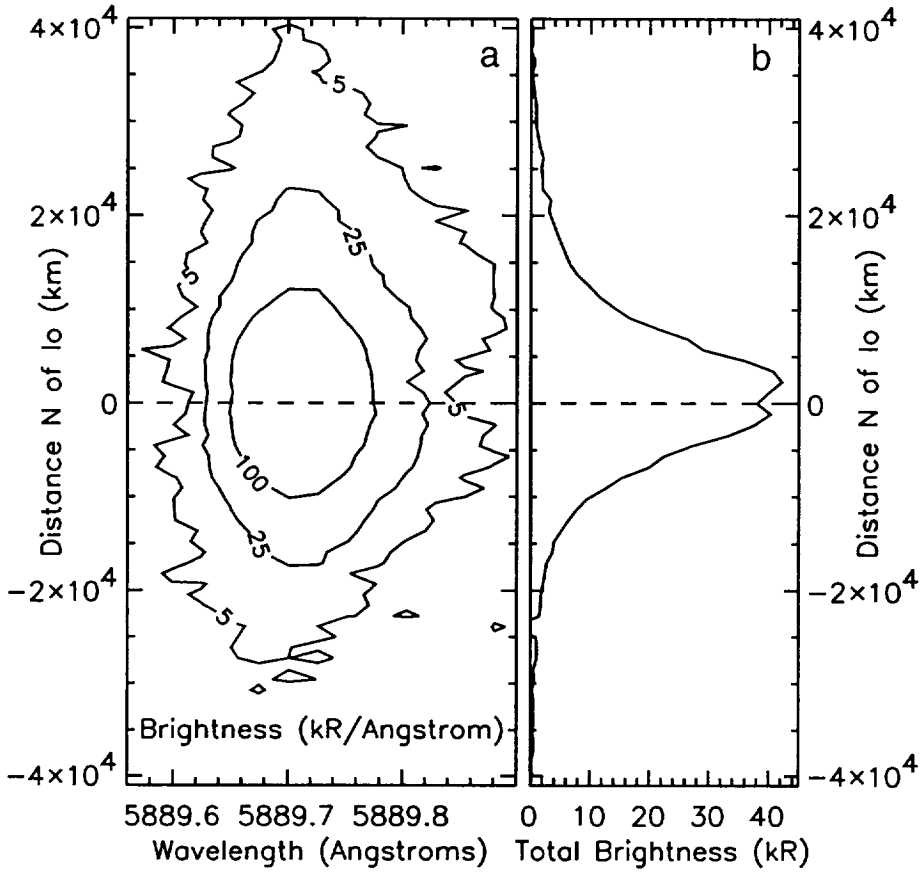

Figure 1. Near-Io Sodium D_2 (5890 Å) Emission Brightness. For an Io observation for the D_2 brightness acquired on 3/21/95 in a north-south Io-centered slit by L. M. Trafton, a 2-D spatial/spectra map is shown in (a) and the corresponding 1-D asymmetric brightness profile along the north-south slit is shown in (b) for an Io phase angle of 300° and an Io System III longitude of 231°.

source distribution at the exobase by using suitably summed monoenergetic sources at Io's exobase in the neutral cloud model calculations to simulate the 2-D map pattern. The expected spatial nature of the north-south asymmetry of the D_2-line brightness near Io is illustrated in Figure 2 by a neutral cloud model calculation for a simple isotropic 2.6 km/s monoenergetic exobase source for Io with a geocentric phase angle of 270° (western elongation) and a System III longitude of 230°. By extracting the 2-D spatial-spectral information from a suitably placed north-south slit in different monoenergetic model calculated images, such as illustrated in Figure 2, we will attempt to reproduce the 2-D observed maps with the model calculation and thereby extract the source rate and velocity distribution. This modeling process will be undertaken in the

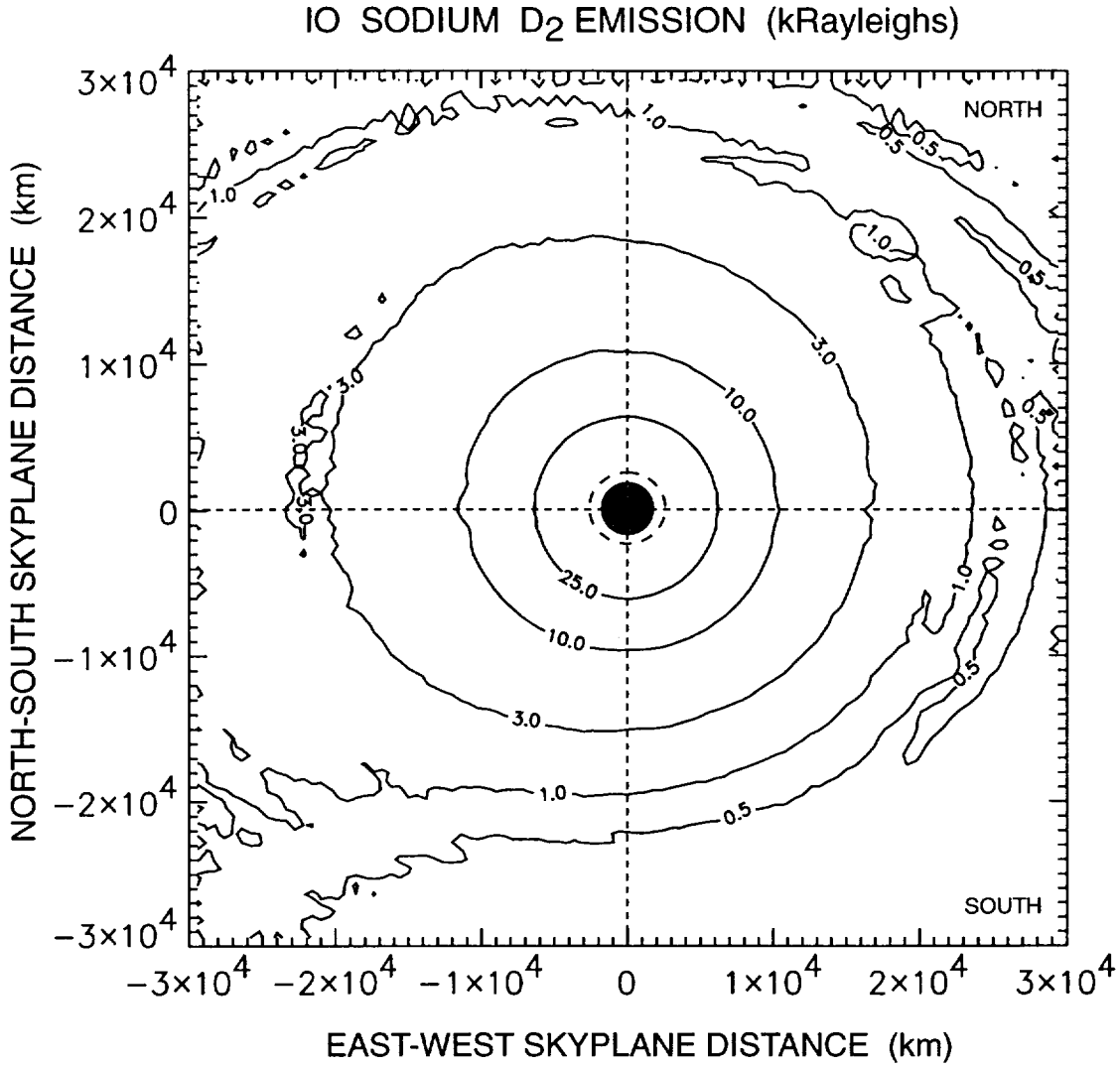

Figure 2. Model Calculation for the Near-Io Sodium D_2 (5890 Å) Emission Brightness. A neutral cloud model calculation for the D_2 emission brightness (in kR) near Io is shown for a simple isotropic 2.6 km/s monoenergetic sodium source of 1 x 10^{26} atoms/s at Io's exobase for an Io phase angle of 270° (western elongation) and Io System III longitude of 230°, well north of the dense plasma in the centrifugal symmetry plane of the plasma torus.

continuation project and will provide a promising avenue to explore the dependence of the Io sodium source on System III longitude and the Io geocentric phase angle.

2.3. East-West Sodium Distribution about Io (Schneider Collaboration)

During the time interval of October 13-18, 1987, Schneider obtained a data set for 110 high-quality sodium D_1 and D_2 line emission observations using a ~1" x 80" Io-centered east-

west aligned observing slit (see Table 1). These measurements, recorded at the Catalina Observatory with the high-resolution LPL echelle spectrograph/CCD (~3 km s^{-1} FWHM), provide a usable 2-D map (1-D spatially, $\leq \pm 40$ R_{Io} along the slit and 1-D in wavelength) with a spectral resolution of ~60 mÅ. The integration time for each measurement (~10 minutes) is short compared to 3.25 hr (one-fourth of the ~13 hr oscillation period of the plasma torus centrifugal symmetry plane about Io's orbital plane). Each 2-D map captures a Doppler-decomposed east-west spatial brightness profile about Io. An exact overlap in dates for the east-

Table 1. 1987 Io Sodium East-West Observation Chronology

Date	Number of East Observations	Number of West Observations	Total No. of Observations
13 Oct	5	6	11
15 Oct	17	4	21
16 Oct	18	13	31
17 Oct	17	6	23
18 Oct	14	10	24
	71	39	110

west observations of Schneider and the north-south observations of Trafton was noted for the time interval 13-15 October 1987 prior to the final reduction of the Trafton observations discussed above. This overlap provides a potentially excellent model analysis opportunity to study the spectral-spatial nature of sodium about Io. Such an analysis can be undertaken using the sodium cloud model to calculate "sodium cloud Doppler-sliced images" (i.e., sodium emission data cubes: a two-dimensional brightness image on the sky plane with the third-dimension being the Doppler wavelength of the sodium cloud atoms determined by their instantaneous velocity along the direction of the sky-plane line-of-sight) for different assumptions about the angular distribution and strength of sodium source at Io's exobase source. After finally reduced of the Trafton observations discussed above, there are, however, only six good observations on October 15 (all of which are not absolutely calibrated) which precisely overlap with seven observations of Schneider in Table 1 for Io east of Jupiter. The question of the absolute calibration of these observations is presently being pursued with Trafton. However, the joint modeling opportunity for the observations on October 15 and the more general modeling for the Schneider east-west observations have been postponed to a future project due to

the only recently completed preparation of the Trafton data set for modeling and the lack of yet receiving from M.N. Schneider a significant portion of his finally reduced data set.

III. Studies for SO_2: Galileo Magnetometer Ion Cyclotron Waves for SO_2^+

To estimate the source strength of SO_2 at the Io's exobase, we have investigated the spatial distribution of SO_2^+ obtained from the Galileo spacecraft in its December 7, 1995 encounter with Io when it flew downstream of the satellite through Io's magnetospheric wake with a closest approach distance above the surface of ~900 km. This research, presented in Smyth and Marconi (1998, in Appendix B), is summarized briefly below.

An SO_2^+ density profile has been deduced from magnetic field fluctuations with periods of ~2 to 3 sec measured by the Galileo magnetometer and interpreted as ion cyclotron waves produced by fresh SO_2^+ Iogenic pickup ions created near Io (Kivelson et al. 1996a,b). Calculations for the SO_2^+ density profile along the Galileo trajectory were undertaken using the AER neutral cloud model for SO_2, where SO_2^+ is produced from SO_2 by electron impact and charge exchange reactions in the plasma torus. By adopting for SO_2 the isotropic incomplete collisional cascade flux source velocity distribution recently deduced for atomic sodium at the exobase (Smyth and Combi 1997, in Appendix A), we were able to match the minimum SO_2^+ density profile determined by Huddleston et al. (1997) in their analysis of the ion cyclotron waves for an SO_2 source rate at Io's exobase of ~4 x 10^{27} molecules sec^{-1} (225 kg sec^{-1}) which created in the magnetosphere a total SO_2^+ production rate of 1.1 x 10^{26} ions sec^{-1} (29 kg sec^{-1}). Most (>90%) of the SO_2 that undergoes interactions in the plasma torus is, however, rapidly dissociated primarily by electron impact producing O, S, SO, and O_2 which subsequently undergo ionization, dissociation, and charge exchange reactions in the plasma torus producing additional mass and energy pickup plasma loading rates that are larger than the SO_2^+ production rate of 29 kg sec^{-1} by more than an order of magnitude. This substantial exobase source rate for SO_2 of ~4 x 10^{27} molecules sec^{-1} is a factor of only about two less than the estimated SO_2 source rate of 8.9 x 10^{27} s^{-1} suggested from the earlier analysis of the O(^{1}D) 6300 Å emission brightness near Io by Scherb and Smyth (1993). About half of the molecules in the incomplete collisional cascade source distribution for SO_2 are not energetic enough to escape the Lagrange sphere of the satellite (~10,550 km or 5.81 R_{Io}) and hence will populate ballistic orbits above the exobase and create a density gradient in the satellite corona. This density gradient plays a central role in matching the steepness of the deduced SO_2^+ density profile at closer distances to Io (within a radius of ~3 satellite radii). The agreement of the model and observationally derived SO_2^+ density profiles thus implies that sodium and SO_2 have a very similar incomplete

collisional cascade flux velocity distribution at the satellite exobase as would be expected if sodium atoms (a trace species in the atmosphere) were produced in the same volume by the same incomplete collisional cascade processes. This agreement also implies that the collisional cascade flux velocity distribution at the exobase for other species, such as atomic oxygen and atomic sulfur, would also be similar.

IV. Studies for O and S

4.1. [O I] 6300 Å Ground-based Observations for Io (Scherb Collaboration)

In our collaboration with Dr. F. Scherb at the University of Wisconsin-Madison, steady progress has been made in this project in the accumulation and the reduction of a very large ground-based data set obtained over the 1990-1998 time period for the observations of [O I] 6300 Å emission near Io. This progress has recently been reported (1) by Oliversen et al. (1998) at the AAS Division for Planetary Sciences (DPS) meeting held in Madison, Wisconsin during the week of October 12-16, 1998, (2) by Oliversen et al. (1999) at the American Astronomy Society held in Chicago, Illinois during the week of May 30 to June 3, 1999, and (3) by Scherb et al. (1999) at the Magnetospheres of the Outer Planets (MOP) meeting held in Paris during the week of August 9-14, 1999.

The reduced data set provides an average [O I] 6300 Å emission brightness in a 5.2 by 5.2 arc second aperture centered on Io as well as Doppler emission width information for each measurement acquired at a specific Io geocentric phase angle and Io System III longitude angle. This data set is extremely valuable for understanding Io's atmosphere and its interaction with the magnetosphere. One of the primary goals of the observational program has been to acquire a sufficient number of these observations so as to study the nature of the short-time variability of the emission brightness and to document the dependence of the emission brightness on the Io geocentric phase and Io System III longitude angles. The data set will also provide an opportunity to explore the east-west brightness effect produced by the east-west electric field and may provide an opportunity to study the influence on the brightness distribution near Io of the plasma wake detected by the Galileo spacecraft. When the current data set and new data presently being acquired in 1999 are completely reduced, its cumulative size should be large enough to address these goals.

The number of observations acquired within the 1990-1998 time interval are summarized in Table 2 with a total number of 1486. The number of observations in the data set can be seen

to have increased dramatically in 1997 and 1998 due to an increased level of funds in the Observing Program to secure observing time at Kitt Peak. At present more than half of these observations have been reduced using the new Voigt-fitting procedure. The distribution of these observations in the two-angle observing parameter plane of Io System III longitude and Io geocentric phase angles is presented in Figure 3 and can be seen to be relatively uniform, but there are still some smaller angular regions where no data coverage has been obtained.

Table 2
Number of [O I] 6300 Å Emission Observations Near Io

Year of Observation	Number of Observations
1990	6
1991	28
1992	4
1993	13
1994	191
1995	---
1996	61
1997	441
1998	742
Total:	1486

The nature of the dependence of the emission brightness on Io System III longitude angles is becoming more apparent as more of the data set in Figure 3 is reduced. For currently reduced data, the [O I] 6300 Å emission brightness is shown in Figure 4 as a function of Io System III longitude for Io both east and west of Jupiter. The [O I] 6300 Å brightness does not have a peak at 200°, as appeared to be likely earlier (Scherb and Smyth 1993) based upon the much smaller 1990-1993 data set with much larger data gaps. The more complete coverage in Figure 4 has a more complex pattern with peak values that occur near 130° and 310°. This pattern is shifted about 20° beyond the System III longitude angles where Io crosses the plasma torus equator plane at 110° and 290° and is likely related to the enhanced electron impact

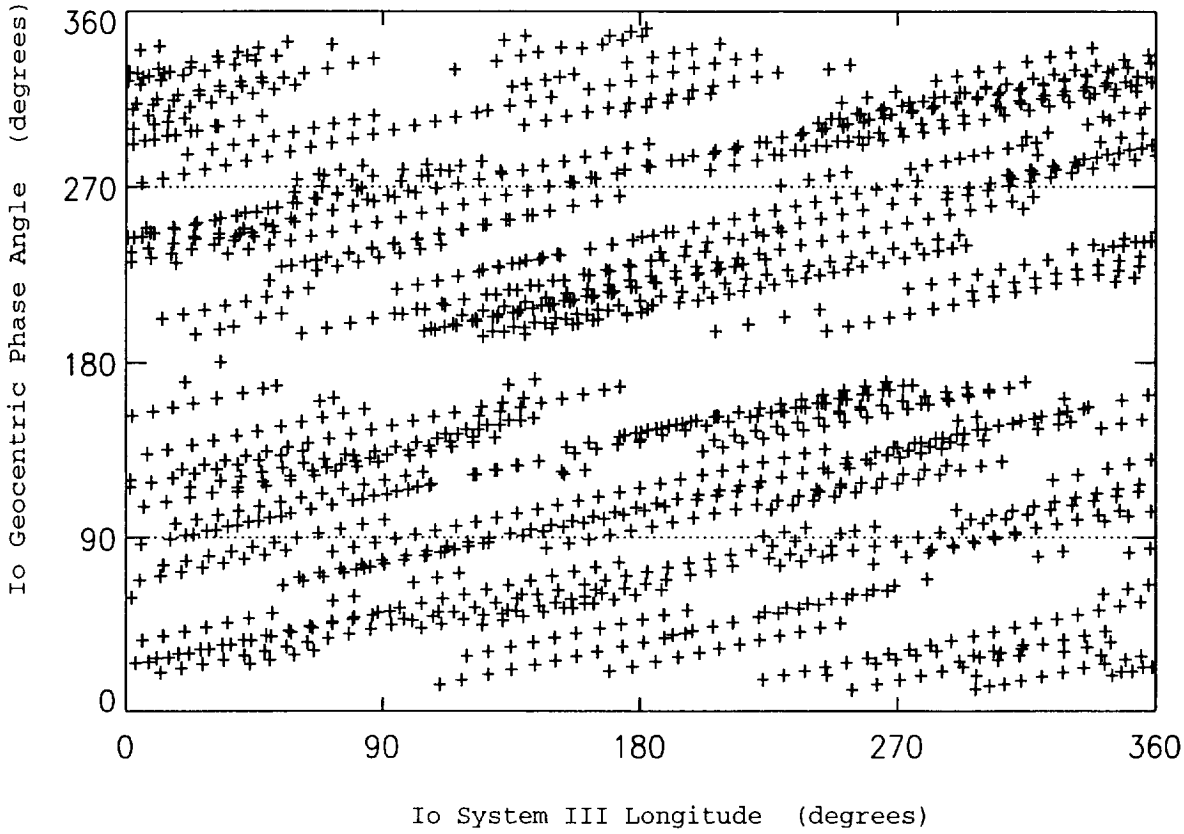

Figure 3. Io [O I] 6300 Å Emission: 1990-1998 Ground-based Data Coverage. The location of Io in the two angle plane for each observation of the [O I] 6300 Å emission near Io is shown by a + symbol.

excitation in the dense equator-plane portion of the plasma torus. The larger average [O I] 6300 Å brightness of 8.3 kR for Io west of Jupiter (dashed line) compared to 7.5 kR for Io east of Jupiter is thought to be related to the hotter plasma torus properties at Io orbit that occur for Io west of Jupiter.

The dependence of the emission brightness on the Io geocentric phase angle is shown in Figure 5. Although there are still gaps in the angular coverage, more so for Io east (0 to 180°) of Jupiter, the dependence of the [O I] 6300 Å brightness appears to have the unexpected behavior with a minimum in the average value both near eastern elongation (90°) and near western elongation (270°). For better data coverage at western elongation, the peaks are located in the

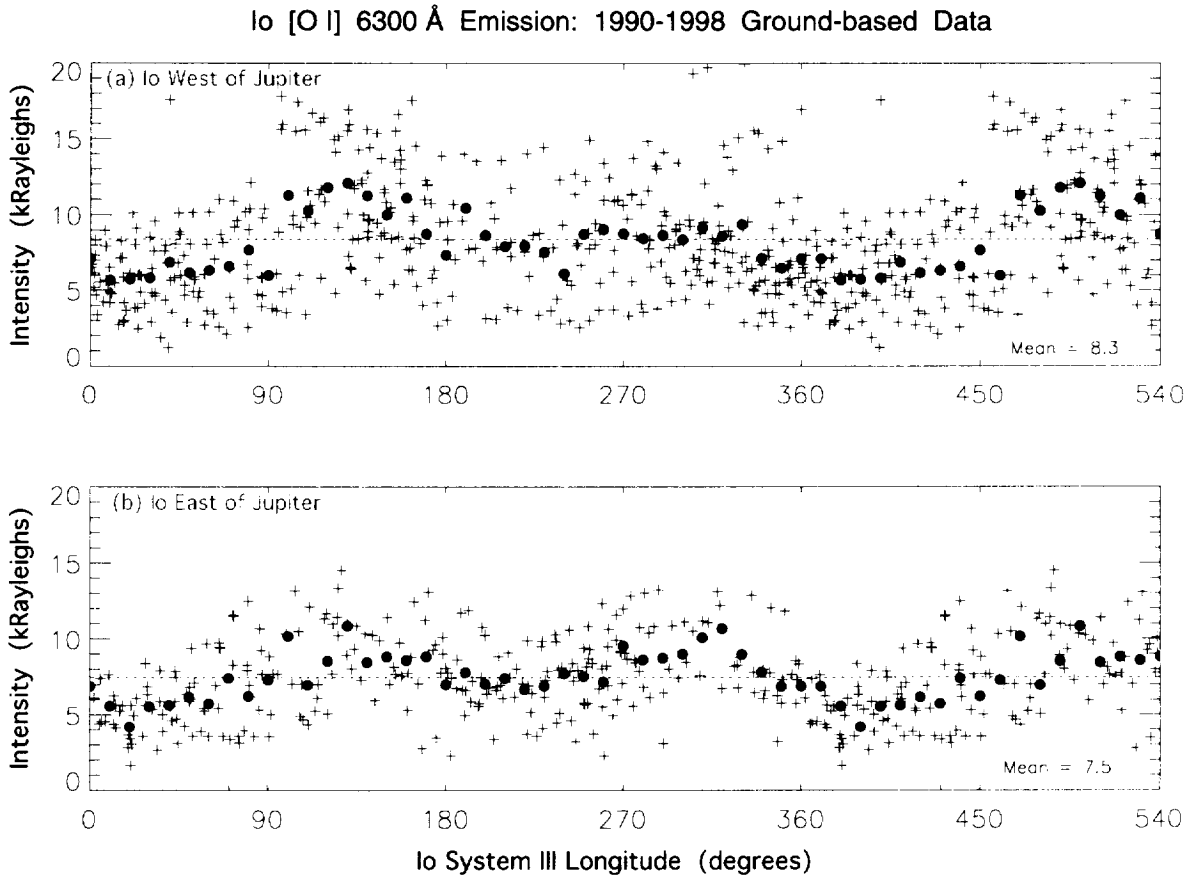

Figure 4. Io [OI] 6300 Å Emission Brightness as a Function of Io System III Longitude. The [O I] 6300 Å emission brightness is shown in (a) for Io west of Jupiter and in (b) for Io east of Jupiter. Individual measurements are denoted by the + symbols while average values are indicated by the green • symbol. The brightness values are referenced to Io's disk area. The dashed line indicates the average brightness in (a) of 8.3 kR and in (b) of 7.5 kR.

angular interval before (180° to 270°) and after (270° to 360°) western elongation. For Io near western elongation, this behavior might be related to enhanced emissions visible in the spatial region of the Io plasma wake, which is hidden behind the satellite disk when Io is near western elongation. A similar pattern may be present in Figure 5 at eastern elongation (90°) but the lack of reduced data there precludes a definite conclusion at present and indicates the importance of reducing more of the available data already acquired in Figure 3. For Io near eastern elongation, the Io plasma wake would be visible in front of the satellite disk. For this geometry, the Io plasma wake would be above the dayside sublimation atmosphere and the plasma properties in the wake might be considerably different than at western elongation where the Io plasma wake is above the nightside atmosphere.

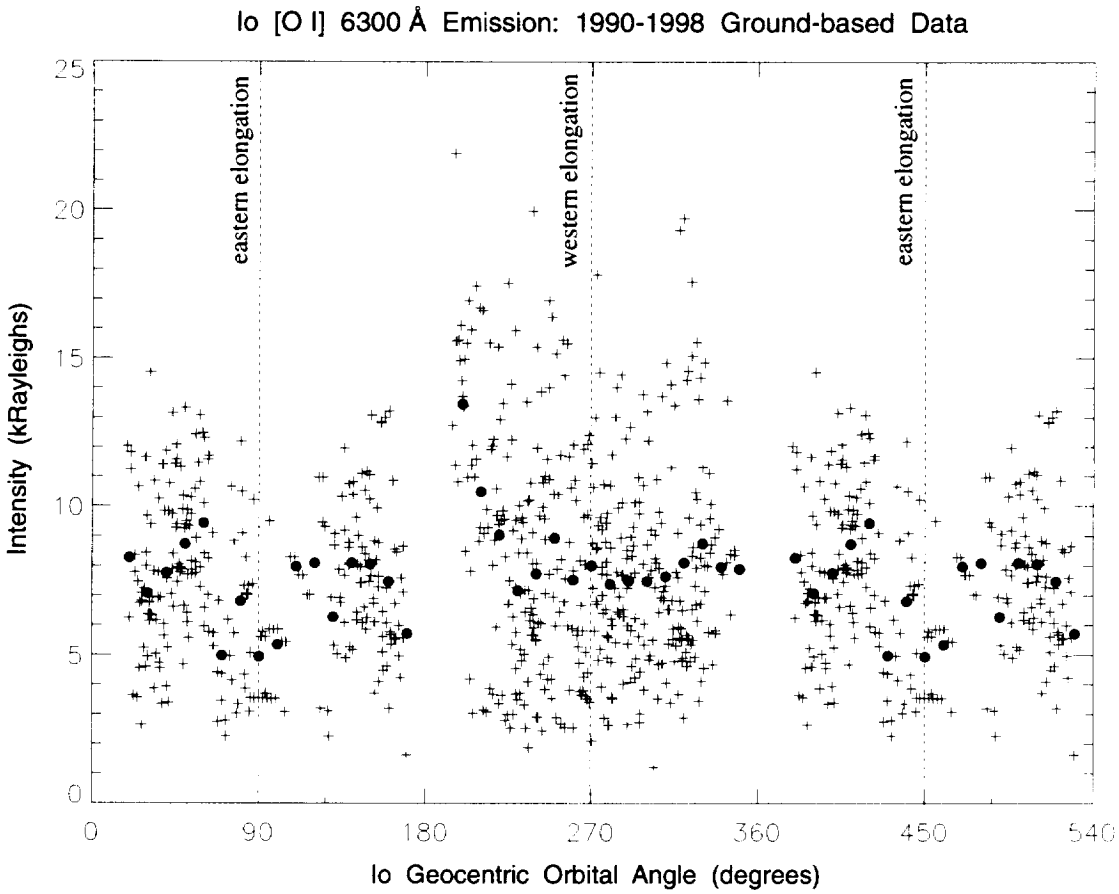

Figure 5. Io [OI] 6300 Å Emission Brightness as a Function of the Io Geocentric Phase Angle. The [O I] 6300 Å emission brightness is referenced to Io's disk area. Individual measurements are denoted by the + symbols while average values are indicated by the green • symbol. The vertical dotted lines show the locations of eastern and western elongation.

4.2. Investigation of the Brightness of O and S in the Io Plasma Wake

The Io geocentric phase angle dependence of the [O I] 6300 Å brightness in Figure 5 suggests that an enhanced O and S emission pattern may be produced by the dense Io plasma wake located downstream of the satellite. Such a spatially confined emission source would be visible both in the angular interval before (180° to 270°) and after (270° to 360°) western elongation and would likely be mostly (if not entirely) blocked by Io's disk when the satellite was near western elongation. To explore this possibility, we have included in the Io neutral cloud model an empirical model for the Io plasma wake based upon nominal Galileo-spacecraft Io-encounter-like plasma parameters and have undertaken preliminary exploratory calculations for the brightness near Io of [O I] 6300 Å and some O and S ultraviolet emission lines. The denser plasma in the wake increases both the electron impact ionization rate (which lowers the

oxygen abundance) and also the excitation rates for atomic oxygen. For atomic oxygen near Io, the model calculated column density distribution excluding the Io plasma wake description is shown in Figure 6 for a simple isotropic monoenergetic source at Io's exobase and for Io located before western elongation and north of the equator plane of the plasma torus (see the figure

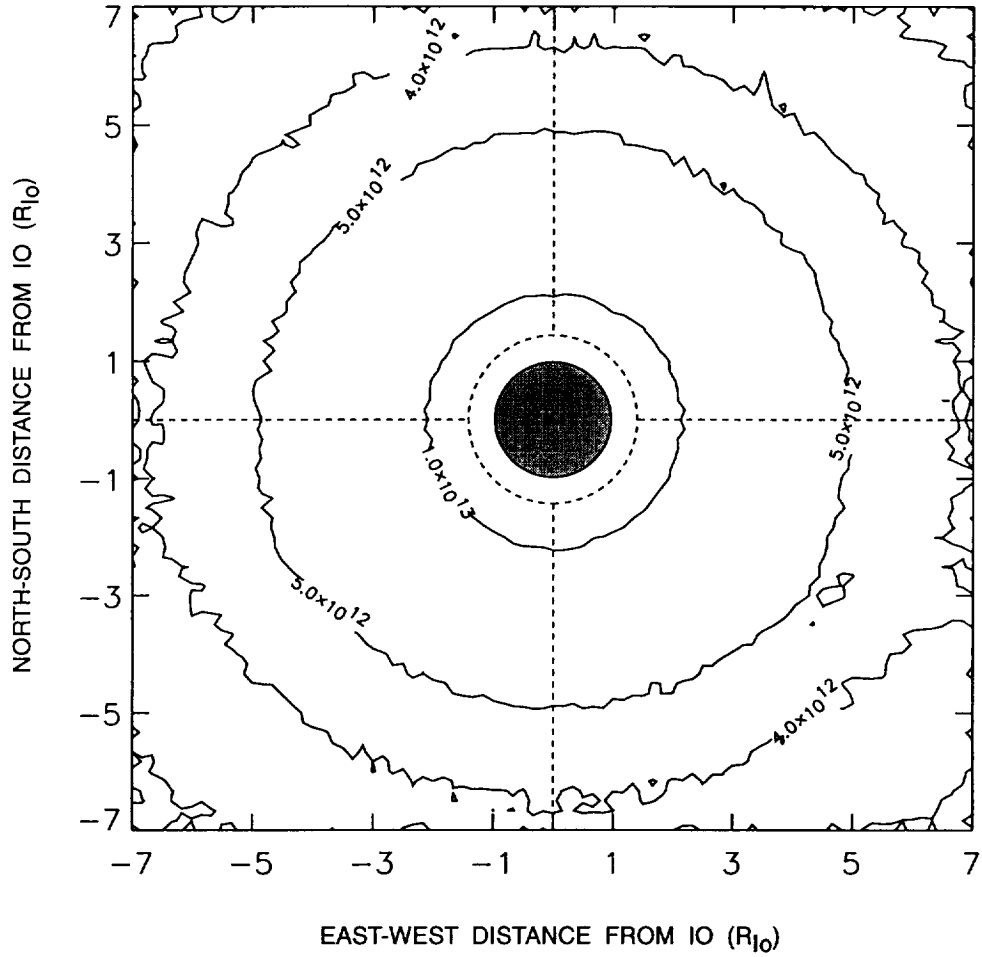

Figure 6. Model Calculated Atomic Oxygen Column Density Near Io. Column density contours are calculated for no Io plasma wake. A nominal isotropic atomic oxygen exobase source of 3.2 x 10^{27} s^{-1} ejected with a speed of 2.6 km/sec is adopted. The calculation is undertaken for an Io geocentric phase angle of 210° and an Io System III longitude of 230°. Io's location is shown by the shaded disk, and the assumed exobase radius of 2600 km is shown by the dashed circle.

caption for details). The column density distribution is symmetric about Io since the lifetime of oxygen in the plasma torus is long compared to the population time of oxygen atoms in this near-Io spatial region that extends only just beyond Io's Lagrange sphere radius of 5.81 R_{Io}.

For [O I] 6300 Å emission, the brightness distributions about Io excluding and including the Io plasma wake description are shown, respectively, in Figures 7 and 8. In Figure 7 with the plasma wake excluded, the brightness distribution about Io is slightly asymmetric in the north-south direction. This asymmetry occurs because Io is still considerably north of the plasma

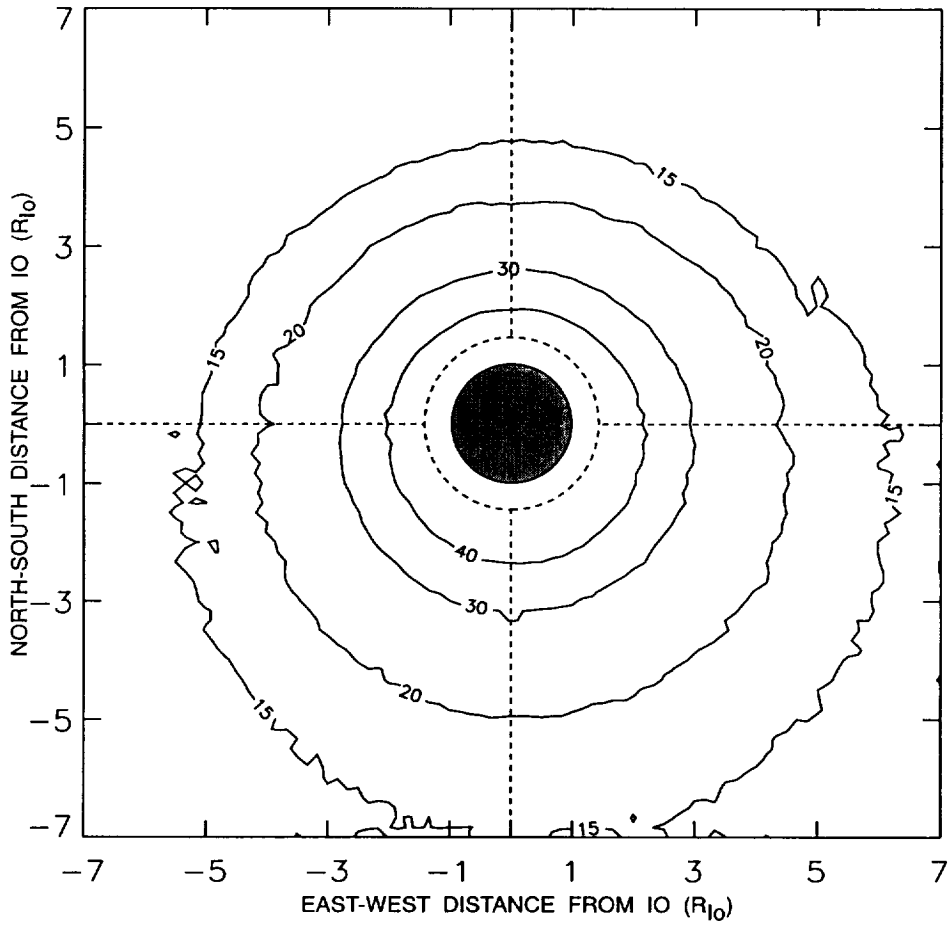

Figure 7. Model Calculated 6300 Å Atomic Oxygen Emission Brightness Near Io. Brightness contours (in Rayleighs) are calculated assuming excitation by electron impact in the plasma torus with no Io plasma wake with the same oxygen source, Io geocentric phase angle, and Io System III longitude as adopted in Figure 6.

torus; hence, for this geometry the instantaneous excitation rate in the plasma torus for the surrounding oxygen corona increases south of Io. Note that the maximum brightness contour occurs at the exobase and is nearly symmetric about the satellite. In Figure 8, with the plasma wake included, the brightness distribution about Io is significantly altered in the downstream

direction (positive east-west direction) by the presence of the plasma torus. The maximum brightness is significantly enhanced over the no plasma wake case and now occurs in a rather

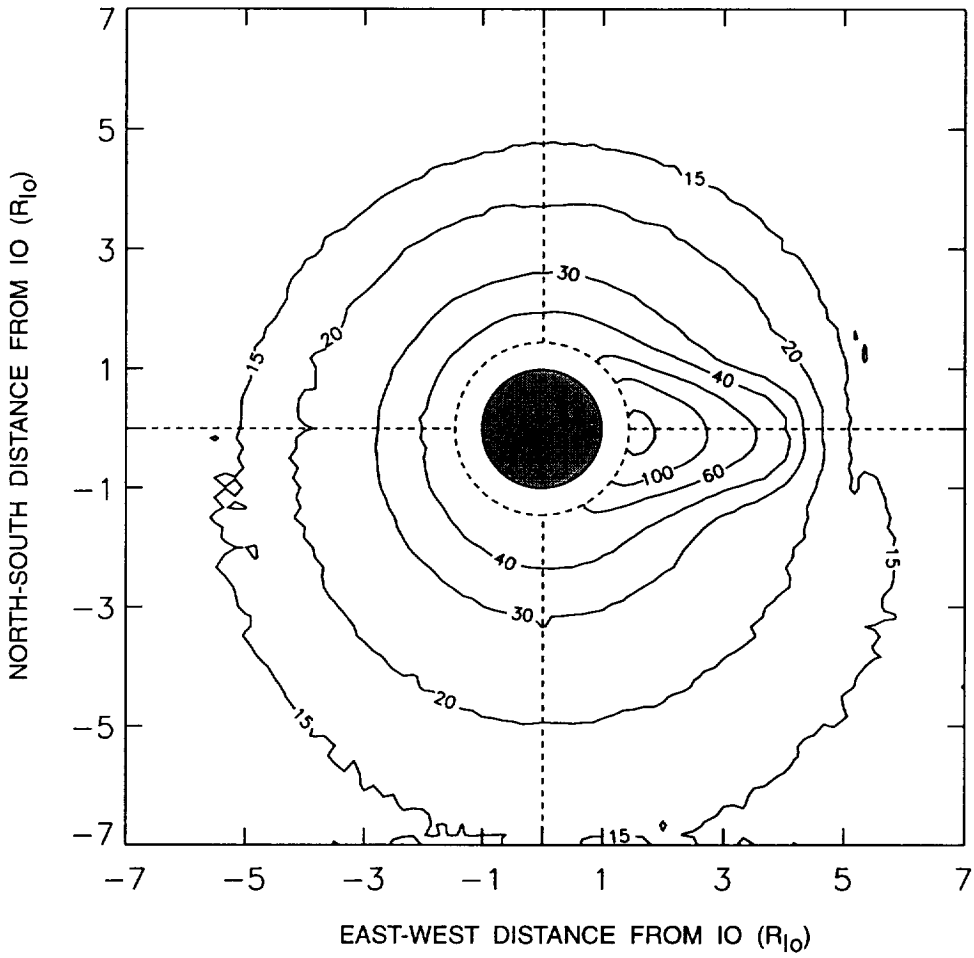

Figure 8. Model Calculated 6300 Å Atomic Oxygen Emission Brightness Near Io. Brightness contours (in Rayleighs) are calculated assuming excitation by electron impact in the plasma torus including an Io plasma wake with the same oxygen source, Io geocentric phase angle, and Io System III longitude as in Figure 6. The inner contour has a value of 200 Rayleighs.

concentrated spatial region where the plasma wake meets the exobase. The wake can, therefore, be expected to enhance the average [O I] 6300 Å brightness measured in the 5.2 by 5.2 arc second observing aperture centered on the satellite (i.e., ~ ±5.2 satellite radii about Io).

For 1356 Å emission from atomic oxygen and 1479 Å emission from atomic sulfur, the brightness distribution near Io including the Io plasma wake description are shown, respectively,

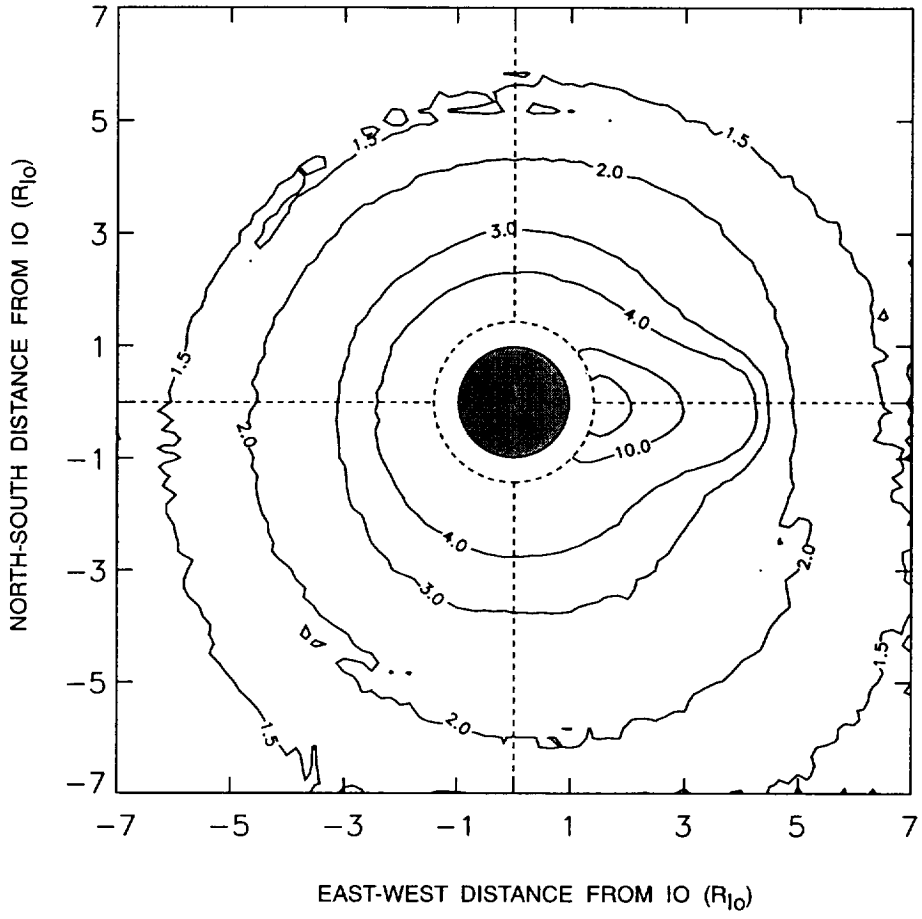

Figure 9. Model Calculated 1356 Å Atomic Oxygen Emission Brightness Near Io. Brightness contours (in Rayleighs) are calculated assuming electron impact excitation in the plasma torus with an Io plasma wake with the same O source, Io geocentric phase angle, and Io System III longitude as in Figure 6.

in Figures 9 and 10. The impact of the Io plasma wake on the O and S brightness pattern is qualitatively similar to that for the [O I] 6300 Å brightness in Figure 8. When an more realistic source rate for the flux velocity distribution containing significantly lower ballistic-speed components, such as given by Smyth and Combi (1997), is adopted in a model calculation, the absolute brightness nearer Io will be larger than the values shown in Figures 7-10 by roughly an order of magnitude.

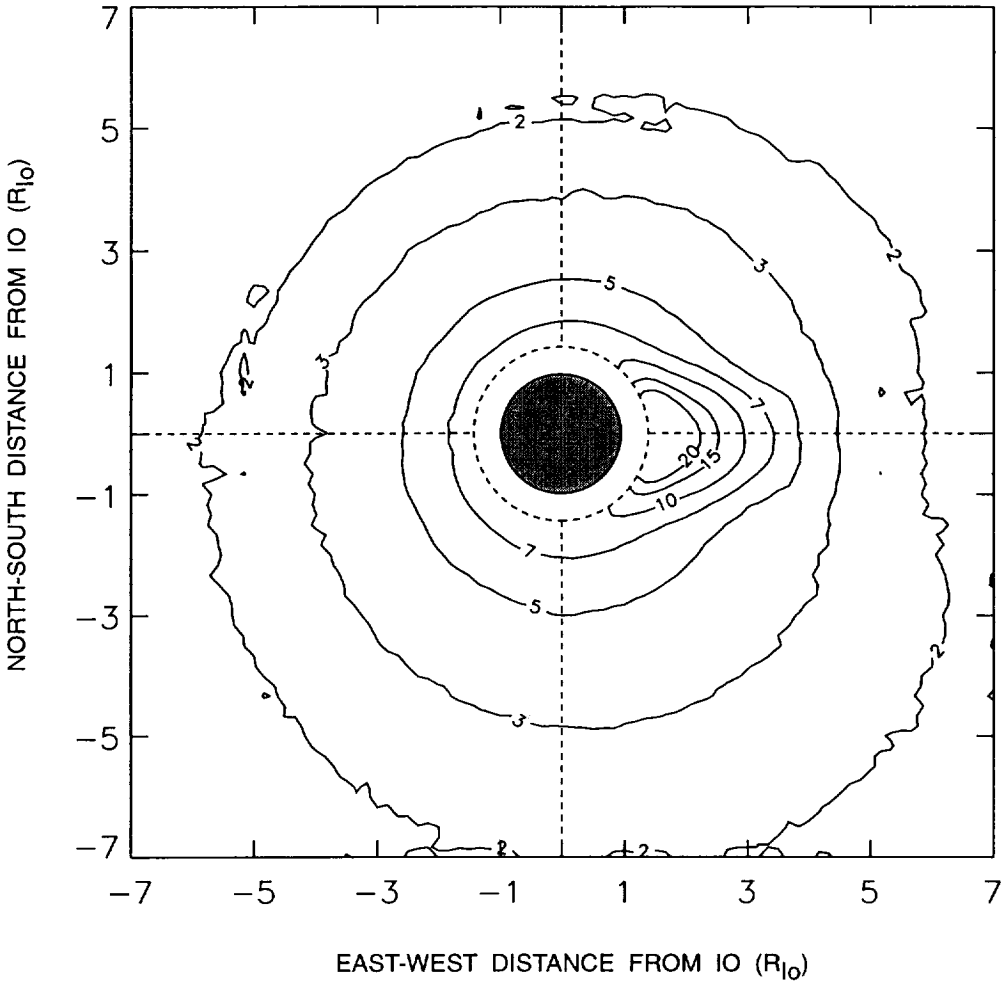

Figure 10. Model calculated 1479 Å Atomic Sulfur Emission Brightness Near Io. Brightness contours (in Rayleighs) are calculated assuming excitation by electron impact in the plasma torus including an Io plasma wake with an atomic sulfur source equal to half of the oxygen source assumed in Figure 6 and with the same Io geocentric phase angle, and Io System III longitude adopted in Figure 6.

4.3. HST Observations for O and S (Ballester Collaboration)

In the HST observing program for Io undertaken by G. E. Ballester, several ultraviolet emission lines have been measured for neutral O and S very near Io and also for ultraviolet emission lines for S^+ in the plasma torus. G. E. Ballester is presently in the process

Table 3. HST Observations of Ultraviolet Emissions Near Io

Date		Exposure Time (UT)	Io Phase Angle (degree)	Io System III Longitude (degree)	Instrument	Wavelengths[a] (Å)	Type[b] of Observation (arcsec)	Aperture Size (arcsec^2)
Eclipse Observations								
1992	26 Jan	07:19-08:04		152-179	FOS-BL/G13OH[c]	1200-1500	eclipse ingress (07:30)	1.4x4.3[d]
1993	18 Feb				GHRS/G160M	~1304	eclipse ingress (16:05)	2.0x2.0[d]
	23 Feb				GHRS/G200M	~1900	eclipse ingress (23:30)	2.0x2.0[d]
1994	15 Jul	05:24-05:51	18-21	276-288	GHRS/G140L	1230-1510	eclipse egress (05:40)	1.74x1.74
1995	21 Sept	20:04-22:12	18-36	73-132	GHRS/G140L	1230-1510	eclipse egress (20:16)	1.74x1.74
	9 Oct	12:49-13:15	16-20	358-10	FOS-BL/G190H	1650-1925	eclipse egress (13:05)	1.2x3.7
1996	23 Mar	19:29-20:00	338-343	31-49	GHRS/G140L	1230-1510	eclipse ingress (19:38)	1.74x1.74
	4 Sep	11:09-13:27	12-32	68-132	GHRS/G140L	1230-1510	eclipse egress (12:01)	1.74x1.74
	2 Oct	19:25-21:49	18-36	253-311	FOS-RD/G190H	1650-1925	eclipse egress (19:42)	1.2x3.7
East-West Observations								
1994	8 Jun	08:45-10:38	77-93		FOS-BL/G190H	1650-1925	eastern elongation	1.2x3.7
	9 Jun	07:16-09:09	268-284		FOS-BL/G190H	1650-1925	western elongation	1.2x3.7
1996	3 Oct	03:51-04:12	90-93	127-137	FOS-RD/G190H	1650-1925	eastern elongation	1.2x3.7
	4 Oct	00:45-01:06	267-270	349-358	FOS-RD/G190H	1650-1925	western elongation	1.2x 3.7
Scan Observations								
1994	6 Jun	16:49-16:59	98-100	140-145	GHRS/G140L	1230-1510	eastern elongation, S/N scan	1.74x1.74
	6 Jun	18:06-18:33	109-113	176-188	GHRS/G140L	1230-1510	eastern elongation, W/E scan	1.74x1.74
	14 Jun	15:57-16:24	279-283	52-65	GHRS/G140L	1230-1510	western elongation, W/E scan	1.74x1.74
	14 Jun	17:34-17:45	293-294	97-102	GHRS/G140L	1230-1510	western elongation, S/N scan	1.74x1.74
	16 Jun	09:48-10:15	274-278	135-148	GHRS/G140L	1230-1510	western elongation, W/E scan	1.74x1.74
	16 Jun	11:25-11:35	291-293	176-181	GHRS/G140L	1230-1510	western elongation, S/N scan	1.74x1.74
Consecutive Observations								
1996	26 Jun	04:27-10:40	106-158	352-163	GHRS/G140L	1230-1510	System III longitude coverage	1.74x1.74

[a]Only a portion of the FOS spectra is presented here.

[b]UT Times of eclipse egress (reappearance) or ingress (disappearance) in parentheses.

[c]Observations by Clarke et al. (1994), included for reference and completeness of all GHRS and FOS HST Io eclipse data.

[d]Pre-COSTAR values.

of completing two papers to describe the observing program, the data reduction procedures, and new results determined from the analysis of these data. Relevant HST ultraviolet observations for O emission lines (1304 Å multiplet, 1356 Å multiplet) and S emission lines (1389 Å multiplet, 1429 Å multiplet, 1479 Å multiplet, 1900 Å multiplet) are summarized in Table 3. The observation can be divided into four basic types: (1) eclipse events, where brightness measurements were acquired through a small aperture centered on Io before and after the satellite either entered or exited Jupiter's shadow, (2) east-west measurements, where brightness measurements were acquired through a small aperture centered on the satellite when Io was either near eastern or western elongation, (3) spatial scan measurements centered on Io to acquire both east-west and north-south brightness profile, and (4) consecutive measurements over a longer time interval (6 hours) to investigate how the brightnesses in an aperture centered on Io might depend upon Io System III longitude.

4.3.1. Brief Overview of the HST Data Set

The eight eclipse observations for Io [3 ingress (Io west of Jupiter) and 5 egress (Io east of Jupiter)] were acquired over the time interval from February 18, 1993 to October 2, 1996. Six of the eight observations show a brighter emission when Io is in the sunlight rather than when Io is in Jupiter's shadow. The brightness change for a given emission line, however, is different for the different observations. For example, the two egress observations on September 21, 1995 and September 4, 1996 were acquired for very similar System III longitudes, but the former observation has a much smaller brightness change than the latter. Whether this difference is attributed to changes in the torus properties over the one-year time interval or to temporal changes that occur on a much faster time scale remains to be determined.

Observations of the O and S emission lines in Table 3 for Io near eastern and western elongation, both for the stationary aperture and for the scan observations, indicate a significant brightness asymmetry. The O and S emissions are brighter when Io is west of Jupiter. This east-west brightness asymmetry is similar to that reported earlier from IUE measurements (Ballester 1989) and is related to the presence of an east-west electric field in the Jupiter system. This east-west asymmetry in the HST measurements, however, exhibits some apparent time variability both in the absolute brightness as well as the location of the maximum in its brightness profile relative to Io's location. For example, the O 1356 Å and the S 1479 Å emissions have symmetric profiles relative to Io for the June 14, 1994 measurements (Io phase angles 279-283°, Io System III longitudes 52-65°) whereas the profiles are asymmetric for the June 16, 1994 measurements (Io phase angles 274-278°, Io System III longitudes 135-148°) with more emission on the side facing away from Jupiter. For the June 16, 1994 measurements, the spatial brightness profiles

are detectable at least out to 1500 km (almost an Io radius) above the surface. The HST FOS observations acquired on October 2-4, 1996, which are spectral in nature but also contain spatial information for an extended source) indicate that some of the asymmetry about Io in the emission brightness may be caused by the presence of Io's plasma wake located in the downstream flow (i.e., above the leading hemisphere of Io).

System III longitude variability in the O and S emissions has also been measured by using the observations over a six hour time interval in Table 3. Although the emissions are weak, they show an anti-correlation with Io System III longitude in the plasma torus. The emission brightness appears to decrease when Io crosses the plasma torus centrifugal plane at ~112°. These observations, which occur for an eastern Io phase range of 106-158° and an Io System III longitude range of 352-163°, may also, upon reduction, be analyzed using our O and S neutral cloud models.

4.3.2. Initial Investigation of Io Eclipse Observations

Late in the third project year, we have received in our collaboration with G. E. Ballester some of her data for the observed O and S brightness variations occurring in the ingress and egress Io eclipse measurements. Although we have not yet received all of these eclipse data and have not had sufficient time to analyze them, very preliminary conclusions are suggested. In egress observations, where the time variability of the emission may be measured over a longer time interval, the O and S brightness, although time dependent, appear to increase by a factor of only about two or three. This indicates that the O and S atomic species do not collapse in eclipse by an order of magnitude or more as are expected from model calculations for a sublimation atmosphere where only gas phase chemistry and a surface sink are operative. Apart from localized volcanic sources, this suggests that an additional source likely exists during eclipse for the creation of O and S in Io's atmosphere. A likely and appropriate source appears to be electron impact dissociation of SO_2 and SO, which is dominated in the day atmosphere by photodissociation but which is estimated to be the dominant source in the Io's eclipse atmosphere and comparable to the surface sink loss rate during eclipse. Preliminary Io eclipse model calculations to analyze the eclipse data will be presented at the Division for Planetary Sciences meeting in Padua, Italy during the week of October 10-15, 1999.

4.4. Electron Impact Emission Rates for Atomic Oxygen and Sulfur Lines

The electron impact emission rates for various O and S emission lines are important in modeling and studying the ultraviolet and visible brightnesses of atomic oxygen and sulfur in Io's corona and extended neutral clouds. A number of these O and S emission lines have been calculated using the Collisional Radiative Equilibrium (COREQ) model developed by Shemansky (1990) with updated atomic data files for atomic oxygen and sulfur also supplied by Shemansky (1992). For an electron temperature of 60,000 K, these emission rates are summarized in Table 4 for three different values of the electron density, which are typical of the range of values that occur in the plasma torus near Io. Examination of Table 4 reveals that the emission rates for all the oxygen lines and for the sulfur lines at the 1814 Å multiplet and higher wavelengths are approximately independent of the electron density. For the sulfur lines with lower wavelength, however, the emission rates for some individual emission lines in a multiplet can vary significantly with changing electron density while the emission rates for other individual emission lines in the same multiplet are essentially constant. A dramatic example of this variation occurs for the dominant 1385.51 Å emission line of the 1389 multiplet where the emission rate can be seen in Table 4 to increase by a factor of 4.7 when the electron density varies from 500 cm^{-3} to 3000 cm^{-3}. For even larger electron densities that have been shown by Galileo spacecraft measurements (Gurnett et al. 1996) to be present in the upstream Io plasma wake with peak values up to ~40,000 cm^{-3}, the variation of the emission rate for the 1385.51 Å emission line increases even more. For an electron temperature of 60,000 K, for example, the emission rate changes by a factor of about 6.8 as the electron density is increased from 500 cm^{-3} to 5000 cm^{-3} and by a factor of 17.2 as the electron density is increased from 500 cm^{-3} to 40,000 cm^{-3}. If these rates are correct, the brightness of the 1385.51 Å emission line, which is proportional to the electron density times the emission rate, would therefore change by a factor of 68 and 1376 for these two cases.

In our collaboration with Dr. G. E. Ballester of the University of Michigan, we have undertaken preliminary comparison of the calculated and observed relative strengths of various ultraviolet emission line multiplets of interest for atomic oxygen and sulfur measured near Io. In a number of important cases, this agreement is poor, suggesting that the incomplete atomic data upon which the calculations are based require improvement. The matter is presently under further study by Dr. G. E. Ballester to ascertain the nature of the disagreements and to determine possible improvements to be incorporated in the calculation of the emission rates. Clearly detailed laboratory measurements would be very useful, particularly for atomic sulfur.

Table 4
Atomic Oxygen and Sulfur Line Emission Rates

Species	Vacuum Wavelength (Å)	Transition Array	Multiplet	Emission Rates* ($cm^3 sec^{-1}$) (n_e=1000 cm^{-3})	(n_e=2000 cm^{-3})	(n_e=3000 cm^{-3})
OI	1304 multiplet	$2s^2\ 2p^3\ (^4S^0)3s$	$^3S^0$			
	1302.17	(J=1→2)		6.602×10^{-10}	6.603×10^{-10}	6.603×10^{-10}
	1304.86	(J=1→1)		3.937×10^{-10}	3.938×10^{-10}	3.937×10^{-10}
	1306.03	(J=1→0)		1.312×10^{-10}	1.313×10^{-10}	1.312×10^{-10}
OI	1356 multiplet	$2s^2\ 2p^3\ (^4S^0)3s$	$^5S^0$			
	1355.60	(J=2→2)		1.929×10^{-10}	1.929×10^{-10}	1.928×10^{-10}
	1358.52	(J=2→1)		5.622 x 10-11	5.621×10^{-11}	5.619×10^{-11}
	1359.79	(J=2→0)		0.0	0.0	0.0
OI	6302.11	$2s^2\ 2p^4\ (^1D \rightarrow ^3P)$		2.419×10^{-9}	2.416×10^{-9}	2.412×10^{-9}
OI	5578.89	$2s^2\ 2p^4\ (^1S \rightarrow ^1D)$		2.210×10^{-10}	2.219×10^{-10}	2.227×10^{-10}
SI	1299 multiplet	$3s^2\ 3p^3\ (^2P)4s''$	$^3P^0$			
	1295.65	(J=2→2)		5.257×10^{-10}	5.130×10^{-10}	5.033×10^{-10}
	1296.17	(J=1→2)		9.285×10^{-11}	9.669×10^{-11}	9.939×10^{-11}
	1302.33	(J=2→1)		7.229×10^{-11}	7.053×10^{-11}	6.920×10^{-11}
	1302.86	(J=1→1)		5.488×10^{-11}	5.715×10^{-11}	5.875×10^{-11}
	1303.10	(J=0→1)		7.496×10^{-12}	1.357×10^{-11}	1.869×10^{-11}
	1305.88	(J=1→0)		7.313×10^{-11}	7.616×10^{-11}	7.829×10^{-11}
SI	1256 multiplet	$3s^2\ 3p^3\ (^4S)\ 6d$	$^3D^0$			
	1247.10	(J=1→2)		5.466×10^{-14}	8.261×10^{-14}	1.033×10^{-13}
	1247.13	(J=2→2)		2.113×10^{-12}	2.258×10^{-12}	2.383×10^{-12}
	1247.15	(J=3→2)		4.106×10^{-11}	3.952×10^{-11}	3.831×10^{-11}
	1253.29	(J=1→1)		8.128×10^{-13}	1.228×10^{-12}	1.536×10^{-12}
	1253.32	(J=2→1)		6.278×10^{-12}	6.708×10^{-12}	7.080×10^{-12}
	1256.09	(J=1→0)		1.107×10^{-12}	1.674×10^{-12}	2.093×10^{-12}
SI	1389 multiplet	$3s^1\ 3p^5$	$^3P^0$			
	1381.55	(J=1→2)		1.208×10^{-12}	1.259×10^{-12}	1.293×10^{-12}
	1385.51	(J=0→1)		9.244×10^{-12}	1.683×10^{-11}	2.317×10^{-11}
	1388.43	(J=2→2)		2.191×10^{-12}	2.196×10^{-12}	2.205×10^{-12}
	1389.15	(J=1→1)		3.809×10^{-13}	3.968×10^{-13}	4.075×10^{-13}
	1392.59	(J=1→0)		1.163×10^{-12}	1.212×10^{-12}	1.245×10^{-12}
	1396.11	(J=2→1)		2.270×10^{-12}	2.276×10^{-12}	2.286×10^{-12}

Table 4 (continued)
Atomic Oxygen and Sulfur Line Emission Rates

Species	Vacuum Wavelength (Å)	Transition Array	Multiplet	Emission Rates* ($cm^3 sec^{-1}$) (n_e=1000 cm^{-3})	(n_e=2000 cm^{-3})	(n_e=3000 cm^{-3})
SI	1429 multiplet	$3s^2\ 3p^3\ (^4S)3d$	$^3D^0$			
	1425.03	(J=3→2)		2.412×10^{-9}	2.322×10^{-9}	2.251×10^{-9}
	1425.19	(J=2→2)		1.221×10^{-10}	1.304×10^{-10}	1.376×10^{-10}
	1425.22	(J=1→2)		3.145×10^{-12}	4.751×10^{-12}	5.940×10^{-12}
	1433.28	(J=2→1)		3.701×10^{-10}	3.952×10^{-10}	4.170×10^{-10}
	1433.31	(J=1→1)		5.032×10^{-11}	7.602×10^{-11}	9.504×10^{-11}
	1436.97	(J=1→0)		6.290×10^{-11}	9.503×10^{-11}	1.188×10^{-10}
SI	1479 multiplet	$3s^2\ 3p^3\ (^2D)4$	$^3D^0$			
	1474.00	(J=3→2)		5.238×10^{-10}	5.042×10^{-10}	4.887×10^{-10}
	1474.38	(J=2→2)		3.452×10^{-11}	3.688×10^{-11}	3.892×10^{-11}
	1474.57	(J=1→2)		1.008×10^{-12}	1.523×10^{-12}	1.904×10^{-12}
	1483.04	(J=2→1)		7.272×10^{-11}	7.769×10^{-11}	8.200×10^{-11}
	1483.23	(J=1→1)		1.115×10^{-11}	1.685×10^{-11}	2.107×10^{-11}
	1487.15	(J=1→0)		1.320×10^{-11}	1.944×10^{-11}	2.493×10^{-11}
SI	1814 multiplet	$3s^2\ 3p^3\ (^4S)\ 4s$	$^3S^0$			
	1807.31	(J=1→2)		1.721×10^{-9}	1.723×10^{-9}	1.725×10^{-9}
	1820.34	(J=1→1)		9.209×10^{-10}	9.221×10^{-10}	9.230×10^{-10}
	1826.24	(J=1→0)		3.058×10^{-10}	3.062×10^{-10}	3.065×10^{-10}
SI	1900 multiplet	$3s^2\ 3p^3\ (^4S)\ 4$	$^5S^0$			
	1900.29	(J=2→2)		6.780×10^{-10}	6.780×10^{-10}	6.781×10^{-10}
	1914.70	(J=2→1)		1.952×10^{-10}	1.952×10^{-10}	1.952×10^{-10}
	1921.23	(J=2→0)		0.0	0.0	0.0
SI	10820 multiplet	$3s^2\ 3p^4\ (^1D \rightarrow ^3P)$				
	10824.10	(J=2→2)		7.125×10^{-9}	7.120×10^{-9}	7.115×10^{-9}
	11308.96	(J=2→1)		2.065×10^{-9}	2.064×10^{-9}	2.063×10^{-9}
	11540.69	(J=2→0)		1.286×10^{-12}	1.285×10^{-12}	1.284×10^{-12}

*** Emission rate determined for an electron temperature of 60,000 K**

4.5. Neutral O and S Energy Budget

Estimates for the rate at which energy is required to sustain the O and S atoms escaping from near Io's exobase because of the interaction of Io's atmosphere with the corotating magnetospheric plasma were made in the first project year for three source processes: (1) incomplete collisional cascade, (2) slow-velocity charge exchange and direct ejection, and (3) fast-velocity charge exchange. These results and their implications for Io's local environment and the plasma torus were published (Smyth 1998, in Appendix C) and are briefly summarized below.

For the incomplete collisional cascade, the required energy supply rate is estimated to be 7.5×10^9 watts. If this energy supply rate is, as expected, ~20% of the total incomplete collisional cascade energy deposition rate in the heating layer, then it implies that 56% of the upstream ion kinetic energy flow rate of 6.7×10^{10} watts for a reference cross sectional area of an Io disk area is required for this process. This is a factor of 2.8 times larger than the previously adopted value of 20% and implies that the effective deflection of magnetospheric plasma out of the interaction region near Io is less than previously thought for the collisional cascade process. For slow-velocity charge exchange and direct ejection (centered about 20 km/sec), the energy supply rate is estimated to be 3.3×10^{10} watts, which is 50% of the reference upstream ion kinetic energy flow rate. For fast-velocity charge exchange (centered about ~60 km/sec), the energy supply rate is much larger and is the dominant energy loss mechanism with an estimated value of 6.04×10^{11} watts, which is ~900% of the reference upstream ion kinetic energy flow rate. The total estimated neutral energy loss rate for all three processes (including radiative loss processes) is 6.75×10^{11} watts and is too large by an order of magnitude to be provided by the reference upstream initial ion kinetic energy flow rate.

The required neutral energy supply rate (i.e., power) is, however, matched by the magnetic field energy density flow rate of 7.9×10^{11} watts for the upstream reference area and implies that the charge exchange energy loss rates are capable of producing a large pickup current as well as a significant reduction in the local planetary magnetic field in the interaction region near Io. The magnitude of the current and the reduction in the local magnetic field will depend critically upon the volume of the interaction region established by the solution of the three-dimensional magnetospheric flow problem past Io including these complex plasma-neutral interactions. Rough estimates suggest a pickup current in the range of $\sim 4 \times 10^6$ to 2×10^7 A and a reduction (ΔB) in the local magnetic planetary field of ~450 nT. This estimated reduction of the magnetic field is similar to the remaining and unexplained ΔB of ~400-500 nT determined in

a recent analysis (Khurana et al. 1997) of the magnetic field depression measured near Io by the Galileo Magnetometer (Kivelson et al. 1996 a,b) and attributed by them to an internal magnetic dipole field for Io. Hence, we conclude that the reduction of the planetary magnetic field measured by Galileo near Io may be a direct reflection of the local charge exchange source and need not require an internal magnetic field for the satellite.

V. Studies for the HST/STIS UV Observations of Io (Roesler Collaboration)

During this project, a collaboration with F. L. Roesler of the University of Wisconsin-Madison was established to study the spectacular high-resolution (~90 km/pixel) ultraviolet images of Io acquired in the multiplets of several O and S emission lines by the new Space Telescope Imaging Spectrometer (STIS) aboard the Hubble Space Telescope (HST). The HST/STIS images were acquired in a long slit with a width of 2 arc seconds that was centered on Io. The images provide (1) a detailed picture on and near the satellite disk (~1 arc second in diameter) to study Io's O and S atmospheres and their plasma torus interactions and (2) O and S brightness profiles along the slit to study Io's corona and near extended neutral clouds. In addition to the O and S emissions, which had similar morphology and time variability near Io's disk and along the slit, the HST/STIS images also contained the surprising discovery of hydrogen Lyman-α emission that remained relatively constant in time and that occurred only on the satellite disk within a localized region near the north and south poles. A paper (Roesler et al. 1999, in Appendix D) has been published in Science describing the HST/STIS high-resolution image observations acquired in 1997 when Io was located near western elongation. Additional investigations of these 1997 images and of new 1998 image observations are ongoing in this project. A brief summary of progress of these investigations is given below.

5.1. HST/STIS Ultraviolet Observations for O and S

Very spectacular HST/STIS ultraviolet images in several multiplet components of O and S ultraviolet emission lines have been acquired simultaneously in 1997 (Roesler et al. 1999) and in 1998 (Roesler 1999) in a long 2" wide slit centered on Io and inclined about 50° relative to the spin axis of Jupiter. These O and S images (~90 km/pixel) show these morphological features: (1) bright equatorial spots located near the sub- and anti-Jupiter points of the satellite that rock up and down in the same sense as the rotating tangent points of the dipole planetary magnetic field at Io and suggest that the spots are associated with closure of the Birkeland current (i.e., equatorial aurora) at Io, with the equatorial spot near the anti-Jupiter point (centered on Io's outer hemisphere) significantly brighter and larger than the equatorial spot near the sub-Jupiter point

(centered on Io's inner hemisphere); (2) limb glow all around the disk with a brighter pole hemisphere facing the plasma torus centrifugal equator plane, consistent with the two earlier HST images (~160 km/pixel) acquired in [O I] 6300 Å emission by Trauger et al. (1997) and with a set of visible (0.38 to 1.04 micron) eclipse images of Io (Geissler et al. 1999) acquired by the Galileo Solid State Instrument (SSI); and (3) extended emissions along the slit that are seen out to ~15-20 R_{Io} in the near-Io neutral clouds where the signal is then lost in the background.

The spatial profiles for the extended emission along the STIS slit for the two strongest multiplet emission lines, O (1356 Å) and S (1479 Å), are very similar in shape and are illustrated for S in Figure 11a for the sum of two October 14, 1997 observation and in Figure 11b for the sum of three August 23, 1998 observations. At the mid point of the observations, the Io geocentric phase angle in Figure 11a is 249° (21° before western elongation at 270°, see insert) so that any Io plasma wake enhanced emission (shaded cone) would appear to the right of Io, and in Figure11b is 312° (42° after western elongation, see insert) so that any Io plasma wake enhanced emission (shaded cone) would appear to the left of Io. Note that the emission profiles are indeed asymmetric by a factor of ~2 to the right in Figure 11a and a factor of ~4 to the left in Figure 11b. This pattern is evident in all of the separate O and S extended emission profiles and

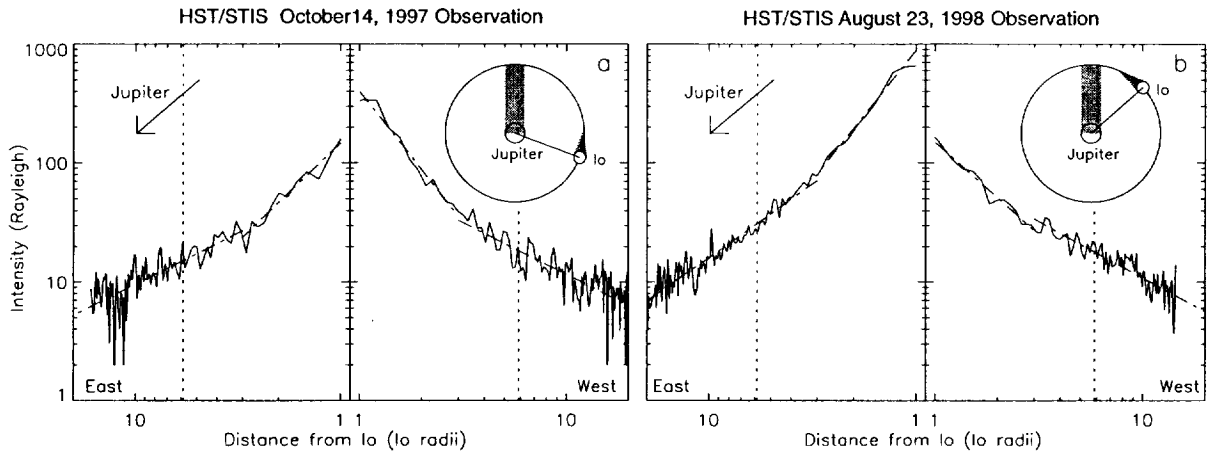

Figure 11. Io Atomic Sulfur 1479 Å Emission Brightness Acquired by HST/STIS. The sulfur 1479 Å emission brightness profile along an Io-centered slit tilted 50° toward Jupiter acquired by the HST/STIS instrument is shown by the solid lines (dashed lines are fits) in (a) for the composite of two October 14, 1997 measurements with a mid-point Io geocentric phase angle of 249° and Io System III longitude of 17.5°, and in (b) for the composite of three August 14, 1998 measurements with a mid-point Io geocentric phase angle of 312° and Io System III longitude of 85°. Also indicated are the slit-half that is closer to Jupiter (arrow), the location of Io's Lagrange sphere (dotted vertical lines), and a top-view insert showing the location of Io and attached plasma wake on its orbit about Jupiter with attached shadow.

strongly suggests that the Io plasma wake provides a clear enhancement signature that is visible from Io's limb to distances at least as far as the Lagrange sphere at 5.85 R_{Io}. A similar enhancement likely due to Io's plasma wake was seen in [O I] 6300 Å emission (see Figure 5). Neutral cloud model calculations for the 1356 Å emission brightness of O and the 1479 Å emission brightness of S with and without the Io plasma wake (see Section 4.2) indeed show significant wake emission enhancements near Io. Hence, it would appear possible to study the HST/STIS brightness profile for O and S to determine simultaneously (1) on the "non-wake side" of Io (excited by the plasma torus electrons) the exobase source strength and velocity distribution from modeling the emission profile for O and S within the corona and near extended cloud, and (2) on the "wake side" of Io (excited by the plasma torus and plasma wake electrons) the wake emission contribution and a characterization of the Io plasma wake properties. This modeling opportunity is to be undertaken in a future continuation project using refined background subtracted and corrected O and S brightness profiles that are currently being produced.

In addition, of particular importance is the temporal variability of the HST/STIS ultraviolet O and S line intensities for the equatorial spots and extended profiles which was strongly correlated with simultaneous ground-based observations of the [O I] 6300 Å emission intensity, as discussed in Roesler et al. (1999). This correlation is extremely important since it tells us (1) that both the visible and ultraviolet emission lines for oxygen (and sulfur) are experiencing globally a similar time-variable excitation phenomena, and (2) that the large 1990-1998 data set for the visible [O I] 6300 Å emission intensity (see Section 4.1) can now be studied to probe the nature of the excitation phenomena for both short term (~1 hour) variability, time-average System III longitude variability, and local-time variability.

5.2. HST/STIS Ultraviolet Observations for H Lyman-α

The surprising detection of ~2,000 Rayleighs of hydrogen Lyman-α emission confined near north and solar polar patches on the satellite disk was reported by Roesler et al. (1999, see Fig. 2e in Appendix D) with two very preliminary interpretations for these polar patches presented. First, the Lyman-α patches may reflect a localized Iogenic H gas source at the polar regions likely excited by solar resonance scattering. Such local polar H sources may possibly be created by plasma impact of the surface (e.g., H liberated by surface sputtering and/or H^+ converted to H at the surface) or by patchy frost deposits at the poles. Second, the Lyman-α patches may, alternatively, only be reflected sunlight from Io's surface that has been absorbed more strongly near Io's equator by a thicker SO_2 gas column (or possibly reflected more weakly by a smaller surface albedo) and less strongly absorbed near Io's poles by a thinner SO_2 gas

column (or possibly reflected more strongly by a larger surface albedo). Ongoing investigations for both of these possibilities are being currently pursued. The recent Galileo identifications of a fresh source of H^+ ions from Io (Frank and Paterson 1999; Chust et al. 1999) suggest that some Iogenic H should be present and converted to H^+ primarily by charge exchange with O^+ plasma torus ions. Some preliminary investigation for such an H source has been undertaken in this project and is reported below.

5.3. Model Development and Calculations for H and H^+ at Io

A neutral cloud model at AER for atomic hydrogen has been developed in this project. This has been motivated by (1) the recent detection of H Lyman-α emission in Io's atmosphere near both the north and south polar regions (Roesler et al. 1999) and (2) the detection of pickup H^+ ions in the near vicinity of Io by the PLS instrument of the Galileo spacecraft (Frank and Paterson 1999) and the PWS instrument of the Galileo spacecraft (Chust et al. 1999). Preliminary model calculations to explore the relationship of the H source strength, the H column density, and the H^+ pickup ion density have been undertaken.

5.3.1. A Neutral Cloud Model for Atomic Hydrogen

The inclusion of atomic hydrogen in the neutral cloud model requires the specification, implementation, and calculation of the lifetime processes in the plasma torus and of the excitation processes for the Lyman-α emission line. A significant amount of work has been expended to accomplish this objective as summarized briefly below.

The primary lifetime processes for atomic hydrogen are electron impact and charge exchange with O^+ and H^+.

$$H + e \text{ ----> } H^+ + 2e \qquad \text{(R1)}$$
$$H + O^+ \text{ ----> } H^+ + O \qquad \text{(R2)}$$
$$H + H^+ \text{ ----> } H^+ + H \quad . \qquad \text{(R3)}$$

For plasma torus properties typical of the Voyager 1 spacecraft encounter time, approximate H lifetimes for these three reactions at Io's orbital position near western elongation are ~140 hrs, ~28 hrs, and ~122 hrs, respectively. The first lifetime value is based upon the assumption of an electron density of 2000 cm^{-3} and an electron temperature of 5 eV. The second lifetime is based upon a corotational speed of ~57 km sec^{-1} and an O^+ density of 1000 cm^{-3}. The third lifetime is based upon a corotational speed of ~57 km sec^{-1}, an ion temperature of 40 eV, and a likely H^+

density of 100 cm^{-3}. The thermalized H^+ density in the plasma torus is not well known. The H^+ ion is so light that its pickup speed of ~57 km sec^{-1} is equivalent to only about 17 eV of gyrational kinetic energy, which is less than its assumed thermalized energy of ~40 eV with an equivalent Maxwell-Boltzmann average speed of ~88 km sec^{-1}. Hence, an H^+ ion upon thermalizing with the heavy ions (O^+, O^{++}, S^+, S^{++}, etc.) of the plasma torus will actually increase its gyrational kinetic energy, in contrast to the heavy ions which decrease their gyrational kinetic energies. The rate for reaction (R3) thus depends both upon the corotational velocity and the ion temperature. The lifetimes for the three reactions above have been implemented in the neutral cloud model.

Two plasma torus excitation mechanisms for H Lyman-α emission (1216 Å) have also been being incorporated in the neutral cloud model. The first is electron impact

$$H(1s) + e \text{ ----> } H(2p) + 2e \qquad \text{(R4)}$$

and the second is solar resonance scattering by H atoms. It has only been in the past decade that formalism for calculating the electron impact Lyman-α excitation rate for atomic hydrogen has been effectively solved. This underscores the extreme difficulty of dealing accurately with the ultraviolet emission line rates of much heavier atoms, such as atomic oxygen and sulfur. Assuming at Io the same (optically and electron-impact thin) column of atomic hydrogen, H Lyman-α excitation by solar resonance scattering is about 20 times brighter than excitation by plasma torus electron impact.

5.3.2. Model Calculations for the Distribution of H and H^+ near Io

For the Galileo spacecraft encounter with Io downstream of the satellite on December 7, 1995, Frank and Paterson (1999) have reported the detection of ~30 new pickup H^+ ions cm^{-3} from the analysis of the PLS measurements, and Chust et al. (1999) have reported the detection of ≥20 new pickup H^+ ions cm^{-3} from analysis of PWS measurements. These measurements suggest that there is an H source at Io that is primarily converted into H^+ by charge exchange with O^+ [reaction (R2)]. Using the new H neutral cloud model described above, preliminary calculations have been undertaken to determine the H source rate at Io's exobase necessary to sustain the measured H^+ pickup ion density of ~30 cm^{-3} determined by Frank and Paterson (1999) downstream of the satellite and also to calculate the corresponding column density and Lyman-α brightness distributions above the exobase in Io's corona. The pickup ion density is calculated in a parallel method to that for the SO_2^+ pickup ion density about Io (see Section III above and Smyth and Marconi 1999, in Appendix B). For a typical gas temperature at Io's exobase of

~1500 K, H atoms have an average thermal speed of 5 km s^{-1} and will therefore rapidly escape Io's Lagrange sphere since the satellite surface escape speed is only 2.56 km s^{-1}. To achieve the downstream H^+ pickup ion density of ~30 cm^{-3}, a simple source of 4.5 x 10^{27} H atoms s^{-1} ejected isotropically at 5 km s^{-1} from Io's exobase (dashed circle) is required and produced the calculated H column density and Lyman-α brightness distribution shown in Figures 12 and 13, respectively.

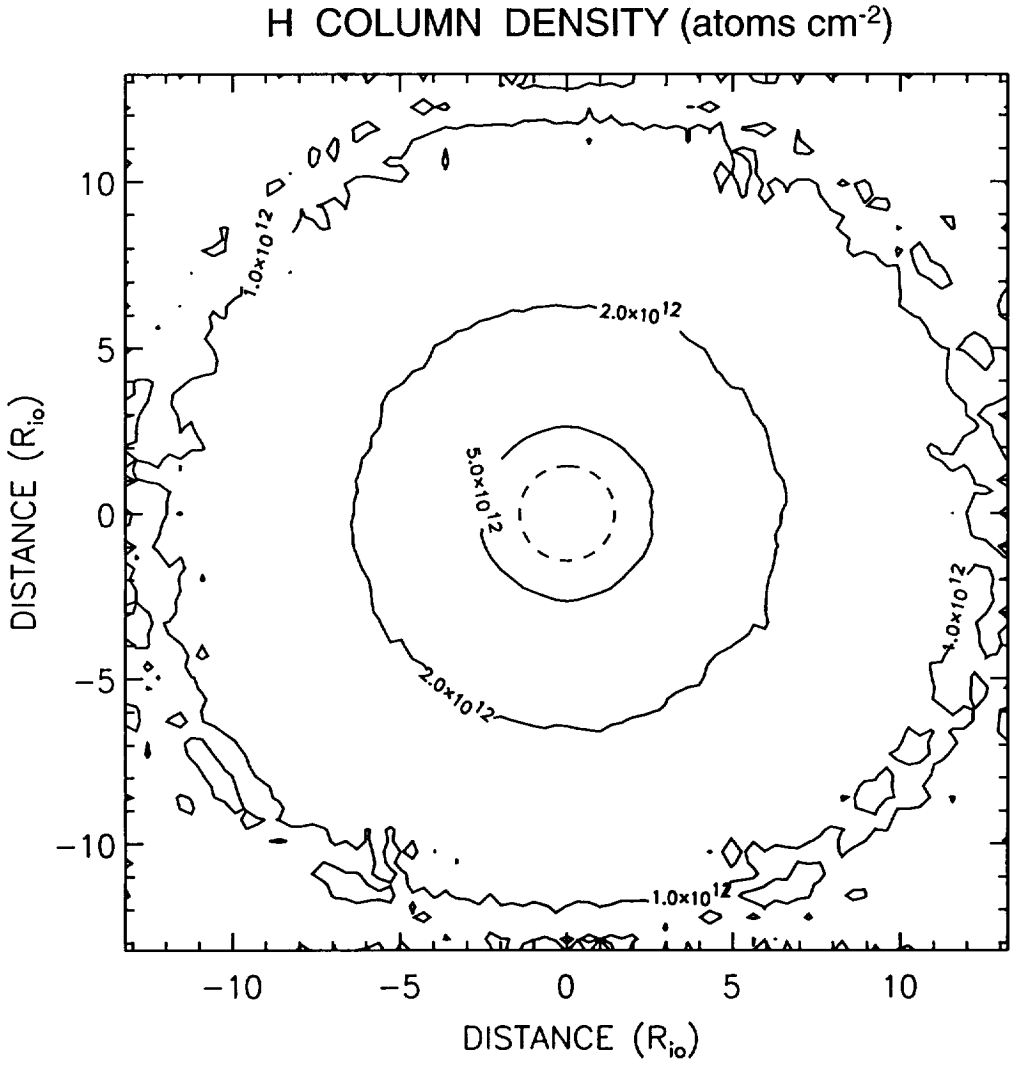

Figure 12. Hydrogen Column Density near Io. The column density (atoms cm^{-2}) was calculated for a source of 4.5 x 10^{27} H atoms s^{-1} ejected isotropically at 5 km s^{-1} from Io's exobase (dashed circle) with an assumed radius of 2600 km. The H source strength (and hence the corresponding column density) was calibrated by requiring at roughly the downstream distance of the Galileo spacecraft trajectory the total H^+ pickup ion density to be 30 ions cm^{-3} as determined by Frank and Paterson (1999). The satellite was located at an Io geocentric phase angle of 270° (western elongation) and at an Io System III longitude angle of 230° (well north of the plasma torus equator plane). The box size for collection of the column density was 600 km. In the neutral cloud model calculation, 8100 orbits for H atoms were used at the exobase.

In Figure 12, the H column density near the exobase is ~5 x 10^{12} cm^{-2}. In Figure 13, the brightness contour of 500 Rayleighs lies just above and also just below the exobase (dashed circle) near the location of Io's disk and is based upon the maximum excitation for solar resonance scattering (line-center g-factor at 1 AU of 2.72 x 10^{-3} photons $atom^{-1}$ s^{-1}) that occurs at

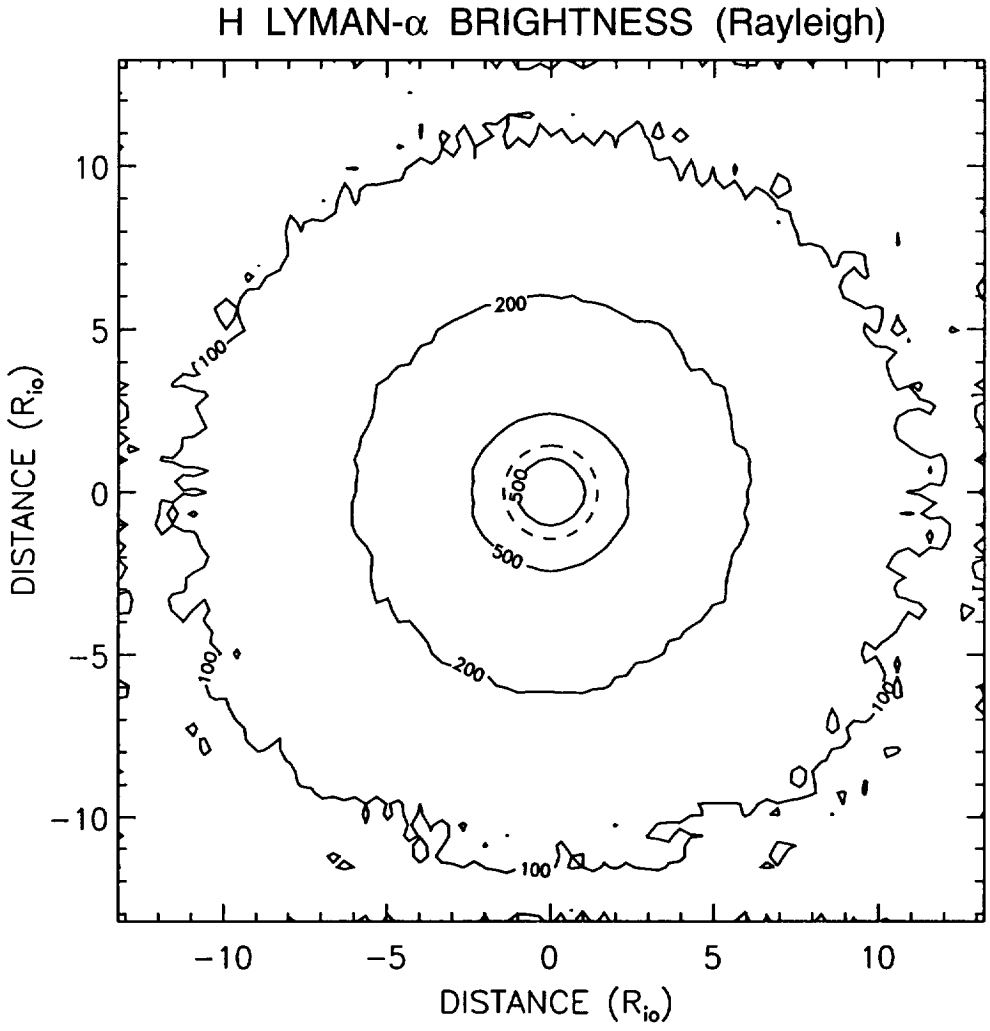

Figure 13. Hydrogen Lyman-α Brightness near Io. The brightness (Rayleighs) was calculated for a source of 4.5 x 10^{27} H atoms s^{-1} ejected isotropically at 5 km s^{-1} from Io's exobase (dashed circle) with an assumed radius of 2600 km. The H source strength (and hence the corresponding brightness) was calibrated by requiring at roughly the downstream distance of the Galileo spacecraft trajectory the total H^+ pickup ion density to be 30 ions cm^{-3} as determined by Frank and Paterson (1999). The line-center g-factor at 1 AU of 2.72 x 10^{-3} photons $atom^{-1}$ s^{-1} adopted for H Lyman-α solar resonance scattering is for solar maximum. The satellite was located at an Io geocentric phase angle of 270° (western elongation) and at an Io System III longitude angle of 230° (well north of the plasma torus equator plane). The box size for collection of both pickup ion density and sky-plane brightness was 600 km. In the neutral cloud model calculation, 8100 orbits for H atoms were used at the exobase.

solar maximum. For the HST/STIS observation on October 14, 1997, however, the line-center g-factor at 1 AU was smaller (1.5×10^{-3} photons $atom^{-1}$ s^{-1}) by a factor of 0.552 so that the 500 Rayleigh contour is reduced to ~275 Rayleighs. If the polar patches of the H Lyman-α emission detected in the HST/STIS observations discussed above are to be produced by a larger SO_2 column at Io's equator, then the equatorial SO_2 column density must be in the range of ~0.5 to 1.0×10^{16} cm^{-2} so as to produce a corresponding equatorial H Lyman-α brightness of only ~400-500 Rayleighs. Hence given that only 275 Rayleighs of H Lyman-α emission is required to sustain the measured H^+ pickup ion density, it then seems possible that this H atmosphere/corona for Io may coexist and be consistent with an enhanced SO_2 atmosphere at Io's equator which could then provide a valid interpretation for the ~2,000 Rayleigh Lyman-α polar patches detected in the HST/STIS measured.

VI. Studies for Galileo SSI Io Eclipse Images (Belton Collaboration)

6.1. Descriptions of the Io Eclipse Image Observations

Since 1995, the Solid State Imager (SSI) instrument aboard the Galileo spacecraft has acquired a unique set of high-resolution (~10's km/pixel) images of Io when the satellite was eclipsed by Jupiter's shadow. These images have been obtained with different SSI wavelength filters including the violet (3800-4450 Å), green (5100-6050 Å), red (6150-7100 Å), clear (3800 and 10400 Å), and 1-micron (9350-10900 Å) filters. About half of these images have been obtained with the clear filter in which diffuse emission as well as localized hot spots are visible in Io's atmosphere. In contrast, only the localized hot spots are seen in the 1-micron filter. One set of color (violet, green, red) images was acquired during each of the E4, G7 and E15 Galileo orbits. The most complete and best set of Io eclipse images was acquired on May 31, 1998 during the first of two eclipses in orbit E15. These images were first presented at the October 1998 Division for Planetary Sciences meeting in Madison, Wisconsin (Geissler et al. 1998). A paper discussing these eclipse images (Geissler et al. 1999, in Appendix E) where the PI contributed as a co-author, has recently been published in Science and is briefly summarized below in Section 6.3.

Collectively the SSI Io eclipse images show (1) small bright hot spots associated with surface features associated with the known locations of volcanoes, (2) faint diffuse glows likely due to electronic excitation of the gases around the limb and near active volcanic vents extending to altitudes of several hundred kilometers and often appear brighter near the sub- and anti-Jupiter

points of the satellite, and (3) an enhanced polar hemispherical limb glow on the polar hemisphere facing the plasma torus centrifugal equator plane. The diffuse emissions are generally brighter above Io's surface at the sub- and anti-Jupiter points where the equatorial auroras were discovered in the HST-STIS ultraviolet image observations.

An examination of a set of the fourteen best Io eclipse images obtained in the clear filter has been undertaken in this project with analysis and conclusions to be published in a second paper. The examination shows that the images can be naturally divided into two subsets that are based upon the sub-Io longitude viewing-angle of the spacecraft. The first subset is for non Io plasma wake images, where the line-of-sight of the spacecraft is primarily viewing the trailing hemisphere of Io (centered on 270° longitude and imaging the anti-wake side of Io). The second subset is for Io plasma wake images, where the line-of-sight of the spacecraft is primarily viewing the leading hemisphere of Io (centered on 90° longitude where the Io plasma wake is attached). The most distinct features in the non Io plasma wake images are the equatorial aurora emission and limb emissions with a lack of distinct diffuse emission over Io's disk. The brightest spots and diffuse emission on the limb are always seen to rock up and down as a pair with magnetic latitude in a fashion similar to the equatorial spots seen in the HST/STIS ultraviolet images. In contrast, the Io plasma wake images show a distinct hazy cloud of brightness over most of Io's disk in addition to the bright spots and diffuse emission above the limb emission. The brightest spots and diffuse emission on the limb are sometimes seen to rock up and down as a pair with magnetic latitude but sometimes do not have this behavior which may be due to the additional pattern of the distinct hazy cloud of brightness over most of Io's disk. The distinct hazy cloud of brightness over most of Io's disk was identified in the May 31, 1998 Io eclipse images and interpreted by Geissler et al. (1999) as being produced by Io plasma wake electron impact excitation of gas in Io's atmosphere.

6.2. Sources of Visible Emissions in the Galileo SSI Io Eclipse Images

Candidate species for the producing gas emission in the red (6150-7100 Å) filter and hence also in the clear (3800 and 10400 Å) filter include [OI] 6300 Å, 6363 Å, Hα 6563 Å, and SII (6716 Å, 6731 Å). Candidate species for the producing gas emission in the green (5100-6050 Å) filter and consequently in the clear (3800 and 10400 Å) filter are [OI] 5577 Å and Na (5889 Å, 5896 Å). Recent ground-based spectral observations of Io in eclipse from Keck (Brown 1999) identified oxygen (6300 Å, 6363 Å, and 5577 Å) lines and found sodium D-line 5889 Å and 5896 Å emissions to be brighter than the oxygen green line, as expected from relative electron impact excitation rates determined for Na in this project and shown in Figure 14.

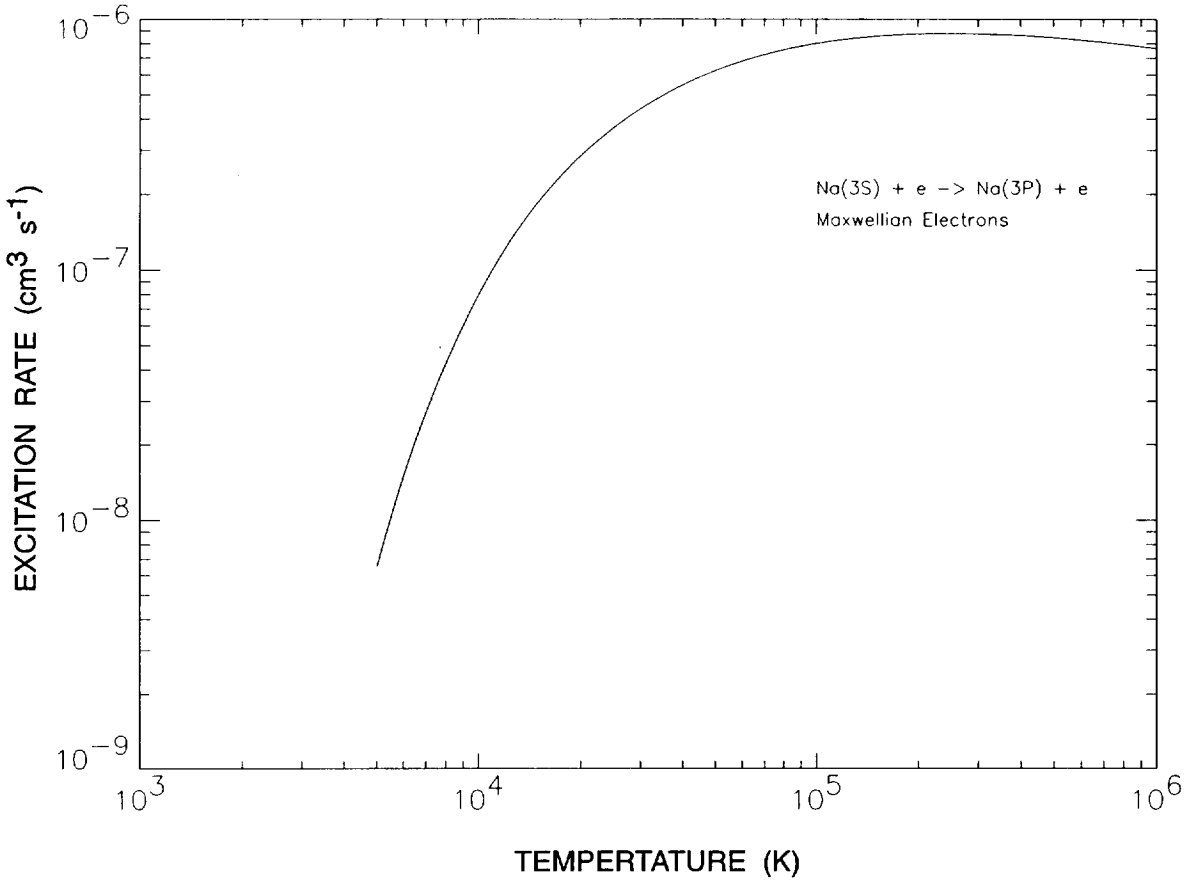

Figure 14. Electron Impact Excitation of Atomic Sodium in the D-lines. The total (D_1 + D_2) excitation rate ($cm^3 s^{-1}$) of Na from the 3S to the 3P state by the impact of Maxwellian electrons is shown as a function of electron temperature (K). The atomic excitation information is from Clark et al. (1982).

The brightness of the [O I] 6300 Å line near Io for electron impact excitation is estimated to be ~2.4 kR as based upon typical plasma conditions in the torus near Io's orbit of 2000 electrons cm^{-3} with a temperature of 5 eV and a likely atomic oxygen column near Io's exobase of ~5 x 10^{14} cm^{-2} (Wong and Smyth 1999). This brightness is comparable to the [O I] 6300 Å emission brightness of approximately a few kR measured in 1997 by HST (Trauger et al. 1997) near the limb of the satellite just after Io entered Jupiter's shadow. Assuming a likely atomic sodium column near Io's exobase of ~1 x 10^{12} cm^{-2} (Schneider et al. 1991) and again assuming 2000 electrons cm^{-3} with a temperature of 5 eV, the total sodium D-line brightness is ~1.4 kR. This total sodium brightness is thus comparable to the estimated [O I] 6300 Å emission brightness. Since, in optically thin conditions, the D_2 to D_1 sodium emission lines are in the ratio

of 2 to 1, the sodium brightness corresponds to ~1 kR of the D_2 emission brightness. This ~1 kR of D_2 emission brightness at the exobase produced by electron impact is, however, small compared to the typical solar resonance scattering D_2 emission line brightnesses at Io's exobase for Io in sunlight of ~100 kR (Smyth and Combi 1997). In earth-based observations with Io in sunlight, this ~1 kR of the D_2 emission brightness has, therefore, previously not been of particular importance. Atomic oxygen and sodium are thus considered the most likely candidates to provide diffuse emission in the red filter and green filter, respectively.

No identifiable emission lines (such as those from OI or OII) were seen from 4200 to 4450 Å, the portion of the SSI violet (3800-4450 Å) filter bandpass covered by the ground-based

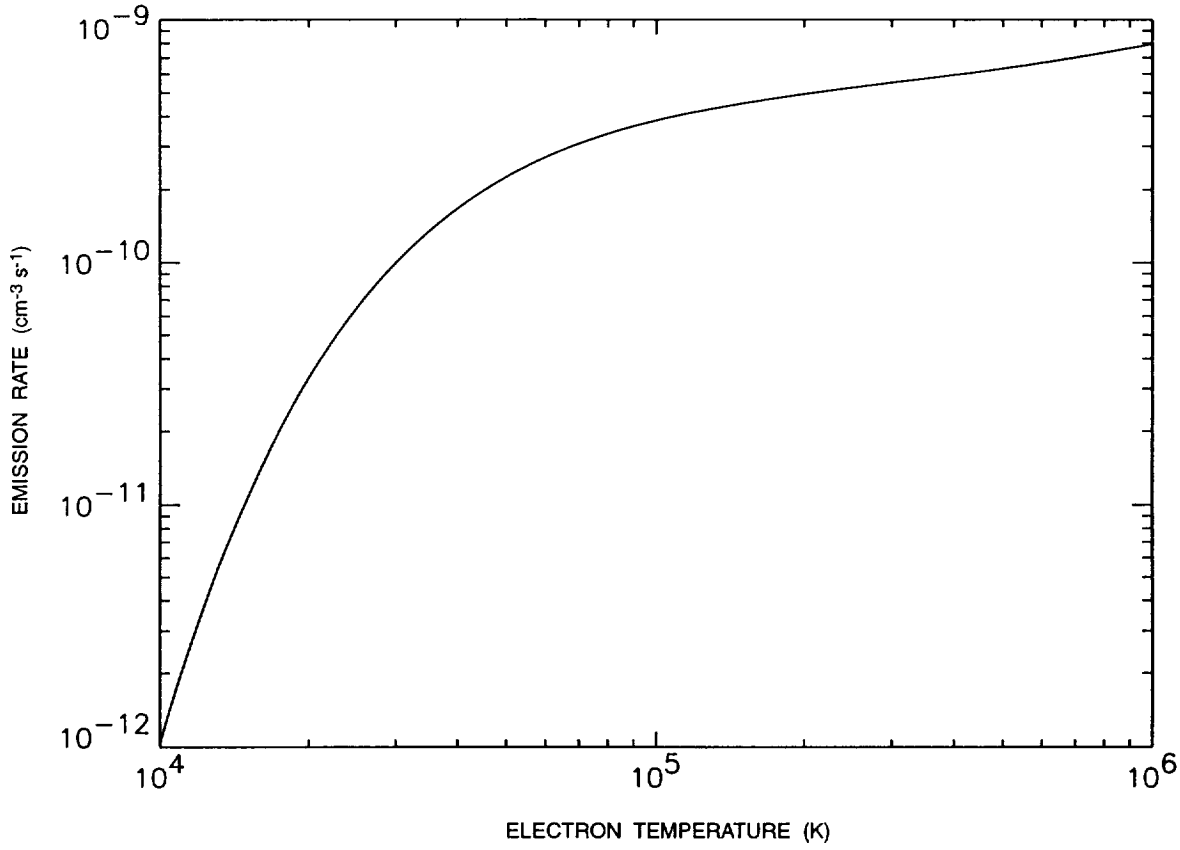

Figure 15. SO_2 Electron Impact Excitation Rate (3800 to 4450 Å). The excitation rate is computed using the measurements of Miller and Becker (1987) and assuming that the line shape below 10 eV is identical to that above 10 eV. The actual line shape is not known and the cross-section values below 10 eV are somewhat questionable. For electron energies greater than 100 eV, the cross-sections of Ajello et al. (1992) have been adopted.

observations. Io's violet filter emission is probably due to molecular emission from SO_2, known to be abundant in volcanic plumes. Effort in this project has thus been focused upon obtaining an electron impact excitation rate for the molecular band structures of SO_2 appropriate to the SSI violet filter. An approximate electron impact excitation rate for the violet filter was constructed using the laboratory SO_2 measurements of Miller and Becker (1987) and of Ajello et al. (1992), with guidance in this process given by Becker (1999). This excitation rate is shown in Figure 15. The excitation rates in Figure 14 and 15 are used to make rough estimates of species abundances in Section 6.3.

6.3. Preliminary Assessment of Io Eclipse Images on May 31, 1998

The eclipse images provide single-event high-resolution insight into the optical emission structure of Io's atmosphere. The best set of SSI Galileo Io eclipse images on May 31, 1998 are centered near longitude 70° W, on the orbital leading hemisphere of Io that is also the location of the plasma wake. At 11 minutes after the start of the eclipse, one set of color images in the SSI violet (3800-4450 Å), green (5100-6050 Å), red (6150-7100 Å), clear (3800 and 10400 Å), and 1–micron (9350-10900 Å) filters was taken and a second clear-filter image was taken 42 minutes later. The clear-filter images show both diffuse atmospheric emissions and discrete volcanic hot spots on Io's leading hemisphere, whereas only the hot spots are apparent in the 1-micron filter.

A composite color image for the three visible color frames was constructed and is shown in Figure 16. Diffuse emissions with three distinct distributions can be seen at red, green and violet (blue glow) wavelengths. The brightest emissions are the blue glows close to the equator near the sub- and anti-Jupiter points, extending several hundred km above the limb and having maximum brightnesses more than 300 kR emanate from volcanic plumes. A second, weaker glow running continuously along the limb is seen primarily in the red filter image, and is particularly bright along the north polar limb. The third component is a faint glow against the disk of Io at green filter wavelengths. In the E15 observations, this green glow appears to be concentrated on the night side of Io. Qualitatively similar emission distributions are seen in the noisier color eclipse data from orbit G7, except that the red polar limb glow is brighter in the southern hemisphere than in the north. The polar glow is brighter on the polar hemisphere that is facing the plasma torus equator plane, similar to the pattern seen in HST observations in polar optical (6300 Å) oxygen emission (Trauger et al. 1997) and also polar ultraviolet oxygen and sulfur emissions (Roesler et al. 1999).

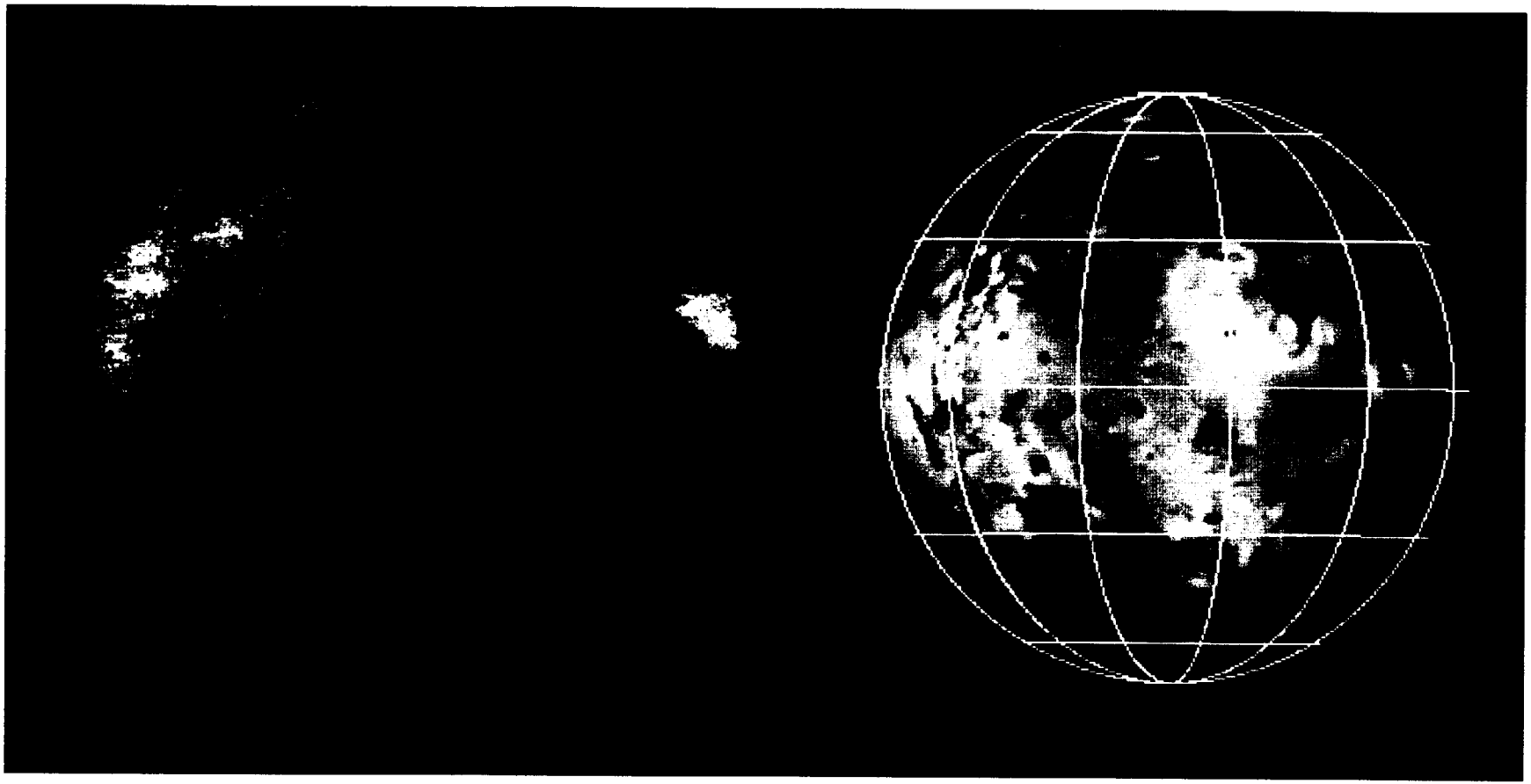

Figure 16. Enhanced Visible Color (red, green, violet) Image of Io in Eclipse. Three distinct components make up Io's visible aurorae: (1) bright blue glows emanate from volcanic plumes near the sub- and anti-Jupiter points (longitudes 0 and 180), (2) weaker red glows seen along the polar limbs, brighter in the north than in the south, and (3) a faint green glow that appears against the disk of Io, concentrated on the night side (longitudes 90 and beyond). The red and green glows appear brighter than natural in this contrast-stretched picture.

Using these excitation rates, estimates for the column densities of Na, O and SO_2 developed earlier, rough estimates can be made both for the Io disk average brightnesses and the maximum brightnesses in the images. These results and their implications are discussed in the paper by Geissler et al. (1999) and are briefly summarized here. For electron impact excitation of atomic sodium to match the maximum observed nightside disk brightness of 19.5 kR in the green filter, the electron density must be at least an order of magnitude larger than the nominal plasma torus density of 2000 electrons cm^{-3} if an optically thick column of sodium (~10^{13} cm^{-2}) is assumed. This suggests that the enhanced electron density of ~20,000 to 40,000 cm^{-3} in the Io plasma wake, centered on the leading hemisphere at 90 degrees, is likely responsible for the broad green nightside emissions. The brighter green emissions on Io's leading nightside (left half in Fig. 1) may be due to the electron shielding of sodium by SO_2 in the thicker leading dayside (right half, longitudes 268° W to 88° W) atmosphere, consistent with the diurnal behavior predicted from atmospheric models (Wong and Smyth 1999). Such intense electron impact excitation of atomic oxygen would produce the disk-averaged brightness of 6.8 kR and the maximum brightness at the north polar limb of 21 kR seen in the red filter for a column density of ~1 x 10^{14} cm^{-2} and a few x 10^{14} cm^{-2}, respectively. This is likely near the maximum emission brightness of atomic oxygen (6300 Å, 6363 Å) since it is limited by collisional quenching. Because of attenuation in Io's atmosphere, a significantly smaller population of magnetospheric electrons is available at low altitudes to excite the more energetic SO_2 emissions (~4 to 5.6 eV photons) than to excite the less energetic OI and Na emissions (~2eV). If we attribute the disk-averaged brightness of 8.2 kR and the maximum brightness at Acala of 85.7 kR in the violet filter to the SO_2 ultraviolet-visible emission, the electron impact excitation rate for the these emissions implies an approximate SO_2 column density that approaches 1 x 10^{16} molecules cm^{-2} and 1 x 10^{17} molecules cm^{-2}, respectively. This is more than an order of magnitude larger than the atomic oxygen columns estimated above, similar to ratios in model calculations for Io's atmosphere (Wong and Smyth 1999).

VII. Studies for Observations of Io's Neutral Oxygen Cloud

7.1. Ground-based [O I] 6300 Å Observations of Io's Neutral Oxygen Cloud

A new ground-based observation for the Io oxygen cloud in the 6300 Å emission line has recently been reported by Thomas (1996). This observation used a slit oriented perpendicular to Io's orbital plane and placed at the eastern elongation point of the orbit near (~0.5 Jupiter radius ~20 Io radii), but not including, the disk of Io. The slit is so located to measure the forward oxygen cloud. A north-south brightness profile close to the satellite plane was obtained for the

6300 Å emission line with a peak brightness of 8.8 (±1.7) Rayleigh. This brightness is similar to the 8 (±4) Rayleigh 6300 Å emission brightness measured by Brown (1981) in a much smaller slit sampling the forward oxygen cloud near the western elongation point of Io's orbit.

In this project, modeling analysis has been undertaken for both the observations of Thomas (1996) and Brown (1981). Earlier modeling of the Brown (1981) observation was reported by Scherb and Smyth (1993) based upon an atomic oxygen source of 3.2 x 10^{27} sec^{-1} ejected radially and uniformly with a speed of 2.6 km/sec from Io's exobase of assumed radius 2600 km. This 2.6 km/sec monoenergetic source was adopted for oxygen from earlier modeling of the sodium cloud where it was shown to characterize reasonably well the general sodium cloud morphology near Io's orbit. For the trace species sodium, the full flux speed distribution at Io's exobase has recently been determined in this project (Smyth and Combi 1997). For the forward sodium cloud near Io's orbit, the flux speed distribution responsible for its creation is an incomplete collisional cascade distribution that peaks at about 0.5 km/sec (well below the exobase escape speed of ~2 km/sec) and has a tail that extends to many 10's of km/sec. For the incomplete collisional cascade process, this source distribution should also apply equally well to atomic oxygen. This source distribution has a significant flux of atom with (1) ballistic trajectories that only populate the corona of the satellite, (2) low-speed escape trajectories that have similar speeds to the monoenergetic 2.6 km/sec source adopted by Scherb and Smyth (1993), and (3) higher-speed escape trajectories that quickly move away from Io's orbit and do not contribute significantly to the forward cloud. By adopting the more realistic incomplete collisional cascade source distribution at the exobase and requiring the same number of atoms to populate the forward cloud near Io's orbit, the oxygen source rate at the exobase will, necessarily, be larger than the value determined by Scherb and Smyth (1993) using the 2.6 km/sec monoenergetic source. A paper (Smyth and Marconi 1999, in Appendix F) describing the analysis and implications for the plasma torus has recently submitted for publication. The research was also presented at the AGU Meeting in Boston, Massachusetts, May 26-29, 1998 (Marconi and Smyth 1998).

7.2. Modeling Analysis of Io's Neutral Oxygen Cloud in [O I] 6300 Å Emission

Modeling analysis has been undertaken for ground-based observations of Io's neutral oxygen cloud near the satellite's orbit in the 6300 Å emission line acquired by Brown (1981) west of Jupiter and by Thomas (1996) east of Jupiter for a slit with a field of view that was well removed from Io's immediate vicinity. Neutral cloud model calculations for oxygen in the analysis are based upon the formalism of Smyth and Combi (1988), where a Voyager epoch

space-time dependent description of the plasma torus is adopted for electron impact excitation and ionization and for charge exchange processes and where an isotropic oxygen source at Io's exobase is assumed with the incomplete collisional cascade source velocity distribution recently determined for atomic sodium by Smyth and Combi (1997). The model calculations matched Brown's slit-averaged emission brightness of 8 ± 4 Rayleighs for an exobase source of 1.27 x 10^{28} atoms sec^{-1} and Thomas' north-south emission profile with a maximum brightness of 8.8 ± 1.7 Rayleighs for an exobase source of 1.47 x 10^{28} atoms sec^{-1}. These new oxygen source rates (escaping and non-escaping) for the cascade source are ~4 times larger than earlier estimates and correspond to an escaping component (38%) that is ~1.5 to 1.75 times larger than earlier estimates.

Implications for the local heating and escaping energy rates of neutrals at Io and for the ion pickup energy input rates to the plasma torus produced by this larger oxygen cascade source and also by other atomic oxygen and sulfur source processes approximately scaled from the oxygen cascade source are significant. The input power to sustain these neutral processes is estimated to be 1.62 x 10^{12} W and is divided between 0.74 x 10^{12} W for neutral escape and 0.88 x 10^{11} W for heating of Io's atmosphere. The total ion pickup input power to the plasma torus produced by atomic oxygen and sulfur is estimated to approach ~2 x 10^{12} W with an "outer source region" (neutral extended clouds above Io's exobase created by the cascade source) to "inner source region" (charge exchange processes below Io's exobase) torus power input ratio in the range of 1:2 to 1:3. This picture provides a viable solution to the mass loading and energy crisis (Shemansky 1988; Smith et al. 1988) of the plasma torus. The "inner source region" is the heterogeneous energy source favored by Shemansky (1988) to supply the additional energy input to the plasma torus that could not be supplied by the "neutral cloud theory" and is also proposed here to create a thin "power ribbon" that may provide a rationale for the "flashes and sparkles" of the ultraviolet brightness of the torus S^{++} plasma ribbon (Sandel and Broadfoot 1982; Volwerk et al. 1997) and the apparently chaotic time variability of the [O I] 6300 Å emission brightness observed at Io (Scherb and Smyth 1993; Scherb et al. 1999).

REFERENCES

Ajello, J. M., G. K. James, and I. Kanik, The Complete UV Spectrum of SO_2 by Electron Impact 2. The Middle Ultraviolet Spectrum, J. Geophys. Res. 97, 10,501-10,512, 1992.

Ballester, G. E., Ultraviolet Observations of the Atmosphere of Io and the Plasma Torus, Ph.D. Thesis, The John Hopkins University, 1989.

Becker, K. private communication, 1999.

Brown, M. E., private communication, 1999.

Brown, R. A., The Jupiter Hot Plasma Torus: Observed Electron Temperature and Energy Flow, Ap. J. 244, 1072-1080, 1981.

Chust, T., A. Roux, S. Perraut, P. Lourain, W. Kurth and D. Gurnett, Gailleo Plasma Wave Observations of Iogenic Hydrogen, preprint 1999.

Clark, R.E.H., N.H. Magee, J.B. Mann and A.L. Merts, Collisional Excitation Rates of Complex Atomic Ions, Ap. J. 254, 412-418, 1982.

Frank, L.A. and W.R. Paterson, Production of Hydrogen Ions at Io, J. Geophys. Res. 104, 10345-10354, 1999.

Geissler, P.E., A.S. McEwen, W. Ip, M.J.S. Belton, T.V. Johnson, and Galileo SSI Team, Io's Aurorae: Relationship to Plumes and Magnetospheric Interactions, Bull. Am. Astron. Soc, 30, 116-117, 1998.

Geissler, P.E., A.S. McEwen, W. Ip, M.J.S. Belton, T.V. Johnson, W.H. Smyth, and A.P. Ingersoll, Galileo Imaging of Atmospheric Emissions from Io, Science 285, 870-874, 1999.

Gurnett, D.A., W.S. Kurth, A. Roux, S..J. Bolton and C.F. Kennel, Galileo Plasma Wave Observations in the Io Plasma Torus and Near Io, Science 274, 391-392, 1996.

Huddleston, D.E., R.J. Strangeway, J. Warnecke, C.T. Russell, and M.G. Kivelson, Ion Cyclotron Waves Observed at Galileo's Io Encounter: Warm Plasma Dispersion Analysis. Geophys. Res. Lett. 24, 2143-2146, 1997.

Kivelson M.G., Khurana, K.K., Walker, R.J., Russell, C.T., Linker, J.A., Southwood, D.J., and Polanskey, C., A Magnetic Signature at Io: Initial Report from the Galileo Magnetometer, Science 273, 337-340, 1996a.

Kivelson, M. G., Khurana, K. K., Walker, R. J., Warnecke, J., Russell, C. T., Linker, J. A., Southwood, D. J., and Polanskey, C., Io's Interaction with the Plasma Torus: Galileo Magnetometer Report Science 274, 396-398, 1996b.

Khurana, K., M.G. Kivelson, and C.T. Russell, Interaction of Io with its Torus: Does it Have an Internal Magnetic Field?, Geophys. Res. Lett. 24, 2391, 1997.

Marconi, M.L. and Smyth, W.H. The Iogenic Neutral Oxygen Source, EOS 79, S200, 1998.

Miller, K. and K. Becker, Ultraviolet and Visible Fluorescence Produced by Controlled Electron Impact on SO_2, Can. J. Phys. 65, 530-534, 1987.

Oliversen, R.J., F. Scherb, F.L. Roesler, J. Corliss, R.C. Woodward, M.E. Freed, O.L. Lupie, and W.H. Smyth, Io [O I] 6300 Å Observations, BAAS 30, 1116, 1998.

Oliversen, R.J., F. Scherb, F.L. Roesler, J. Corliss, R.C. Woodward, M.E. Freed, O.L. Lupie, and W.H. Smyth, Ground-based Io [OI] 6300 Å Observations, paper presented at the 194th meeting of the American Astronomy Society, Chicago, Illinois, 30 May-June 3, 1999.

Roesler, F.L, private communication, 1999.

Roesler, F.L., H. W. Moo, R.J. Oliversen, R.C. Woodward, K.D. Rutherford, F, Scherb, M. McGrath, W.H. Smyth, P.D. Feldman, and D.F. Strobel, Far Ultraviolet Imaging Spectroscopy of Io's with HST/STIS, Science, 283, 353-357, 1999.

Sandel, B.R., and A.L. Broadfoot, Io's Hot Plasma Torus - a Synoptic View from Voyager, J. Geophys. Res., 87, 212-218, 1982.

Scherb, F. and W.H. Smyth, Variability of [O I] 6300-Å Emission Near Io. J. Geophys. Res. 98, 18729-18736, 1993.

Scherb, F., R.J. Oliversen, M.E. Freed, W.H. Smyth, J. Corliss, R.C. Woodward, P. Morgenthaler, and O.L. Lupie, Ground-based observations of [O I] 6300 Angstrom emission from Io, Paper presented at the "Magnetospheres of the Outer Planets Meeting", Paris, France, 9-14 August, 1999.

Schneider, N.M., D.M. Hunten, W.K. Wells, A.B. Schultz, and U. Fink, The Structure of Io's Corona, Ap.J. 368, 298-315, 1991.

Shemansky, D.E., Energy Branching in the Io plasma torus: The Failure of the Neutral Cloud Theory, J. Geophys. Res., 93, 1773-1784, 1988.

Shemansky, D.E., personal communication, 1990.

Shemansky, D.E., personal communication, 1992.

Smith, R.A., F. Bagenal, A.F. Cheng, and D.F. Strobel, On the Energy Crisis in the Plasma Torus, Geophys. Res. Letts., 15, 545-548, 1988.

Smyth, W.H., Energy Escape Rate of Neutrals from Io and the Implications for Local Magnetospheric Interactions, J. Geophys. Res. 103, 11941-11950, 1998.

Smyth, W.H. and M.R. Combi, Io's Sodium Exosphere and Spatially Extended Cloud: A Consistent Flux Speed Distribution, Icarus 126, 58-77, 1997.

Smyth, W.H., and M.R. Combi, A General Model for Io's Neutral Gas Cloud. I. Mathematical Description, Ap. J. Supp. 66, 397-411, 1988.

Smyth, W.H. and M.L. Marconi, Io's Oxygen Source: Determination from Ground-based Observations and Implications for the Plasma Torus, J. Geophys. Res., submitted 1999.

Smyth, W.H. and M.L. Marconi, An Initial Look at the Iogenic SO_2^+ Source during the Galileo Flyby of Io, J. Geophys. Res. 103, 9083-9089, 1998.

Thomas, N., High Resolution Spectra of Io's Neutral Potassium and Oxygen Clouds, Astron. Astrophys. 313, 306-314, 1996.

Trauger, J. T., K.R. Stapelfeldt, G.E. Ballester, J.T. Clarke, and WFPC2 Science Team, HST Observations of [O I] Emission from Io in Eclipse, Bull. Am. Astron. Soc. 29, 1002, 1997.

Volwerk, M., M.E. Brown, A.J. Dessler, and B.R. Sandel, Evidence for Short Cooling Time in the Io Plasma Torus, Geophys. Res Letts., 24, 1147-1150, 1997.

Wilson, J.K., M. Mendillo and J. Baumgardner, A Decade of Jupiter's Sodium Nebula, BAAS 30, 1118, 1998.

Wong, M.C. and W.H. Smyth, Model Comparison of Io's Atmosphere at Eastern and Western Elongations, Icarus, submitted, 1999.

REPORT DOCUMENTATION PAGE

Form Approved
OMB No. 0704-0188

1. AGENCY USE ONLY *(Leave blank)*	2. REPORT DATE	3. REPORT TYPE AND DATES COVERED
	September 17, 1999	Final, September 23, 1996 to September 22, 1999

4. TITLE AND SUBTITLE
Studies for the Loss of Atomic and Molecular Species from Io

5. FUNDING NUMBERS
NASW-96020

6. AUTHORS
William H. Smyth

7. PERFORMING ORGANIZATION NAME(S) AND ADDRESS(ES)
Atmospheric and Environmental Research, Inc.
840 Memorial Drive
Cambridge, MA 02139

8. PERFORMING ORGANIZATION REPORT NUMBER
P-658

9. SPONSORING/MONITORING AGENCY NAME(S) AND ADDRESS(ES)
NASA Headquarters
Headquarters Contract Division
Washington, DC 20546

10. SPONSORING/MONITORING AGENCY REPORT NUMBER

11. SUPPLEMENTARY NOTES

12a. DISTRIBUTION/AVAILABILITY STATEMENT

12b. DISTRIBUTION CODE

13. ABSTRACT *(Maximum 200 words)*

A summary discussion of research undertaken in this project is presented and is related to six published papers attached in the appendix. The discussion is divided into six sections describing a variety of studies for the loss of atomic and molecular species from Io: (1) studies for atomic sodium, (2) studies for SO_2, (3) studies for O and S, (4) studies for spectacular high-spatial resolution ultraviolet image observations of O, S, and possibly H in Io's atmosphere and/or corona acquired by the Space Telescope Imaging Spectrometer (STIS) of the Hubble Space Telescope (HST), (5) studies for spectacular high-spatial resolution visible Io eclipse image observations acquired by the Solid State Imager (SSI) of Galileo spacecraft, and (6) studies for ground-based observations of Io's neutral cloud in [O I] 6300 Å emission. New source rates at Io's exobase for SO_2, O, and H are given and a variety of interesting implications for Io's atmosphere and for the Io plasma torus are discussed.

14. SUBJECT TERMS	15. NUMBER OF PAGES
Io, satellite atmospheres	46
	16. PRICE CODE

17. SECURITY CLASSIFICATION OF REPORT	18. SECURITY CLASSIFICATION OF THIS PAGE	19. SECURITY CLASSIFICATION OF ABSTRACT	20. LIMITATION OF ABSTRACT
Unclassified	Unclassified	Unclassified	

Appendix A

Io's Sodium Exosphere and Spatially Extended Cloud: A Consistent Flux Speed Distribution

ICARUS 126, 58–77 (1997)
ARTICLE NO. IS965633

Io's Sodium Corona and Spatially Extended Cloud: A Consistent Flux Speed Distribution

WILLIAM H. SMYTH

Atmospheric and Environmental Research, Inc., Cambridge, Massachusetts 02139
E-mail: smyth@aer.com

AND

MICHAEL R. COMBI

Space Physics Research Laboratory, University of Michigan, Ann Arbor, Michigan 48109

Received November 1, 1993; revised October 3, 1996

A data set composed of different groundbased observations for Io's sodium corona and spatially extended sodium cloud and covering the spatial range from Io's nominal exobase of 1.4 satellite radii to east–west distances from Io of ±100 satellite radii (R_{Io}) is used to investigate the velocity distribution of sodium at the exobase. The data set is composed of the novel 1985 eclipse measurements of Schneider *et al.* (1991, *Astrophys. J.* 368, 298–315) acquired from ~1.4 to ~10 R_{Io}, the 1985 east–west emission data of Schneider *et al.* acquired from ~4 to ~40 R_{Io}, and sodium cloud image data acquired near Io's orbital plane from ~10 to ~100 R_{Io} by a number of different observers in the 1976 to 1983 time frame. A one-dimensional east–west profile that contains Io is constructed from the data set and is analyzed using the sodium cloud model of Smyth and Combi (1988, *Astrophys. J. Supp.* 66, 397–411; 1988, *Astrophys. J.* 328, 888–918). When the directional feature in the trailing cloud is either north or south of this east–west line (i.e., not at the null condition), an isotropic modified [incomplete ($\alpha = 7/3$) collisional cascade] sputtering flux speed distribution at the satellite exobase with a peak at 0.5 km sec^{-1} provides an excellent fit to the data set for a sodium source of 1.7×10^{26} atoms sec^{-1}. In particular, the model calculation reproduces (1) the essentially symmetric column density distributions exhibited by the eclipse measurements about Io within the Lagrange sphere radius (5.85 R_{Io}, i.e., the gravitational grasp of the satellite), (2) the change in the slope of the column density observed just beyond the Lagrange sphere radius in the east–west profile of the forward cloud, but not in the trailing cloud, and (3) the distinctly different east–west brightness profiles exhibited by the forward and trailing clouds in the emission data at the more distant (~ ±20–100 R_{Io}) portions of the cloud. In contrast, the speed dispersion at the exobase for either an isotropic Maxwell–Boltzmann flux speed distribution or an isotropic classical ($\alpha = 3$) sputtering flux speed distribution (which has a higher velocity-tail population than the Maxwell–Boltzmann, but not as high as the incomplete collisional cascade sputtering distribution) is shown to be inadequate to fit the data set. To fit the enhanced trailing east–west profile observed when the directional feature is at the null condition, an additional enhanced high-speed (~15–20 km sec^{-1}) sodium population is required which is nonisotropically ejected from the satellite exobase so as to preferentially populate the trailing cloud. The need for such a nonisotropic high-speed population of sodium has also been recognized in the earlier modeling analysis of the directional features (Pilcher *et al.*, 1984, *Astrophys. J.* 287, 427–444), in the more recent lower-velocity component required in modeling the sodium zenocorona (Smyth and Combi, 1991, *J. Geophys. Res.* 96, 22711–22727; Flynn *et al.*, 1992, *Icarus* 99, 115–130), and in the very recent modeling of the directional feature reported by Wilson and Schneider (1995, *Bull. Am. Astron. Soc.* 27, 1154). A complete sodium source rate speed distribution function at Io's exobase from 0–100 km sec^{-1} is then constructed by combining the isotropic modified [incomplete ($\alpha = 7/3$) collisional cascade] sputtering flux speed distribution, the nonisotropic directional feature (lower-velocity zenocorona) source (~15–20 km sec^{-1}), and the higher-speed (~20–100 km sec^{-1}) charge-exchange source required to simulate the sodium zenocorona far from Jupiter.

1. INTRODUCTION

Atomic sodium in the Jupiter system originating from a satellite source at Io has been observed in the D_2 (5889.95 Å) and D_1 (5895.92 Å) emission lines during the past 25 yr from groundbased facilities. Using an observing slit, the sodium emission which is excited by solar resonance scattering was first discovered in 1972 by Brown (1974) very near Io, where its intensity is brightest [~many tens of kiloRaleighs (kR)] and where the sodium density is dominated by low-speed (~2 km sec^{-1} or less) ballistic atom orbits in the satellite "corona." By occultation of the

0019-1035/97 $25.00

bright region near Io, image observations (Murcray 1978; Murcray and Goody 1978; Matson *et al.* 1978) were first acquired in 1976 and 1977 for fainter (~ few to ~0.5 kR) sodium more distant from Io but still near its circular orbit (radius of 5.9 Jupiter radii) about the planet and revealed the presence of a predominant "forward cloud" and a less spatially extensive "trailing cloud" that moved with the satellite. This sodium has been characterized primarily by a source of low-speed (~2.6–4 km sec^{-1}) atoms that have sufficient energy to just escape from Io with an excess velocity of only ~1 km sec^{-1} (or so) and thereby remain gravitationally bound to Jupiter fairly near the satellite orbit. Additional observations (Pilcher *et al.* 1984; Goldberg *et al.* 1984) of even fainter (~1 to 0.2 kR) sodium in the early 1980's revealed a "directional feature" attached to Io in the trailing cloud that oscillated north and south about the satellite plane with a phase and period determined by the Io System III longitude angle. This sodium source was characterized by atoms with speeds ~20 km sec^{-1} ejected nonisotropically from the satellite so as to populate the trailing cloud and the circumplanetary space at larger radial distances beyond Io's orbit. From earlier slit measurements in 1974 (Trafton and Macy 1978), fainter (~30 R) sodium emissions well beyond Io's orbit had been observed at a radial distance of ~60 planetary radii, while from more recent images (Mendillo *et al.* 1990), very faint (~1 R) sodium emissions were observed at radial distances of ~400–500 planetary radii. Sodium at these larger radial distances is called the "magneto-nebula" or "sodium zenocorona" and is thought to be populated primarily by a nonisotropic charge-exchange source of high speed (~15–100 km sec^{-1}) atoms at Io with velocity skewed in the forward direction of corotational plasma motion past the satellite, and secondarily by a narrow forward sodium jet produced by a spatially distributed molecular ion source (Wilson and Schneider 1994). Most of this sodium escapes the Jupiter system, forms a sodium pause in the sunward direction at ~2300 planetary radii because of solar radiation acceleration, and is eventually lost to the solar wind by photoionization (Smyth and Combi 1991).

The observations of sodium emissions on many different spatial scales in the Jupiter system thus indicate that its atomic source at Io's exobase must have a wide dispersion of speeds. Modeling of these observations has in the past been mostly undertaken separately for only one of these spatial regions at a time. Although the higher velocity dispersions for the sodium zenocorona may be reasonably well understood because of its large spatial structure and the lack of any significant sodium lifetime impact of the magnetosphere, a consistent source for the slower sodium in Io's corona and in the forward and trailing clouds near its orbit has not been established. The recent determination of the sodium spatial profile in the Io corona obtained from the groundbased eclipse data of Schneider (1988; Schneider *et al.* 1987, 1991) coupled with earlier emission observations, however, now provides a viable observational base from which it is possible to pursue the nature of this slower sodium. The investigation of a consistent exobase sodium source for Io's corona and the forward and trailing clouds near its orbit is therefore undertaken in this paper. A consistent flux speed distribution at the exobase is determined, and the corresponding sky-plane spatial distribution of sodium near Io is presented. Sodium source information obtained from previous modeling analysis of Io's corona and the forward and trailing clouds is first summarized in Section 2. The observational data base to be investigated in this paper is presented in Section 3. Modeling of an east–west spatial profile determined from this observational data base is undertaken in Section 4. Discussion and conclusions are presented in Section 5.

2. EARLIER SODIUM MODELING

The major modeling analysis studies for the spatial distribution of sodium near Io and its orbit are summarized in Table I. The summary is divided into three observed spatial regions: (1) the Io corona located within the satellite Lagrange sphere (average radius of 5.81 R_{Io} or ~3 arcsec), (2) the neutral cloud located beyond the Lagrange sphere and near Io's orbit, and (3) the north–south oscillating directional feature, observed to trail Io in its orbit. Modeling analysis studies for the Io corona are further subdivided into early observations of the average intensity in an 8 × 3 arcsec slit centered on Io reported by Bergstralh *et al.* (1975, 1977) that indicated an east–west intensity asymmetry of ~1.25 and later observations for one-dimensional column density profiles within the Lagrange sphere reported by Schneider *et al.* (1987, 1991).

2.1. *Corona: East–West Intensity Asymmetry*

In Table I, the early studies of Smyth (1983) for sodium atoms ejected monoenergetically from Io's exobase established that small scale structures in the D-line intensity profile observed as a function of the Io geocentric phase angle (Bergstralh *et al.* 1975, 1977) could arise from modulation of the atoms' escape rate from Io caused by the action of solar radiation acceleration in the D-lines. These modulations occur primarily for exobase speeds near 2.0 and 2.1 km sec^{-1}, which are near the escape-speed threshold of the Lagrange sphere. Later studies of Smyth and Combi (1987a) showed that the main reason for the east–west intensity asymmetry was, however, an east–west electric field which altered the plasma properties at Io's orbit so as to increase the sodium lifetime and hence sodium abundance when Io was preferentially east of Jupiter. More complex modeling studies of Smyth and Combi (1988b) constrained the flux velocity dispersion for sodium at Io's exobase by simultaneously fitting the average east–west

TABLE I
Summary of Modeling Studies for the Spatial Distribution of Sodium Near Io and Its Orbit

		Sodium Source								Sodium Lifetime		Orbital Dynamics			
		Mono-energetic Atom Ejection	Maxwell-Boltzman Flux Distribution		Cascade Flux Speed Distribution										
Spatial Region	Topic Studied	Speed ($km\ s^{-1}$)	T (K)	V_{peak} ($km\ s^{-1}$)	α	V_b ($km\ s^{-1}$)	V_{peak} ($km\ s^{-1}$)	V_{max} ($km\ s^{-1}$)	Angular Nature[a]	Plasma Torus Description	Lifetime (hrs)	Io's Mass Included	Jupiter's Mass Included	Radiation Pressure Included	Reference
I. Corona	e-w intensity asymmetry[b]	2.0-2.6	-	-	-	-	-	-	isotropic	cut-off	20	yes	yes	yes	Smyth 1983
	e-w intensity asymmetry[b]	2.6	-	-	-	-	-	-	isotropic	2-D	variable	yes	yes	yes	Smyth and Combi 1987a
	e-w intensity asymmetry[b]	-	460; 12,300	0.71; 3.65	7/3	<0.4; 2.2	<0.5; 2.9	46.6	band, isotropic	2-D	variable	yes	yes	yes	Smyth and Combi 1988b
	column-density profile[c]	2.6	-	-	-	-	-	-	isotropic	2-D	varialbe	yes	yes	yes	Smyth and Combi 1987b,c
	column-density profile[c]	-	-	-	3	0[d]	-	∞	isotropic	cut-off	3, ∞	yes	no	no	McGrath 1988
	column-density profile[c]	-	1000	1.04	-	-	-	-	isotropic	uniform	∞	yes	no	no	Summers et al. 1989
	column-density profile[c]	3.0	-	-	-	-	-	-	isotropic	uniform	?	yes	no	no	Ip 1990
	column-density profile[e]	-	1500	1.28	-	-	-	-	isotropic	uniform	∞	yes	no	no	Schneider et al. 1991
II. Cloud	general spatial nature	3.5	-	-	-	-	-	-	isotropic	uniform	30, 47	yes	yes	no	Carlson et al. 1975
	general spatial nature	-	5000	2.3	-	-	-	-	isotropic	long-lived limit	-	no	yes	no	Fang et al. 1976
	evolution and 2-D nature	2, 3	-	-	-		-	-	isotropic	cut-off	50	yes	yes	no	Smyth and McElroy 1977
	1-D brightness morphology[f]	-	-	-	3	4	4	∞	I-L hemisphere[g]	uniform	28	yes	yes	no	Matson et al. 1978
	2-D brightness morphology[h]	2.6, 3	-	-	-	-	-	-	I, I-T hemisphere[i]	cut-off	15, 20	yes	yes	no	Smyth and McElroy 1978
	e-w orbital asymmetry[j]	2.6	-	-	-	-	-	-	I-T hemisphere[i]	cut-off	20	yes	yes	yes	Smyth 1979
	radial and vertical structure	(3,5,7,9,11,13)[k]	-	-	-	-	-	-	I hemisphere	uniform	56	no	yes	no	Macy and Trafton 1980
	1-D brightness morphology	-	-	-	3[l]	4[l]	4[l]	∞[l]	I-L hemisphere[l]	1-D	variable	yes	yes	no	Goldberg et al. 1980
	e-w orbital asymmetry	2.6	-	-	-	-	-	-	I hemisphere	cut-off	20	yes	yes	yes	Smyth 1983
	2-D brightness morphology	2.6	-	-	-	-	-	-	band, isotropic	2-D	variable	yes	yes	yes	Smyth and Combi 1988b
III. Directional Feature	spacetime structure[m]	~20	-	-	-	-	-	-	O, ~⊥ to Io's motion	2-D	variable	yes	yes	yes	Pilcher et al. 1984
	collision cross sections	-	-	-	3	0[n]	-	-	~⊥ to Io's motion	-	-	-	-	-	Sieveka and Johnson 1984
	nearer zenocorona structure	-	-	~20± 12[p]	-	-	-	-	tangential ± isotropic	photoionization	~400 hr	no	no; Sun yes	yes	Smyth and Combi 1991
	nearer zenocorona structure	-	-	~20± 12[p]	-	-	-	-	tangential ± isotropic	photoionization	~400 hr	no	yes	no	Flynn et al. 1992
	spacetime structure	-	-	20± 10-20[q]	-	-	-	-	tangential ± isotropic	none	∞	no	yes	no	Wilson and Schneider 1995

[a] regarding Io's exobase, L=leading, I=inner, T=trailing, O=outer.
[b] east-west intensity asymmetry data of Bergstralh et al. (1975, 1977).
[c] early (i.e., partial) Na eclipse data set from Schneider et al. (1987).
[d] used cut-off energy: Emin ≤ E < ∞; Emin = k $T_{exobase}$; $T_{exobase}$=1500 K (i.e. a 1.04 km s^{-1} cut-off speed).
[e] complete eclipse data set from Schneider (1988) and Schneider et al. (1991).
[f] two sodium cloud images of Matson et al. (1978).
[g] I-L hemisphere centered 30° longitude (0° longitude facing Jupiter, 90° longitude is the leading point in the orbit).
[h] fifty-six sodium cloud images of Murcray (1978) and Murcray and Goody (1978).
[i] I-T hemisphere centered on -40° longitude.
[j] east-west orbital asymmetry data of Goldberg et al. (1978).
[k] velocity components equally weighted.
[l] distribution parameters from Carlson (1995, private communication); I-L hemisphere centered on 45° longitude.
[m] from images of Pilcher et al. (1984).
[n] used cut-off energy of 0.5 ev (i.e., Na cut-off speed of 2.0 km s^{-1}).
[p] tangential speed to Io's orbit at Io position ± most probable speed of an isotropic Maxwell-Boltzmann.
[q] tangential speed to Io's orbit at Io position ± most probable speed of an isotropic Gaussian.

intensity asymmetry and also the general spatial morphology of the forward sodium cloud, located on a much larger spatial scale well beyond the Lagrange sphere. These studies showed that the sodium ejection speed at the exobase required to fit the east–west intensity asymmetry is double-valued, having a lower value of ≤ 1 km sec^{-1} and a higher value in the range 2.6–3.65 km sec^{-1}. For a Maxwell–Boltzmann flux distribution, the lower and higher most probable speed values were 0.71 km sec^{-1} (T = 460 K) and 3.65 km sec^{-1} (T = 12,300 K). Neither distribution was, however, suitable for properly populating the forward cloud. The lower value produces essentially only ballistic atom orbits which could not populate the forward cloud, while the higher value was significantly larger than the nominal ~2.6 km sec^{-1} characteristic monoenergetic velocity required to reproduce the proper spatial morphology of the forward cloud as a function of the Io geocentric phase angle. For a Maxwell–Boltzmann flux distribution with a more nominal thermal exobase temperature in the range ~1000–2000 K, the calculated east–west intensity ratio was much higher than the observed value, with the atoms still contributing primarily to the corona density and again far too deficient in energy to contribute any significant sodium to the forward cloud. For the preferred (α = 7/3) modified-sputtering distribution of Smyth and Combi (1988b) with source strength ~2×10^{26} atoms sec^{-1}, the lower and higher speed values were ≤ 0.5 and ~2.9 km sec^{-1}, respectively, with the latter value being preferred because of its closer proximity to the ~2.6 km sec^{-1} characteristic velocity for the forward cloud. Interestingly, however, it is actually the lower value that will be shown in this paper to reproduce the correct spatial profile for sodium both within the Lagrange sphere and beyond in the more distant neutral cloud.

2.2. *Corona: Column Density Profile*

In Table I, modeling studies of Smyth and Combi (1987b,c) determined that typical forward cloud brightness data for the sodium cloud could be properly simulated well beyond the Lagrange sphere radius of ~5.81 R_{Io} by a sodium source of ~1×10^{26} atoms sec^{-1} ejected monoenergetically from Io's exobase with a characteristic velocity of ~2.6 km sec^{-1}. They also established that this same sodium source reproduced the column density profile of Schneider *et al.* (1987) within the Lagrange sphere down to a radius of ~3.5 R_{Io}. For a radius smaller than ~3.5 R_{Io}, the calculated profile was lower than the observed profile, indicating that lower (ballistic) velocity components are required, in addition, as part of a more realistic flux velocity dispersion. A similar behavior for the simulated column density profile, with an even more dramatic departure from the observed profile both inside and outside the Lagrange sphere, was also later shown by a model calculation of Ip (1990), who assumed an exobase speed of 3 km sec^{-1} but did not include the gravity of Jupiter so as to properly include the near zero escape speed conditions for sodium at the Lagrange sphere. Adopting for sodium atoms at the exobase a simple (i.e., binding-energy velocity v_b = 0) classical sputtering energy distribution with a low energy cut-off and also excluding Jupiter's gravity, McGrath (1988) modeled the column density within the Lagrange sphere and produced a profile with a slope slightly less steep than the observation for an infinite sodium lifetime and a slope somewhat steeper than the observation for a sodium lifetime of 3 hr. Alternatively adopting a Maxwell–Boltzmann flux distribution, assuming an infinite sodium lifetime, and similarly excluding Jupiter's gravity, Summers *et al.* (1989) and Schneider *et al.* (1991) modeled the column density within the Lagrange sphere region and produced a profile that reasonably well matched the observed profile for an exobase temperature, respectively, of 1000 K based on the partial eclipse data set (Schneider *et al.* 1987) and of 1500 K based on the complete eclipse data set (Schneider *et al.* 1991). Although these different flux velocity distributions reasonably fit the observations within the Lagrange sphere, it is clear from the earlier studies of Smyth and Combi (1988b) that these Maxwell–Boltzmann distributions are energetically deficient and inappropriate for populating the neutral cloud and, furthermore, that the more energetically promising sputtering distribution cannot be investigated adequately near or beyond the Lagrange sphere radius without properly including the gravity of Jupiter, solar radiation acceleration, and the spacetime variable sodium lifetime in the plasma torus. This study will be undertaken in Section 4.

2.3. *Sodium Cloud*

The early studies in Table I for the sodium cloud were general in nature, probing its poorly documented spatial and angular extent about the planet. Based upon the solar resonance scattering excitation mechanism for sodium (Bergstralh *et al.* 1975) and limited angular extent data determined by slit-averaged intensity data, Carlson *et al.* (1975) undertook monoenergetic (3.5 km sec^{-1}) model calculations and estimated that the sodium cloud lifetime (assumed to be spatially uniform) was likely determined by electron impact ionization by the (then very poorly characterized) plasma in the planetary magnetosphere. This general picture for the cloud was confirmed by more extensive model calculations performed by Fang *et al.* (1976) and Smyth and McElroy (1977), the latter of which explored the time evolution and two-dimensional nature of the cloud for exobase velocities near the Io Lagrange escape speed. The acquisition of sodium cloud images in late 1976 and early 1977 brought this subject into dramatic focus. For a classical sputtering flux distribution that peaked at 4 km sec^{-1}, Matson *et al.* (1978) successfully

modeled a one-dimensional east–west brightness profile (derived from a cloud image) which extended from Io in the forward cloud to ~80 R_{Io} and in the trailing cloud to ~40 R_{Io} but which excluded sodium emission within Io's corona. The analysis (Smyth and McElroy 1978) of a much larger sodium cloud image data set (Murcray 1978) also indicated that the forward cloud could be characterized by an exobase ejection speed of ~2.6 km sec^{-1} and that its changing intensity pattern could be understood as the changing viewing perspective of an approximately steady state cloud on the sky plane as Io moved on its orbit around Jupiter. The observed predominance of the forward sodium cloud over the trailing cloud was accomplished in all these models by limiting the exobase source area to a hemisphere (see Table I) and by limiting the assumed spatially uniform lifetime so as to dynamically select sodium atom orbits that would primarily populate the forward cloud. Additional modeling studies by Macy and Trafton (1980) of the radial and vertical cloud structure on a larger spatial scale indicated source dispersion speeds at least up to 13 km sec^{-1} were, however, required to explain a variety of other observations. Additional model studies (Smyth 1979, 1983) showed that the newly discovered east–west orbital asymmetry of the sodium cloud (Goldberg *et al.* 1978) was not source related but was due to the perturbing action of solar radiation acceleration on the sodium atom orbits. Adopting a one-dimensional radially dependent sodium lifetime in the plasma torus based upon limited Voyager spacecraft data and an asymmetric exobase source for a classical sputtering distribution with a peak velocity at 4 km sec^{-1}, Goldberg *et al.* (1980) successfully modeled a one-dimensional east–west brightness profile acquired during the Voyager 1 encounter for distances extending from Io in the forward cloud to ~80 R_{Io} and in the trailing cloud to ~30 R_{Io}. Later modeling by Smyth and Combi (1988b) using a more accurate two-dimensional space- and time-dependent sodium lifetime in the plasma torus and an isotropic (or near isotropic) exobase sodium source of ~2 × 10^{26} atoms sec^{-1} demonstrated that the predominant forward cloud was caused by the highly radially dependent sink for sodium in the plasma torus and not by a nonisotropic source. The deduced characteristic or most probable exobase speed for the more definitive modeling of the forward sodium cloud above is, therefore, in the range ~2.6 to 4 km sec^{-1} and is much larger than required to characterize the sodium column density profile in Io's corona. A new flux speed distribution is therefore needed for consistency and is determined in Section 4.

2.4. *Directional Feature*

In Table I, observations acquired in 1980 and 1981 by Pilcher *et al.* (1984) for weaker D-line emissions in the trailing portion of the sodium cloud allowed them to discover an elongated feature in the brightness distribution that on the sky plane was directed away from Jupiter and was inclined sometimes to the north and sometimes to the south of the satellite's orbital plane. The north–south direction of the feature was shown to be correlated with Io's magnetic longitude and suggested a formation mechanism involving the oscillating plasma torus. Modeling analysis by Pilcher *et al.* indicated that the feature resulted from a high-velocity (~20 km sec^{-1}) sodium source that was at near right angles to Io's orbital motion with a source strength required on the outer satellite hemisphere of ~1 × 10^{26} atoms sec^{-1}. This peculiar directionality of the source was investigated by Sieveka and Johnson (1984), who concluded that it was likely produced by direct collisional ejection of neutral sodium from the exosphere by the corotating plasma flow past Io. Modeling of the sodium zenocorona (Smyth and Combi 1991; Flynn *et al.* 1992) showed that it was consistent with a two-component exobase source: a similar high-velocity (~20 km sec^{-1}) sodium source of ~1 × 10^{26} atoms sec^{-1} for the spatial distribution nearer the planet and an even higher-velocity (~57 km sec^{-1}) sodium source of ~2 × 10^{26} atoms sec^{-1} for the spatial distribution further from the planet. Both source components, however, were based on ion–neutral charge exchange processes in Io's exosphere and were hence composed of a speed tangential to Io's orbit at Io's position plus an isotropic Maxwell–Boltzmann distribution with a most probable speed of about one-third of the tangential speed in the Jupiter frame (i.e., one-third of ~37 and ~74 km sec^{-1}, respectively). In Table I, the lower component is therefore symbolically denoted in the Io frame by 20±12 km sec^{-1}. Recent modeling of the directional features has also been reported by Wilson and Schneider (1995), who used a similar lower component source denoted in Table I by 20 ± 10–20 km sec^{-1}, where the isotropic portion of their source may be variable in magnitude. A spatially distributed molecular-ion source has also been used to model the sodium zenocorona (Flynn 1993), but appears to be of secondary importance due to its smaller source rate and erratic presence.

3. OBSERVATIONAL DATA BASE FOR MODELING

To describe the entire spatial distribution of sodium in Io's corona and beyond in the extended neutral clouds, three different types of sodium observations obtained on very different spatial scales are combined. For Iocentric distances, the combined data set is composed of the novel 1985 eclipse measurements of Schneider *et al.* (1991) acquired from ~1.4 to ~10 R_{Io}, the 1985 east–west emission data of Schneider *et al.* (1991) acquired from ~4 to ~40 R_{Io}, and sodium cloud image data acquired near Io's orbital plane from ~10 to ~100 R_{Io} by a number of different

TABLE II
Io Eclipse and Emission Observations for 1985

Date	UT Midpoint	Io Geocentric Phase Angle Range (deg)	Io System III Longitude Range (deg)	Spectrum ID	Type of Observation		Dominant Spatial Profile	Directional Feature Orientation	Enhance Doppler Signature	D_2 Emission Profile Power Law Fit [f] Exponent		Amplitude (kR)	
					Eclipse	Emission				East Profile	West Profile	East Profile	West Profile
August 27	0714	61.4 ± 0.7	29.9 ± 2.3	85g188		1	forward	null	trailing/forward	1.67 (F)	1.57 (T)	191	124
	0720	62.3 ± 11.0	32.9 ± 35.8	a	1		—	—	—				
	0830	72.2 ± 1.1	65.1 ± 3.4	85g196		2	symmetric	south	no	1.85 (S)	1.80 (S)	169	142
September 13	0641	276.6 ± 0.7	194.7 ± 2.3	85h032		3	trailing	null/north	trailing	—	—	—	—
September 14	0245	87.7 ± 0.7	31.4 ± 2.3	85h102		4	trailing	null	trailing	1.23 (S/T)	1.80 (S/F)	89	188
	0326	93.5 ± 4.2	50.5 ± 13.7	b	2		—	—	—				
	0416	100.6 ± 0.4	73.6 ± 1.4	85h113		5	g	south	no	1.27 (T)	—	66	—
September 15	0316	294.7 ± 0.7	353.7 ± 3.0	85h152		6	trailing	null	trailing	—	—	—	—
	0500	309.4 ± 11.5	41.7 ± 37.4	c	3		—	—	—				
September 21	0604	100.5 ± 1.6	112.5 ± 5.2	d	4		—	—	—				
September 23	0230	117.2 ± 0.7	267.6 ± 2.3	85h433		7	forward	north	no	2.05 (T)	1.57 (F)	342	135
	0301	121.6 ± 0.4	281.9 ± 1.2	85h436		8	forward	north	no	1.96 (T)	1.54 (F)	283	138
	0356	129.3 ± 2.0	307.3 ± 6.7	e	5		—	—	—				
	0534	143.1 ± 0.7	352.9 ± 2.3	85h457		9	forward	null	no	2.16 (T)	1.64 (F)	374	165

a. Eclipse 1 : 85g179, 85g181, 85g185, 85g188, 85g192, 85g193, 85g196

b. Eclipse 2 : 85h103, 85h104, 85h105, 85h106, 85h107, 85h108, 85h109, 85h110, 85h112

c. Eclipse 3 : 85h153, 85h154, 85h155, 85h157, 85h159, 85h162, 85h163

d. Eclipse 4 : 85h287, 85h288, 85h289, 85h290, 85h291, 85h292, 85h293, 85h294, 85h295

e. Eclipse 5 : 85h441, 85h442, 85h443, 85h444, 85h445, 85h446, 85h447, 85h448, 85h449, 85h450

f. Profile points inside of 4 R_{Io} are excluded; power law fit $A\,r^{\beta}$, where A is the amplitude, β is the exponent, and r is in units of R_{Io}; F = forward cloud; S = symmetric turning point; T = trailing cloud.

g. Not sufficient data west of Io to compare spatial profils (see Table III).

(Note one lower-bound data point from eclipse 4 at a distance from the center of Io of 1.17 R_{Io} is excluded in the analysis since it is well within the nominal exobase radius of 1.4. R_{Io})

observers in the 1976 to 1983 time frame. For modeling purposes in Section 4, a one-dimensional east–west profile centered on Io is constructed from this data set. From the data of Schneider *et al.* (1991), five higher quality eclipse profiles and nine higher quality emission profiles have been selected, and their observational dates, times, Io angular parameters, spectral ID numbers, and the numbering of these interleaved observations as adopted in this paper are summarized in Table II. The D_2 brightnesses for the emission profiles in Table II, previously published only in a graphical format, are given numerically in Table III as provided by Schneider (1990, 1995, both private communications). For the sodium cloud data, fourteen images in the D_2 emission line acquired in the 1976–1983 time interval (Murcray 1978; Murcray and Goody 1978; Matson *et al.* 1978; Goldberg *et al.* 1980, 1984; Morgan 1984, private communication) have been selected, with values for the east–west D_2 brightness profiles of the forward and trailing clouds extracted and summarized in Table IV.

The eclipse observations provide the most accurate information in the radial interval from ~1.4 to 6 R_{Io} for the atomic sodium column density profile in the corona within the Lagrange sphere of Io (i.e., a radius of 5.81 R_{Io}) and yield an essentially symmetric column density profile about Io with a power law fit $N\ (1.4 \le r \le 5.85) = 2.55 \times 10^{12} r^{-2.48}$, where N is in units of atoms cm^{-2} and r is the distance from the Io's center in units of R_{Io}. This power law fit, however, undercuts the eclipse data beyond the Lagrange radius, and this reduced slope will later be seen to be caused by the dominant planetary gravitational field beyond Io's Lagrange radius. The emission observations provide accurate information for the sodium D_2 brightness from just within the Lagrange sphere outward into the nearer portion of the sodium cloud (i.e., ~4–40 R_{Io} from Io's center) with a power law fit $I_{D_2}(r \ge 4) = 101\ r^{-1.45}$, where I_{D_2} is in units of kiloRayleighs (kR) and where the D_2 brightness of ~100 kR as r approaches Io's surface is consistent (see Brown and Yung 1976) with the maximum sodium column density of ~1×10^{12} atoms cm^{-2} deduced from the eclipse data. The brightnesses for the different observed profiles in Table III, however, vary by a factor of ~3 to almost 5 at the same distance from Io but have error bars that are no larger than ±30%, suggesting that the large variation is real and likely correlated with Io geocentric phase angle, Io System III longitude, and the east–west asymmetry in the plasma torus, as is the case for sodium cloud image data. The closer spatial regions covered by the eclipse data and the near Io emission data are, however, masked in the cloud images by a circular (or nearly circular) occulting mask of ~10 R_{Io} in radius centered on Io. The sodium cloud image data in Table IV, as illustrated in Fig. 1, hence contribute to the east–west brightness profiles for Iocentric distances from ~10 to ~100 R_{Io}.

The structure of the sodium cloud emission brightness on the sky plane has been historically divided into a forward cloud, so-called because it appears ahead of the satellite in its orbit (i.e., in Fig. 1 located right (west) of Io in image A and left (east) of Io in images B and C), and a corresponding trailing cloud that appears behind the

TABLE III
Emission Data for 1985

	Radial Distance From Io (satellite radii)	D_2 Intensity‡(kR) Emission 1 61.4° 27 August (85g188)	Emission 2 72.2° 27 August (85g196)	Emission 4 87.7° 14 September (85h102)	Emission 5 100.6° 14 September (85h113)	Emission 7 117.2° 23 September (85h433)	Emission 8 121.6° 23 September (85h436)	Emission 9 143.1° 23 September (85h457)	Emission 3* 276.6° 13 September (85h032)	Emission 6 294.7° 15 September (85h152)
	-29.92					0.69 ± 0.17	0.93 ± 0.18	0.66 ± 0.16		
	-29.65									1.12 ± 0.19
	-24.48								1.40 ± 0.21	
	-21.76					1.19 ± 0.19	0.84 ± 0.17	0.95 ± 0.18		
	-16.32					1.38 ± 0.20	2.10 ± 0.26		2.22 ± 0.27	
	-15.78							1.74 ± 0.23		2.15 ± 0.26
	-14.96				1.91 ± 0.24					
	-10.88	3.16 ± 0.35				2.90 ± 0.33	3.29 ± 0.36	3.38 ± 0.37	4.40 ± 0.46	
↑	-9.52			3.17 ± 0.35						
West	-6.80	5.21 ± 0.54	4.50 ± 0.47	6.41 ± 0.66		7.49 ± 0.76	7.76 ± 0.79		11.54 ± 1.16	
	-4.08	14.65 ± 1.47	11.29 ± 1.14	14.71 ± 1.48				7.54 ± 0.77	28.69 ± 2.87	
	-3.81									18.75 ± 2.63
	-2.18	24.31 ± 3.40	18.39 ± 2.57	24.12 ± 3.38		25.61 ± 3.59	25.01 ± 3.50	21.00 ± 2.94	45.47 ± 6.37	
	-1.09	27.46 ± 3.84	19.99 ± 2.80	27.14 ± 3.80		29.95 ± 4.19	28.72 ± 4.02	23.89 ± 3.34	48.61 ± 6.81	
	-0.82									24.85 ± 3.48
Io	0.00	27.44 ± 3.84	19.19 ± 2.69	27.14 ± 3.80		27.90 ± 3.91	30.16 ± 4.22	23.97 ± 3.36	45.56 ± 6.38	
	0.27									25.27 ± 3.54
	1.09	25.87 ± 3.62	19.35 ± 2.71	26.65 ± 3.73	23.03 ± 3.22	26.31 ± 3.68	26.39 ± 3.69	22.84 ± 3.20	39.45 ± 5.52	
	1.36									22.90 ± 3.21
	2.18	25.19 ± 3.53	16.87 ± 2.36	25.68 ± 3.60	19.60 ± 2.74	22.42 ± 3.14	23.91 ± 3.35	20.21 ± 2.83	33.60 ± 4.70	
	3.26									11.53 ± 1.61
	4.08	17.60 ± 1.77	11.92 ± 1.20	18.10 ± 1.82	11.87 ± 1.20	15.54 ± 1.56	14.83 ± 1.49	12.52 ± 1.26	20.06 ± 2.01	
	5.98									4.79 ± 0.50
East	6.80	8.31 ± 0.84	5.52 ± 0.57	8.17 ± 0.83	5.52 ± 0.57	7.09 ± 0.72	7.10 ± 0.73	6.02 ± 0.62	7.52 ± 0.77	
↓	10.06									1.66 ± 0.22
	10.88	3.40 ± 0.37	1.94 ± 0.25	3.84 ± 0.41	3.21 ± 0.35	2.47 ± 0.29	2.47 ± 0.29	2.26 ± 0.27	2.73 ± 0.31	
	15.50									0.77 ± 0.17
	16.32			2.84 ± 0.32	1.81 ± 0.24	1.03 ± 0.18	1.11 ± 0.19	0.82 ± 0.17	1.39 ± 0.20	
	21.76			2.25 ± 0.27		0.68 ± 0.16	0.75 ± 0.17	0.52 ± 0.16		
	23.66									0.53 ± 0.16
	24.48				1.24 ± 0.19				1.06 ± 0.18	
	27.20			1.39 ± 0.21						
	35.36			1.27 ± 0.20					1.00 ± 0.18	
	46.24								0.83 ± 0.17	

‡Nonuniform spatial coverage occurs because of different distance intervals adopted to obtain good average brightness values (given different signal to noise ratios) and because of signal drop-out associated with constraints imposed on positioning the slit profile on the CCD detector during interleaved eclipse and emission measurements.

*Calibration uncertain

TABLE IV
East–West D_2 Brightness Profiles for Sodium Cloud Image Data

UT Date	UT Time	Image ID Number	Io Geocentric Phase Angle (deg)	Io System III Longitude (deg)	East-West Distance from Io for Specified D_2 Brightness Level (satellite radii)							
Image Data Set Reference: Murcray (1978)					0.5 kR		1.0 kR		1.5 kR		2.0 kR	
					Forward	Trailing	Forward	Trailing	Forward	Trailing	Forward	Trailing
1976 Nov. 16	0806	ES 328B	256	262	–	–	51	29	46	24	28	14
1977 Jan 27	0024	ES 369A	86	193	60	38	50	22	44	19	32	16
	0217	ES 370D	102	245	>83	30	56	25	46	21	24	19
Image Data Set Reference: Goldberg(1988†)					0.2 kR		0.5 kR		1.0 kR		2.0 kR	
					Forward	Trailing	Forward	Trailing	Forward	Trailing	Forward	Trailing
1981 May 5	0819	SIP 418/31-33	102	300	78	69	63	40-66	45	37	24	21
May 12	0848	SIP 420/30-32	91	302	66	86	41	37	35	29	20	21
May 13	0346	SIP 421/21-23	253	108	74-103	73	70	41	41	27	29	20
	0555	SIP 421/32-33	271	168	124	65	112	44	51	30	26	19
June 6	0436	SIP 424/10-12	103	300	81	75	68	71	36	26	20	23
Image Data Set Reference: Morgan (1984†)					0.3 kR		0.6 kR		0.9 kR		1.8 kR	
					Forward	Trailing	Forward	Trailing	Forward	Trailing	Forward	Trailing
1983 June 13	0714	i 8492	274	230	–	39	58	26	37	19	20	–
	0722	i 8494	275	233	–	35	52	22	40	20	20	–
	0729	i 8496	276	237	>93	36	52	22	37	17	22	–
	0827	i 8501	284	264	>93	39	61	25	42	19	23	–
	0949	i 8509	296	301	>93	47	63	26	44	17	24	–
	1010	i 8511	299	311	>93	41	63	23	44	16	19	–

†Image observational data obtained by private communication.

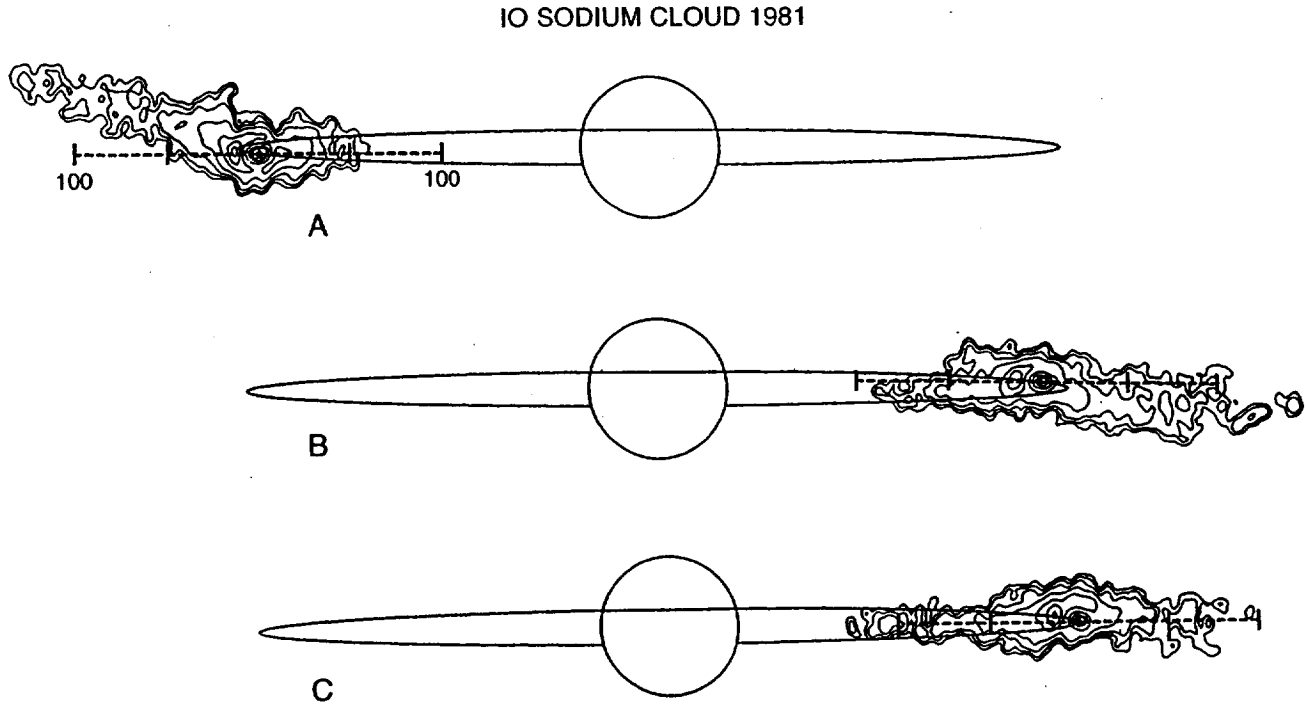

FIG. 1. Io sodium cloud images. Three calibrated D_2 emission images of the Io sodium cloud from the JPL Table Mountain Data Set are shown to proper scale with Jupiter and Io's orbit as viewed from earth in 1981 (Smyth and Goldberg 1993). The Io System III longitude and corresponding orientation of the trailing directional feature in image A are 247° and north, in image B are 104° and south, and in image C are 178° and only very slightly north. An east–west spatial scale of ±100 satellite radii about Io is shown for reference, with tick marks also located at ±50 satellite radii. Contour levels for the D_2 brightness, from outside to inside, are 0.2, 0.5, 1, 2, 4, 6, 8, and 10 kR. An occulting mask of ~10 R_{Io} in radius is centered on Io so that brightness values within this distance are not accurate.

satellite. The forward cloud changes in length, brightness, and east–west orientation relative to the satellite's location as Io moves about Jupiter (i.e., as a function of the Io geocentric phase angle). This change in orientation is well documented (Murcray 1978; Murcray and Goody 1978; Goldberg *et al.* 1984) and is due primarily to the projection upon the two-dimensional sky plane of a three-dimensional cloud (Smyth and McElroy 1978), slightly altered from mirror symmetry by solar radiation pressure (Smyth 1979, 1983), which passes through an east symmetric turning point between about 65° and 85° to 90° and a west symmetric turning point at about 235° (Goldberg *et al.* 1984). A detailed examination of the emission data of Schneider *et al.* (1991), summarized in the last seven columns of Table II, shows that the forward and trailing profiles for the emission data are quite consistent with this known behavior of the Io sodium cloud images. In the trailing cloud, the time-dependent change in the north–south inclination of the fainter directional feature (see Fig. 1) has been shown to be correlated with the System III longitude of Io (Pilcher *et al.* 1984; Goldberg *et al.* 1984) with the directional feature changing from a south to north inclination (a first null point) at an Io System III longitude near 165° and changing from a north to south inclination (a second null point) for a rather poorly defined Io System III longitude somewhere between about 320° and 25°. When the directional feature is near the null location, as illustrated in Fig. 1, an increase in both the spatial extension and brightening of the trailing cloud along the east–west oriented (dashed) line is readily apparent. In addition, since the trailing cloud is associated with a high-speed Io sodium source (~15–20 km sec^{-1}), an increase in the Doppler width of the spectral line in the trailing cloud brightness along an east–west slit is also expected near the null location and is indeed observed in the emission data of Schneider *et al.* (1991), as indicated in Table II.

Information for the sodium D_2 brightness profiles in both the forward and trailing clouds is presented in Fig. 2. The forward and trailing cloud orientation depicted in Fig. 2 is chosen for Io near eastern elongation in order to facilitate the comparison with the 1985 emission data profiles, mostly acquired for Io east of Jupiter. The five emission profiles of Schneider *et al.* (1991) for Io east of Jupiter are shown by different symbol together with their power-law fits ($I_{D_2}(r \geq 4) = Ar^{-\beta}$) given in Table II. For the Io sodium cloud images, the extracted east–west D_2 brightness profiles in Table IV for the forward and trailing clouds are shown by shaded areas, which represent appro-

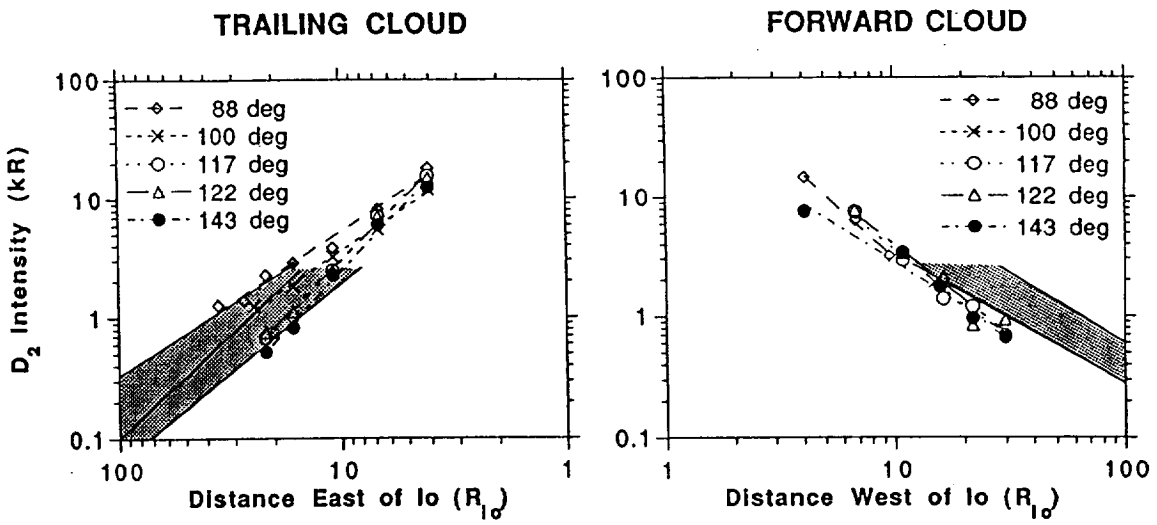

FIG. 2. East and west brightness profiles for selected 1985 emission data and image cloud data. The spatial profiles both east and west of Io for the sodium D_2 emission brightness in units of kilorayleighs are shown as a function of the distance along the observing slit from the center of Io. Five emission observations identified by their satellite geocentric phase angles are shown by the different symbols. These five profiles occur when Io is east of Jupiter and past the satellite phase angle where the forward cloud has its symmetric turning point so that the trailing cloud profiles are all to the east (left) of Io and the forward cloud profiles are all to the west (right) of Io. A power law fit to each profile is also shown. At larger distances from Io, an envelope for the east–west D_2 emission profile acquired from sodium image data is shown by the shaded area. For the trailing profile, the shaded area is divided into two parts: the lower area corresponding to sodium cloud data when the directional feature is oriented either north or south and the upper area corresponding to the directional feature oriented along the east–west direction (i.e., the null condition).

priate bounds for the brightness profiles when Io is somewhat near the elongation points of its orbit. For the trailing cloud, two different shaded areas are shown in Fig. 2 for the two different basic orientations of the directional feature: (1) lower area, when the directional feature is inclined either north or south, and (2) upper area, when the directional feature is at or near the null locations. As expected, the shaded area for the directional feature near the null locations is both brighter and less steep than the shaded area for the directional feature with either a significant north inclination or a significant south inclination. At larger distances from Io (>30 R_{Io}), however, note that both shaded areas for the trailing sodium cloud are dimmer and more closely confined to Io than the shaded area for the forward cloud. In the forward cloud, all the emission brightness profiles are fairly tightly confined and have a slightly steeper slope than the shaded area due to increasing Io geometric plase angle. In the trailing cloud, the brightest and least steep of these profiles is for the emission 4 (Io phase angle 87.7°) acquired for the directional feature at the null condition, while the next brightest profile is for the emission 5 (Io phase angle 100.6°), acquired ~1.5 hr later.

4. ANALYSIS OF THE OBSERVATIONS

Modeling analysis of the one-dimensional sodium distribution described in the previous section will now be undertaken. Collectively, the eclipse measurements for the corona near Io, the emission measurements that extend into the near sodium cloud, and the sodium cloud image derived profiles that reach to distances of $\pm 100\ R_{Io}$, provide a set of spatially overlapping observations that will be used to study and constrain the initial velocity dispersion of the sodium source atoms at the exobase. In the modeling analysis, one-dimensional profiles are calculated using the numerical sodium cloud model of Smyth and Combi (1988a,b), where the electron impact ionization sink for sodium is determined for a 7° tilted corotating plasma torus with an offset-dipole planetary magnetic field in the presence of a nominal (i.e., ~2.8 mV m^{-1} in Io's frame) east–west electric field. A System III longitudinal asymmetry, although present in the torus ion emission, is not included but deferred to a later time when the electron dependence is available.

To investigate the nature of the initial velocity dispersion of the sodium source, two different source flux speed distributions discussed earlier by Smyth and Combi (1988b; see their Appendix D) are considered: (1) a Maxwell–Boltzmann flux distribution and (2) a modified-sputtering flux distribution. The Maxwell–Boltzmann flux distribution $\phi(v; T)$ is based on the Maxwell–Boltzmann velocity distribution and is defined as

$$\phi(v; T) = \phi_0 \left(\frac{R_S}{R_E}\right)^2 \frac{2}{v_T} \left(\frac{v}{v_T}\right)^3 e^{-(v/v_T)^2} \qquad (1)$$

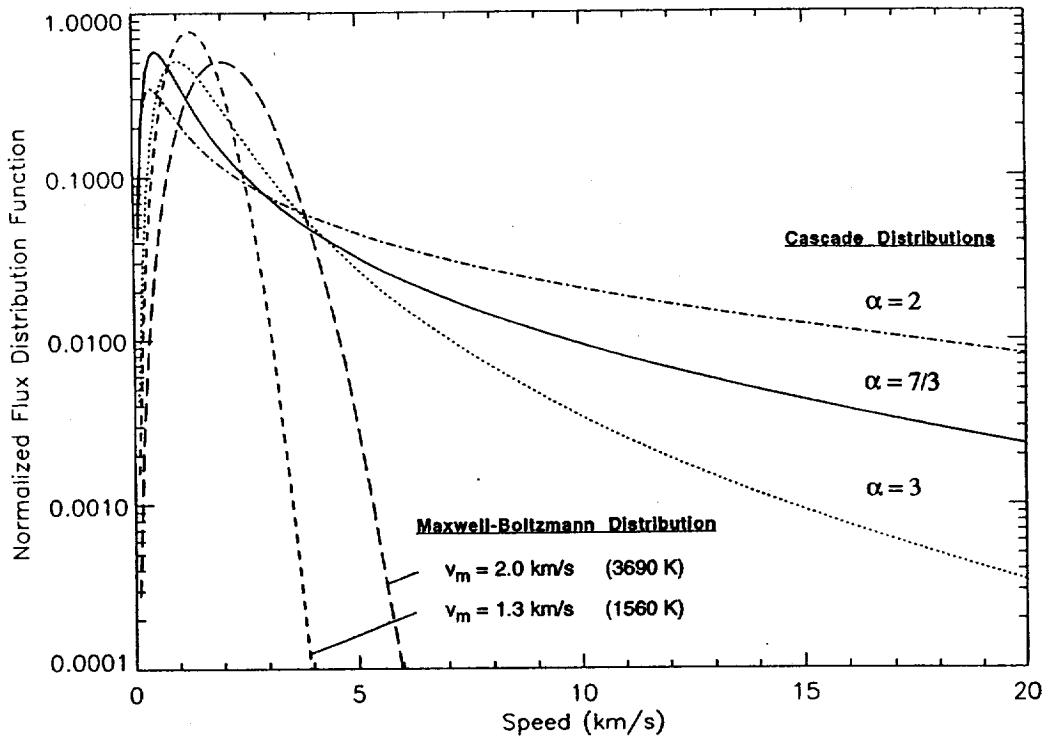

FIG. 3. Flux speed distribution functions for sodium at Io's exobase. Maxwell–Boltzmann flux speed distributions for sodium are shown for most probable speeds, v_m, of 1.3 km sec^{-1} and 2.0 km sec^{-1}. Modified sputtering flux speed distributions are also shown for $\alpha = 3$ and a most probable speed of 1.0 km sec^{-1}, for $\alpha = 7/3$ and a most probable speed of 0.5 km sec^{-1}, and for $\alpha = 2$ and a most probable speed of 0.4 km sec^{-1}. All of the flux speed distributions are normalized to unit area under the curve.

where $v_T = \sqrt{2kT/m}$ is the most probable speed of the velocity distribution for an atom of mass m. The Maxwell–Boltzmann flux distribution is proportional to the local velocity integrated flux ϕ_0 referenced here to the satellite radius R_S not the exobase radius R_E and depends upon one parameter, the exobase temperature T (or alternatively v_T), which determines both the most probable speed $v_m = \sqrt{3kT/m}$ and the speed dispersion of the flux distribution. The modified-sputtering flux distribution $\phi(v; \alpha, v_b, v_M)$ is proportional to the local velocity integrated flux ϕ_0 and depends upon three parameters, an exponent α and two velocity parameters v_b and v_M,

$$\phi(v; \alpha, v_b, v_M) = \phi_0 \left(\frac{R_S}{R_E}\right)^2 \frac{1}{v_b D(\alpha, v_M/v_b)} \left(\frac{v}{v_b}\right)^3 \left(\frac{v_b^2}{v^2 + v_b^2}\right)^\alpha \left[1 - \left(\frac{v^2 + v_b^2}{v_M^2}\right)^{1/2}\right], \quad (2)$$

where $D(\alpha, v_M/v_b)$ is a normalization constant (see Smyth and Combi 1988b). The exponent α primarily determines the dispersion of the distribution, which has a greater high-speed population as α decreases. The exponent α has a value of 3 for a classical sputtering distribution (i.e., a complete collisional cascade process) and a value of 7/3 for a Thomas–Fermi modified-sputtering flux distribution (i.e., the limit of a single elastic collisional ejection process), where the latter distribution is based upon a Thomas–Fermi differential scattering cross section. The velocity parameter v_b is related nonlinearly to the most probable speed v_m of the flux speed distribution and primarily determines v_m (see Smyth and Combi, 1988b, Appendix D). The velocity parameter v_M primarily determines the maximum speed for the flux distribution and depends upon the maximum relative speed (and masses) of the plasma torus ion and sodium atom. For different values of their parameters, two Maxwell–Boltzmann flux distributions and three modified-sputtering flux distributions are shown in Fig. 3 and will be utilized in the subsequent modeling analysis.

In calculating the column density and the D_2 emission brightness in the numerical sodium cloud model, a smaller two-dimensional sky-plane grid centered on Io ($\pm 15\ R_{Io}$) is used to cover a spatial scale near the satellite more appropriate to the eclipse data while a much larger two-dimensional sky-plane grid centered on Io is used to cover a larger spatial scale more appropriate for the emission data and the sodium cloud image data. A one-dimensional profile for the eclipse data is obtained from the smaller

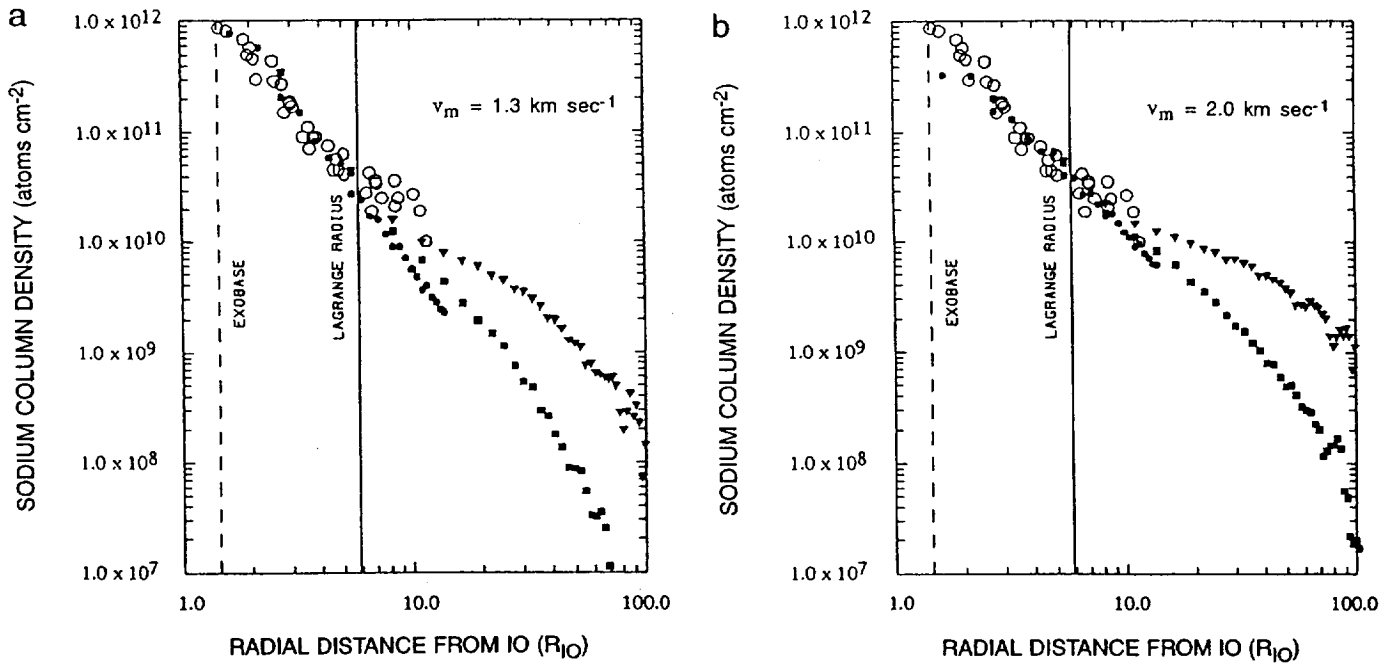

FIG. 4. Model calculations for the Io eclipse data using a Maxwell–Boltzmann flux speed distribution. The atomic sodium column density profile near Io determined from the 1985 eclipse data by Schneider *et al.* (1991) is shown by the open circles. The model calculated column density profiles are shown by solid dots for the (cylindrically averaged) corona, by solid triangles for the forward cloud along the east–west slit direction, and by solid squares for the trailing cloud along the east–west slit direction. These column density profiles were calculated using the Io sodium cloud model of Smyth and Combi (1988b) for their case C description of the plasma torus and for an Io geocentric phase angle of 92.9° and an Io System III longitude angle of 48.6°, which are similar to the emission 4 observation conditions in Table II. Sodium was ejected uniformly from an assumed exobase of 2600 km radius with a velocity dispersion for a Maxwell–Boltzmann flux distribution, where in (a) v_m = 1.3 km sec^{-1} and ϕ_0 = 3.0 × 10^8 atom cm^{-2} sec^{-1}, and in (b) v_m = 2.0 km sec^{-1} and ϕ_0 = 1.8 × 10^8 atom cm^{-2} sec^{-1} (see text).

two-dimensional sky-plane grid by extracting an average radial profile. This average radial profile (called the calculated eclipse profile) will be denoted by the filled circles in Figs. 4–7. A one-dimensional east–west D_2 brightness profile (and also a corresponding column density profile) for the emission data and the sodium cloud image data is obtained from the larger two-dimensional sky-plane grid by selecting only the east–west grid elements that occur in the grid row containing Io. In Figs. 4–7, the calculated east–west brightness and column density profiles are denoted by filled triangles for the forward cloud profile and by filled squares for the trailing cloud profile. To construct an eclipse or east–west profile, monoenergetic model calculations are performed for 18 different nonuniformly spaced speeds ranging from 0.4 to 10 km sec^{-1}. Profiles for speeds beyond 10 km sec^{-1} are determined by an inverse speed extrapolation of the model results. The individual profiles for the different speeds are appropriately weighted for a given source flux speed distribution and then added to obtain the final profile. Model calculations are performed for an Io geocentric phase angle of 92.9° and an Io System III longitude angle of 48.6°. These satellite conditions are similar to those for the emission 4 and eclipse 2 observations of Table II, which are the observations closest to the eastern elongation point. This choice is also appropriate for all the eclipse data, which has no discernible dependence on these two Io related angles, and for the Io sodium cloud image data which have east–west profile areas in Fig. 2 that are representative of the satellite near its orbital elongation points. Modeling analysis results are summarized in Table V and discussed below.

For the first Maxwell–Boltzmann flux distribution in Fig. 3 with a most probable speed of v_m = 1.3 km sec^{-1} (i.e., an exobase temperature of ~1560 K) and with a flux ϕ_0 of 3.0 × 10^8 atoms cm^{-2} sec^{-1} (i.e., a total source of ~1.2 × 10^{26} atoms sec^{-1}), the model calculated eclipse profile (filled circles) in Fig. 4a provides an excellent fit within the Lagrange sphere to the eclipse observations (open circles) and also compares very favorably with the east–west column density profiles calculated for the forward (filled triangle) and trailing cloud (filled squares). This fit verifies and is similar to the earlier 1500 K Maxwell–Boltzmann flux distribution fit of Schneider *et al.* (1991) noted in Section 2. Beyond the Lagrange sphere in Fig. 4a, however, all three of these calculated profiles fall below the eclipse observations, which is considered less accurate

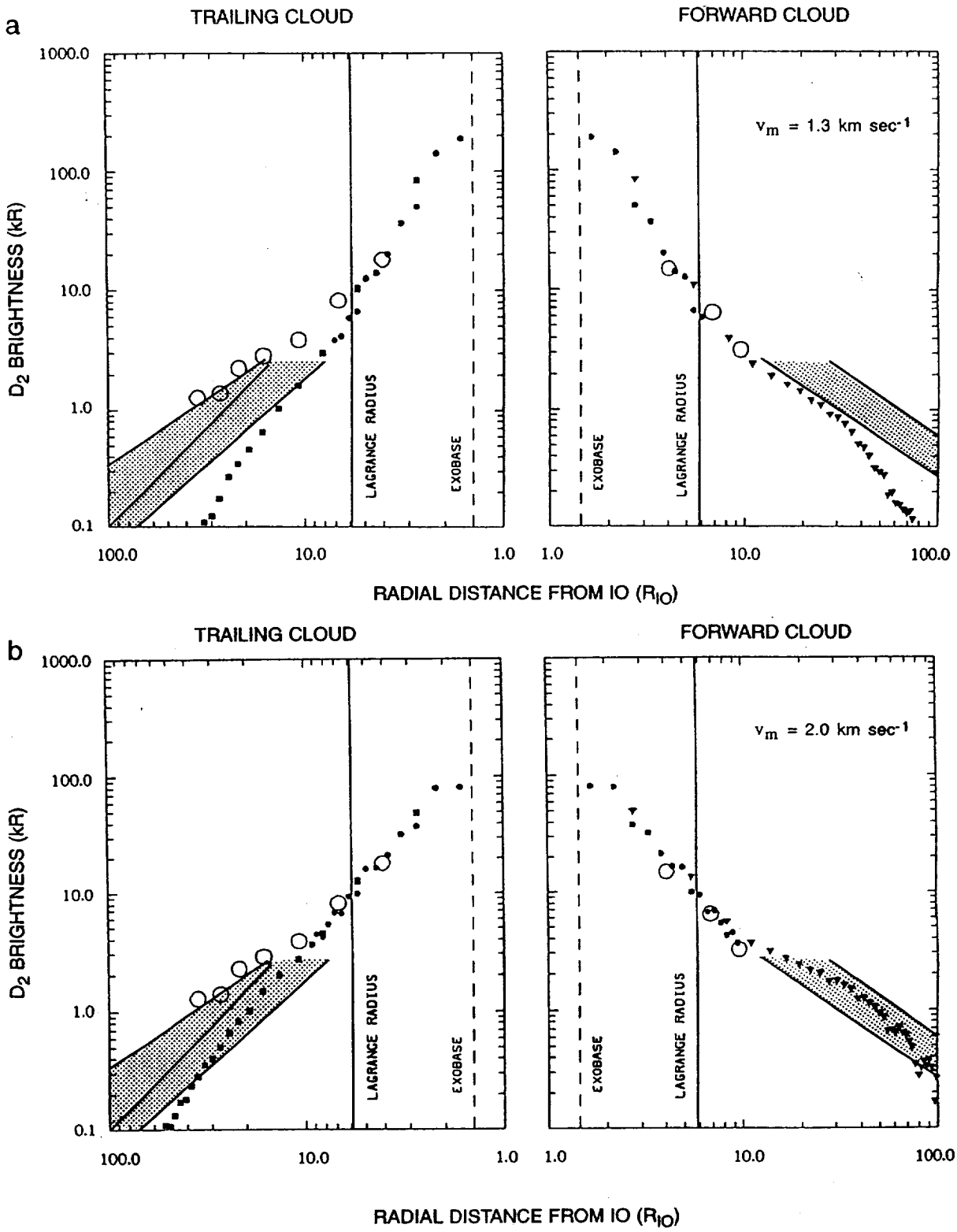

FIG. 5. Model calculations for the east–west D_2 brightness profiles using a Maxwell–Boltzmann flux speed distribution. The east–west D_2 brightness profiles near Io in both the trailing and forward cloud directions as determined by the emission 4 data of Schneider *et al.* (1991) are shown by the open circles. The east–west profile envelopes in both the trailing and forward cloud directions as determined from the sodium cloud image data are shown by the shaded areas (see Fig. 2 caption). The descriptions for the calculated profile symbols, the sodium cloud model and plasma torus, and the Maxwell–Boltzmann flux distribution in (a) and (b) are the same as in the caption of Fig. 4.

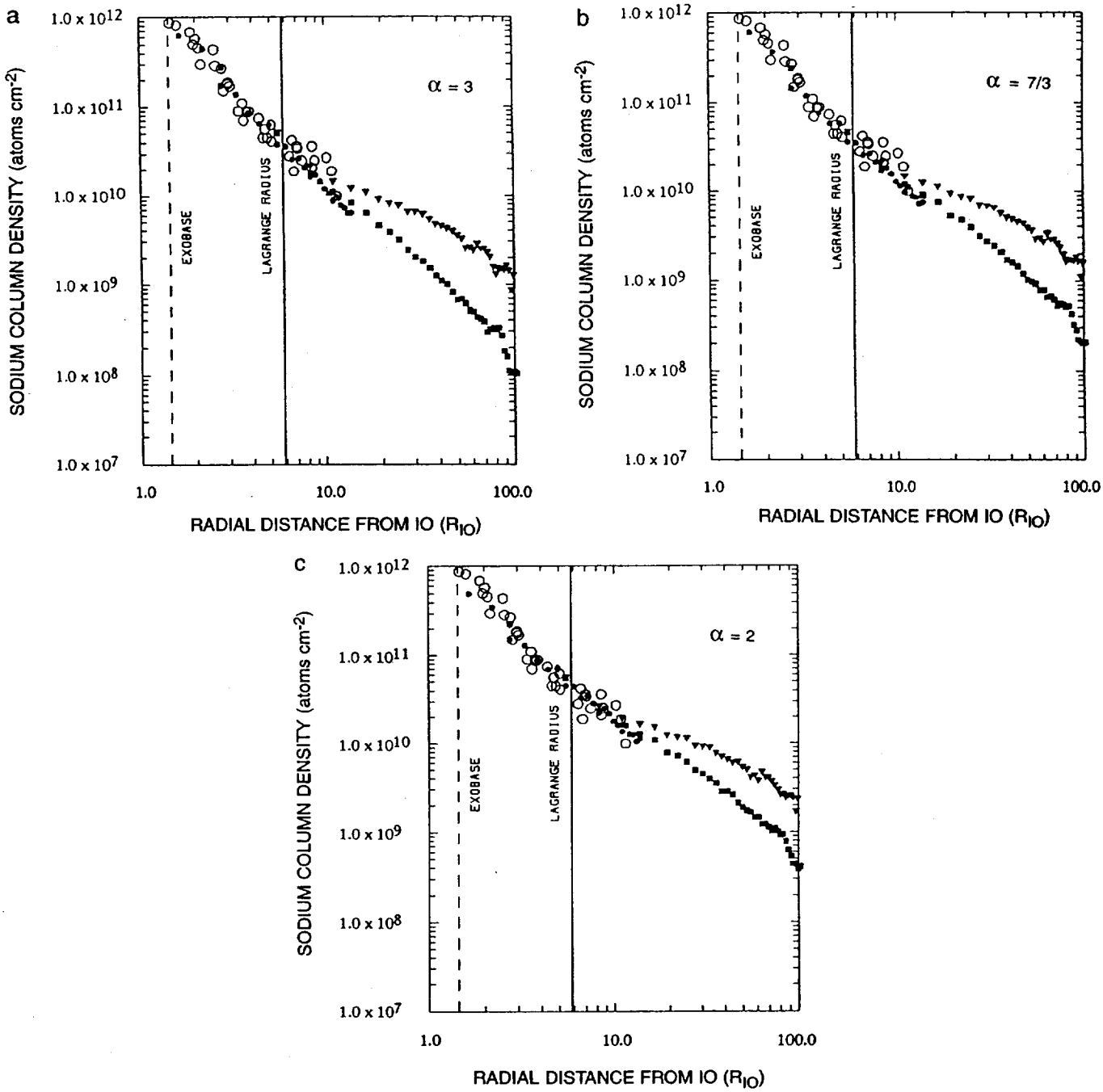

FIG. 6. Model calculations for the eclipse data using a modified sputtering flux speed distribution. The atomic sodium column density profile near Io determined from the 1985 eclipse data by Schneider *et al.* (1991) is shown by the open circles. The model calculated column density profiles are shown by solid dots for the (cylindrically averaged) corona, by solid triangles for the forward cloud along the east–west direction, and by solid squares for the trailing cloud along the east–west direction. These column density profiles were calculated using the Io sodium cloud model of Smyth and Combi (1988b) for their case C description of the plasma torus and for an Io geocentric phase angle of 92.9° and an Io System III longitude angle of 48.6°, which are similar to the emission 4 observation conditions in Table II. Sodium was ejected uniformly from an assumed exobase of 2600 km radius with a velocity dispersion for a modified sputtering flux distribution, where in (a) $\alpha = 3$, $v_m = 1.0$ km sec^{-1}, and $\phi_0 = 3.2 \times 10^8$ atom cm^{-2} sec^{-1}, in (b) $\alpha = 7/3$, $v_m = 0.5$ km sec^{-1}, and $\phi_0 = 4.2 \times 10^8$ atom cm^{-2} sec^{-1}, and in (c) $\alpha = 2$, $v_m = 0.4$ km sec^{-1}, and $\phi_0 = 4.7 \times 10^8$ atom cm^{-2} sec^{-1}.

at these distances. At and beyond about 8 R_{Io}, the calculated east–west forward (filled triangle) and trailing (filled squares) profiles rise above the calculated eclipse profile (filled circles) because the column density is no longer spherically symmetric about Io, with the forward cloud profile having the largest column density and showing a distinct change in its slope compared to the trailing cloud profile. The corresponding model profiles for the D_2 emission brightness are given in Fig. 5a. For both the forward and trailing profiles, the calculated eclipse and calculated east–west profiles are in good agreement with each other inside the Lagrange radius, with a maximum brightness of about 200 kR near the exobase. The calculated east–west profile threads the three emission 4 data points for the forward cloud, but falls well below the emission 4 data points in the trailing cloud. For both the forward and trailing clouds at larger radial distances, the calculated east–west profiles fall well below the areas for both the forward and trailing cloud images. This behavior indicates that there is a large deficiency in the high-speed population for this source flux speed distribution.

Model calculations were therefore performed for the second Maxwell–Boltzmann flux distribution in Fig. 3 with a higher most probable speed of v_m = 2.0 km sec^{-1} (i.e., an exobase temperature of ~3690 K) and with a flux ϕ_0 of 1.8 × 10^8 atoms cm^{-2} sec^{-1} (i.e., a total source of ~0.75 × 10^{26} atoms sec^{-1}) and are shown in Figure 4b and Figure 5b. For the D_2 emission brightness profiles in Figure 5b, the calculated east–west profile now threads the center of the forward cloud image area for a radial distance up to about 70 R_{Io} and the lower trailing cloud image area for a radial distance of about 25 R_{Io} before it falls off too steeply. This improved fit at larger radial distances, however, reduces the D_2 emission brightness at the exobase to about 80 kR in Figure 5b and causes the calculated eclipse profile in Figure 4b to fall below the measured eclipse profile for radial distances inside about 3 R_{Io}. The Maxwell–Boltzmann flux distribution therefore cannot fit both the corona profile near Io and the sodium cloud east–west profiles at large distances from the satellite. A flux distribution that has a broader dispersion with enhanced populations for both the low-speed and high-speed atoms is required. The three modified-sputtering flux distributions in Fig. 3, which have a broader dispersion, are thus

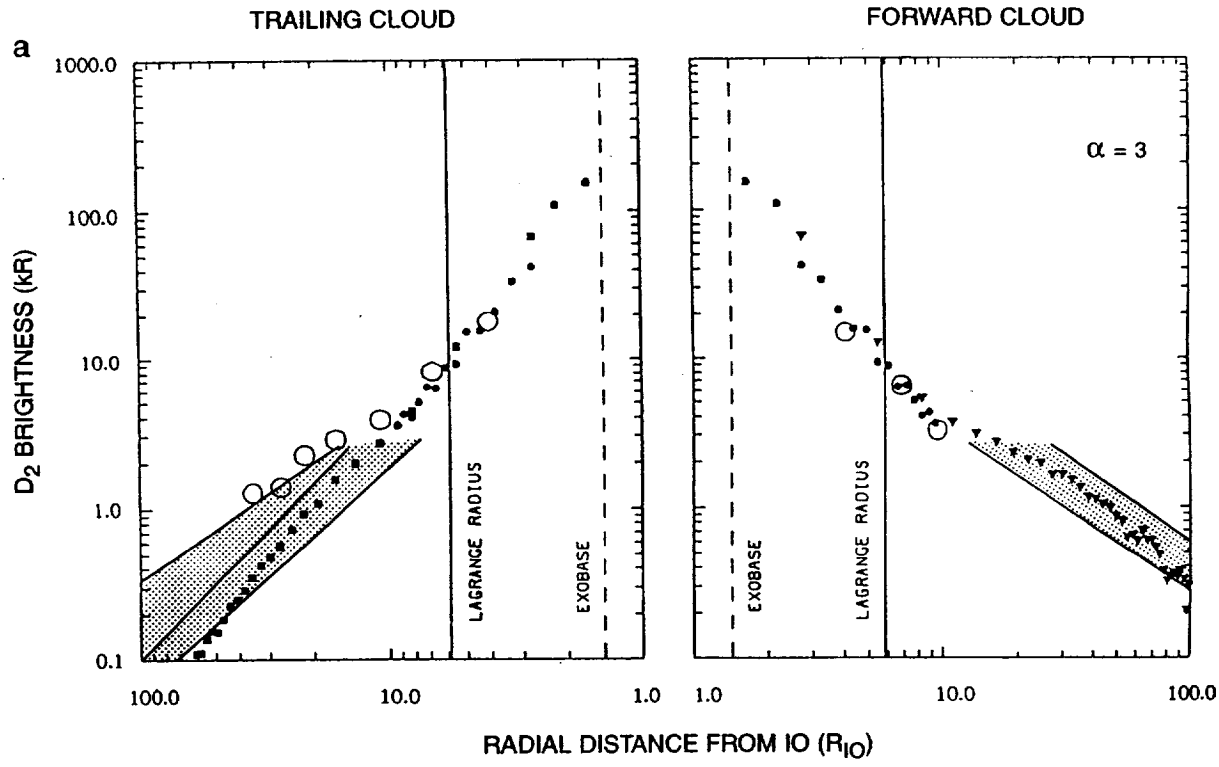

FIG. 7. Model calculations for the east–west D_2 brightness profiles using a modified sputtering flux speed distribution. The east–west D_2 brightness profiles near Io in both the trailing and forward cloud directions determined from the emission 4 data of Schneider *et al.* (1991) are shown by the open circles. The east–west profile envelopes determined from the sodium cloud image data are shown by the shaded areas (see caption of Fig. 2). The descriptions for the calculated profile symbols, the sodium cloud model and plasma torus, and the modified sputtering flux distribution in (a), (b), and (c) are the same as in the caption of Fig. 6.

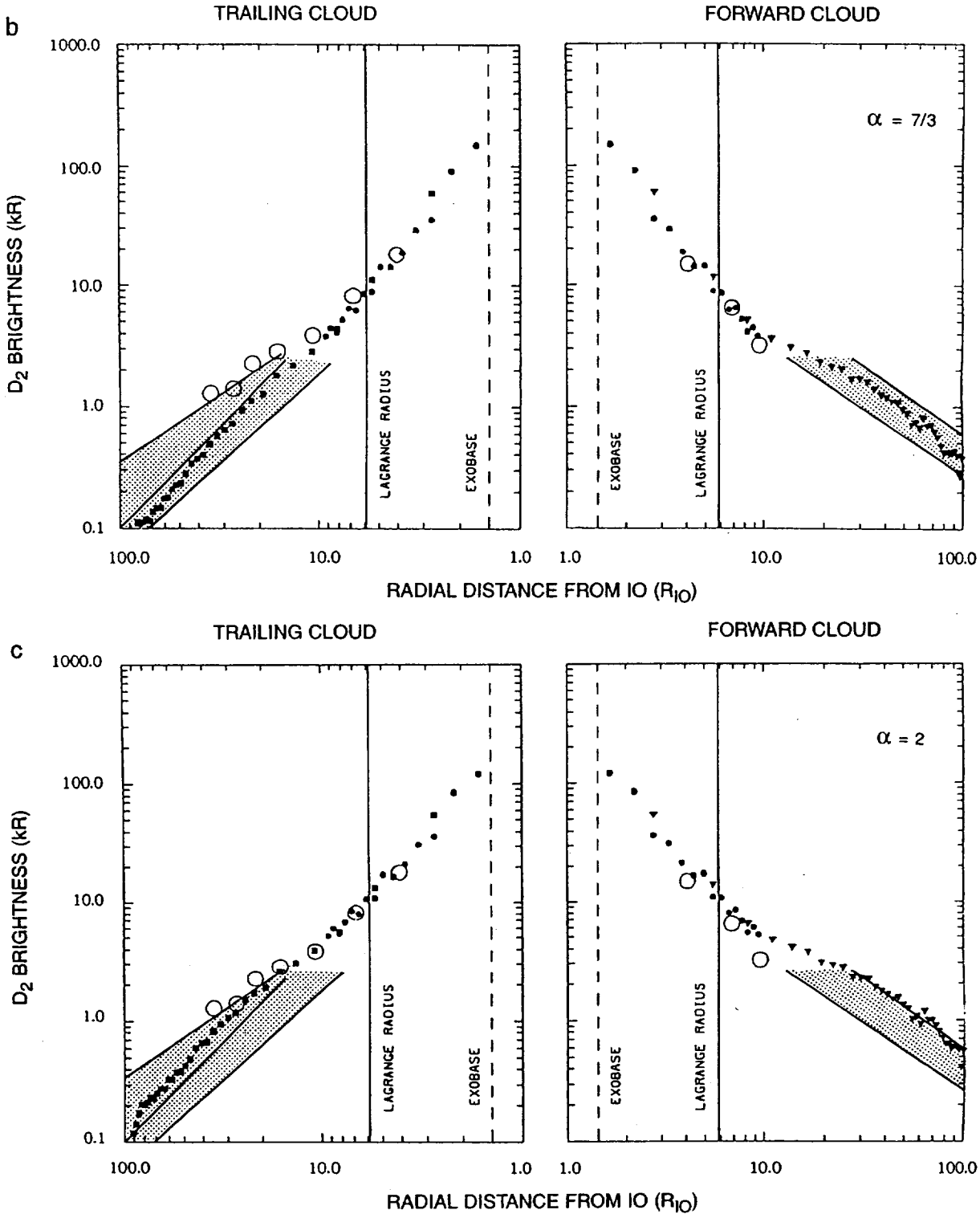

FIGURE 7—*Continued*

TABLE V
Summary Comparison of Modeled and Observed East–West Sodium Profiles for Different Flux Speed Distributions at Io's Exobase

			Corona	Forward Cloud		Trailing Cloud (not null)		Trailing Cloud (null)	
Observations: E/W Radial Interval (R_{Io}):			1.4-6	6-10	10-100	6-10	10-100	6-10	10-100
Distribution Speed Peak (km/s)		Exobase Source Rate (10^{26} atoms/s)	Fits Eclipse Column Profile	Fits Near Io Emission Profile	Fits Far Cloud E/W Profile	Fits Near Io Emission Profile	Fits Far Cloud E/W Profile	Fits Near Io Emission Profile	Fits Far Cloud E/W Profile
1. Maxwell Boltzmann Flux Distribution									
1.3		1.24	YES	YES	too low	little low	too low	too low	too low
2.0		0.75	too low	YES	slightly low	YES	little low	little low	too low
2. Collisional Cascade Flux Distribution									
(classical sputtering)									
$\alpha = 3$	1.0	1.32	YES	YES	tiny low	YES	tiny low	little low	too low
(incomplete cascade: higher velocity tail)									
$\alpha = 7/3$	0.5	1.74	YES	YES	YES	YES	YES	little low	too low
$\alpha = 2$	0.4	1.90	tiny low	too high	too high	too high	too high	YES	YES

considered in the remainder of the paper with model calculations presented in Figs. 6 and 7.

Model calculations for a classical sputtering flux distribution ($\alpha = 3$) and a modified-sputtering flux distribution ($\alpha = 7/3$) are presented in Figs. 6a and 6b for the eclipse observations and in Figs. 7a and 7b for the east–west D_2 emission brightness profiles. For these two flux distributions, the most probable speeds are, respectively, 1.0 km sec^{-1} and 0.5 km sec^{-1}, and the sodium fluxes ϕ_0 are, respectively, 3.2×10^8 atoms cm^{-2} sec^{-1} (i.e., a total source of $\sim 1.3 \times 10^{26}$ atoms sec^{-1}) and 4.2×10^8 atoms cm^{-2} sec^{-1} (i.e., a total source of $\sim 1.7 \times 10^{26}$ atoms sec^{-1}). From the exobase to radial distances of ~ 8 R_{Io}, just beyond the Lagrange radius, both sputtering flux distributions provide a very good fit in Figs. 6a and 6b to the observed eclipse column density profile (open circles) and correspond to an exobase D_2 emission brightness of about 150 kR in Figs. 7a and 7b. For the classical sputtering flux distribution in Fig. 7a, the calculated D_2 emission brightness profile for the forward profile is slightly above the measured data point (open circles) inside the Lagrange radius, matches the two measured data points beyond the Lagrange radius, and then threads the forward cloud image area nicely between about 20 R_{Io} and 80 R_{Io} before it falls too rapidly and drops below this area. An excellent fit for the forward profile is, however, provided by the modified sputtering distribution ($\alpha = 7/3$) in Fig. 7b where the calculated D_2 emission brightness profile matches the measured data points (open circles) both inside and beyond the Lagrange radius as well as nicely threading the forward cloud image area all the way to 100 R_{Io}. For the trailing cloud, the calculated D_2 emission brightness profile for the classical sputtering flux distribution in Fig. 7a matches the measured data point inside the Lagrange radius, is slightly below the two measured data points outside the Lagrange radius, and then threads the lower of the two trailing cloud image areas nicely between about 15 R_{Io} and 35 R_{Io} before it falls too rapidly and drops below this area. An excellent fit for the trailing profile is, however, provided by the modified sputtering distribution ($\alpha = 7/3$) in Fig. 7b where the calculated D_2 emission brightness matches the measured data point inside the Lagrange radius, is slightly below the two measured data points outside the Lagrange radius, and then threads the lower (non-null) trailing cloud image area nicely all the way to 100 R_{Io}. It is particularly noteworthy that the isotropic ejection of sodium from the exobase with a modified sputtering flux distribution with $\alpha = 7/3$ provides a complete fit to the combined eclipse, emission, and forward/trailing sodium cloud image profile data for this non-null condition from 1.4 to 100 R_{Io}.

In order to fit the trailing cloud (upper area) profile for the directional feature at the null condition, it is then clear that a flux distribution is required with an even more enhanced higher-speed population (~ 20 km sec^{-1}) than the modified sputtering flux distribution with $\alpha = 7/3$. Since the modified sputtering flux distribution for $\alpha = 7/3$ corre-

sponds to the limit of a single collision cascade process described by a Thomas–Fermi cross section (see Smyth and Combi 1988b), reducing the value of α to a smaller value becomes somewhat physically questionable but will be used here for the purposes of simply illustrating the impact of a more enhanced higher-speed sodium population in the model calculation. As discussed earlier, this higher-speed sodium is thought to be nonisotropically ejected from Io's exobase and attributed to some combination of direct collisional and lower-velocity charge exchange ejection. Choosing the modified sputtering flux distribution with $\alpha = 2$ in Fig. 3 which has a most probable speed of 0.4 km sec^{-1} and selecting an isotropic exobase source rate of 1.9×10^{26} atoms sec^{-1} (i.e., a flux ϕ_0 of 4.7×10^8 atoms cm^{-2} sec^{-1}), the model-data comparison is shown in Fig. 6c for the eclipse column density and in Fig. 7c for the east–west D_2 emission brightness. The sputtering flux distribution provides a reasonably good fit to the observed column density data points in Fig. 6c with only a small departure very near the exobase and produces a column density profile beyond 10 R_{Io} that is significantly enhanced compared to the $\alpha = 7/3$ case in Fig. 6b. In Fig. 7c, this enhancement in the forward cloud is obvious, where the calculated D_2 emission brightness profile is significantly above the measured data points both inside and outside the Lagrange radius and is above or in the very top of the forward cloud image area all the way to 100 R_{Io}. The additional enhanced high-speed population of the $\alpha = 2$ modified sputtering flux distribution is too large and therefore not consistent with the observed forward profile. In contrast for the trailing cloud in Fig. 7c, the calculated D_2 emission brightness profile matches the measured data points inside and outside of the Lagrange radius very well and then threads the upper of the two trailing cloud image areas nicely all the way to ~90 R_{Io}. This demonstrates that the trailing cloud can be fitted with an enhanced higher-speed population of sodium atoms in the flux distribution. It also immediately demonstrates that the flux distribution at the exobase must be nonisotropic with the enhanced high-speed population weighted toward vector directions that will preferentially populate the trailing cloud. As discussed in Section 2, this nonisotropic requirement for a flux distribution for speeds of ~20 km sec^{-1} is similar to the conclusions reached by earlier modeling analyses (Pilcher *et al.* 1984; Smyth and Combi 1991; Wilson and Schneider 1995).

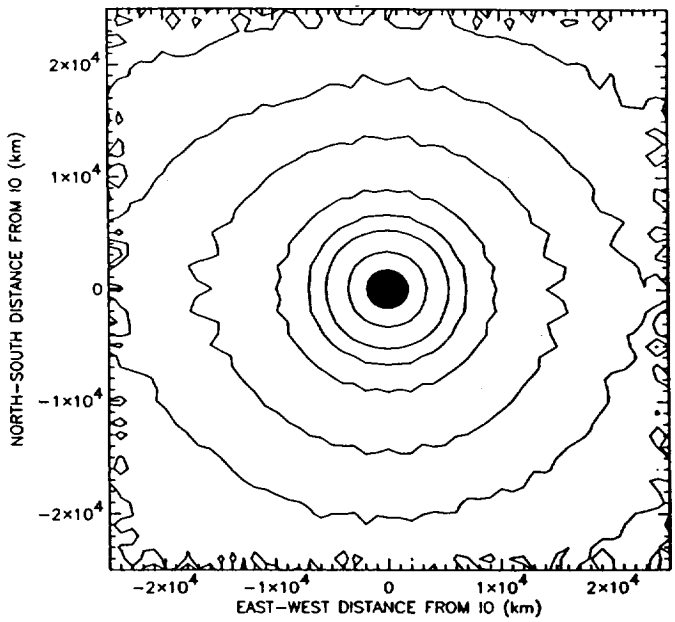

FIG. 8. Two-dimensional nature of the sodium column density near Io. Contours for the two-dimensional column density near Io are shown in the sky-plane of the earth as determined from the sodium cloud model calculation for the modified sputtering flux speed distribution described in Fig. 6(b) for $\alpha = 7/3$. The vertical and horizontal directions are the projected directions that are, respectively, perpendicular and parallel to the semimajor axis of the Io's orbital ellipse on the sky plane. Io's location and size are shown to scale by the black circle. The sodium column density contours in units of 10^{11} atoms cm^{-2} are, from inside to outside, 5, 2, 1, 0.5, 0.2, 0.1, and 0.05.

5. DISCUSSION AND CONCLUSIONS

The composite spatial information for sodium obtained by combining the eclipse observations (radial distances from Io of 1.4 to ~10 R_{Io}), the emission observations (east–west distances of ±4 to ±30–40 R_{Io}), and the sodium cloud observations (east–west distances of ±10 to ±100 R_{Io}) has been analyzed to extract a basic description for the flux speed distribution at the satellite's exobase. An isotropic modified-sputtering flux speed distribution in Fig. 3 with $\alpha = 7/3$, a most probable speed of 0.5 km sec^{-1}, and a source strength of 1.7×10^{26} atoms sec^{-1} provides a very good fit to these composite observations when the directional feature is either north or south and hence not contributing to the east–west profile of the trailing cloud. It is remarkable that these observations, acquired by a number of ground-based programs over very different spatial scales and at different times during the 1976–1985 decade, are so self-consistent. Near Io, the two-dimensional sodium column density produced by this modified sputtering distribution as calculated by the sodium cloud model in the profile analysis above is shown in Fig. 8 and can be seen at larger distances from Io to become nonspherical and more confined near the satellite plane. This flattening near the satellite plane is the merging of the near Io corona into the sodium cloud and is caused naturally by orbital dynamics beyond the satellite Lagrange sphere where the gravity of Jupiter is dominant. The forward cloud portion of the east–west emission data profiles has a rather tightly confined slope that, in the absence of the trailing cloud

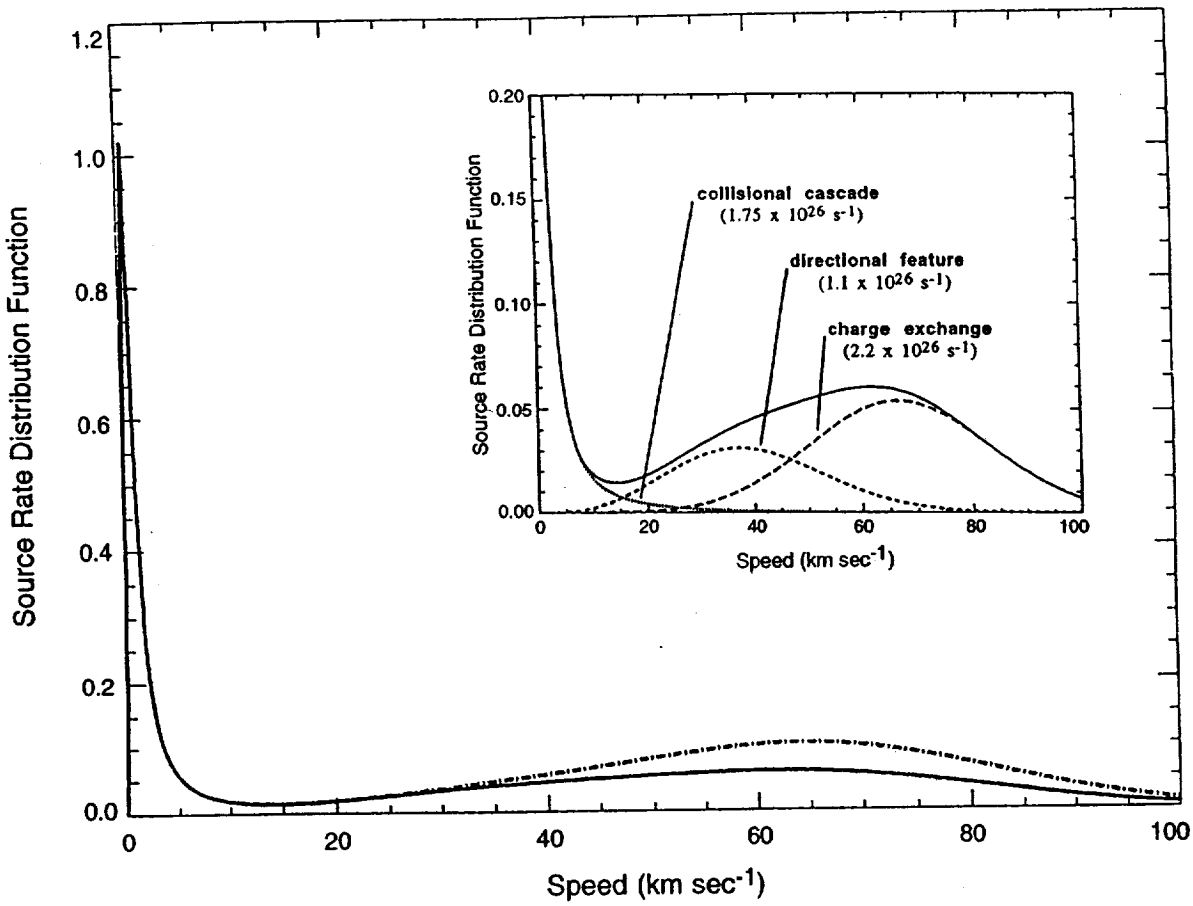

FIG. 9. Total source rate speed distribution function for sodium at Io's exobase. The total source rate speed distribution function at Io's exobase, in units of 10^{26} atoms sec^{-1} (km/sec)$^{-1}$, is composed of three separate source rate speed distributions as discussed in the text and is shown for two different source strengths for the higher-speed zenocorona source centered about 57 km sec^{-1}. The lower (solid line) and upper (dashed-dot line) curves correspond, respectively, to the sodium zenocorona higher-speed source rates of 2.2×10^{26} atoms sec^{-1} (Smyth and Combi 1991) and 4×10^{26} atoms sec^{-1}. The two source rates for the higher-speed zenocorona source are shown to exhibit its typical time-variable source strength range of ~2–4 $\times$ 10^{26} atoms sec^{-1} as reported by Flynn *et al.* (1994). The decomposition of the solid curve into its three separate source rate speed distributions is shown in the cutout and is determined by combining (1) the isotropic modified sputtering source rate distribution (dotted line in the cutout) for $\alpha = 7/3$, $v_m = 0.5$ km sec^{-1} and a source strength of 1.7×10^{26} atom sec^{-1}, (2) the nonisotropic lower-speed source rate distribution (short dashed line in the cutout) for the sodium zenocorona and directional feature centered about 20 km sec^{-1}, with a source strength of 1.1×10^{26} atoms sec^{-1} as determined by Smyth and Combi (1991), and (3) the nonisotropic higher-speed source rate distribution (longer dashed line in the cutout) for the sodium zenocorona centered about 57 km sec^{-1}, with a charge exchange source strength of 2.2×10^{26} atoms sec^{-1} as determined by Smyth and Combi (1991).

enhancement at the null condition, is less steep and is brighter than the trailing cloud profiles. In order, however, to reproduce the extended east–west profile in the trailing sodium cloud when the directional feature is in the satellite plane (i.e., the null location), additional nonisotropic high-speed sodium is required.

The sodium atoms ejected from Io's exobase as described above by the modified sputtering flux distribution have speeds primarily in the range from 0 to a few tens of km sec^{-1}. This neutral flux distribution represents the spatially integrated effect of the incomplete collisional cascade process that occurs from the collisional interactions of heavy ions in the corotating plasma torus with neutrals in Io's atmosphere. This flux speed distribution can be alternatively described as a source rate speed distribution by multiplying it by the satellite surface area. In addition to these ion-neutral elastic collisional encounters, resonance charge exchange between plasma torus sodium ions and neutral sodium in Io's atmosphere is also responsible for producing a sodium source with higher speeds relative to Io. These speeds are centered about the corotational ion speed (~57 km sec^{-1}) relative to Io's motion and have a dispersion reaching from several tens of km sec^{-1} to ~100 km sec^{-1}. Such high speed sodium ($\leq$80 km sec^{-1}) has

recently been observed near Io by Cremonese *et al.* (1992). As discussed in Section 2, this higher-speed nonisotropic source of sodium together with the lower speed (~15–20 km sec^{-1}) nonisotropic source for the directional feature form the source for the sodium zenocorona or magnetonebula. Earlier modeling studies (Smyth and Combi 1991; Flynn *et al.* 1992) indicated that the higher-speed source was $\sim 2 \times 10^{26}$ atoms sec^{-1} while the lower speed source was $\sim 1 \times 10^{26}$ atoms sec^{-1}. More recent observations and analysis (Flynn *et al.* 1994) have shown that the higher-speed sodium source is time variable and in the range $\sim 2\text{–}4 \times 10^{26}$ atoms sec^{-1}. A total source rate speed distribution for sodium at Io's exobase has hence been constructed by combining the modified sputtering source rate distribution determined in this paper with the two source rate distribution for the zenocorona as given by Smyth and Combi (1991) and is shown in Fig. 9. The lower (solid line) and upper (dashed-dot line) curves correspond, respectively, to the sodium zenocorona higher-speed source rates of 2.2×10^{26} and 4×10^{26} atoms sec^{-1}. Total source rate speed distribution functions at Io's exobase expected for other atomic species, such as K, O, and S, can be constructed in a similar fashion by adopting the estimated source rates given by Smyth and Combi (1991).

Future studies for the sodium flux speed distribution at Io's exobase are anticipated using much larger data sets now available for east–west and north–south sodium emission observations. It will then be possible to analyze the combined spatial and spectral information and refine the nonisotropic nature of the flux distribution and also to search for other possible east–west and System III related variations. Once this information is determined for sodium, the implications for the more abundant species in Io's atmosphere will be particularly important in other related studies for the many-faceted and complex phenomena in the Io–Jupiter system.

ACKNOWLEDGMENTS

We are grateful to N. M. Schneider for helpful discussions and for providing the numerical data for the 1985 emission observations. We also thank the two referees for their helpful comments. This research was supported by the Planetary Atmospheres Program of the National Aeronautical and Space Administration under Grant NAGW-3585 to the University of Michigan and under Contracts NASW-4416, NASW-4471, and NASW-4804 to Atmospheric and Environmental Research, Inc.

REFERENCES

Bergstralh, J. T., D. L. Matson, and T. V. Johnson 1975. Sodium D-line emission from Io: Synoptic observations from Table Mountain Observatory. *Astrophys. J. Lett.* **195,** L131–L135.

Bergstralh, J. T., J. W. Young, D. L. Matson, and T. V. Johnson 1977. Sodium D-line emission from Io: A second year of synoptic observation from Table Mountain Observatory. *Astrophys. J. Lett.* **211,** L51–L55.

Brown, R. A. 1974. Optical line emission from Io. In *Exploration of the Planetary System* (A. Woszczyk and C. Iwaniszewska, Eds.), Proceedings IAU Symposium No. 65, Torun, Poland, Sepetember 5–8, 1973, pp. 527–531. Reidel, Dordrecht.

Brown, R. A., and Y. L. Yung 1976. Io, its atmosphere and optical emissions. In *Jupiter: Studies of the Interior, Atmosphere, Magnetosphere, and Satellites* (T. Gehrels, Ed.), pp. 1102–1145. Univ. of Arizona Press, Tucson.

Carlson, R. W., D. L. Matson, and T. V. Johnson 1975. Electron impact ionization of Io's sodium emission cloud. *Geophys. Res. Lett.* **2,** 469–472.

Cremonese, G., N. Thomas, C. Barbieri, and C. Pernechele 1992. High resolution spectra of Io's neutral sodium cloud. *Astron. Astrophys.* **256,** 286–298.

Fang, T.-M., W. H. Smyth, and M. B. McElroy 1976. The distribution of long-lived gas clouds emitted by satellites in the outer Solar System, *Planet. Space Sci.* **25,** 577–588.

Flynn, B. 1993. Oscillating ion streamline model of Jupiter's neutral sodium nebula. *Adv. Space Science* **13,** 325–330.

Flynn, B., M. Mendillo, and J. Baumgardner 1992. Observations and modeling of the jovian remote sodium emission. *Icarus* **99,** 115–130.

Flynn, B., M. Mendillo, and J. Baumgardner 1994. The jovian sodium nebula: Two years of ground-based observations. *J. Geophys. Res.* **99,** 8403–8409.

Goldberg, B. A., R. W. Carlson, D. L. Matson, and T. V. Johnson 1978. A new asymmetry in Io's sodium cloud, *Bull Am. Astron. Soc.* **10,** 579.

Goldberg, B. A., Yu. Mekler, R. W. Carlson, T. V. Johnson, and D. L. Matson 1980. Io's sodium emission cloud and the Voyager 1 encounter. *Icarus* **44,** 305–317.

Goldberg, B. A., G. W. Garneau, and S. K. LaVoie 1984. Io's sodium cloud. *Science* **226,** 512–516.

Ip, W.-H. 1990. Neutral gas–plasma interaction: The case of the plasma torus, *Adv. Space Res.* **10,** 15–23.

Macy, W. W., Jr., and L. M. Trafton 1980. The distribution of sodium in Io's cloud: Implications. *Icarus* **41,** 131–141.

Matson, D. L., B. A. Goldberg, T. V. Johnson, and R. W. Carlson 1978. Images of Io's sodium cloud. *Science* **199,** 531–533.

Mendillo, M., J. Baumgardner, B. Flynn, and W. J. Hughes 1990. The extended sodium nebula of Jupiter. *Nature* **348,** 312–314.

McGrath, M. A. 1988. *Ion Bombardment of Io and Mercury.* Ph.D. Thesis, Dept. of Astronomy, University of Virginia.

Murcray, F. J. 1978. *Observations of Io's Sodium Cloud.* Ph. D. Thesis, Dept. of Physics, Harvard University.

Murcray, F. J., and R. M. Goody 1978. Pictures of the Io sodium cloud. *Astrophys. J.* **226,** 327–335.

Pilcher, C. B., W. H. Smyth, M. R. Combi, and J. H. Fertel 1984. Io's sodium directional features: Evidence for a magnetospheric-wind-driven gas escape mechanism. *Astrophys. J.* **287,** 427–444.

Schneider, N. M. 1988. *Sodium in Io's Extended Atmosphere.* Ph.D. Thesis, Department of Planetary Sciences, Univ. of Arizona.

Schneider, N. M., D. M. Hunten, W. K. Wells, and L. M. Trafton 1987. Eclipse measurements of Io's sodium atmosphere. *Science,* **238,** 55–58.

Schneider, N. M., D. M. Hunten, W. K. Wells, A. B. Schultz, and U. Fink 1991. The structure of Io's corona. *Astrophys. J.* **368,** 298–315.

Sieveka, E. M., and R. E. Johnson 1984. Ejection of atoms and molecules from Io by plasma-ion impact, *Astrophys. J.* **287,** 418–426.

Smyth, W. H. 1979. Io's sodium cloud: Explanation of the east–west asymmetries. *Astrophys. J.* **234,** 1148–1153.

SMYTH, W. H. 1983. Io's sodium cloud: Explanation of the east–west asymmetries. II. *Astrophys. J.* **264,** 708–725.

SMYTH, W. H., AND M. R. COMBI 1987a. Correlating east–west asymmetries in the jovian magnetosphere and the Io sodium cloud, *Geophys. Res. Lett.* **14,** 973–976.

SMYTH, W. H., AND M. R. COMBI 1987b. Time variability of the sodium cloud, poster paper at the international conference "Time-Variable Phenomena in the Jovian System," Flagstaff, Arizona, August 25–27.

SMYTH, W. H., AND M. R. COMBI 1987c. Nature of Io's atmosphere and its interaction with the planetary magnetosphere. *Bull. Am. Astron. Soc.* **19,** 855.

SMYTH, W. H., AND M. R. COMBI 1988a. A general model for Io's neutral gas cloud. I. Mathematical description. *Astrophys. J. Supp.* **66,** 397–411.

SMYTH, W. H., AND M. R. COMBI 1988b. A general model for Io's neutral gas clouds. II. Application to the sodium cloud. *Astrophys. J.* **328,** 888–918.

SMYTH, W. H., AND M. R. COMBI 1991. The sodium zenocorona. *J. Geophys. Res.* **96,** 22711–22727.

SMYTH, W. H., AND B. A. GOLDBERG 1993. The Io sodium cloud: Space–time signatures of east–west and system III longitudinal asymmetries in the jovian magnetosphere. Paper presented at Io: An international conference, San Juan Capistrano, California, June 22–25.

SMYTH, W. H., AND M. B. MCELROY 1977. The sodium and hydrogen gas clouds of Io, *Planet. Space Sci.* **25,** 415–431.

SMYTH, W. H., AND M. B. MCELROY 1978. Io's sodium cloud: Comparison of models and two-dimensional images. *Astrophys. J.* **226,** 336–346.

SUMMERS, M. E., D. F. STROBEL, Y. L. YUNG, J. T. TRAUGER, AND F. MILLS 1989. The structure of Io's thermal corona and implications for atmospheric escape. *Astrophys. J.* **343,** 468–480.

TRAFTON, L., AND W. MACY, JR. 1978. On the distribution of sodium in the vicinity of Io, *Icarus* **33,** 322–335.

WILSON, J. K., AND N. M. SCHNEIDER 1994. Io's fast sodium: Implications for molecular and atomic atmospheric escape, *Icarus* **111,** 31–44.

WILSON, J. K., AND N. M. SCHNEIDER 1995. Io's sodium directional feature: Evidence for ionospheric rip-off, *Bull. Am. Astron. Soc.* **27,** 1154.

Appendix B

An Initial Look at the Iogenic SO_2^+ Source during the Galileo Flyby of Io

JOURNAL OF GEOPHYSICAL RESEARCH, VOL. 103, NO. A5, PAGES 9083–9089, MAY 1, 1998

An initial look at the Iogenic SO_2^+ source during the Galileo flyby of Io

William H. Smyth and M. L. Marconi
Atmospheric and Environmental Research, Inc., Cambridge, Massachusetts

Abstract. Galileo in its December 7, 1995, encounter with Io flew downstream of Io and through the magnetospheric wake of the satellite with a closest approach altitude of ~900 km. Magnetospheric instruments were therefore able to sample the Iogenic plasma source both outside as well as deeply within the Lagrange sphere of Io (~5.81 satellite radii) where the gravity of Io dominates and where the plasma pickup processes are expected to be highly peaked about the satellite. The presence of both long-lived atomic ions (H^+, O^+, O^{++}, S^+, S^{++}) and short-lived molecular ions (SO^+, SO_2^+) was detected along the spacecraft trajectory. We have undertaken preliminary calculations for the density profile of SO_2^+. These calculations are compared with the SO_2^+ density profiles deduced from magnetic field fluctuations with periods of ~2–3 s measured by the Galileo magnetometer and interpreted as ion cyclotron waves produced by fresh SO_2^+ Iogenic pickup ions created near Io. By matching the absolute SO_2^+ model density with the minimum ion density determined by *Huddleston et al.* [1997] in their analysis of the ion cyclotron waves, an SO_2 source rate of $\sim 4 \times 10^{27}$ molecules s^{-1} (425 kg s^{-1}) at Io's exobase and a corresponding SO_2^+ source rate of 2.8×10^{26} ions s^{-1} (30 kg s^{-1}) in the magnetosphere are determined. Most of the SO_2 that undergoes interactions in the plasma torus is, however, rapidly dissociated primarily by electron impact, producing O, S, SO, and O_2. These species subsequently undergo ionization and charge exchange reactions in the plasma torus, producing much larger mass and energy pickup plasma loading rates, including an SO^+ source rate estimated to be somewhat smaller than the SO_2^+ source rate. Since the lifetime of SO_2 is highly variable with Io's position in the plasma torus, it follows that the spatial profile for the amplitude of these magnetic fluctuations will also be highly space and time variable and will depend upon both Io System III longitude and Io geocentric phase angle.

1. Introduction

The close encounter with Io (~900 km above the satellite surface) of the Galileo orbiter on December 7, 1995, provides an unprecedented wealth of in situ measurements that are well suited to studying the Iogenic plasma source and its interactions with the planetary magnetosphere. The Iogenic plasma source is produced by neutral gases that are lost from Io and that subsequently undergo ionization and charge exchange reactions with the magnetospheric plasma and also by direct ion loss from the satellite. A significant amount of neutral gases escapes Io [*Hill et al.*, 1983; *Summers et al.*, 1989; *Smyth and Combi*, 1991; *Smyth*, 1992; *Summers and Strobel*, 1996] and produces extended neutral clouds that spatially lead and follow Io in its orbit about Jupiter. As one approaches Io, the neutral densities increase, particularly at distances as close as Io's Lagrange sphere (i.e., the atmospheric corona region inside of which the satellite gravitational field dominates the planetary gravitational field, which is located at a radius of ~10,550 km or 5.81 satellite radii (R_{Io} = 1815 km)). Inside the Lagrange sphere the atmospheric corona density increases more steeply and merges into a bound although perhaps nonuniform thick atmosphere with a collisional exobase thought to be located within an Io radius above the satellite surface. In the Io encounter, the spacecraft made the first in situ measurements within the Lagrange sphere as it passed downstream of the satellite and entered the magnetospheric wake of the satellite with a closest approach radial distance of ~1.5 R_{Io}.

The rate at which new ions are added to the magnetosphere and the rate at which old ions are energized by ion-neutral charge exchange reactions are therefore expected to be highly peaked at Io's instantaneous positions [*Marconi and Smyth*, 1996], a region well sampled by the particle and field measurements of Galileo. Indeed, the large change in the ion temperature and plasma velocity determined from the Galileo Plasma Analyzer (PLS) data [*Frank et al.*, 1996] together with the large change in the magnetic field recorded by the Galileo magnetometer [*Kivelson et al.*, 1996] in and near the Io wake is likely due in large part to the strong and highly localized mass loading (M. L. Marconi and W. H. Smyth, On the effects of strong momentum loading by charge exchange on the magnetic field in the vicinity of Io, submitted to *Geophysical Research Letters*, 1997; W. H. Smyth, Energy loss rate of neutrals from Io and the implications for local magnetospheric interactions, submitted to *Journal of Geophysical Research*, 1997). A direct signature of this mass loading is the monochromatic and predominately transverse magnetic fluctuations with periods of ~2–3 s, detected by the Galileo magnetometer for radial distances from Io of ~18 to 3 R_{Io} on the inbound spacecraft trajectory and of ~3 to 7 R_{Io} on the outbound trajectory. These fluctuations, shown in Figure 1 for a small segment of the inbound spacecraft trajectory starting just within Io's Lagrange sphere but ending prior to the large changes in the ion temperature

Paper number 97JA03066.
0148-0227/98/97JA-03066$09.00

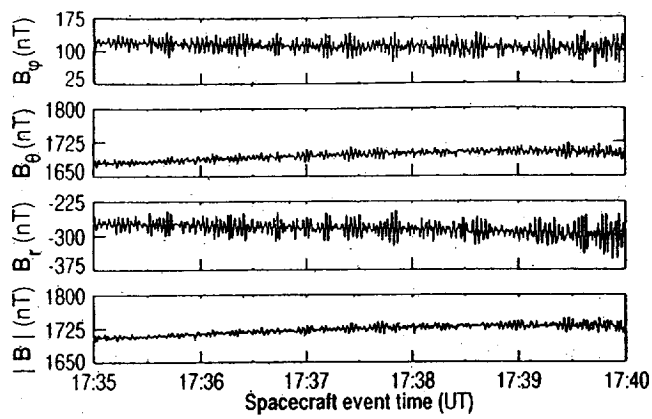

Figure 1. Galileo field measurements near Io. The components and magnitude of the magnetic field B (in nanoteslas) as measured by the Galileo magnetometer [*Kivelson et al.*, 1996] are shown for the expanded data from 1735 to 1740 SCET, a segment of the inbound spacecraft trajectory that is just within the Lagrange sphere but that is not yet at the flank region of Io where the magnetic field and ion temperature [*Frank et al.*, 1996] change significantly. The small-amplitude fluctuations in the magnetic field have been interpreted as ion cyclotron waves. Reprinted with permission from *Kivelson et al.* [1996, Figure 3]. Copyright 1996 American Association for the Advancement of Science.

and magnetic field very near the Io encounter, have been interpreted as ion cyclotron waves and have a period near the gyration period of SO_2^+ [*Kivelson et al.*, 1996; *Warnecke et al.*, 1997; *Huddleston et al.*, 1997]. These waves are thought to be driven by the large anisotropic velocity distribution of fresh SO_2^+ pickup ions near Io.

In this paper we will focus on the plasma pickup processes that occur on the two flank regions on either side of Io and their outward extensions, which can be monitored downstream along the Galileo orbiter's trajectory. In particular, we will restrict our attention to a preliminary investigation of the spatial abundance of the short-lived molecular ion species SO_2^+ near Io. A more complete investigation for the long-lived atomic oxygen (O^+, O^{++}) and sulfur (S^+, S^{++}, S^{+++}) ions in the plasma torus will be undertaken at a later date when the charged particle observations for Galileo have been more fully reduced and are available. In this paper the model used to calculate the SO_2^+ density is first described. The Galileo magnetometer measurements relevant to SO_2^+ plasma pickup are then briefly reviewed. Model-data comparisons are then presented and are followed by a discussion of conclusions and their implications.

2. Model for the SO_2^+ Plasma Source

The basic approach followed here to study Io's interactions with the magnetosphere and the Iogenic plasma source is to undertake three-dimensional (3-D) modeling calculations for SO_2 ejected from Io's exobase and to calculate the combined space-time electron-impact ionization and charge exchange production rate for SO_2^+ in volume elements near Io. The integration of the instantaneous volumetric production rate $P_{SO_2^+}$ in tubular volume elements along the corotational direction s from far upstream (where the production rate is essentially zero) to the spacecraft location then determines the instantaneous SO_2^+ pickup source rate $S_{SO_2^+} = A\ \phi_{SO_2^+}$ in this portion of each tube (with cross section area A of 600 km × 600 km adopted here) and hence the instantaneous SO_2^+ flux $\phi_{SO_2^+}$ at the spacecraft location. When this flux $\phi_{SO_2^+}$ is divided by the local corotational velocity v, the ratio gives the pickup ion density $n_{SO_2^+}$ at the spacecraft location in the tube, which may also be expressed as the integration in time of the instantaneous production rate $P_{SO_2^+}$ along the corotational trajectory of the pickup plasma in the tube:

$$n_{SO_2^+} = \frac{\phi_{SO_2^+}}{v} = \frac{S_{SO_2^+}}{Av} = \frac{1}{Av}\int_{\text{tube}} P_{SO_2^+}\, dV$$

$$= \int_{\text{tube}} P_{SO_2^+}\frac{ds}{v} = \int_{\text{tube}} P_{SO_2^+}\, dt \qquad (1)$$

Note that no loss processes for the SO_2^+ pickup ions have been included in (1), since the time interval (~5 min or so) for ion convection in the tubes near Io, where the instantaneous production rate $P_{SO_2^+}$ is appreciable, is small compared with the electron impact dissociation time (~ few hours) of SO_2^+ in the plasma torus. It has also been assumed that the change in the magnitude of the plasma velocity and the change in its direction relative to the tube axis are negligible.

The instantaneous SO_2^+ production rate $P_{SO_2^+}$ is computed here by using the SO_2 neutral cloud model developed over the last decade and described mathematically by *Smyth and Combi* [1988a, b] and *Scherb and Smyth* [1993]. The preliminary calculations were undertaken for the time of Galileo's closest approach to Io (1745:46 SCET (spacecraft event time) or 1837:44 UT) for which the Io geocentric phase angle was 178.4° and the Io System III longitude angle was 273.2°. For the SO_2 source at the satellite exobase (assumed here at a radius of 2600 km), we have adopted in these calculations the incomplete collisional cascade flux velocity distribution recently determined at Io's exobase for sodium atoms by *Smyth and Combi* [1997]. This flux velocity distribution peaks at 0.5 km s^{-1}, well below the exobase escape speed of ~2 km s^{-1}, and has a velocity tail that extends to many tens of kilometers per second. In the model, an isotropic source rate at the exobase is assumed for SO_2 that is consistent with the nature of the source determined for sodium, and the absolute SO_2 source rate is determined by the comparison of the modeled and observed SO_2^+ density profiles.

The relevant reactions and lifetimes for SO_2 in the plasma torus are summarized in Table 1, where nominal relative and absolute rates are given for Io's radial distance in the centrifugal equator of the plasma torus at western elongation. The major loss process for SO_2 is electron impact dissociation. The major channels for production of SO_2^+ are electron impact ionization and charge exchange with O^+ and S^{++}, all more than an order of magnitude slower than the electron impact dissociation rate. The actual electron impact and charge exchange lifetimes for SO_2 near Io will, however, be space and time variable because of the oscillation of the centrifugal plasma plane about the satellite orbit, the offset of the magnetic field relative to the center of Jupiter, and the variation of plasma properties caused by east-west and System III longitude asymmetries in the plasma torus. Since a full description of the plasma torus for the time of the Galileo encounter with Io is at present not available (e.g., the electron temperature and ion composition along the spacecraft trajectory are not

Table 1. SO_2 Loss Processes in the Plasma Torus Near Io

Reaction Number	Reaction		Relative Rate, %	Lifetime, hours
1	$SO_2 + e$	$\rightarrow SO + O + e$	72.62	1.4
		$\rightarrow S + O_2 + e$	14.52	7.2
2	$SO_2 + e$	$\rightarrow SO_2^+ + 2e$	4.44	24
		$\rightarrow SO^+ + O + 2e$	1.15	91
		$\rightarrow S^+ + O_2 + 2e$	0.34	310
		$\rightarrow SO + O^+ + 2e$	0.03	3,300
3	$SO_2 + O^+$	$\rightarrow SO_2^+ + O$	2.03	52
4	$SO_2 + O^{++}$	$\rightarrow (SO_2^+)^* + (O^+)^*$	0.04	≥2,700
5	$SO_2 + S^+$	$\rightarrow SO_2^+ + S(^3P)$	0.01	≥19,000
6	$SO_2 + S^{++}$	$\rightarrow (SO_2^+)^* + (S^+)^*$	1.27	≥82
7	$SO_2 + S^{+++}$	$\rightarrow SO_2^+ + S^{++}(^3P)$		
		$\rightarrow SO_2^+ + S^{++}(^1D)$		
		$\rightarrow SO_2^+ + S^{++}(^1S)$	0.18	580
		$\rightarrow SO_2^+ + S^{++}(^3D_0)$		
		$\rightarrow SO_2^+ + S^+$		
8	$SO_2 + h\nu$	$\rightarrow SO + O$	2.45	43
		$\rightarrow S + O_2$	0.88	118
		$\rightarrow SO_2^+ + e$	0.04	2,880

Electron impact rates are from D. E. Shemansky (private communication, 1992) and Voyager 1 electron properties representative of Io's orbital distance at western elongation. Charge exchange rates are from cross sections of *McGrath and Johnson* [1989] and Voyager 1 plasma properties representative of Io's orbital distance at western elongation. Photodissociation and ionization rates are from *Huebner et al.* [1992] for active Sun conditions evaluated at 5.20 AU.

known, let alone a 3-D description) because of yet to be completed data reduction and analysis work, a plasma torus description based upon the Voyager 1 inbound encounter conditions near western elongation [see *Smyth and Combi*, 1988b] is used for this preliminary calculation. This is a reasonable preliminary choice since the decrease in the lifetime produced by the larger electron densities (approximately a factor of 2) at the Galileo encounter [*Gurnett et al.*, 1996] could well be offset by the likely cooler electron temperatures in the denser plasma. The adopted Voyager 1 plasma torus description is based upon an offset-tilted dipole magnetic field and includes an inherent System III longitudinal asymmetry as well as an east-west asymmetry which is produced by a nominal (ε = 0.025) east-west electric field. Based upon this plasma torus description, the lifetime of SO_2 at Io's location in the plasma torus is shown in Figure 2 and can be seen to vary approximately by an order of magnitude (i.e., from ~0.5 hour to 5 hours) with Io geocentric phase angle and Io System III longitude.

3. Galileo Observations for SO_2^+

The dominant atomic ions in the plasma torus are oxygen (O^+, O^{++}) and sulfur (S^+, S^{++}, S^{+++}), which are long-lived species in the sense that once produced they remain locally until they are lost by outward radial transport (timescales of ~20–100 days in the plasma torus). In contrast, the molecular ions SO_2^+ and SO^+ are short-lived species in the plasma torus because they are almost certainly rapidly destroyed by electron impact dissociation in the warm torus regions (timescale of a few hours or less) or are removed from the plasma torus altogether by electron recombination in the cold torus regions. Because of these very different lifetime behaviors for the atomic ion and the molecular ion species, their velocity distributions are expected to be quite different. For the atomic ions O^+ and S^+ the velocity distribution will be composed of two basic components: a primary thermalized velocity core of old ions and a secondary enhanced population in the velocity wings of new pickup ions. For the higher-charged atomic ions O^{++}, S^{++}, and S^{+++}, the secondary enhanced population in the velocity wings will be small at best, since these higher-charged ions are almost entirely produced by the ionization of resident O^+ and S^+ ions. For the molecular ions the primary thermalized velocity core of old ions will, however, be missing because of the short residence time of this species. The velocity distributions of SO_2^+ and SO^+ will therefore be very anisotropic and hence capable of creating in the vicinity of Io a larger instability for the generation of ion cyclotron waves, which were detected by the Galileo magnetometer as small-amplitude fluctuations in magnetic field [*Kivelson et al.*, 1996].

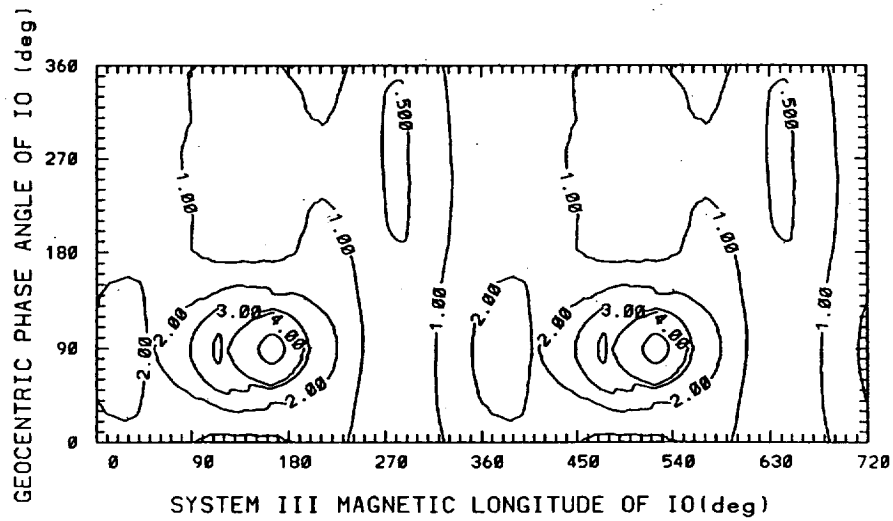

Figure 2. SO_2 lifetime at Io's location in the plasma torus. The lifetime of SO_2 adopted in the model (given in units of hours) is calculated for Voyager 1 plasma conditions with an offset-tilted dipole planetary magnetic field, a nominal east-west electric field, and an inherently asymmetric plasma torus in System III longitude similar to that observed by *Morgan* [1985a, b].

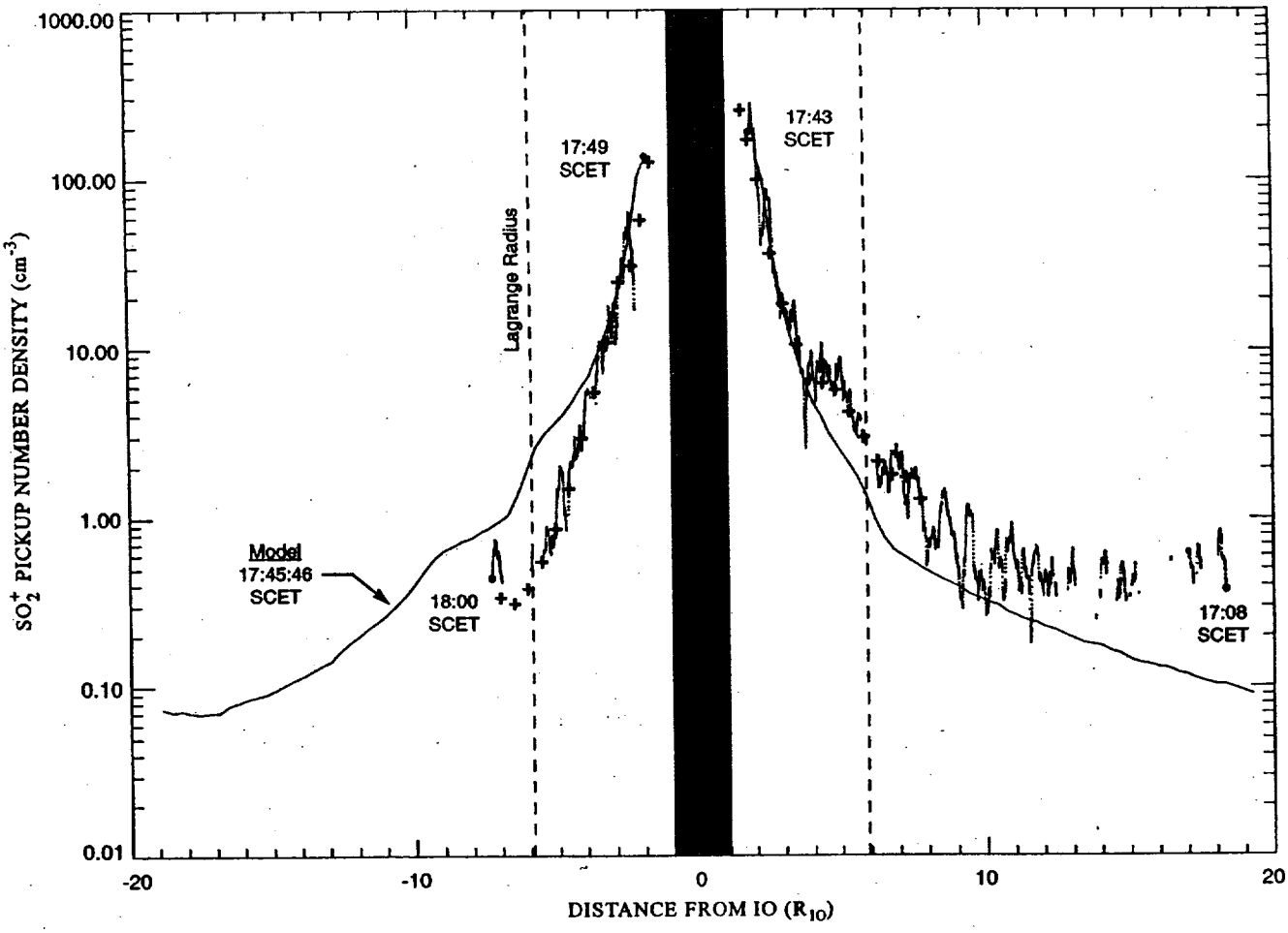

Figure 3. Comparison of model and observationally deduced SO_2^+ minimum density profiles and the wave power profiles near Io. The minimum SO_2^+ density profiles deduced from the small amplitude fluctuations in the magnetic field observed by the Galileo magnetometer during its encounter with Io on December 7, 1995, are shown by the plus symbols from the analysis of *Huddleston et al.* [1997]. The spatial profiles for the wave power used in the analysis of Huddleston et al. are shown by the lighter solid line as determined by the analysis of *Warnecke et al.* [1997], where the latter has been put on an absolute scale by comparison with the former. The model calculated SO_2^+ profile is shown by the heavier solid line for an isotropic incomplete collisional cascade velocity distribution at the satellite exobase with SO_2 source strength of 4×10^{27} molecules s^{-1}. The inbound Galileo trajectory is to the right (positive coordinate), and the outbound trajectory is to the left (negative coordinate). The shaded region indicates the geometric wake of Io, and the vertical dashed lines indicate the location of the Lagrange sphere of Io.

Their small-amplitude fluctuations have been most recently analyzed by *Huddleston et al.* [1997] and *Warnecke et al.* [1997]. Their results are shown in Figure 3, where the inbound Galileo trajectory is to the right of Io's geometric wake (shaded area) on the positive distance axis and the outbound trajectory is to the left of Io on the negative distance axis. Huddleston et al. determined near Io a minimum SO_2^+ absolute spatial density profile (plus symbols) along the spacecraft trajectory (making the assumption that the local SO_2^+ density is proportional to the wave power with no convective gain of the wave amplitudes in their propagation). Warnecke et al. provided a relative spatial profile (narrow solid line) for the wave power over a wider spatial interval, which has been normalized to the Huddleston et al. values in Figure 3, and sought to include convective gain by relating the wave power to the integral of the instantaneous volumetric SO_2^+ production rate from the spacecraft position back in time along the two convective ray paths of the costreaming and counterstreaming waves. In the integral they assumed a very simplified expression for the instantaneous volumetric SO_2^+ production rate that was proportional to the product of a constant ionization rate and the local SO_2 density, where the latter was assumed to have the form of a point source with no gravity, a constant outflow speed, and a constant decay lifetime. This integration of the SO_2^+ production rate, although different because of the simple assumed form adopted by Warnecke et al., is similar physically to our expression (1) used to obtain the SO_2^+ pickup density, except that our integration path is back in time along the corotational direction and not along the convective ray path directions. In Figure 3 the observationally deduced profiles are highly peaked at the location of Io. The spatial profile of the wave power derived by Warnecke et al. on the inbound spacecraft trajectory from ~18 to 3 R_{Io} varies as approximately R^{-3}, where R is the radial distance from the center of Io, whereas the spatial profile of

the wave power measured on the outbound spacecraft trajectory from ~3 to 7 R_{Io} is steeper and varies as approximately R^{-4}, both similar to the R^{-3} and the $R^{-3.5}$ behaviors, respectively, reported initially by *Kivelson et al.* [1996].

4. Model-Data Comparison

For the time of the Galileo spacecraft's closest approach to Io (1745:46 SCET or 1837:44 UT), a model calculated profile for the instantaneous spatial distribution of the SO_2^+ pickup ion number densities approximately along the Galileo trajectory near Io is shown in Figure 3 and compared with the observationally deduced profiles. At this closest approach time, Io has a geocentric phase angle of 178.4° and a System III longitude of 273.2° so that the satellite is still north of the plasma torus centrifugal equator but moving closer to it in time (Io's orbital plane and the plasma torus centrifugal plane intersect at a System III longitude of about 290°). Near the satellite the rapid rise in the SO_2^+ density profile (plus symbols) deduced by *Huddleston et al.* [1997] from the magnetospheric data is well matched by the model calculation for an isotropic exobase source rate of ~4×10^{27} SO_2 molecules s^{-1}. This source rate corresponds to a total instantaneous SO_2^+ creation rate in the magnetosphere of 2.8×10^{26} ions s^{-1}. The model profile, however, underestimates the derived wave power profile (narrow solid line) of *Warnecke et al.* [1997] on the inbound Galileo trajectory (positive distance from Io), which corresponds to observational times between 1708 and 1743 SCET, but overestimates the derived wave power profile of Warnecke et al. on the outbound Galileo trajectory (negative distance from Io), which corresponds to observational times between 1749 and 1800 SCET.

The deviation of the model SO_2^+ density profile from the deduced minimum SO_2^+ density (or wave power) profile at larger distances from Io may be due to a number of factors including the use of Voyager 1 plasma data in calculating the SO_2^+ density profile, the difference in integration paths noted above, or the assumption of a constant SO_2 source strength at Io. Regarding this latter factor, the (horizontal) sidestep in the inbound wave power profile centered at ~4.5 R_{Io} is peculiar since the slope of the wave power curve is similar to the model curve both prior and after the step, suggesting a possible change in the upstream SO_2^+ production rate perhaps due to a sudden decrease in the amount of material loss from Io for times corresponding to spacecraft measurements inside of about 5 R_{Io}. The underestimate and overestimate pattern of the model-data comparison for the inbound and outbound spacecraft trajectories, however, is also qualitatively consistent with the time-varying inflation and deflation of the SO_2 neutral density near Io and its corresponding time-varying SO_2^+ production rate over the ~1-hour time interval for accumulation of the data. For the beginning of the data accumulation on the inbound trajectory at 1708 SCET, Io is located further upstream at a System III longitude of about 255.7°, where it is well above the centrifugal equator of the plasma torus (where the plasma density is maximum) and has been even farther above the plasma torus for several hours prior to this time (a System III longitude of about 200° corresponds to Io's northern most magnetic latitude). The SO_2 cloud densities that are at distances near and beyond the Lagrange sphere at 1708 SCET were produced at even earlier times when the lifetime of SO_2 at Io's position in the plasma torus (see Figure 2) was even larger, so that the SO_2 densities near the Lagrange sphere are consequently somewhat inflated. Between the measurement times of 1708 SCET and 1800 SCET (Io is now at a System III longitude of about 279.8° and still above the centrifugal equator), the more distant inflated densities are now being deflated rapidly in time as a result of the time-decreasing SO_2 lifetime at Io's position in the plasma torus and are consequently creating an inflated SO_2^+ production rate. The total instantaneous SO_2^+ production rate at these larger distances from Io then establishes (at these earlier times) an SO_2^+ density profile along the inbound trajectory that is enhanced in comparison to the model calculation in Figure 3 which is determined at the later time of closest approach. In a similar manner on the outbound Galileo trajectory, between the time of closest approach (1745:46 SCET) and the end of the data set (1800 SCET), the size of the SO_2 cloud (for times nearer the end of the time interval) has continued to deflate so that the model profile in Figure 3 calculated instantaneously at the time of closest approach will overestimate the SO_2^+ density profile at larger Io distances along the outbound trajectory.

5. Discussion and Conclusions

The isotropic exobase source rate determined for SO_2 in the aforementioned model-data comparison of ~4×10^{27} s^{-1} is a factor of only ~2 less than the estimated SO_2 source rate of 8.9×10^{27} s^{-1} suggested from the earlier analysis of the O(^1D) 6300-Å emission brightness near Io by *Scherb and Smyth* [1993]. About half of the molecules in the incomplete collisional cascade source distribution adopted here are not energetic enough to escape the Lagrange sphere of the satellite (~10,550 km or 5.81 R_{Io}) and hence will populate ballistic orbits above the exobase and create a density gradient in the satellite corona. This density gradient plays a central role in the steepness of the model-calculated SO_2^+ density profile in Figure 3 at closer distances to Io (within a radius of ~3 R_{Io}). The agreement of the model and observationally derived SO_2^+ density profiles thus implies that sodium and SO_2 have a very similar collisional cascade flux velocity distribution at the satellite exobase as would be expected if sodium atoms (a trace species in the atmosphere) were produced in the same volume by the same incomplete collisional cascade processes. This agreement also implies that the collisional cascade flux velocity distribution at the exobase for other species, such as atomic oxygen and atomic sulfur, would also be similar.

The rapid rate and large nominal branching ratio (~90% in Table 1) for the dissociation of SO_2 molecules primarily by magnetospheric electron impact within and beyond the Lagrange sphere will also give rise to an additional and significant population of atoms (O, S) and molecules (SO, O_2) in a spatially extended region about Io. The volume of this spatially extended region will depend upon the time variable lifetime of SO_2 at Io as well as the initial velocity distribution of the dissociative species, which in turn will depend upon the unknown exothermic nature of the dissociative reactions. In the magnetosphere these dissociative species will subsequently undergo electron impact ionization and charge exchange (as well as some neutral escape from Jupiter) within this spatially extended region with a large fraction of the collisional cascade source of ~4×10^{27} SO_2 molecules s^{-1} (425 kg s^{-1}) at the exobase contributing mass (~200 kg s^{-1}) and pickup energy locally to the plasma torus. Although occupying a spatially extended volume element near Io, this rate of plasma input is much larger than the direct production rate of SO_2^+ from SO_2

with an instantaneous source rate estimated above of 2.8×10^{26} ions s^{-1} (30 kg s^{-1}). In addition to an SO_2 collisional cascade source at Io, collisional cascade sources from other atomic and molecular species at Io's exobase would also be expected to contribute additional mass and energy to the plasma torus. The question as to the relative escape rates of atomic and molecular species from Io's exobase is, however, at present an open one. The loss of atomic and molecular species from Io's atmosphere by direct charge exchange reactions near the exobase will also provide an additional large pickup energy rate for the magnetosphere. Hence taken at face value, the large source rate of SO_2 determined here suggests that there should be a substantial mass loading rate (measured in hundreds of kilograms per second) and an even larger corresponding energy loading rate for the plasma torus at the time of the Galileo encounter with Io. Such rates are similar to pre-Galileo estimated rates for the Voyager epoch plasma torus [*Hill et al.*, 1983; *Smyth and Combi*, 1991; *Smyth*, 1992] but much larger than the erroneous loading rates of tens of kilograms per second mistakenly suggested more recently by *Russell et al.* [1997] for the Galileo encounter. More precise estimates for these plasma rates will be forthcoming in the near future when the complete in situ electron and ion data acquired by the Galileo spacecraft become available.

A significant production of SO^+ pickup ions may also be anticipated in the vicinity of Io from the dissociation rate of SO_2, which has a nominal branching ratio of ~75% for production of SO in Table 1. Since most of these SO molecules will, however, undergo rapid dissociation by electron impact and photons with only a small branching ratio of about 7.5% producing SO^+ ions, the overall effective branching ratio for production of SO^+ ions will be only ~5.6% (i.e., $0.75 \times 0.075 = 0.05625$) of the cascade source molecules that can actually undergo an interaction. In simple physical terms, the fraction, $(1 - e^{-t_F/\tau})$, of these SO source atoms that will actually undergo ionization will depend upon the ratio of the effective flight time t_F, during which the SO molecules may be ionized, to the total (dissociation plus ionization) lifetime τ. For a given SO source velocity distribution this fraction will vary from very small values near zero for the smaller velocities (~0 to 1 km s^{-1}) that produce SO ballistic orbits deep in Io's corona where $t_F \ll \tau$, to values near unity for velocities (~2–4 km s^{-1}) near Io's escape speed producing SO orbits near the satellite orbit where $t_F \gg \tau$, to values decreasing again toward zero for larger velocities (~ tens of kilometers per second) producing trajectories that rapidly move well beyond the plasma torus where $\tau \gg t_F$. By adopting a nominal overall fraction of 1/5 for the two-stage reaction sequence, the estimated SO^+ ion production rate in the plasma torus would be of the order of $(4 \times 10^{27}\ s^{-1}) \times (0.05625) \times (1/5) = 4.5 \times 10^{25}\ s^{-1}$. Although this production rate is likely distributed over a larger volume element than the production rate for SO_2^+, the total estimated SO^+ ion production rate is somewhat smaller than the SO_2^+ production rate determined above of $2.8 \times 10^{26}\ s^{-1}$. A more detailed calculation of these relative molecular ion production rates is beyond the scope of this paper and will be addressed in the future.

It should be noted that the density profiles for SO_2^+ and SO^+ near Io are expected to be highly time variable owing to the changing lifetime of SO_2 and similarly SO in the plasma torus, as illustrated for SO_2 in Figure 2. Consequently, near Io, the small-amplitude fluctuations in the magnetic field observed by the magnetometer of Galileo and attributed to the generation of ion cyclotron waves by SO_2^+ (and possibly SO^+) pickup ions are expected to be time variable with Io System III longitude and Io geocentric phase angle. In addition, the absolute density of the SO_2^+ and SO^+ profiles near Io may also be expected to vary on longer timescales with time variable volcanic phenomena at Io which together with other physical processes may regulate the relative abundances of the molecular and atomic species in the interaction region at the upper atmosphere of Io. The ability of the minor plasma torus SO_2^+ and SO^+ pickup ions to generate the observed ion cyclotron waves occurs, as was noted earlier, because these molecular ions are short-lived species that are rapidly destroyed by electron impact in less than a System III longitude period of ~13 hours for Io in the plasma torus and hence have no appreciably thermalized core velocity distribution. The long-lived (O^+, S^+, S^{++}, S^{+++}) ion species in the plasma torus will have a well-established thermalized core velocity distribution in addition to an instantaneous supply of pickup ions and will be the subject of interesting future studies when the in situ Galileo particle data become available.

Acknowledgments. We are grateful to J. Warnecke and D. E. Huddleston for sharing their SO_2^+ and wave power derived spatial profiles prior to publication and also for helpful comments. This research was supported by the National Aeronautical and Space Administration under contracts NASW-4804 and NASW-96020 from the Planetary Atmospheres Program and 959538 from the Galileo Mission Project.

The Editor thanks V. M. Vasyliunas and another referee for their assistance in evaluating this paper.

References

Frank, L. A., W. R. Patterson, K. L. Ackerson, V. M. Vasyliunas, F. V. Coroniti, and S. J. Bolton, Plasma observations at Io with the Galileo spacecraft. *Science*, *274*, 394–395, 1996.

Gurnett, D. A., W. S. Kurth, A. Roux, S. J. Bolton, and C. F. Kennel, Galileo plasma wave observations in the Io plasma torus and near Io, *Science*, *274*, 391–392, 1996.

Hill, T. W., A. J. Dessler, and C. K. Goertz, Magnetospheric models, in *Physics of the Jovian Magnetosphere*, chap. 10, pp. 353–394, Cambridge Univ. Press, New York, 1983.

Huddleston, D. E., R. J. Strangeway, J. Warnecke, C. T. Russell, M. G. Kivelson, and F. Bagenal, Ion cyclotron waves in the Io torus during the Galileo Encounter: Warm plasma dispersion analysis, *Geophys. Res. Lett.*, *24*(7), 2143–2146, 1997.

Huebner, W. F., J. J. Keady, and S. P. Lyon, *Solar Photo Rates for Planetary Atmospheres and Atmospheric Pollutants*, Kluwer Acad., Norwell, Mass., 1992.

Kivelson, M. G., K. K. Khurana, R. J. Walker, J. Warnecke, C. T. Russell, J. A. Linker, D. J. Southwood, and C. Polanskey, Io's interaction with the plasma torus: Galileo magnetometer report, *Science*, *274*, 396–398, 1996.

Marconi, M. L., and W. H. Smyth, Io plasma torus: Nature of the Iogenic plasma torus (abstract), *Bull. Am. Astron. Soc.*, *28*, 1155, 1996.

McGrath, M. A., and R. E. Johnson, Charge exchange cross sections for the plasma torus, *J. Geophys. Res.*, *94*, 2677–2683, 1989.

Morgan, J. S., Temporal and spatial variations in the Io torus, *Icarus*, *62*, 389–414, 1985a.

Morgan, J. S., Models of the Io torus, *Icarus*, *63*, 243–265, 1985b.

Russell, C. T., F. Bagenal, A. F. Cheng, W.-H. Ip, A. Roux, W. H. Smyth, S. J. Bolton, and C. A. Polanskey, Io's interaction with Jovian magnetosphere, *Eos Trans. AGU*, *78*(9), 93, 100, 1997.

Scherb, F., and W. H. Smyth, Variability of [O I] 6300-Å emission near Io, *J. Geophys. Res.*, *98*, 18,729–18,736, 1993.

Smyth, W. H., Neutral cloud distribution in the Jovian system, *Adv. Space Res.*, *12*(8), 337–346, 1992.

Smyth, W. H., and M. R. Combi, A general model for Io's neutral gas cloud, I, Mathematical description, *Astrophys. J. Suppl.*, *66*, 397–411, 1988a.

Smyth, W. H., and M. R. Combi, A general model for Io's neutral gas

cloud, II, Application to the sodium cloud, *Astrophys. J.*, *328*, 888–918, 1988b.

Smyth, W. H., and M. R. Combi, The sodium zenocorona, *J. Geophys. Res.*, *96*, 22,711–22,727, 1991.

Smyth, W. H., and M. R. Combi, Io's sodium exosphere and spatially extended cloud: A consistent flux speed distribution, *Icarus*, *126*, 58–77, 1997.

Summers, M. E., and D. F. Strobel, Photochemistry and vertical transport in Io's atmosphere and ionosphere, *Icarus*, *120*, 290–316, 1996.

Summers, M. E., D. F. Strobel, Y. L. Yung, J. T. Trauger, and F. Mills, The structure of Io's thermal corona and implications for atmospheric escape, *Astrophys. J.*, *343*, 468–480, 1989.

Warnecke, J., M. G. Kivelson, K. K. Khurana, D. E. Huddleston, and C. T. Russell, Ion cyclotron waves observed at Galileo's Io encounter: Implications for neutral cloud distribution and plasma composition. *Geophys. Res. Lett.*, *24*(17), 2139–2142, 1997.

M. L. Marconi and W. H. Smyth, Atmospheric and Environmental Research, Inc., 840 Memorial Drive, Cambridge, MA 02139. (e-mail: smyth@aer.com)

(Received June 10, 1997; revised September 11, 1997; accepted October 21, 1997.)

Appendix C

Energy Escape Rate of Neutrals from Io and the Implications for Local Magnetospheric Interactions

JOURNAL OF GEOPHYSICAL RESEARCH, VOL. 103, NO. A6, PAGES 11,941–11,950, JUNE 1, 1998

Energy escape rate of neutrals from Io and the implications for local magnetospheric interactions

William H. Smyth

Atmospheric and Environmental Research, Inc., Cambridge, Massachusetts

Abstract. The rate at which energy is carried away by atomic oxygen and sulfur escaping from Io because of the interaction of its atmosphere with the corotating magnetospheric plasma is calculated for three different ion-neutral collisional processes: (1) incomplete collisional cascade, (2) slow-velocity charge exchange and direct ejection (centered ~20 km/s), and (3) fast-velocity charge exchange (centered ~60 km/s). The calculations are based on information for the O and S source rates and their velocity distributions at Io as independently determined from the combined results of previous studies for the observed column density and/or brightness morphology of the satellite's neutral corona and extended neutral clouds. The calculated energy escape rates for the three processes are 7.5×10^9 W, 3.3×10^{10} W, and 6.04×10^{11} W and are ~11%, 50%, and 900%, respectively, of the upstream ion kinetic energy flow rate of 6.7×10^{10} W determined for a Voyager corotating plasma flowing through a minimum interaction area of πR_{Io}^2, where R_{Io} is Io's radius. A larger more physically appropriate upstream interaction area of $2\pi R_{\mathrm{Io}}^2 = \pi(1.414\ R_{\mathrm{Io}})^2$ would reduce these percentages by a factors of 2. For incomplete collisional cascade, the calculated energy escape rate is expected to be only ~20% of the total energy deposition rate for this process, indicating a heating rate for the atmosphere of 3.0×10^{10} W (the remaining ~80%). This implies that 56% of the minimum upstream ion kinetic energy flow rate is supplied to the atmosphere through the collisional cascade process, a factor of 2.8 times larger than the previously adopted value, and that the effective deflection of magnetospheric plasma out of the interaction region near Io is less than previously estimated. The total estimated neutral energy rate for all three processes (including heating) is 6.75×10^{11} W and is so large that it can only be supplied by the magnetic field energy, which is partially converted near Io to kinetic energy for the neutrals by the ion pickup current created by these processes. This is possible since an ion after a collision with a neutral can rapidly regain its original local corotational and gyration energies by acceleration in the local corotational electric field and magnetic field and may undergo many collisions in the interaction region and hence transfer many times its initial kinetic energy to the atmospheric neutrals. The magnitude of the pickup current and its magnetic field reduction near Io will depend critically upon the volume of the interaction region established by the solution of the three-dimensional magnetospheric flow problem past Io, including these complex plasma-neutral interactions. Rough estimates given here suggest a pickup current in the range of $\sim 5 \times 10^6$ to 2×10^7 A and a reduction (ΔB) in the local magnetic field of ~450 nT. This estimated reduction of the magnetic field is similar to the remaining and unexplained ΔB of ~400 nT determined in a recent analysis [*Khurana et al.*, 1997] of the magnetic field depression measured near Io by the Galileo magnetometer [*Kivelson et al.*, 1996a, b] and attributed in their treatments (where pickup current was neglected) to an internal magnetic dipole field for Io. Hence the remaining and unexplained ~400-nT reduction of the magnetic field measured by Galileo near Io may be a direct reflection of the local charge exchange source and need not require an internal magnetic field for the satellite.

1. Introduction

The interaction of the corotating magnetospheric plasma with Io supplies an important source of energy for the satellite atmosphere. Some fraction of this energy for the atmosphere is trapped locally and heats the atmosphere and corona. This heat is ultimately lost by downward heat conduction and/or radiation. The remaining fraction of this energy for the atmosphere, however, escapes directly from local volume elements in the interaction region as an outward gravitationally escaping kinetic energy flux of neutrals. This flux of escaping neutrals is responsible for creating the extended neutral clouds of Io as well as producing, through subsequent ionization and charge exchange reactions in the plasma torus, a spatially extended heavy-ion plasma source for Jupiter's magnetosphere. In the interaction region, the mechanism for energy transfer from the corotating plasma to the neutrals is essentially collisional in nature, involving primarily various ion neutral collision cross sections and the number densities of the ions and neutrals as well as their relative speeds. Since an ion, upon collision with a neutral, can regain its local corotational and gyration ener-

Paper number 98JA00362.
0148-0227/98/98JA-00362$09.00

gies on the order of one gyration period (i.e., ~0.5 and 1 s for O^+ and S^+, respectively), the amount of kinetic energy that one ion is able to transfer to neutrals in the interaction region may be several times its original kinetic energy. For a particular ion, this multiple of the original ion kinetic energy that is transferred to neutrals will depend upon its travel time through the interaction region (at least ~100 s, assuming corotational speed and a distance of πR_{Io}, where R_{Io} is an Io radius) as well as the number and type of ion neutral encounters that occur. Hence the rate of energy transfer from the corotating magnetospheric plasma to neutrals is a complex and coupled three-dimensional interaction problem. The problem is difficult to solve from first principles since it involves the plasma flow pattern around the satellite which is altered by the atmospheric interaction, the structure and composition of the atmosphere which is altered by the plasma flow, and the multicollisional ion and neutral trajectories that are produced in the interaction region.

An alternative and independent approach may, however, be pursued to gain insight into this complex and coupled three-dimensional interaction of the corotating magnetospheric plasma and Io's atmosphere. This approach is to study ground- and space-based observations of the spatial brightness distributions of various emission lines produced by the escaping neutral species and to deduce from the spatial brightness information the neutral source rates and their velocity distributions. Using this approach, source rates for the dominant SO_2 family neutral species (SO_2, SO, O, S) detected to date in Io's atmosphere, corona, and/or extended clouds have been estimated and published in the past several years [*Smyth and Combi*, 1991; *Smyth*, 1992; *Scherb and Smyth*, 1993; *Smyth and Marconi*, 1998]. For O and S, the very dim emission line brightnesses from which their source rates have been extracted are, however, only barely detectable near Io and its orbit and fall far short of providing enough spatial information from which to determine their neutral source velocity distributions that are created in the interaction region. For the much brighter emission lines of the trace species atomic sodium, however, which has been the brightest and most studied neutral species observed in the Io-Jupiter system for the past 25 years, a complete description for the source velocity distribution (from 0 to 100 km/s) has recently been determined [see *Smyth and Combi*, 1997]. This complete description for the source velocity distribution has emerged by combining a number of different studies for sodium emission observations ranging spatially from Io's bound corona (radial Iocentric distances from ~1.4 to 5.8 R_{Io}), to Io's orbit about the planet (radius of 5.9 Jupiter radii), to the distant zenocorona (or magneto-nebula) detected out to 400–500 planetary radii from Jupiter. From these combined studies, the sodium source velocity distribution at Io's exobase has been determined to be composed of three primary physical components: (1) an incomplete collisional cascade distribution (peaked at ~0.5 km/s and organized somewhat isotropically about Io) which is required to populate the sodium corona near Io and the sodium cloud near Io's orbit and is thought to be produced by ion sputtering in the deeper and more dense regions of the atmosphere; (2) a slow charge exchange and direct collisional ejection distribution (centered ~20 km/s and anisotropically organized about the corotational direction) which is required to populate the trailing sodium directional feature and also the lower velocity component of the sodium zenocorona and is thought to be produced by some combination of charge exchange collisions involving ions that have been slowed from their corotational speed (or created with slower speeds locally) within Io's atmosphere and knock-on ion neutral collisions occurring in the atmosphere and corona; and (3) a fast charge exchange distribution (centered about ~60 km/s and anisotropically organized about the corotational direction) which is required to populate the higher velocity component (and hence more distant portion) of the sodium zenocorona and is thought to be produced by ions with their full corotational speed that in charge exchange reactions create neutrals which are able to escape collisionally unimpeded from the atmosphere and corona. The sodium observations have thus revealed the basic nature of the physical mechanisms and their neutral velocity distributions created in the interaction region near Io. For the dominant neutral species (SO_2, SO, O, S), these same physical processes (albeit with different cross sections and ion fluxes) must also be operative. Hence it is now possible, for the first time, to combine the source rates estimated earlier from observations for the dominant neutral species and the physical mechanisms and their velocity distributions deduced from the sodium studies in order to investigate the complex and coupled three-dimensional interaction of the corotating magnetospheric plasma for the dominant neutral species in Io's atmosphere. The physical processes in the interaction region that give rise to the energy escape rates of neutrals will also produce an electric conductivity and current as well as an associated modification of the magnetic field near Io and thereby provide an interesting and independent avenue to explore in a global fashion these important magnetospheric effects.

In this paper, the O and S source rates deduced from earlier studies of observational data are combined with their appropriate source velocity distributions based upon the three physical components or collisional mechanisms deduced for sodium. Using this information, the rate at which energy is carried away from Io by the O and S escaping neutrals created near the satellite exobase because of the interaction of Io's atmosphere with the corotating magnetospheric plasma is calculated in section 2. These calculated rates are discussed in section 3. It is shown that the total energy escape rate of neutrals is larger compared to the upstream impinging initial kinetic energy flow rate of the ions and that the energy escape rate of neutrals is dominated by the fast charge exchange component. This indicates that the ion neutral interaction is more intense than previously estimated and that the corotational ions transfer many times their initial kinetic energy to the neutrals in the interaction region. In section 4, the magnetospheric impact of the large escaping neutral energy rate on the interaction region is discussed with estimates given for both the ion pickup conductivity and current near Io as well as the reduction of the local planetary field near Io. Conclusions are summarized in section 5.

2. Energy Escape Rate of Neutrals From Io

In this section, the rate at which energy is supplied to the neutral species O and S escaping from Io's atmosphere because of its interaction with the corotating magnetosphere is calculated. The calculation, as discussed in section 1, is based on combining previously published source rate and velocity distribution information for the three different ion neutral collisional processes: (1) incomplete collisional cascade, to be labeled "(cascade,)" (2) slow-velocity charge exchange and direct ejection, to be labeled "(slow CE/DE)," and (3) fast-

velocity charge exchange, to be labeled "(fast CE)." The neutral energy escape rate or power, $\dot{\varepsilon}$, is consequently divided into three parts:

$$\dot{\varepsilon} = \sum_i [\dot{\varepsilon}_i^{(\text{cascade})} + \dot{\varepsilon}_i^{(\text{slow CE/DE})} + \dot{\varepsilon}_i^{(\text{fast CE})}]. \quad (1)$$

In (1) the sum is over the relevant ith escaping neutral species near the satellite exobase. By denoting the collisional process by the index (k), each term in (1) may be written in the same convenient form

$$\dot{\varepsilon}_i^{(k)} = \tfrac{1}{2} m_i (\bar{v}_i^2)^{(k)} S_i^{(k)}. \quad (2)$$

Expression (2) is divided into the product of two basic terms: $m_i(\bar{v}_i^2)^{(k)}/2$, which is the average kinetic energy per unit source rate for the ith neutral species produced by the (k) process, and $S_i^{(k)}$ which is the source rate for the ith neutral species (i.e., number of ith neutrals per second) energized by the (k) process. Here m_i is the mass and $\bar{v}_i^2$ is the average value per unit source rate of the square of the velocity for the ith neutral species. Substituting (2) into (1), the neutral energy escape rate $\dot{\varepsilon}$ becomes

$$\dot{\varepsilon} = \sum_i \tfrac{1}{2} m_i [(\bar{v}_i^2)^{(\text{cascade})} S_i^{(\text{cascade})} + (\bar{v}_i^2)^{(\text{slow CE/DE})} S_i^{(\text{slow CE/DE})} + (\bar{v}_i^2)^{(\text{fast CE})} S_i^{(\text{fast CE})}]. \quad (3)$$

To evaluate the first term in (3), the terms $(\bar{v}_i^2)^{(\text{cascade})}$ and $S_i^{(\text{cascade})}$ will first be expressed in terms of a flux velocity distribution $\phi_i(\mathbf{v})$ per neutral for the incomplete collisional cascade processes at the exobase

$$(\bar{v}_i^2)^{(\text{cascade})} = \frac{1}{S_i^{(\text{cascade})}} \int_{\text{exo. area}} n_i^{(\text{neutral})}\, dA \int_{\text{upper hem.}} v^2 \phi_i(\mathbf{v})\, d\mathbf{v} \quad (4a)$$

$$S_i^{(\text{cascade})} = \int_{\text{exo. area}} n_i^{(\text{neutral})}\, dA \int_{\text{upper hem.}} \phi_i(\mathbf{v})\, d\mathbf{v}, \quad (4b)$$

where $n_i^{(\text{neutral})}$ is the number density of the ith neutral species and the flux velocity distribution $\phi_i(\mathbf{v})$ is defined in terms of the (normalized to unity) neutral velocity distribution $f_i^{(\text{neutral})}(\mathbf{v})$ for the incomplete collisional cascade processes,

$$\phi_i(\mathbf{v}) = \mathbf{v} \cdot \hat{n} f_i^{(\text{neutral})}(\mathbf{v}), \quad (4c)$$

where $\hat{n}$ is the upward unit vector. In (4a) and (4b) the first integral is over the exobase area, and the second integral is over the local upper hemisphere of the three-dimensional neutral velocity vector $\mathbf{v}$. For the simple case of an isotropic flux velocity distribution and a uniform neutral flux Φ_i (i.e., neutrals $\text{cm}^{-2}\,\text{s}^{-1}$) at the exobase with area A_{exobase}, (4a) and (4b) reduce to

$$(\bar{v}_i^2)^{(\text{cascade})} = \int_{\text{upper hem.}} v^2 \phi_i(\mathbf{v})\, d\mathbf{v} \Big/ \int_{\text{upper hem.}} \phi_i(\mathbf{v})\, d\mathbf{v} \quad (4d)$$

$$S_i^{(\text{cascade})} = A_{\text{exobase}} \Phi_i. \quad (4e)$$

To evaluate the second and third terms in (3), the terms $(\bar{v}_i^2)^{(k)}$ and $S_i^{(k)}$ will first be expressed in terms of the velocity distribution functions for the slow $f_j^{(\text{slow ion})}$ and fast $f_j^{(\text{fast ion})}$ magnetospheric ions of the jth species in the Io reference frame and the appropriate neutral ion cross sections $\sigma_{ij}^{(\text{slow})}$ and $\sigma_{ij}^{(\text{fast})}$ for charge exchange and/or direct collisional ejection:

$$(\bar{v}_i^2)^{(\text{slow CE/DE})} = \frac{1}{S_i^{(\text{slow CE/DE})}} \int_{\text{int. region}} n_i^{(\text{neutral})}\, dV \cdot \sum_j n_j^{(\text{ion})} \int v^2 \sigma_{ij}^{(\text{slow})} |\mathbf{v}_{ij}^{\text{rel}}| f_j^{(\text{slow ion})}(\mathbf{v})\, d\mathbf{v} \quad (5a)$$

$$S_i^{(\text{slow CE/DE})} = \int_{\text{int. region}} n_i^{(\text{neutral})}\, dV \cdot \sum_j n_j^{(\text{ion})} \int \sigma_{ij}^{(\text{slow})} |\mathbf{v}_{ij}^{\text{rel}}| f_j^{(\text{slow ion})}(\mathbf{v})\, d\mathbf{v} \quad (5b)$$

$$(\bar{v}_i^2)^{(\text{fast CE})} = \frac{1}{S_i^{(\text{fast CE})}} \int_{\text{int. region}} n_i^{(\text{neutral})}\, dV \cdot \sum_j n_j^{(\text{ion})} \int v^2 \sigma_{ij}^{(\text{fast})} |\mathbf{v}_{ij}^{\text{rel}}| f_j^{(\text{fast ion})}(\mathbf{v})\, d\mathbf{v} \quad (5c)$$

$$S_i^{(\text{fast CE})} = \int_{\text{int. region}} n_i^{(\text{neutral})}\, dV \sum_j n_j^{(\text{ion})} \int \sigma_{ij}^{(\text{fast})} |\mathbf{v}_{ij}^{\text{rel}}| f_j^{(\text{fast ion})}(\mathbf{v})\, d\mathbf{v}, \quad (5d)$$

where $n_j^{(\text{ion})}$ is the number density of the jth ion species and $\mathbf{v}_{ij}^{\text{rel}}$ is the relative velocity between the ith neutral species and the jth ion species. As noted earlier, the slow ions for the velocity distribution functions $f_j^{(\text{slow ion})}$ are not part of the upstream ion distribution but are created near Io by a mix of processes that locally slow the ion's upstream corotational speeds and that locally produce new ions with reduced speeds. In (5) the first integral is over the three-dimensional volume of the interaction region about Io, and the second integral is over the three-dimensional ion velocity vector $\mathbf{v}$. To simplify (5), note that for the faster ejected neutral velocities produced by these processes, the neutrals near the exobase prior to their collisional interactions are effectively at rest so that $\mathbf{v}_{ij}^{\text{rel}} = \mathbf{v}$. Also, to our present level of understanding, the slow and fast velocity distributions for the dominant magnetospheric ions are species independent (i.e., $f_j^{(k)}(\mathbf{v}) = f^{(k)}(\mathbf{v})$). Expressions (5a) and (5b), for example, then become

$$(\bar{v}_i^2)^{(\text{slow CE/DE})} = \frac{1}{S_i^{(\text{slow CE/DE})}} \int_{\text{int. region}} n_i^{(\text{neutral})}\, dV \cdot \left(\sum_j n_j^{(\text{ion})} \right) \int \sigma_i^{(\text{slow})} v^3 f^{(\text{slow ion})}(\mathbf{v})\, d\mathbf{v} \quad (6a)$$

$$S_i^{(\text{slow CE/DE})} = \int_{\text{int. region}} n_i^{(\text{neutral})}\, dV \left(\sum_j n_j^{(\text{ion})} \right) \int \sigma_i^{(\text{slow})} v f^{(\text{slow ion})}(\mathbf{v})\, d\mathbf{v} \quad (6b)$$

$$S_i^{(\text{slow CE/DE})} = \int_{\text{int. region}} n_i^{(\text{neutral})} / \tau_i^{(\text{slow CE/DE})}\, dV, \quad (6c)$$

Table 1. Energy Escape Rate of Neutrals From Io

Collisional Process	Neutral Source Rates: S_{oxygen} atoms s^{-1}	Neutral Source Rates: S_{sulfur} atoms s^{-1}	Average Speed per Unit Flux $(\bar{v}^2)^{1/2}$, km s^{-1}	Neutral Energy Loss Rate $\Sigma_i \frac{1}{2} m_i v^2 S_i$, W	Height Integrated Minimum Pickup Conductivity at Io, $\Sigma_i m_i S_i/(B^2 4\pi R_{Io}^2)$, mho	Charge Exchange Pickup Current at Io, $\Sigma_i m_i S_i \lvert\mathbf{E}\rvert/(B^2\delta)$, A
Incomplete collisional cascade	4.6×10^{27}	2.3×10^{27}	8.66, 6.95	7.54×10^{9}	...	...
Low-velocity CE and direct ejection	1.7×10^{27}	0.8×10^{27}	27.6	3.34×10^{10}	0.63	0.21×10^{7} $(\frac{1}{4}R_{Io}/\delta)$*
Full-velocity charge exchange	6.0×10^{27}	1.8×10^{27}	68.8	6.04×10^{11}	1.83	1.74×10^{7} $(\frac{1}{4}R_{Io}/\delta)$
Total	12.3×10^{27}	4.9×10^{27}		6.45×10^{11}	2.46	1.95×10^{7} $(\frac{1}{4}R_{Io}/\delta)$

*Assuming the neutral escape process is all low-velocity charge exchange with a pickup speed of 20 km s^{-1}.

where the average cross sections $\sigma_i^{(\text{slow})}$ and slow neutral production times $\tau_i^{(\text{slow CE/DE})}$ are

$$\sigma_i^{(\text{slow})} = \sum_j n_j^{(\text{ion})} \sigma_{ij}^{(\text{slow})} \Big/ \sum_j n_j^{(\text{ion})} \tag{6d}$$

$$\frac{1}{\tau_i^{(\text{slow CE/DE})}} = \left(\sum_j n_j^{(\text{ion})} \right) \int \sigma_i^{(\text{slow})} |\mathbf{v}| f^{(\text{slow ion})}(\mathbf{v})\, d\mathbf{v} \tag{6e}$$

with similar expressions for (5c) and (5d). In addition, since the interaction region near Io is effectively a point source for these faster neutral velocities as viewed on the larger spatial scale occupied by these fast neutrals where their flux velocity distributions may be observed, the expressions can be further simplified by approximating the cross sections $\sigma_i^{(\text{slow})}$ and $\sigma_i^{(\text{fast})}$ by their appropriate volumetric averaged values $\bar{\sigma}_i^{(\text{slow})}$ and $\bar{\sigma}_i^{(\text{fast})}$. The expressions for $(\bar{v}_i^2)^{(k)}$ and $S_i^{(k)}$ then may be written as

$$(\bar{v}_i^2)^{(\text{slow CE/DE})} = \int v^3 f^{(\text{slow ion})}(\mathbf{v})\, d\mathbf{v} \Big/ \int v f^{(\text{slow ion})}(\mathbf{v})\, d\mathbf{v} \tag{7a}$$

$$S_i^{(\text{slow CE/DE})} = \eta_i^{(\text{slow CE/DE})} / \bar{\tau}_i^{(\text{slow CE/DE})} = \eta_i^{(\text{slow CE/DE})} \phi^{(\text{ion})} \bar{\sigma}_i^{(\text{slow})} \tag{7b}$$

$$(\bar{v}_i^2)^{(\text{fast CE})} = \int v^3 f^{(\text{fast ion})}(\mathbf{v})\, d\mathbf{v} \Big/ \int v f^{(\text{fast ion})}(\mathbf{v})\, d\mathbf{v} \tag{7c}$$

$$S_i^{(\text{fast CE})} = \eta_i^{(\text{fast CE})} / \bar{\tau}_i^{(\text{fast CE})} = \eta_i^{(\text{fast CE})} \phi^{(\text{ion})} \bar{\sigma}_i^{(\text{fast})}. \tag{7d}$$

In the above, $\eta_i^{(\text{slow CE/DE})}$ and $\eta_i^{(\text{fast CE})}$ are, respectively, the number of neutrals in source reservoirs in the interaction region volume for the slow and fast processes and may be expressed as

$$\eta_i^{(\text{slow CE/DE})} = \bar{n}_i^{(\text{slow CE/DE})} V_{\text{eff}}^{(\text{slow})} \tag{7e}$$

$$\eta_i^{(\text{fast CE})} = \bar{n}_i^{(\text{fast CE})} V_{\text{eff}}^{(\text{fast})} \tag{7f}$$

where $\bar{n}_i^{(\text{slow CE/DE})}$ and $\bar{n}_i^{(\text{fast CE})}$ are the average number densities of neutrals in the slow and fast source reservoirs, respectively, and $V_{\text{eff}}^{(\text{slow})}$ and $V_{\text{eff}}^{(\text{fast})}$ are the effective volumes of the interaction region for the slow and fast processes. Also, $\bar{\tau}_i^{(\text{slow CE/DE})}$ and $\bar{\tau}_i^{(\text{fast CE})}$ are the average neutral residence times in the interaction region for the slow and fast processes, respectively.

Nominal source rates at Io's exobase for escape of the neutral species O and S have been estimated from modeling analysis studies of observed neutral cloud brightness data and scaling arguments by *Smyth and Combi* [1991] and *Smyth* [1992]. These rates are given for speeds ranging from the low exobase escape speed (~2 km s^{-1}) to the fast corotational charge exchange velocities. As illustrated by the model calculations of *Marconi and Smyth* [1996], the Io source rates for O and S are, however, expected to vary significantly with (1) Io System III longitude because of the oscillation of the plasma torus about Io's orbit and also inherent System III longitudinal asymmetries in the plasma torus and with (2) Io geocentric phase angle because of east-west asymmetries in the plasma torus produced by the presence of an east-west electric field. Since these variations are far from being documented in observational data for the very faint O and S emission lines, the nominal source rates for O and S published by *Smyth and Combi* [1991] and *Smyth* [1992] have been simply adopted here and used to estimate, upon proper subdivision, the exobase source rates $S_i^{(\text{cascade})}$, $S_i^{(\text{slow CE/DE})}$, and $S_i^{(\text{fast CE})}$ which are summarized in the second and third columns of Table 1. These rates reflect the use of torus-average cross sections for $\bar{\sigma}_i^{(\text{slow})}$ and $\bar{\sigma}_i^{(\text{fast})}$ as required in (7b) and (7d) and are discussed in more detail in Appendix A of *Smyth and Combi* [1991].

To calculate the quantity $(\bar{v}_i^2)^{(\text{cascade})}$ in the (4d), the incomplete collisional cascade flux speed distribution $\phi_i(\mathbf{v})$ is required. For the incomplete collisional cascade processes, a general functional form for this flux velocity distribution at the exobase is discussed by *Smyth and Combi* [1988]. For atomic sodium, an explicit set of values for the parameters in this functional form was recently determined by *Smyth and Combi* [1997] from modeling of observational data. This explicitly determined incomplete collisional cascade flux speed distribution is spatially isotropic at the satellite exobase, peaked at a speed of 0.5 km s^{-1}, which is well below the (model adopted 2600 km radius) exobase escape speed of about 2 km s^{-1}, and has a velocity tail extending to many tens of kilometers per second that is more populated than a classical complete collisional cascade velocity distribution (i.e., $\alpha = 7/3$ was appropriate instead of the classical value $\alpha = 3$). Since atomic sodium is a trace species (and collides primarily with the dominant neutral species), it is reasonable to assume that all the dominant neutral species will have essentially the same incomplete collisional cascade flux distribution as sodium. This distribution is therefore adopted in this paper for O and S in the calculation of $(\bar{v}_i^2)^{(\text{cascade})}$ in (4d) and yields (see Appendix A for details) a value of $(\bar{v}_O^2)^{(\text{cascade})} = 74.94$ km^2 s^{-2} = (8.657 km s^{-1})^2 and $(\bar{v}_S^2)^{(\text{cascade})} = 48.31$ km^2 s^{-2} = (6.951 km s^{-1})^2 which are listed in the fourth column of Table 1. Approximately half of the atoms in this incomplete collisional cascade flux speed distribution directly escape Io's gravity while the approximately remaining half are ballistic in nature and are not directly lost but populate the corona density. Hence the escape

rates listed in the second and third columns of Table 1 should be approximately doubled to describe the total cascade rate, but if only the energy escape rate fraction from Io is desired, this doubled rate should then be approximately halved yielding the source values that are listed in Table 1. On the basis of these values the estimated energy escape rate of neutral oxygen and sulfur from Io by the incomplete collisional cascade processes is

$$\sum_i \tfrac{1}{2} m_i (\bar{v}_i^2)^{(\text{cascade})} S_i^{(\text{cascade})} = 7.54 \times 10^9 \text{ W} \qquad (8a)$$

as summarized in the fifth column of Table 1. These source rates correspond to a uniform exobase atomic oxygen and sulfur flux of $\Phi_O = 5.7 \times 10^9$ cm^{-2} s^{-1} and $\Phi_S = 2.8 \times 10^9$ cm^{-2} s^{-1} for a nominal satellite exobase radius of 1.4 R_{Io}.

To calculate the quantities $(\bar{v}_i^2)^{(\text{slow CE/DE})}$ and $(\bar{v}_i^2)^{(\text{fast CE})}$ in (7a) and (7c), a functional form is required for the ion distribution functions $f^{(\text{slow ion})}$ and $f^{(\text{fast ion})}$. The displaced Maxwell-Boltzmann distribution used by *Smyth and Combi* [1991] and also *Flynn et al.* [1992] for both the slower and faster velocity distributions required to fit the large spatial distribution of sodium in the zenocorona or magneto-nebula, which was observed up to 400–500 planetary radii from Jupiter by *Mendillo et al.* [1990], is adopted here for the atomic ion species. The slow and fast displaced Maxwell-Boltzmann distributions are presented in the Appendix B where (7a) and (7c) are evaluated to obtain $(\bar{v}_i^2)^{(\text{slow CE/DE})} = (27.61 \text{ km s}^{-1})^2$ and $(\bar{v}_i^2)^{(\text{fast CE})} = (68.81 \text{ km s}^{-1})^2$ which are listed in the fourth column of Table 1. On the basis of these values the estimated energy escape rates of neutral oxygen and sulfur from Io by the slow charge exchange/direct ejection and fast charge exchange processes are

$$\sum_i \tfrac{1}{2} m_i (\bar{v}_i^2)^{(\text{slow CE/DE})} S_i^{(\text{slow CE/DE})} = 3.34 \times 10^{10} \text{ W} \qquad (8b)$$

$$\sum_i \tfrac{1}{2} m_i (\bar{v}_i^2)^{(\text{fast CE})} S_i^{(\text{fast CE})} = 6.04 \times 10^{11} \text{ W} \qquad (8c)$$

respectively, as summarized in the fifth column of Table 1. Note that the fast charge exchange process dominates the neutral energy escape rate from Io and corresponds to neutral source reservoirs in the interaction region volume for atomic oxygen and sulfur of $\eta_O^{(\text{fast CE})} = 2.2 \times 10^{32}$ O atoms and $\eta_S^{(\text{fast CE})} = 3.0 \times 10^{32}$ S atoms, assuming in (7d) a nominal ion flux ϕ^{ion} of 1×10^{10} cm^{-2} s^{-1} and the averaged charge exchange cross sections given by *Smyth and Combi* [1991] for which the fast average neutral residence times in the interaction region are $\bar{\tau}_O^{(\text{fast CE})} = 13.5$ hours and $\bar{\tau}_S^{(\text{fast CE})} = 36.1$ hours. The effective volume V_{eff} of the interaction region is not well defined and will depend upon the detailed spatial structure of the Io's local atmosphere and also the plasma flow pattern established about the satellite. The absolute size of this effective volume is particularly important in determining the magnitude of the pickup electrical conductivity, its associated current, and its modification of the planetary magnetic field near Io produced by the charge exchange processes, which are estimated in section 4.

3. Discussion

The estimates in Table 1 for the source rates and energy escape rates of neutrals from Io are presented in pictorial form in Figure 1. As a minimum unit of measure, the undisturbed corotating plasma upstream of Io that flows through an Io disk area ($A_{Io} = \pi R_{Io}^2 = 1.035 \times 10^{17}$ cm^2) is shown to the left and represents an ion source rate of $\sim 1 \times 10^{27}$ ions s^{-1} for a corotational speed of 56.8 km s^{-1}. This corresponds to an ion kinetic energy flow rate of 6.7×10^{10} W (100%, which will be a minimum reference point for the initially available ion kinetic-energy power) and, for an equal number of oxygen and sulfur ions, an upstream ion mass flow rate of 41.3 kg s^{-1}. Since Io and its atmospheric interaction will likely present for the upstream plasma a larger downstream projected target than the minimum disk area of Io (A_{Io}), a second larger and perhaps more realistic bounding upstream "physical interaction area" of $2 A_{Io} = \pi(1.414 R_{Io})^2$ may be more appropriate. A larger area is consistent with the Galileo flyby of Io [*Frank et al.*, 1996; *Kivelson et al.*, 1996b] which detected a highly disturbed region of similar size near the satellite. This larger "physical interaction area" also has the virtue that results determined by the "minimum interaction area" can be easily adjusted by multiplication or division by a factor of 2.

The escape rates for the incomplete collisional cascade ion-neutral interactions are summarized in Figure 1. A combined O and S source rate of 6.9×10^{27} atoms s^{-1} (245 kg s^{-1}) escapes Io with an average energy flux characterized by a velocity of ~7–8.7 km s^{-1}. This source rate corresponds to a neutral energy escape rate of 7.5×10^9 W, which is only ~11% of the upstream ion kinetic energy flow rate for the minimum interaction area A_{Io}. In atmospheric model simulations, the upward escaping collisional cascade neutral energy escape rate has been shown to be only a modest fraction of the total ion-sputtering energy deposition rate in the heating layer with a value determined by *Pospieszalska and Johnson* [1996] of ~22% for an appropriate ion neutral collision cross section of 5×10^{-16} cm^{-2} and a value determined by *Marconi et al.* [1996] of ~25% for an ion neutral collision cross section of 3×10^{-16} cm^{-2}. Assuming here that the power of the escaping neutrals in the cascade component is 20% of the ion-sputtering energy deposition rate in the heating layer (denoted by the shaded annulus in Figure 1) with the remaining 80% of the energy (3.0×10^{10} W) heating the atmosphere and ultimately lost in downward atmospheric heat conduction and radiative loss processes, then the total rate at which ion-sputtering supplies energy to the heating layer would be 3.8×10^{10} W, which is a large fraction (56%) of upstream ion kinetic energy flow rate for the minimum interaction area. This 56% estimate is a factor of 2.8 times larger than the nominal 20% value based on the minimum interaction area that has been adopted by *Pospieszalska and Johnson* [1992, 1996] and based on the fraction of corotating ion energy estimated to reach the exobase by the MHD calculations of *Linker et al.* [1989]. This larger 56% value implies that the ion neutral interaction near Io is much stronger than estimated from the calculations of *Linker et al.* [1989]. If, alternatively, the larger physical interaction area of $2 A_{Io}$ is appropriate, then only 28% of the upstream ion kinetic energy flow rate would be required.

Rates for the two charge exchange escape processes are also summarized in Figure 1. For the slow charge exchange and direct ejection ion neutral interactions, a combined O and S source rate of 2.5×10^{27} atoms s^{-1} (88 kg s^{-1}) escapes Io with an average energy flux characterized by a velocity of 27.6 km s^{-1}. This source rate corresponds to a neutral energy escape rate of 3.3×10^{10} W, which is ~50% of the upstream ion kinetic energy flow rate for the minimum interaction area A_{Io}

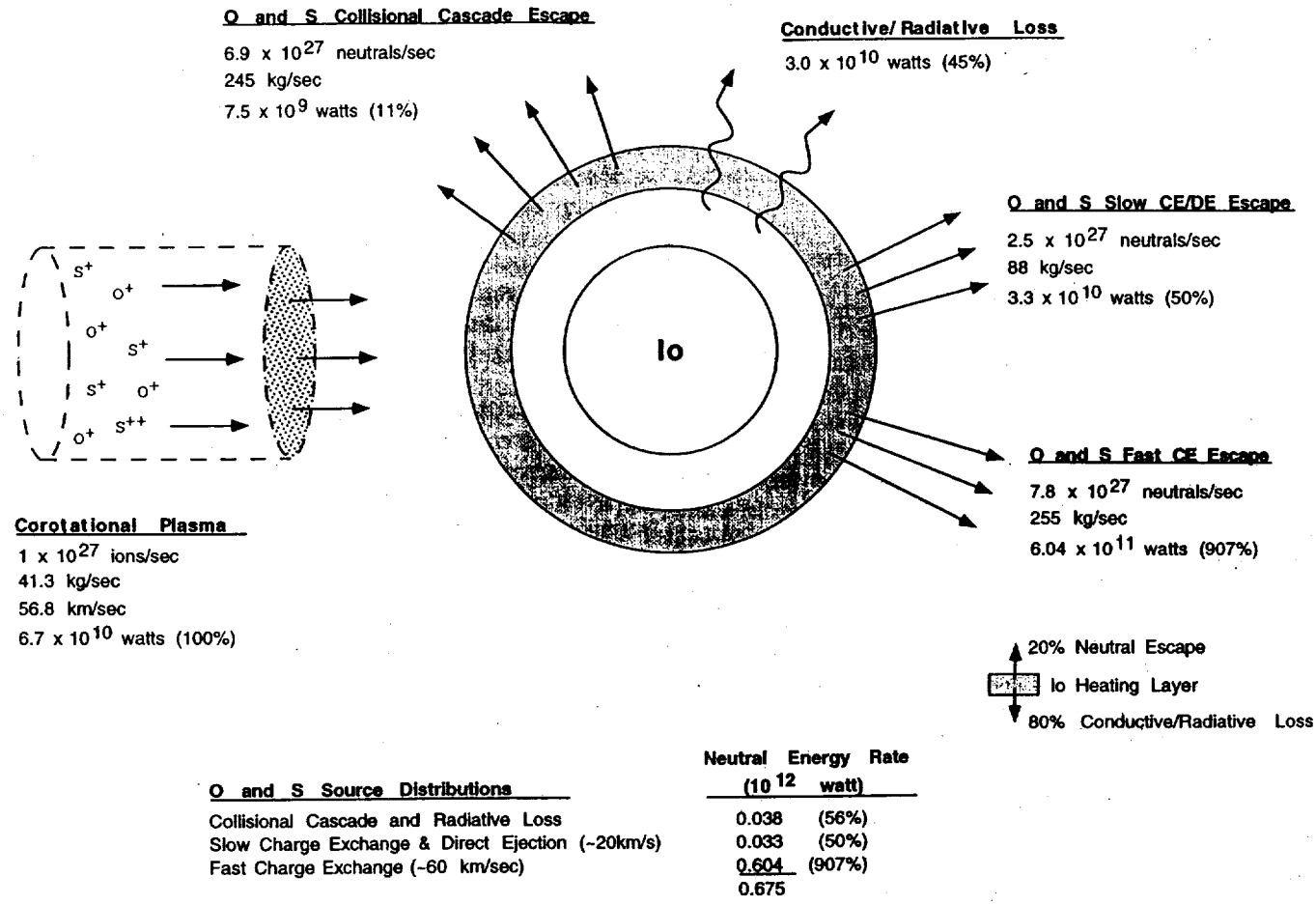

O and S Source Distributions	Neutral Energy Rate (10^{12} watt)	
Collisional Cascade and Radiative Loss	0.038	(56%)
Slow Charge Exchange & Direct Ejection (~20km/s)	0.033	(50%)
Fast Charge Exchange (~60 km/sec)	0.604	(907%)
	0.675	

Figure 1. The energy escape rate of neutrals from Io. Estimates are summarized for the source, mass, and energy rates at which O and S neutrals (collectively) are escaping Io for three collisional processes in the interaction region (shaded annulus around Io) because of the impact of the corotating plasma with Io's atmosphere. The estimated conductive/radiative loss rate (also shown) is based upon the assumed branching ratio that 20% of the energy deposition rate of the incomplete collisional cascade process is lost upwardly by escaping neutrals and the remainder 80% is lost by downward heat conduction and/or radiation. The total energy rate (including the estimated conductive and radiative loss) of 0.675×10^{12} W supplied to the atmosphere by the corotating plasma is about ten times the initial kinetic energy source rate (6.7×10^{10} W) of the corotating ions flowing through the adopted upstream minimum interaction area of πR_{Io}^2 illustrated to the left.

or 25% of the upstream ion kinetic energy flow rate for the physical interaction area $2\,A_{Io}$. For the fast charge exchange ion neutral interactions, a combined O and S source rate of 7.8×10^{27} atoms s^{-1} (255 kg s^{-1}) escapes Io with an average energy flux characterized by a velocity of 68.8 km s^{-1}. This source rate produces the dominant neutral energy escape rate of 6.04×10^{11} W, which is ~907% of the upstream ion kinetic energy input rate for the minimum interaction area or ~454% of the upstream ion kinetic energy input rate for the physical interaction area.

The total estimated rate at which neutral kinetic energy is escaping from Io for all three processes is then 6.45×10^{11} W with at least an additional 0.3×10^{11} W deposited as heat in the interaction region. The total energy supplied to escaping neutrals is therefore estimated to be a factor of ~10 larger than the upstream ion kinetic energy flow rate of 6.7×10^{10} W for the minimum interaction area or, alternatively, a factor of ~5 larger than the upstream ion kinetic energy flow rate of 1.3×10^{11} W for the larger physical interaction area. This large multiple of the upstream ion kinetic energy flow rate implies that on average an ion in the interaction region is able to transfer to neutrals ~5–10 times its original upstream kinetic energy. Since this neutral energy escape rate is dominated by fast charge exchange reactions, it implies that for each ion on average ~4.5–9 fast charge exchange reactions occur in the interaction region. For ions of corotational speed and a travel time through the interaction region of at least ~100 s, this implies an ion collision time of ~20 to 10 s which would occur at a level in the atmosphere where the local neutral density would be ~0.5 to 1×10^8 cm^{-3}. This level is physically reasonable since it lies below the nominal exobase level of the atmosphere, for which the neutral density is approximately a few $\times 10^7$ cm^{-3}, but above the region of the atmosphere where corotation will cease (i.e., when the ion gyration to collision frequency ratio is of order unity), for which the neutral density is approximately a few $\times 10^9$ cm^{-3}. It should be noted, however, that the large energy escape rate responsible for this ~4.5–9 fast charge exchange reactions in the interaction region is based upon the assumption that all fast charge exchange reactions are centered about the full corotational speed (56.81

km s^{-1}, see equation (B3)), as has been documented to be the case for atomic sodium, and that the source rates for O and S are sustained at the adopted values. Regarding the latter point, it should be noted that the fast charge exchange source rates adopted here are based only upon one brightness observation for the atomic oxygen 6300-Å emission line [*Brown*, 1981] measured near Io's orbit at western elongation and upon suitable scaling arguments [*Smyth and Combi*, 1991]. The scaling arguments also depend upon the (unknown) spatial distribution and the relative abundance of the neutral species in the interaction region. The nominally scaled source rates adopted here could therefore possibly be smaller or larger. The general scenario presented is, nevertheless, expected to occur even if the source rates are eventually found to be altered by a factor of 2 or so.

4. Impact of the Energy Escape Rates Near Io

The estimate for the total kinetic energy supply rate to escaping neutrals of 0.645×10^{12} W is perhaps surprising when first compared to the upstream ion kinetic energy flow rate. Such a value would be expected, however, when compared to the estimated energy supply rate to the plasma torus of $\sim 1 \times 10^{12}$ W [see *Smyth*, 1992] by pickup ions produced by electron impact ionization and charge exchange of neutrals. Even this ion energy supply rate of $\sim 1 \times 10^{12}$ W is less than estimates for the plasma torus radiative energy loss rate of ~ 3–5×10^{12} W and implies that other neutral (and perhaps direct ion) loss processes may be operative at Io as well as other energy sources in the plasma torus. The ion energy supply rate $\sim 1 \times 10^{12}$ W to the plasma torus is approximately equally split between the near Io charge exchange sources in the interaction volume V_{eff} and the more spatially distributed (but still peaked at Io) ion sources produced eventually by the collision cascade neutrals. This power for the neutrals and plasma torus is ultimately supplied [*Eviatar and Siscoe*, 1980] by the rotational energy of Jupiter through a Birkeland current. Relative to Io, the two local upstream sources of power for the neutrals are the initial upstream ion kinetic energy and the magnetic field energy $B^2/(2\,\mu_0)$. For an upstream minimum interaction area ($A_{\text{Io}} = \pi R_{\text{Io}}^2$) and a corotational flow ion speed, these two power sources are the following:

Ion kinetic energy rate

$$\tfrac{1}{2} m_{\text{ion}} v_{\text{ion}}^2 \phi_{\text{ion}} A_{\text{Io}} = 6.66 \times 10^{10} \text{ W} \tag{9a}$$

Magnetic field energy rate

$$\frac{B^2}{2\mu_0} v_{\text{ion}} A_{\text{Io}} = 7.88 \times 10^{11} \text{ W}. \tag{9b}$$

These terms are physically just the two main diagonal terms in the divergence term of the total energy conservation equation for the plasma and neutral species applied to the upstream surface area in Figure 1 (i.e., the diagonal terms provide a generalized Bernoulli's law to be used below).

The power source for the upstream ion kinetic energy, as noted earlier, is far too small even if it is doubled or tripled by choosing a larger interaction area upstream, corresponding to an effective interaction radius of ~ 1.414 or $1.732\ R_{\text{Io}}$ or a nominal interaction altitude of 750 or 1330 km when projected to Io. The power source for the magnetic field energy is, however, just adequate assuming the upstream minimum interaction area A_{Io} and is larger by a factor of ~ 2 if the larger physical interaction areas $2\,A_{\text{Io}}$ were adopted. Such a significant drain of the upstream magnetic energy implied by the neutral energy escape rates from Io would significantly reduce the local Jovian magnetic field near Io, with the size of the reduction determined by the detailed spatial size of the interaction region. If, for example, we assume the more physically likely interaction area of $2\,A_{\text{Io}}$ upstream (an effective disk interaction radius of $\sim 1.414\ R_{\text{Io}}$), then the total energy supply rate to the neutrals of 6.75×10^{11} W would approximately reduce the local magnetic energy density in the interaction region by ~43% of its undisturbed upstream value, assuming that the product of the cross-sectional area and normal ion velocity in a connecting Bernoulli tube is comparable upstream and at Io. For an undisturbed magnetic field $B = 1835$ nT near Io's orbit, this would require that the local magnetic field B near Io would be reduced by ~450 nT. This estimate for the reduction of B is very similar to the remaining and unexplained reduction ΔB with a peak value exceeding 400 nT near Io determined in a recent analysis by *Khurana et al.* [1997] of the Galileo magnetometer Io flyby data [*Kivelson et al.*, 1996a, b] after they removed the ΔB contributions for the local plasma currents and Alfvén wing currents (but neglected all pickup current ΔB contributions) from the (longer-time-averaged) magnetic field depression signature measured near Io. Khurana et al. neglected the pickup current ΔB contributions by assuming that the pickup currents were highly localized within $0.1\ R_{\text{Io}}$ of the satellite surface and occurred well upstream of the Galileo trajectory, an unlikely scenario. The remaining unexplained ΔB of ~400 nT was therefore attributed by Khurana et al. to an internal satellite magnetic dipole field. However, on the basis of the above estimates for ΔB this significant remaining unexplained ~400-nT reduction of the planetary magnetic field near Io may be a direct reflection of the local charge exchange source near Io and hence need not require an internal magnetic field for the satellite.

Although the current closure problem in the Io-Jupiter system is a complex problem, an approximate estimate of the local current produced by the energy escape rate from Io may be made. The charge exchange processes near Io produce a local pickup electrical conductivity and an associated local pickup current similar to net mass pickup [*Ip and Axford*, 1980; *Goertz*, 1980]. In addition to charge exchange contributions that are localized in the interaction region near Io, the neutrals liberated by the incomplete collisional cascade processes will subsequently undergo ionization and charge exchange processes and also contribute to the electrical conductivity and an associated local pickup current. The contribution from the incomplete collisional cascade processes will, however, be more broadly peaked about Io beyond the immediate volume V_{eff} of the interaction region and because of its more spatially distributed nature will provide, relative to localized charge exchange, only a small local contribution that will be ignored here. The pickup conductivity for the charge exchange processes near Io is given by

$$\sigma_{pu} = \sum_i m_i S_i^{(\text{CE})}/(B^2 V_{\text{eff}}) = \frac{1}{\delta} \sum_i m_i S_i^{(\text{CE})}/(B^2 A_{\text{eff}}), \tag{10}$$

where the effective volume V_{eff}, over which the source $S_i^{(\text{CE})}$ is distributed, is divided into an effective surface area A_{eff}, presumably some fraction of Io's surface area, and an effective height δ. The height-integrated conductivity is then given by

$$\Sigma_{pu} = \delta\sigma_{pu} = \sum_i m_i S_i^{(CE)}/(B^2 A_{eff}). \quad (11)$$

The magnitude of the current density is

$$|\mathbf{j}| = \sigma_{pu}|\mathbf{E}| = \sum_i m_i S_i^{(CE)}|\mathbf{E}|/(B^2 V_{eff}), \quad (12)$$

where $\mathbf{E}$ is the local electric field, and the pickup current is then given by

$$I = |\mathbf{j}|A_{eff} = \sum_i m_i S_i^{(CE)}|\mathbf{E}|/(B^2\delta). \quad (13)$$

Note that the height-integrated pickup conductivity Σ_{pu} depends on the inverse of the effective area A_{eff}, the current density $|\mathbf{j}|$ depends on the inverse of the effective volume V_{eff}, and the current I depends on the inverse of the effective height δ. A minimum value of the height-integrated pickup conductivity is given by choosing the effective area A_{eff} equal to Io's surface area $4\pi R_{Io}^2$:

$$(\Sigma_{pu})_{min} = \sum_i m_i S_i^{(CE)}/(B^2 4\pi R_{Io}^2). \quad (14)$$

Using the neutral source rates given in Table 1 and a value of the local magnetic field B of 1835 nT, the corresponding values of $(\Sigma_{pu})_{min}$ and the currents I are summarized in Table 1, where a partial corotational electric field corresponding to a corotational speed of 20 km s^{-1} was assumed for the second (low-velocity charge exchange) source and a full corotational speed of 56.8 km s^{-1} was assumed for the third (full-velocity charge exchange) source. A total height-integrated minimum pickup conductivity of 2.46 mho is obtained. The total pickup current in Table 1 is $\sim 2 \times 10^7$ A if the effective height δ is 1/4 R_{Io} (i.e., ~450 km). If, however, the effective local electric field for the current is smaller than the above adopted nominal maximum electric field values by a factor of 2 and the effective height δ is larger by a factor of 2 (i.e., 1/2 R_{Io}), then the total pickup current would be reduced to $\sim 4.9 \times 10^6$ A, which is still substantial and is closer to the total current of 5.6×10^6 A obtained from doubling the south branch of the Alfvén current of 2.8×10^6 A acquired by Voyager measurements [*Acuña et al.*, 1981]. It should be noted that the value of the pickup current near Io is quite dependent upon the size of the pickup interaction region (i.e., V_{eff}) and the nature of the flow pattern of the plasma past Io. A rough estimate of the effective area A_{eff} can, however, be obtained from an expression for the magnetic field reduction ΔB acquired by using Ampère's law and the pickup current density (12) evaluated with the values in Table 1 to obtain

$$\Delta B \approx 270 \text{ nT} \frac{\xi}{\delta} \frac{4\pi R_{Io}^2}{A_{eff}}, \quad (15)$$

where ξ is the scale length of the curl operator. Assuming that the scale lengths ξ and δ are comparable and setting ΔB to the value of 450 nT estimated earlier from neutral energy rate considerations, the effective area A_{eff} is estimated to be ~60% of $4\pi R_{Io}^2$ for the adopted nominal maximum electric field values and ~30% if the effective local electric field for the current density were smaller by a factor of 2. For these values of A_{eff} the pickup conductivity (11) would then be increased from its minimum value of 2.46 mho to ~4.1 and 8.2 mho, respectively. To address this matter further, a detailed understanding of the structure of Io's local atmosphere and interaction region and a three-dimensional treatment of the plasma flow pattern past Io are required.

If the dominant escaping neutral at Io's exobase is SO_2 rather than atomic oxygen and sulfur, as explored above, the interaction volume V_{eff} will likely be increased, and the concentrated effects of the local charge exchange pickup processes noted above will be somewhat reduced. This will occur since the dominant sink in the plasma torus for SO_2 is dissociation by electron impact (primarily $SO_2 + e \rightarrow SO + O + e$, and secondarily $SO_2 + e \rightarrow S + O_2 + e$), while the production rate of SO_2^+ by either electron impact or charge exchange processes near Io is smaller by more than an order of magnitude. Subsequent ionization and charge exchange for the dissociated products (O, S, SO, O_2) will, of course, occur but will be spatially distributed near Io within a volume element for the interaction region that will be larger relative to the case considered here for direct escape of atomic O and S from the satellite exobase. The volume of the interaction region will be increased even more if the dissociative reactions for SO_2 are moderately exothermic and hence provide additional kinetic energy to the dissociative products. Such an increase in the interaction volume V_{eff}, although difficult to predict, would produce a smaller reduction ΔB in the magnitude of the magnetic field near Io as well as a smaller current I when compared to the values estimated above. The question as to the relative escape rates of atomic and molecular species from Io's exobase is, however, at present an open question. The resolution of this question is expected to be forthcoming in the near future from studies of new ground-based, HST, and Galileo spacecraft observations.

5. Conclusions

The energy escape rate for O and S neutrals produced by the interaction of the magnetospheric plasma with Io's atmosphere has been calculated based on published source rates and source velocity distributions for three different ion neutral collisional processes: (1) incomplete collisional cascade, (2) slow-velocity charge exchange and direct ejection, and (3) fast-velocity charge exchange. The energy escape rates for the three processes, respectively, are 7.5×10^9 W, 3.3×10^{10} W, and 6.04×10^{11} W, with the third process dominating because of its large escape speed. If the incomplete collisional cascade energy escape rate is as expected only ~20% of the total incomplete collisional cascade energy deposition rate in the interaction region, then the additional ~80% or 3.0×10^{10} W would heat the atmosphere and ultimately be lost by downward heat conduction and radiation. The total energy rate or power supplied to the atmosphere by the magnetospheric plasma ion neutral interactions for all three processes is then estimated to be 6.75×10^{11} W.

The two local upstream sources in the magnetospheric corotational plasma for this power are the initial ion kinetic energy and the magnetic field energy. Adopting the corotational speed and a minimum upstream interaction area ($A_{Io} = \pi R_{Io}^2$), the local power of these two sources is 6.66×10^{10} W and 7.88×10^{11} W, respectively. Although the upstream ion kinetic energy source is an order of magnitude too small, the magnetic field source is just able to supply the calculated neutral energy rate for this minimum interaction area. A larger upstream physical interaction area of $2A_{Io} = \pi(1.414 R_{Io})^2$, however, may be more appropriate and corresponds when projected to Io's location to a effective interaction satellite

altitude of 750 km. The total energy supply rate to escaping neutrals is therefore estimated to be a factor of ~5–10 larger than the upstream initial ion kinetic energy flow rate depending upon if the larger or the smaller upstream interaction area is adopted. This large multiple for the upstream initial ion kinetic-energy flow rate implies that ions in the interaction region on average are able to transfer ~5–10 times their original upstream kinetic energy to the neutrals, primarily (~90%) by the fast charge exchange process. This is possible since, upon a collision, the newly created charge exchange ions, which are essentially at rest in the Io frame, are accelerated rapidly (of the order of a gyration period of ~0.5–1 s, a time short compared to their transit time of ~100 s) by the local corotational electric field and the magnetic field to their original corotational and gyration energies.

For the incomplete collisional cascade (i.e., sputtering) process, the neutral energy escape rate of 7.5×10^9 W is, for the minimum upstream interaction area, ~11% of the initial ion kinetic energy flow rate and, when combined with the above estimated additional 3.0×10^{10} W deposited in heating, corresponds to ~56% of upstream initial ion kinetic energy flow rate. This 56% estimate is a factor of 2.8 times larger than the nominal 20% value that has been adopted by *Pospieszalska and Johnson* [1992, 1996], which is based on the minimum upstream interaction area, and implies that the ion neutral interaction near Io is much stronger than estimated earlier from the calculations of *Linker et al.* [1989].

The ion neutral collisional processes that give rise to the large neutral energy escape rate are also capable of driving a significant current in the Io-Jupiter system which consequently produces the necessary reduction in the local magnetic field near Io. Rough estimates given here suggest a pickup current in the range of $\sim 5 \times 10^6$ to 2×10^7 A and a reduction ΔB in the local magnetic planetary field of ~450 nT. These values for the pickup current and the reduction in the magnetic field depend critically on the size of the interaction region near Io which has been estimated here but is not well known. The magnetic field reduction estimated here is, however, similar to the remaining and unexplained ΔB of ~400 nT determined in a recent analysis [*Khurana et al.*, 1997] for the magnetic field depression measured near Io by the Galileo magnetometer [*Kivelson et al.*, 1996a, b] and attributed by them to an internal magnetic dipole field for Io. Hence this unexplained reduction of the planetary magnetic field measured by Galileo near Io may be a direct reflection of the local charge exchange source and need not require an internal magnetic field for the satellite.

Appendix A

In Appendix A, the value of (4d) in the text

$$(\bar{v}_i^2)^{(\text{cascade})} = \int_{\text{upper hem.}} v^2 \phi_i(\mathbf{v})\, d\mathbf{v} \Big/ \int_{\text{upper hem.}} \phi_i(\mathbf{v})\, d\mathbf{v} \qquad \text{(A1)}$$

is calculated using the incomplete collisional cascade flux distribution function $\phi_i(\mathbf{v})$ per neutral deduced from observational data by *Smyth and Combi* [1997] at Io's exobase for atomic sodium. This flux distribution function for atomic sodium is determined by a particular specification of the parameters in the more general functional form for the modified-sputtering flux distribution $\phi(v;\ \alpha,\ v_b,\ v_M)$ given by *Smyth and Combi* [1988, Appendix D] which, when expressed per neutral (where n is the neutral number density), is

$$\phi(v;\ \alpha,\ v_b,\ v_M)/n = \frac{1}{C(\alpha,\ v_M/v_b)} \left(\frac{v}{v_b}\right)^3 \left(\frac{v_b^2}{v^2 + v_b^2}\right)^{\alpha} \cdot \left[1 - \left(\frac{v^2 + v_b^2}{v_M^2}\right)^{1/2}\right]. \qquad \text{(A2)}$$

The modified-sputtering flux distribution depends on three parameters, an exponent α and two velocity parameters v_b and v_M, where $C(\alpha, v_M/v_b)$ is an integration constant. The exponent α primarily determines the dispersion of the distribution, which has a greater high-speed population as α decreases. The exponent α has a value of 3 for a classical sputtering distribution (i.e., a complete collisional cascade process) and a value of 7/3 for a Thomas-Fermi modified-sputtering flux distribution (incomplete collisional cascade). The velocity parameter v_b is related nonlinearly to the most probable speed v_m of the flux speed distribution and primarily determines v_m [see *Smyth and Combi*, 1988, Appendix D]. For atomic sodium, *Smyth and Combi* [1997] determined that $\alpha = 7/3$ and $v_m = 0.5$ km s^{-1}. The velocity parameter v_M limits the maximum speed in the flux distribution function that a neutral can have in an elastic collision with an corotating ion. The velocity parameter v_M is proportional to the ion neutral relative speed v_R, which is taken here to be the ion corotation speed in Io's frame of 56.81 km s^{-1}, and depends on the mass M of the ion and the mass m of the neutral in the binary collision:

$$v_M = \frac{2M}{M + m}\, v_R. \qquad \text{(A3)}$$

For an incomplete collisional cascade case where $\alpha = 7/3$, it can be shown that the shape of the integrand for the v^2 weighted flux distribution function $\phi(v;\ \alpha,\ v_b,\ v_M)$ is somewhat sensitive to the maximum speed v_M and hence that the value of the integral is sensitive to v_M. For atomic oxygen, v_M has a minimum value of $v_R = 56.81$ km s^{-1} assuming an oxygen ion mass (15.9994 AMU) for M and a maximum value of $2v_R/(1 + m_O/m_S) = 1.334\ v_R = 75.80$ km s^{-1} assuming a sulfur ion mass (32.06 AMU) for M. For atomic sulfur, v_M has a minimum value of $2\ v_R/(1 + m_S/m_O) = 0.666\ v_R = 37.83$ km s^{-1} assuming an oxygen ion mass for M and a maximum value of $v_R = 56.81$ km s^{-1} assuming a sulfur ion mass for M. Hence an average ion mass of $M = 24.03$ AMU, based on half the sum of the oxygen mass and sulfur mass, is assumed and yields appropriate middle-range values for v_M of 68.21 km s^{-1} for neutral oxygen and 48.68 km s^{-1} for atomic sulfur, which are adopted here. Using these parameter values and upon substituting (A2) for $\phi_i(\mathbf{v})$ in (A1) and numerically performing the integrations, one obtains $(\bar{v}_O^2)^{(\text{cascade})} = 74.94$ km^2 s^{-2} $= (8.657$ km s$^{-1})^2$ and $(\bar{v}_S^2)^{(\text{cascade})} = 48.31$ km^2 s^{-2} $= (6.951$ km s$^{-1})^2$. These values for O and S are similar in nature, but larger as expected, when compared to $(\bar{v}_{SO_2}^2)^{(\text{cascade})} = 30$–$36$ km^2 s^{-2} for the heavier molecule SO_2 as determined by *Pospieszalska and Johnson* [1996] in their model simulations of a pure, nondissociating SO_2 atmosphere for Io.

Appendix B

In Appendix B, the values of (7a) and (7c) in the text

$$(\bar{v}_i^2)^{(\text{slow CE/DE})} = \int v^3 f^{(\text{slow ion})}(\mathbf{v})\, d\mathbf{v} \Big/ \int v f^{(\text{slow ion})}(\mathbf{v})\, d\mathbf{v} \qquad \text{(B1)}$$

$$(\bar{v}_i^2)^{(\text{fast CE})} = \int v^3 f^{(\text{fast ion})}(\mathbf{v})\, d\mathbf{v} \Big/ \int v f^{(\text{fast ion})}(\mathbf{v})\, d\mathbf{v} \qquad \text{(B2)}$$

are calculated. For both the slower and faster velocity distributions the displaced Maxwell-Boltzmann distribution used by *Smyth and Combi* [1991] to fit the large spatial distribution of sodium in the zenocorona (or magneto-nebula) is adopted. The displaced Maxwell-Boltzmann velocity distribution function $f_{\text{MB}}(\mathbf{v})$, normalized to unity in velocity space, is given by

$$f_{\text{MB}}(\mathbf{v}) = \frac{1}{\pi^{3/2} v_T^3} \exp\left[-(\mathbf{v} - \mathbf{v}_0)^2 / v_T^2\right], \qquad \text{(B3)}$$

where v_T is the most probable speed (e.g., the thermal ion gyration velocity prior to a charge exchange collision) of the velocity distribution and $\mathbf{v}_0$ is the directed velocity (e.g., the corotational velocity of the slow or fast ions prior to a charge exchange collision) in Io's reference frame. *Smyth and Combi* [1991] determined for the slow CE/DE processes that the directed velocity was $|\mathbf{v}_0| = 20$ km s^{-1} and the dispersion velocity was $v_T = 12.44$ km s^{-1} while for the fast CE processes that the directed velocity was $|\mathbf{v}_0| = 56.81$ km s^{-1} (the full corotational speed) and the dispersion velocity was $v_T = 25$ km s^{-1}. The dispersion velocity v_T is approximately one third of directed velocity in a Jupiter inertial frame (e.g., 1/3 of (20 + 17.33) km s^{-1} for the slow CE/DE case, where 17.33 km s^{-1} is Io orbital speed). Using these appropriate parameter values in (B3) and upon substituting (B3) for $f^{(\text{slow ion})}$ and $f^{(\text{fast ion})}$ in (B1) and (B2), respectively, and numerically performing the integrations, one obtains $(\bar{v}_i^2)^{(\text{slow CE/DE})} = (27.6 \text{ km s}^{-1})^2$ and $(\bar{v}_i^2)^{(\text{fast CE})} = (68.8 \text{ km s}^{-1})^2$.

Acknowledgments. The author thanks M. L. Marconi for helpful discussion and R. C. Woodward for numerical computations. Support for this research was provided by the National Aeronautical and Space Administration through contract 959538 from the Galileo Spacecraft Mission and through contracts NASW-4804 and NASW-96020 from the Planetary Atmospheres Program.

The Editor thanks Vytenis M. Vasyliunas and Peter L. Israelevich for their assistance in evaluating this paper.

References

Acuña, M. H., F. M. Neubauer, and N. F. Ness, Standing Alfvén wave current system at Io: Voyager 1 observations, *J. Geophys. Res.*, *86*, 8513–8521, 1981.

Brown, R. A., The Jupiter hot plasma torus: Observed electron temperature and energy flow, *Astrophys. J.*, *244*, 1072–1080, 1981.

Eviatar, A., and G. L. Siscoe, Limit on rotational energy available to excite Jovian aurora, *Geophys. Res. Lett.*, *7*, 1085–1088, 1980.

Flynn, B., M. Mendillo, and J. Baumgardner, Observations and modeling of the Jovian remote neutral sodium emission, *Icarus*, *99*, 115–130, 1992.

Frank, L. A., W. R. Patterson, K. L. Ackerson, V. M. Vasyliunas, F. V. Coroniti, and S. J. Bolton, Plasma observations at Io with the Galileo spacecraft, *Science*, *274*, 394–395, 1996.

Goertz, C. K., Io's interaction with the plasma torus, *J. Geophys. Res.*, *85*, 2949–2956, 1980.

Ip, W.-H., and W. I. Axford, A weak interaction model for Io and the Jovian magnetosphere, *Nature*, *283*, 180–183, 1980.

Kivelson, M. G., K. K. Khurana, R. J. Walker, C. T. Russell, J. A. Linker, D. J. Southwood, and C. Polanskey, A magnetic signature at Io: Initial report from the Galileo magnetometer, *Science*, *273*, 337–340, 1996a.

Kivelson, M. G., K. K. Khurana, R. J. Walker, J. Warnecke, C. T. Russell, J. A. Linker, D. J. Southwood, and C. Polanskey, Io's interaction with the plasma torus: Galileo magnetometer report, *Science*, *274*, 396–398, 1996b.

Khurana, K. K., M. G. Kivelson, and C. T. Russell, Interaction of Io with its torus: Does Io have an internal magnetic field?, *Geophys. Res. Lett.*, *24*, 2391–2394, 1997.

Linker, J. A., M. G. Kivelson, and R. J. Walker, The effect of mass loading on the temperature of a flowing plasma, *Geophys. Res. Lett.*, *7*, 763–766, 1989.

Marconi, M. L., and W. H. Smyth, Io plasma torus: Nature of the Iogenic plasma source (abstract), *Bull. Am. Astron. Soc.*, *28*, 1154–1155, 1996.

Marconi, M. L., L. Dagum, and W. H. Smyth, Hybrid fluid/kinetic approach to planetary atmospheres: An example of an immediate mass body, *Astrophys. J.*, *496*, 393–401, 1996.

Mendillo, M., J. Baumgardner, B. Flynn, and W. J. Hughes, The extended sodium nebula of Jupiter, *Nature*, *348*, 312–314, 1990.

Pospieszalska, M. K., and R. E. Johnson, Plasma heating of Io's atmosphere, *Geophys. Res. Lett.*, *19*, 949–952, 1992.

Pospieszalska, M. K., and R. E. Johnson, Monte Carlo calculations of plasma ion-induced sputtering of an atmosphere: SO_2 ejected from Io, *J. Geophys. Res.*, *101*, 7565–7573, 1996.

Scherb, F., and W. H. Smyth, Variability of [O I] 6300-Å emission near Io, *J. Geophys. Res.*, *98*, 18729–18736, 1993.

Smyth, W. H., Neutral cloud distribution in the Jovian system, *Adv. Space Res.*, *12*(8), 337–346, 1992.

Smyth, W. H., and M. R. Combi, A general model for Io's neutral gas cloud, II, Application to the sodium cloud, *Astrophys. J.*, *328*, 888–918, 1988.

Smyth, W. H., and M. R. Combi, The sodium zenocorona, *J. Geophys. Res.*, *96*, 22711–22727, 1991.

Smyth, W. H., and M. R. Combi, Io's sodium exosphere and spatially extended cloud: A consistent flux speed distribution, *Icarus*, *126*, 58–77, 1997.

Smyth, W. H., and M. L. Marconi, An initial look at the Iogenic SO_2^+ source during the Galileo flyby of Io, *J. Geophys. Res.*, in press, 1998.

W. H. Smyth, Atmospheric and Environmental Research, Inc., 840 Memorial Drive, Cambridge, MA 02139.

(Received June 11, 1997; revised January 26, 1998;
accepted December 29, 1997.)

Appendix D

Far Ultraviolet Imaging Spectroscopy of Io's with HST/STIS

Far-Ultraviolet Imaging Spectroscopy of Io's Atmosphere with HST/STIS

F. L. Roesler, H. W. Moos, R. J. Oliversen, R. C. Woodward Jr.,* K. D. Retherford, F. Scherb, M. A. McGrath, W. H. Smyth, P. D. Feldman, D. F. Strobel

Well-resolved far-ultraviolet spectroscopic images of O I, S I, and previously undetected H I Lyman-α emission from Io were obtained with the Hubble space telescope imaging spectrograph (STIS). Detected O I and S I lines (1250 to 1500 angstroms) have bright equatorial spots (up to 2.5 kilorayleighs) that shift position with jovian magnetic field orientation; limb glow that is brighter on the hemisphere facing the jovian magnetic equator; and faint diffuse emission extending to ~20 Io radii. All O I and S I features brightened by ~50 percent in the last two images, concurrently with a ground-based observation of increased iogenic [O I] 6300-angstrom emission. The H I Lyman-α emission, consisting of a small, ~2-kilorayleigh patch near each pole, has a different morphology and time variation.

Jupiter's strong magnetic field and volcanism on Io, the closest of the Galilean satellites, combine to create dynamic physical features in the jovian system, including the Io plasma torus: a plasma predominately of O and S surrounding and corotating with Jupiter near Io's orbit. Detailed and accurate information on Io's extended atmosphere and neutral clouds is vital for understanding the satellite's interaction with the plasma torus and the jovian magnetosphere, but observations of these neutral gases—including the atomic O and S that feed the torus—have proven challenging. Near Io, visible-light observations must contend with the reflected solar continuum (*1*) or be taken during an eclipse of Io (*2*). More than a few Io radii (R_{Io}) from Io the visible emission lines, with the important exceptions of the minor components Na I and K I, are faint. Several researchers have observed Io and its environs in the bright ultraviolet (UV) emission lines of O I and S I (*3*–*7*); none of the available UV instruments, however, had sufficient resolution to study the spatial structure of these emissions in detail until the STIS (*8*, *9*) was installed on the Hubble space telescope (HST) in February 1997. We report here observations of Io made with the STIS to try to detect features in Io's atmosphere and exosphere related to its interaction with the jovian magnetosphere and plasma torus.

Observations. The observations consist of two "visits" of Io of three orbits each on 26 September and 14 October 1997 near western (receding) elongation. ("Orbit" refers to an HST orbit in this work, unless otherwise specified.) During each orbit, two spectrally resolved images were acquired in "time-tag" mode (*10*), yielding, after processing with the standard STIS "pipeline" software (*11*), 12 1024 pixel by 1024 pixel images. We used a 52 arc sec by 2 arc sec slit: wide enough to include the disk of Io (1.15 arc sec or 37 pixels in September, and 1.10 arc sec or 45 pixels in October) and its immediate surroundings in the direction of dispersion, and long enough to capture features 15 to 20 R_{Io} away in the spatial direction (*12*). The data therefore show distinct images of Io at each emission line or multiplet, with a separation distance determined by the grating's dispersion. To balance wavelength coverage and spectral resolution, we used three different gratings (*8*) during the experiment: the medium-resolution G230M (*13*) and G140M gratings in September, tilted to observe the S I] λ1900 (wavelength 1900 Å semiforbidden neutral S) multiplet and the O I] λ1356 and S I λ1389 multiplets, respectively; and the low-resolution G140L grating in October, to observe several O I and S I multiplets simultaneously (at the expense of blending multiplet components). The observational parameters are listed in Table 1. The distinct images of Io in different emission wavelengths give the raw data the appearance of a multiple exposure (Fig. 1). The Io plasma torus emission, terrestrial airglow, and instrumental artifacts are also present in the images.

Oxygen and sulfur. The medium-resolution observations 3a and 3b (Table 1) in September detected the O I] λ1356 and S I λ1389

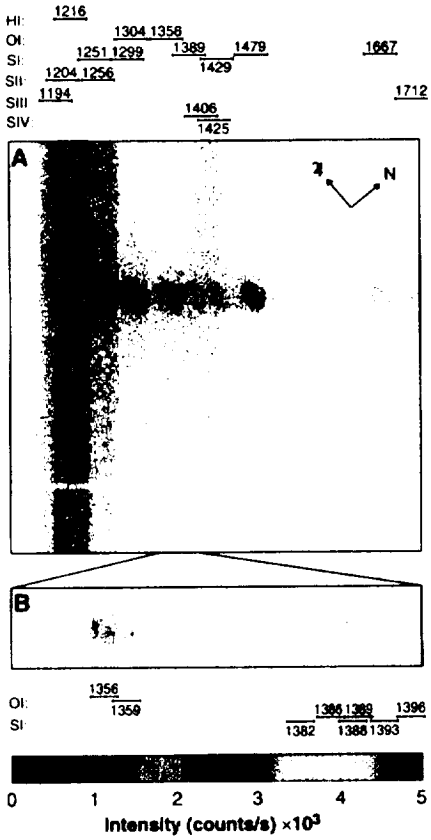

Fig. 1. (**A**) Sum of raw data from the second images of orbits 4 to 6: 1024 pixels by 1024 pixels 0.0244 arc sec squared spatially, with 0.584 Å/pixel dispersion convolved with the spatial information horizontally. The circular features in a row just above mid-image are images of iogenic emission at various O I and S I multiplets; faint, diffuse emission extends above and below the brighter circular features. The vertical green bar is an image of the 52–arc sec by 2–arc sec slit filled with diffuse terrestrial H I Lyman-α emission. Two patches of iogenic H I Lyman-α emission can be seen in the midst of this terrestrial airglow. Also present are several plasma torus lines (vertical bars brighter at the top than the bottom) and the shadow of a 0.5–arc sec fiducial bar in the slit (horizontal band near the bottom). The key above shows the slit positions for various emission wavelengths. The compass shows the directions of Jupiter (east) and jovian north. (**B**) Band from sum of raw data from both images of orbit 3: 1024 pixels by 200 pixels encompassing Io and vicinity. The slit is the same as in (A), but the spatial scale is slightly different (0.031 arc sec/pixel by 0.029 arc sec/pixel), and the spectral resolution is 0.053 Å/pixel. The multiplet components of O I] λ1356 and S I λ1389, as indicated in the key below, are evident; not shown is faint extended emission similar to that in (A). Connecting lines show where the spectral range of (B) maps to (A) at mid-slit.

F. L. Roesler, R. C. Woodward Jr., and F. Scherb are in the Physics Department, University of Wisconsin, 1150 University Avenue, Madison, WI 53706, USA. H. W. Moos, K. D. Retherford, and P. D. Feldman are in the Department of Physics and Astronomy, Johns Hopkins University, Baltimore, MD 21218, USA. R. J. Oliversen is in the Laboratory for Astronomy and Solar Physics, NASA–Goddard Space Flight Center, Greenbelt, MD 20771, USA. M. A. McGrath is at the Space Telescope Science Institute, Baltimore, MD 21218, USA. W. H. Smyth is with Atmospheric and Environmental Research, Cambridge, MA 02139, USA. D. F. Strobel is in the Department of Earth and Planetary Science, Johns Hopkins University, Baltimore, MD 21218, USA.

*To whom correspondence should be addressed.

multiplets; fluxes were calculated for the brighter components of these multiplets (Table 2). The low-resolution observations in October detected O I] λ1356, S I λλ1389, 1429, 1479, 1667, and a blend of O I λ1304 and S I λ1299 (*14*); fluxes were calculated for the brighter of these multiplets (Table 3). These fluxes are consistent with earlier work (*3*, *5*). Morphologically, each image of each line or multiplet is similar: two bright spots above Io's limb near its equator (which we call "equatorial spots"); diskwide emission enhanced along the limb at all Iocentric latitudes ("limb glow"); and fainter emission more than 1 R_{Io} beyond Io's disk, dropping rapidly in intensity with distance from Io ("extended emission"). The extended emission can be seen in Fig. 1, most notably in the O I] λ1356 and S I] λ1479 multiplets; the near-Io emission at selected times and wavelengths is shown in detail in Fig. 2.

Equatorial spots. Enhanced emissions near Io's equator were seen in broadband visible and near-infrared (NIR) images from Galileo's solid state imaging (SSI) experiment (*15*) and [O I] λ6300 images from the HST wide-field planetary camera (WFPC2) (*2*), and inferred from rastered sets of scans of iogenic UV emission from the HST's faint object spectrograph (FOS) (*4*, *16*) and Goddard high-resolution spectrograph (GHRS) (*4*, *17*), but the STIS data show equatorial spots of UV O I and S I emissions in unprecedented detail. The spots are brightest [up to 2.5 kilorayleighs (*18*)] at ~ 200 km above Io's surface and extend several hundred kilometers above that height. At Io's central meridian, emission intensities near the equator are less than or equal to those at higher and lower latitudes; therefore, these equatorial spots on Io's limb are unlikely to be a viewing-geometrcal enhancement of an equatorial ring of emission. The sub- and anti-jovian positions of the spots suggest that they are associated with the Birkeland currents that flow through Io or its ionosphere (*19*). The western, anti-jovian spot has a consistently greater flux and is usually brighter than the eastern, sub-jovian spot. [Viewing geometry may be partially responsible for the observed asymmetry in the first and second HST orbits (Fig. 2, A and C), but not the third (Fig. 2, B and D), of each visit.] This flux asymmetry could be a consequence of asymmetry in the directions of the electron and ion convection patterns as a result of anisotropic ionospheric Hall conductivity (*20*), of a greater abundance of gases from local volcanos, or of a higher SO_2 column density that is expected on the more recently sunlit hemisphere of Io. Observations at eastern elongation could distinguish the last possibility from the first two. Additionally, the spots change Iocentric latitude as Io's jovian magnetic latitude changes (Fig. 2, A to D). This is consistent with an association of the spots with the Birkeland currents; the tangent points of the magnetic field lines at Io would, as a result of the motion of the tilted jovian magnetic field past Io, rotate or rock about Io's equator (Fig. 3). The spots tilt in the same sense as the dipole tangent points, but not always by the same amount. This is not surprising, because the magnetic field near Io is known to be distorted by Birkeland currents, nearby plasma currents, and possibly an intrinsic Ionian field (*21*). In contrast, visible and NIR Galileo SSI images taken over 14 eclipses of Io show sub- and anti-jovian glows that do not change position with magnetic latitude (*22*), but appear to be fixed near known centers of volcanic activity and a newly discovered subjovian field of vents (*23*). Because the SSI filters have broad passbands, however, it is not clear what causes these glows. One way to reconcile our results with those of Galileo is to postulate that Io's volcanos produce relatively immobile local concentrations of gases that are imaged by SSI, and that Birkeland currents excite (and perhaps produce) atomic O and S at varying positions within these gas concentrations.

Limb glow and extended emission. The less intense limb glow lies on or barely above (≤100 km) Io's limb. It is presumably a limb brightening of an all-disk glow and may indicate the presence of a global or hemispherical atmosphere containing S and O. Comparison of orbit 3, when Io was north of the centrifugal equator (*24*) (Fig. 2B), and orbits 4 to 6, when it was south (Fig. 2, C and D), show that the limb glow is consistently brighter on the side facing the equator (Table 1). Similar results have been found in images of [O I] λ6300 emission (*2*). Because Io's diameter (3630 km) is small compared with the latitudinal scale height of the Io plasma torus (~10^5 km), and the bulk torus electron density changes less than 0.1% across Io (*25*), we would not expect this asymmetry in the limb glow to be related to the torus. However, modeling (*20*) and observations by Galileo (*26*, *27*) indicate that plasma near Io slows to 1 to 2 km/s; therefore, >97% of the total electrons in a flux tube could potentially reach Io's atmosphere while the flux tube intersects Io. The greater electron column density above the hemisphere facing the centrifugal equator could thus be responsible for the enhanced emission.

Spatially extended emission in O I λλ1304, 1356, and S I λ1479 is detectable along the slit out to ~20 R_{Io}; it can be seen directly in the raw data (Fig. 1) as faint vertical bands tapering off away from Io and is plotted (for S I λ1479, orbits 4 to 6) in Fig. 4. It drops off approximately as $1/r$ (r is the distance along the slit from the center of Io's disk in the image), the expected behavior for a simple spherically symmetric outflow of gas.

Intensity variations with time. During orbit 6, the O I and S I emission features increased in intensity by a factor of ~1.5 when compared with the previous two orbits that night (Table 3), as well as when compared with the final orbit on 26 September (Table 2). This bright-

Table 1. Instrumental and Iocentric parameters. Io's rotational period is tidally locked to its orbital period, with 0° longitude defined as the average longitude of the sub-jovian spot; thus, Io's central meridian longitude (CML) is equivalent to its orbital phase, with 0° occurring when Io is farthest from the observer. System III is the jovian magnetic longitude system. z_c is the distance of Io north (N) or south (S) of the centrifugal equator (*24*), calculated for an offset tilted dipole magnetic field, in units of the jovian equatorial radius (71,400 km).

Orbit no.*	Starting time (UT)	Integration time (s)	Io system III longitude (°)	Io CML (°)	z_c (R_J)
		26 September 1997 (data set O49D02)†			
1a	10:29	900	79–86	242–244	0.36–0.29 S
1b	10:48		87–94	245–247	0.28–0.20 S
2a	11:51	1180	117–126	253–256	0.05–0.16 N
2b	12:18		129–138	257–260	0.19–0.29 N
3a	13:34	1100	164–173	268–271	0.53–0.58 N
3b	13:56		175–183	271–274	0.59–0.63 N
		14 October 1997 (data set O49D01)‡			
4a	2:45	920	349–356	240–242	0.55–0.59 S
4b	3:04		357–4	243–245	0.59–0.62 S
5a	4:07	1180	27–36	252–254	0.65–0.63 S
5b	4:34		39–48	255–258	0.62–0.58 S
6a	5:44		71–80	265–268	0.41–0.32 S
6b	6:11		84–93	269–272	0.29–0.19 S

*Orbits 1 and 2: wavelength range 1888 to 1978 Å, dispersion 0.087 Å/pixel; orbit 3, 1344 to 1398 Å, 0.053 Å/pixel; orbits 4 to 6, 1150 to 1730 Å, 0.584 Å/pixel. †Pixel size: 0.031 arc sec (dispersion direction) by 0.029 arc sec, or 96 km by 91 km at Io. ‡Pixel size: 0.024 arc sec squared, or 81 km squared at Io.

Table 2. Fluxes of O and S lines observed during orbit 3 (26 September), integrated over a 2 arc sec by 4 arc sec box centered on Io.

Species	Wavelength (Å)	Flux (10^3 photons cm^{-2} s^{-1})
O I	1355.60	1.46 ± 0.15
	1358.52	0.45 ± 0.15
S I	1388.43	0.39 ± 0.17
	1396.11	0.28 ± 0.16

ening (Fig. 5) occurred in all O and S multiplets and in all morphological features of each multiplet image (compare Fig. 2D with Fig. 2, B and C). We obtained simultaneous spectra of [O I] λ6300 emission from Io at Kitt Peak before, during, and after the October orbits (*28*). These data show that iogenic [O I] λ6300 emission increased in intensity simultaneously with the UV multiplets, but by a factor of about 3.5 (Fig. 5), and therefore that the ratios of the UV multiplets to the visible line decrease by about 60%. Our earlier [O I] λ6300 data (*7*) indicate that such large increases in intensity are uncommon, but not unprecedented. Although this brightening coincides with Io's approach to the centrifugal equator, the ground-based data show a sharp drop in emission intensity shortly after the end of the final orbit—just as Io crosses the centrifugal equator, where electron density is expected to be highest. Moreover, the [O I] λ6300 (*29*) and UV emissions (*17*) have exhibited frequent, more modest fluctuations in intensity, on the scale of 15 min or less. The simultaneous brightening of all spatial features of O and S in the STIS images seems inconsistent with sudden outbursts of gas from volcanic vents or other neutral cloud inhomogeneities as explanations. We suggest that large-scale local variations in plasma properties might be responsible; an increase in electron density and decrease in temperature, for example, would be consistent both with the increase in the absolute intensities of the UV and visible emissions and with the decrease in their ratio.

Lyman-α. The most surprising result is the unexpected observation of H I Lyman-α emission near the poles of Io. Lyman-α near Io was initially reported in Pioneer 10 UV photometer data (*30*), but was later discarded after the identification of bright O and S lines within the photometer's passband of 200 to 1400 Å (*31*). In earlier UV spectra of Io, acquired from Earth orbit with the HST-FOS (*5*), HST-GHRS (*4*), Hopkins ultraviolet telescope (HUT) (*6*), and international ultraviolet explorer (IUE) (*3*), the strong terrestrial H I Lyman-α airglow obscured any emission from Io that might have been present, but the imaging capability of the STIS makes it straightforward to distinguish the spatially uniform terrestrial emission from localized iogenic H I Lyman-α (*32*). However, H and H-bearing molecules are not thought to be present on Io's surface or in its atmosphere in significant quantities (*33*); we were therefore surprised to find two H I Lyman-α emission features, with $\sim 3 \times 10^{-4}$ photons cm^{-2} s^{-1} total flux and ~2 kilorayleighs peak intensity, in our data (*34*).

The H I Lyman-α emission (Figs. 2E and 6) differs from the O I and S I emissions we observed. Most of it is concentrated in two bright patches near Io's poles rather than near the equator. Although the patches are reminiscent of terrestrial auroras, they are on the opposite sides of the rotational poles from the presumed entry points of the jovian magnetic field lines. There is no overall disk or limb glow, but the photon noise from the terrestrial airglow would prevent the detection of any features much fainter than a kilorayleigh. Also, unlike emission from the heavier neutrals, the H I Lyman-α patches lie almost entirely within Io's disk, suggesting a source on or near Io's surface. The larger and brighter patch is in the southern hemisphere, the hemisphere away from the centrifugal equator. Finally, during the simultaneous brightening of the O I and S I UV multiplets and the [O I] λ6300 emission seen from the ground, neither patch of H I Lyman-α showed significant brightening (Fig. 5).

It is far from obvious how such emission could arise. Iogenic H may be present in polar caps of H-bearing frost. There is some infrared evidence for surface H_2S (a common volcanic gas on Earth) in the polar regions of Io (*35*, *36*), but the high vapor pressure of H_2S implies a polar temperature at the low end of the expected range (*37*). H_2O has a much lower vapor pres-

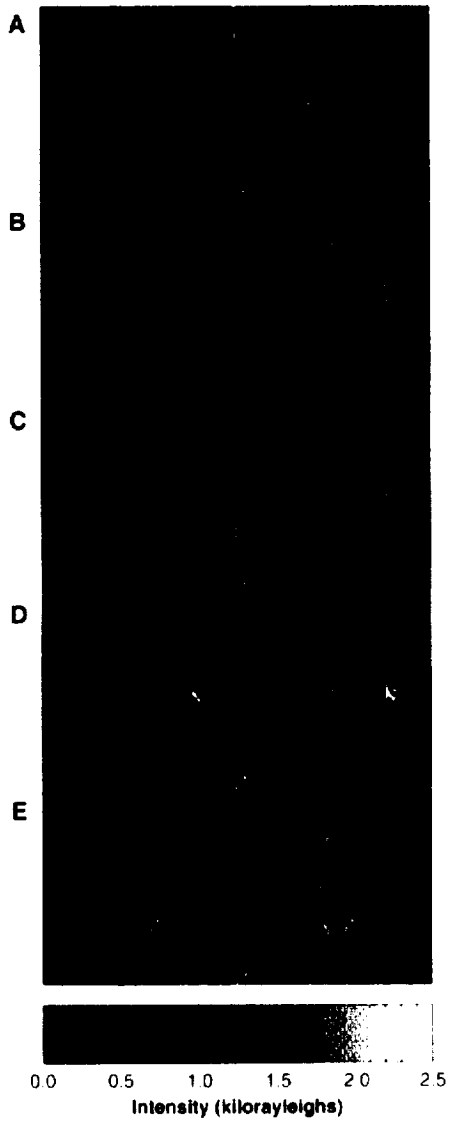

Fig. 2. Details of various emission features near Io. (**A**) S I] λ1900, orbit 1, λ_{III} = 87°; (**B**) O I] λ1356, orbit 3, λ_{III} = 174°; (**C**) O I] λ1356, orbit 4, λ_{III} = 357°; (**D**) O I] λ1356, orbit 6, λ_{III} = 82°; (**E**) H I Lyman-α, orbits 4 to 6. The images have been calibrated and rotated so that Ionian north is up and Jupiter is to the left. The two images from the appropriate orbit have been averaged in rows A to D, and the three images from the second half of each of orbits 4 to 6 have been averaged in row E (to reduce airglow contamination). Each box in the first column is a 2 arc sec by 2 arc sec subimage (65 pixels by 68 pixels for rows A and B; 81 pixels by 81 pixels for rows C to E) centered on Io at a particular wavelength. The second column duplicates the first, with the following features of Io marked: limb (circle), equator (horizontal line), poles (vertical lines), lines of longitude at 180° (dashed half-ellipse) and 270° (solid half-ellipse), and direction of local magnetic field (arrow). (The circles are slightly elliptical in rows A and B to account for the difference in plate scales along and across the direction of dispersion. Because of difficulties in precisely locating Io on the MAMA, we estimate that the positions, but not the scales or orientations, of these diagrams may be off by as much as two pixels.) Note in particular that (i) a line connecting the bright spots is nearly perpendicular to the magnetic field for all O and S images (A to D), but not H (E); (ii) O I] λ1356 is significantly brighter during orbit 6 (D) than orbits 3 and 4 (B and C); (iii) Io's southern limb is brighter than its northern during orbit 3 (B), but its northern limb is brighter during orbits 4 and 6 (C and D); and (iv) the bulk of the O and S emission is on or above the limb (A to D), whereas the H emission is almost entirely within the limb.

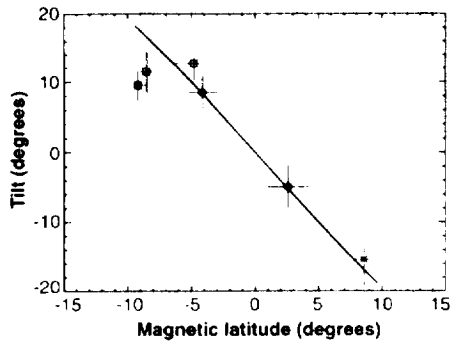

Fig. 3. Plot of tilt (with respect to Ionian equator) of lines connecting centroids of Io's "equatorial spots," in one bright line per orbit, as a function of Io's jovian magnetic latitude at mid-orbit. (●, S I λ1900, orbits 1 and 2; ·, O I] λ1356, orbit 3; ▯, O I] λ1356, orbits 4 to 6.) Vertical error bars are uncertainties in tilts; horizontal bars are the ranges of jovian magnetic latitudes through which Io passed during the orbit. The solid line is the tilt of the local jovian magnetic field (calculated from an offset tilted dipole model with no plasma currents) with respect to Io's south pole, in the plane containing Io and Jupiter.

sure, and evidence for its presence on Io is slightly better (*38*). Alternatively, protons might travel along the magnetic field lines from Jupiter and be preferentially deposited near Io's poles, where the magnetic flux through the surface is greatest, aided perhaps by a thinner polar atmosphere or "funneling" by an intrinsic Ionian magnetic field. This H could be sputtered from the surface or dissociated from sublimated H_2S by the intense, field-aligned, energetic electron beams detected in Io's plasma wake by Galileo (*39*), or some other particle source; it could radiate by resonant scattering of solar H I Lyman-α or by recombination after ionization by the same particles.

Another possible source of this emission is simple reflection of the bright solar H I Lyman-α radiation from the surface of Io, which does not require iogenic H at all. This would require only a 5% geometric albedo at Io's poles; it is consistent with the lack of variation of the H I Lyman-α emission with time, and with the all-disk component of the emission (Fig. 6A). It is more difficult to explain the polar emission enhancement under this hypothesis. One possibility is that a patchy frost or other substance in Io's polar region has a higher albedo at 1216 Å than the equatorial surface. Io is known to have an unidentified surface component near its poles (*40*), but its albedo at 1216 Å is unknown and would have to be significantly different from that at higher wavelengths, where a polar enhancement is not seen (Fig. 6B). Another possibility is that SO_2, a strong absorber of H I Lyman-α [cross section $\sigma = 3.9 \times 10^{-17}$ cm^2 (*41*)], has a higher column density near Io's equator and therefore blocks reflection of H I Lyman-α in that region, making the poles appear bright by contrast. Io's SO_2 atmosphere is still poorly known, however. It may be azimuthally symmetric about the subsolar point (*42*); this would produce a ring of H I Lyman-α emission in our images, just within the limb. It may be patchy, with column densities large enough to block H I Lyman-α ($\sim 2.5 \times 10^{16}$ cm^{-2}) occurring only near active volcanic vents; this would produce a disk of H I Lyman-α emission with dark blotches in our images. This hypothesis also leaves unexplained the recent evidence of iogenic H II from the Galileo PWS (*43*) and PLS (*44*) experiments. Nonetheless, simple diffuse reflection probably contributes to, and might fully explain, the H I Lyman-α emission in our data.

Because either possibility—iogenic H or selective diffuse reflection from Io's poles—has important consequences for our understanding of Io's surface and atmosphere, it is important to determine the extent to which each is responsible for Io's H I Lyman-α emission, and in particular for the polar patches. Possible STIS observations that

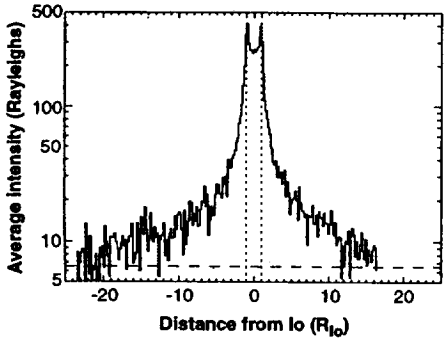

Fig. 4. Spatial profile of S I λ1479 emission from orbits 4 to 6. The six images were combined and binned 4 by 4 to reduce noise; they were then averaged across the combined slit widths of the S I λ1479 multiplet and are plotted here along the slit length. The horizontal dashed line marks the average background, as determined from the shadow of the slit's fiducial bar (the dip at ~ -21 R_{Io}); the vertical dotted lines mark Io's position. Plots of the other S and O lines are similar.

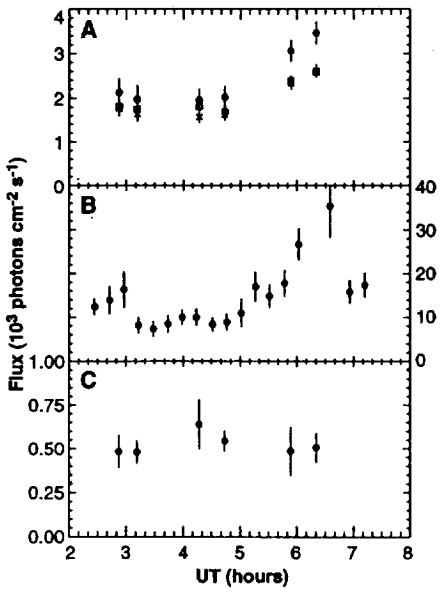

Fig. 5. H I, O I, and S I iogenic emission fluxes versus time for orbits 4 to 6 (14 October 1997). (**A**) S I λ1479 (●), O I] λ1356 (×), and O I λ1304 and S I λ1299 combined (□) STIS fluxes integrated over 2 arc sec by 4 arc sec boxes centered on Io at the appropriate wavelengths. (**B**) [O I] λ6300 fluxes from ground-based spectra acquired through a 5.2 arc sec by 5.2 arc sec squared aperture centered on Io. (**C**) H I Lyman-α STIS fluxes integrated over small boxes enclosing the emission features only (to reduce airglow contamination).

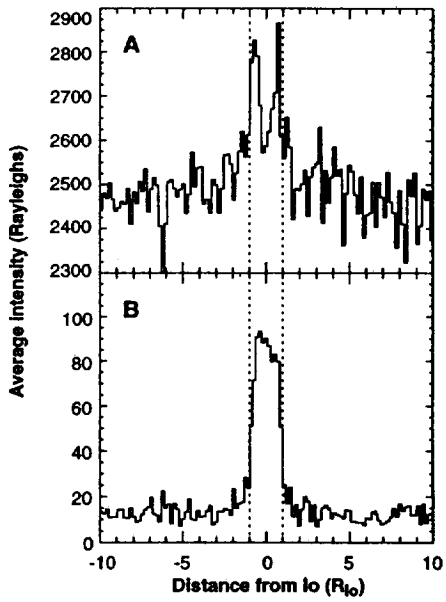

Fig. 6. (**A**) Spatial profile of H I Lyman-α emission from orbits 4 to 6. To reduce airglow noise, we used only the second image from each orbit. The three images were combined, binned 4 by 4, and averaged across a reduced slit width of 1.37 arc sec (1.25 R_{Io}), centered on Io at 1215.6 Å. The vertical dotted lines mark the edges of Io's disk. In addition to the two sharp peaks, corresponding to the patches seen in Figs. 1 and 2, there is an intensity enhancement over the entire disk. The dip at ~ -6 R_{Io} is the shadow of the far-UV MAMA repeller wire. (**B**) Spatial profile of reflected solar continuum from orbits 4 to 6. The six images were combined, binned 4 by 4, and averaged over 1512 to 1642 Å, a spectral range free of known emission lines.

Table 3. Fluxes of O and S multiplets observed during orbits 4 to 6 (14 October), integrated over a 2 arc sec by 4 arc sec box centered on Io (*34*).

Species	Wavelength (Å)	Flux (10^{-3} photons cm^{-2} s^{-1})		
		Orbit 4	Orbit 5	Orbit 6
H I	1216	0.48 ± 0.06*	0.59 ± 0.08*	0.50 ± 0.08*
		0.41 ± 0.07†	0.64 ± 0.09†	0.32 ± 0.09†
O I + S I	1300	1.78 ± 0.11	1.75 ± 0.09	2.49 ± 0.09
O I	1356	1.70 ± 0.13	1.60 ± 0.10	2.48 ± 0.10
S I	1389	1.13 ± 0.15	1.27 ± 0.11	1.91 ± 0.11
	1429	0.88 ± 0.17	1.03 ± 0.14	1.44 ± 0.14
	1479	2.04 ± 0.22	1.99 ± 0.17	3.26 ± 0.17

*H I fluxes are from the two bright polar patches, with an off-Io background subtracted by the average of three different methods: subtraction of a simple average of boxes directly above and below the emission, subtraction of a linear fit to the background emission, and smoothing of the image followed by subtraction of a linear background fit. The three methods gave comparable results. †H I fluxes are from the two bright polar patches, subtracting a background found by averaging an equatorial band 0.5R_{Io} wide on Io (Fig. 6).

would help make this determination are observations over a greater range of magnetic latitudes, to look for changes suggesting a connection with magnetospheric processes; at both east and west elongations, to see if the patches are fixed on Io's surface; during eclipse, to verify that solar H I Lyman-α (whether by diffuse reflection or resonant scattering) is responsible for the emission; and at high spectral resolution, to determine whether the emission from Io has the distinctive solar lineshape and to separate the Ionian emission from terrestrial airglow with a suitable velocity difference.

References and Notes

1. F. Scherb and W. H. Smyth, *J. Geophys. Res.* **98**, 18729 (1993).
2. J. T. Trauger, K. R. Stapelfeldt, G. E. Ballester, J. T. Clarke, WFPC2 Science Team, *Bull. Am. Astron. Soc.* **29**, 1002 (1997).
3. G. E. Ballester *et al.*, *Astrophys. J.* **319**, L33 (1987).
4. G. E. Ballester *et al.*, *Bull. Am. Astron. Soc.* **29**, 980 (1997).
5. J. T. Clarke, J. Ajello, J. Luhmann, N. M. Schneider, I. Kanik, *J. Geophys. Res.* **99**, 8387 (1994).
6. S. T. Durrance *et al.*, *Astrophys. J.* **447**, 408 (1995).
7. G. K. Fox *et al.*, *Astronom. J.* **113**, 1158 (1997); B. R. Sandel and A. L. Broadfoot, *J. Geophys. Res.* **87**, 212 (1982); J. R. Spencer and N. M. Schneider, *Annu. Rev. Earth Planet. Sci.* **24**, 125 (1996).
8. B. E. Woodgate *et al.*, *Proc. Astron. Soc. Pacific* **110**, 1183 (October 1998).
9. R. A. Kimble *et al.*, *Astrophys. J.* **492**, L83 (1998).
10. In time-tag mode, each photon's arrival time and position in the STIS multi-anode microchannel array (MAMA) are recorded individually.
11. M. Voit, Ed., *HST Data Handbook* (Space Telescope Science Institute, Baltimore, ed. 3.0, 1997).
12. The slit was effectively reduced to 30 arc sec by 2 arc sec (September) and 25 arc sec by 2 arc sec (October) by the finite size of the MAMA detectors.
13. The STIS is equipped with two MAMAs, which have different photocathodes sensitive to different wavelength ranges (*8*). Unfortunately, the NUV MAMA (covering 1650 to 3100 Å) was found after launch to have a dark rate exceeding design specification by about an order of magnitude, as a result of excessive phosphoresence in its MgF_2 window (*9*). Consequently, our G230M data (orbits 1 and 2) are noisy, and only the brightest features can be distinguished; these data are largely excluded from this paper.
14. It is unclear whether the near-Io emission at ~1250 Å is predominately S I λ1251 or S II λ1256.
15. A. S. McEwen *et al.*, *Geophys. Res. Lett.* **24**, 2443 (1997).
16. T. E. Smith, M. A. McGrath, P. Sartoretti, *Bull. Am. Astron. Soc.* **27**, 1157 (1995).
17. G. E. Ballester *et al.*, in *Magnetospheres of the Outer Planets* (Boulder, CO, March 1997), unpublished proceedings.
18. One Rayleigh is 10^6 photons 4π sr^{-1} cm^{-2} s^{-1}.
19. Io's electrodynamic interaction with the plasma torus is typical of plasma flowing past an obstacle. In this case it is sub-Alfvénic (v_{plasma} ~ 57 km/s, v_A ~ 300 km/s), with no bowshock forming and standing magnetohydrodynamic Alfvén waves in Io's rest frame. The corotational electric field of 0.114 V/m produces a ~400-kV voltage drop across Io, driving a current of a few million amperes through Io's ionosphere; Alfvén waves carry the current along the essentially equipotential magnetic field lines into Io's inner hemisphere and away from its outer hemisphere. (Electrons, the likely current carriers, would of course flow in the opposite direction.) The current loop can be completed in Jupiter's ionosphere only if the round trip travel time for an Alfvén wave is short compared with the time it takes for torus plasma to sweep past Io; otherwise, the current loop is closed in the plasma torus (*45*).
20. J. Saur, F. M. Neubauer, D. F. Strobel, M. E. Summers, in preparation.
21. M. G. Kivelson *et al.*, *Science*, **273**, 337 (1996); M. G. Kivelson *et al.*, *ibid.* **274**, 396 (1996).
22. P. E. Geissler *et al.*, *Bull. Am. Astron. Soc.* **30**, 1116 (1998).
23. A. S. McEwen *et al.*, *Icarus* **135**, 181 (1998).
24. Jupiter's magnetic equator is tilted 9.6° with respect to its spin equator and Io's orbital plane. Jupiter's centrifugal equator—the locus of points that, of all points on a magnetic field line, are the farthest from Jupiter's spin axis—lies between the magnetic and spin equators. The Io plasma torus is densest at, and approximately symmetric about, the centrifugal equator.
25. R. C. Woodward Jr. and W. H. Smyth, *Bull. Am. Astron. Soc.* **26**, 1139 (1994).
26. L. A. Frank *et al.*, *Science* **274**, 394 (1996).
27. F. Bagenal *et al.*, *Geophys. Res. Lett.* **24**, 2119 (1997).
28. R. J. Oliversen *et al.*, *Bull. Am. Astron. Soc.* **29**, 1315 (1997).
29. F. Scherb, K. D. Retherford, R. C. Woodward Jr., W. H. Smyth, *ibid.* **28**, 1155 (1996).
30. D. L. Judge and R. W. Carlson, *Science* **183**, 317 (1974).
31. F. M. Wu, P. Gangopadhyay, D. L. Judge, *J. Geophys. Res.* **100**, 3481 (1995).
32. The terrestrial glow still contributed significant photon noise to our data, especially because we made these observations 2 months after opposition, and a fraction of the Earth's exosphere along our line of sight was therefore sunlit. This effect was most pronounced at the beginning of each orbit.
33. E. Lellouch, *Icarus* **124**, 1 (1996).
34. No correction has been made for the fact that Io blocks part of the H I Lyman-α emission from the interplanetary medium; all Io H I Lyman-α intensities given in this research article could therefore be 200 to 900 Rayleighs too low. Fluxes given in row 2 of Table 3 are not subject to this correction.
35. D. B. Nash and R. R. Howell, *Science* **244**, 454 (1989).
36. A. S. McEwen, T. V. Johnson, D. L. Matson, L. A. Soderblom, *Icarus* **75**, 450 (1988).
37. E. Lellouch *et al.*, *ibid.* **98**, 271 (1992).
38. F. Salama *et al.*, *ibid.* **107**, 413 (1994); R. W. Carlson *et al.*, *Geophys. Res. Lett.* **24**, 2479 (1997).
39. D. J. Williams *et al.*, *Science* **274**, 401 (1996).
40. J. R. Spencer and N. M. Schneider, *Annu. Rev. Earth Planet. Sci.* **24**, 125 (1996).
41. S. A. Manatt and A. L. Lane, *J. Quant. Spectrosc. Radiat. Transfer* **50**, 267 (1993).
42. M. C. Wong and R. E. Johnson, *J. Geophys. Res.* **101**, 23243 (1996).
43. T. Chust, A. Roux, S. Perraut, D. A. Gurnett, *Ann. Geophys.* **15**, C824 (1997).
44. L. A. Frank, W. R. Paterson, K. L. Ackerson, S. J. Bolton, *Eos* **79**, S201 (1998).
45. D. A. Wolf-Gladrow, F. M. Neubaer, M. Lussem, *J. Geophys. Res.* **92**, 9949 (1987).

46. We thank D. Hall for valuable assistance in planning this experiment, and J. Corliss and M. Freed for long hours spent in data reduction. We also gratefully acknowledge the cooperation and assistance of our co-workers on the STIS Instrument Development Team, and the many people at the Space Telescope Science Institute whose work made these observations possible. We thank anonymous reviewers for valuable comments on the manuscript. A portion of D.F.S.'s research was accomplished at the Observatoire de Paris-Meudon; he thanks Département de Recherche Spatiale for its hospitality. This work was supported by NASA grants NAGW-3319, NAG-4168, and NAGW-6546, and NASA contracts NAS5-30131 and NAS5-30403.

24 August 1998; accepted 10 December 1998

Appendix E

Galileo Imaging of Atmospheric Emissions from Io

instability in the resistance, which we have associated with excitation of the thin-layer moment relative to the thick-layer moment, does have an approximately linear dependence versus H for H greater than the saturation field, although on a fine scale, there are deviations not observed in previous studies (Fig. 3) (*7, 9*). Subsequent transitions at higher bias, which we have associated with magnetic excitations within the Co layers, show more complicated behavior. The measured zero-field intercepts of I_{crit} for the first transition are generally a factor of 2 to 4 lower than those derived from Eq. 2. We consider this satisfactory agreement, since the layers undoubtedly have nonuniform thickness. The observed slopes of I_{crit} versus H also agree with Eq. 2, provided that we assume a value for the phenomenological damping parameter $\alpha_G = 0.05$ to 0.2, which is unusually large compared to more macroscopic samples (*5*). However, we are in a new regime, and there may be large contributions to damping near normal/ferromagnetic interfaces (*3*) and from intralayer processes for nanometer-scale domains.

Our results have both good and bad implications for applications. The bad news is that the existence of magnetic switching caused by spin transfer places a limit on the current (and therefore the signal levels) that can be used for measuring GMR devices. The good news is that the spin-switching effect may enable magnetic random-access memories in which the memory elements are controlled by local exchange-effect forces rather than by long-range magnetic fields. Slonczewski predicts that the spin-transfer torques should dominate over the effects of the self-magnetic fields from flowing currents for devices up to about 100 nm in diameter (*2*), so that the point-contact geometry, with its intrinsically low GMR values, should not be necessary to employ the effect.

References and Notes

1. For reviews of the science and applications of GMR materials, see the collection of articles in *IBM J. Res. Dev.* **42**, (January 1998). (available electronically at www.research.ibm.com/journal/rd42-1.html)
2. J. Slonczewski, *J. Magn. Magn. Mater.* **159**, L1 (1996).
3. L. Berger, *Phys. Rev. B* **54**, 9353 (1996).
4. Ya. B. Bazaliy, B. A. Jones, S.-C. Zhang, *ibid.* **57**, R3213 (1998).
5. J. Slonczewski, *J. Magn. Magn. Mater.* **195**, L261 (1999).
6. R. N. Louie, thesis, Cornell University, Ithaca, NY (1997).
7. M. Tsoi *et al.*, *Phys. Rev. Lett.* **80**, 4281 (1998); erratum, *ibid.* **81**, 493 (1998).
8. J.-E. Wegrowe *et al.*, *Europhys. Lett.* **45**, 626 (1999).
9. J. Z. Sun, *J. Magn. Magn. Mater.* **202**, 157 (1999).
10. K. S. Ralls, R. A. Buhrman, R. C. Tiberio, *Appl. Phys. Lett.* **55**, 2459 (1989).
11. A. G. M. Jansen, A. P. van Gelder, P. Wyder, *J. Phys. C* **13**, 6073 (1980).
12. Fig. 2, B through E, exhibits samples never exposed to a magnetic field, but there are no qualitative differences as a function of magnetic history, as long as $H = 0$.
13. For a review, see M. A. M. Gijs and G. E. W. Bauer, *Adv. Phys.* **46**, 285 (1997).
14. Point-contact measurements of Cu/Co multilayers have previously shown small GMR values; see (6) and M. V. Tsoi, A. G. M. Jansen, J. Bass, *J. Appl. Phys.* **81**, 5530 (1997).

15. We thank J. Slonczewski, S. Guéron, and R. H. Silsbee for discussions. The work was supported by the NSF Materials Research Science and Engineering Centers program (DMR-9632275), the Sloan and Packard Foundations, the Office of Naval Research (N00014-97-1-0745), and Defense Advanced Research Projects Agency, and was performed in part at the Cornell node of the National Nanofabrication Users Network, supported by the NSF. E.B.M. was supported by a U.S. Department of Education grant.

15 April 1999; accepted 22 June 1999

Galileo Imaging of Atmospheric Emissions from Io

P. E. Geissler,[1]* A. S. McEwen,[1] W. Ip,[2] M. J. S. Belton,[3] T. V. Johnson,[4] W. H. Smyth,[5] A. P. Ingersoll[6]

The Galileo spacecraft has detected diffuse optical emissions from Io in high-resolution images acquired while the satellite was eclipsed by Jupiter. Three distinct components make up Io's visible emissions. Bright blue glows of more than 300 kilorayleighs emanate from volcanic plumes, probably due to electron impact on molecular sulfur dioxide. Weaker red emissions, possibly due to atomic oxygen, are seen along the limbs, brighter on the pole closest to the plasma torus. A faint green glow appears concentrated on the night side of Io, possibly produced by atomic sodium. Io's disk-averaged emission diminishes with time after entering eclipse, whereas the localized blue glows brighten instead.

Previous spacecraft and ground-based observations have yielded several indications of a tenuous atmosphere on Io. Dominated by SO_2 and its dissociation products SO, O, and S, Io's atmosphere has been studied at wavelengths ranging from the microwave to the ultraviolet (UV) (*1, 2*). Atomic O, S, Na, and K have been detected in extended neutral clouds escaping from the satellite (*3*), and recent Hubble Space Telescope (HST) observations of Io have imaged intense auroral emissions at far-UV wavelengths (*4*). Visible emissions from Io during eclipse by Jupiter were seen by Voyager 1 (*5*) and suggested to be due to molecular SO_2 (*6*). HST (*7*) and ground-based (*8, 9*) eclipse observations have detected neutral O and Na emissions from Io at visible wavelengths.

The Galileo spacecraft, in orbit around Jupiter since December 1995, can observe optical emissions from Io at a higher spatial resolution than previously possible and from a variety of perspectives unattainable from Earth (*10*). Diffuse emissions from Io have been seen in 16 distinct solid state imager (SSI) observations acquired during 14 eclipses over the course of 10 orbits. Recorded partly to monitor thermal emission from discrete volcanic centers (*11*), these observations provide a detailed look at visible aurorae on a solar system satellite. The bulk of the data was acquired with the SSI clear filter, which covers wavelengths between 380 and 1040 nm (*12*). Two sequences included visible color imaging using the SSI violet (380 to 445 nm), green (510 to 605 nm), and red (615 to 710 nm) filters. Diffuse emissions from Io have not been detected in any of the longer wavelength infrared SSI filters. Here, we describe the morphology of the optical emissions from Io, estimate their brightnesses and radiated powers, and suggest possible interpretations.

The most complete set of eclipse images was acquired on 31 May 1998 during the first of two eclipses in orbit E15 (*13*) (Table 1). These pictures were centered near a longitude of 70°W, on the orbital leading hemisphere of Io that is also the location of the plasma wake. One set of color images in the violet, green, red, and 1-μm (935 to 1090 nm) filters was taken along with two clear-filter pictures comparing Io's appearance 11 min after the start of the eclipse with its appearance 42 min later. The clear-filter images showed diffuse atmospheric emissions as well as discrete volcanic hot spots on Io's leading hemisphere, whereas only the hot spots were visible in the 1-μm filter. Diffuse emissions with three distinct distributions were seen in the visible color frames (Figs. 1 and 2A). The brightest emissions were blue glows close to the equator near the sub- and anti-Jupiter points, extending several hundred kilometers above the limb. They were seen at red, green, and violet wavelengths but were

[1]Lunar and Planetary Laboratory, University of Arizona, Tucson, AZ 85711, USA. [2]Institute of Astronomy, National Central University, Chung-Li, Taiwan 320, Republic of China. [3]National Optical Astronomy Observatories, Tucson, AZ 85719, USA. [4]Jet Propulsion Laboratory, MS 23-201B, 4800 Oak Grove Drive, Pasadena, CA 91109, USA. [5]Atmospheric and Environmental Research, 840 Memorial Drive, Cambridge, MA 02139, USA. [6]Division of Geology and Planetary Sciences, California Institute of Technology, Pasadena, CA 91125, USA.

*To whom correspondence should be addressed. E-mail: geissler@lpl.arizona.edu

brightest in the violet bandpass. A second, weaker glow running continuously along the limb was seen primarily in the red-filter image and was particularly bright along the north polar limb. The third component was a faint glow against the disk of Io at green-filter wavelengths. In the E15 observations, this green glow was concentrated on the night side of Io. Qualitatively similar emission distributions were seen in the noisier color eclipse data from orbit G7, except that the red polar limb glow was brighter in the southern hemisphere than in the northern hemisphere.

In calibrated images (*14*), the brightness of the equatorial blue glows reached >300 kilorayleighs (kR), easily visible to the naked eye (Table 2). This is consistent with the Voyager 1 measurement, which showed glows of several digital numbers above background and had a detection limit of 30 kR (*5*). We estimate that the total optical power (*15*) from Io was ~2×10^9 W. The blue glows in the E15 clear-filter observations contributed 1.5×10^8 W, with ~60% coming from the anti-Jupiter side. The optical power from the red polar limb glow amounted to 1×10^8 W, whereas the larger night-side disk glow accounted for ~7×10^8 W, with 1.6×10^8 W in the green filter alone. For comparison, ~3×10^8 W are expended in visible emissions from each of Io's flux-tube footprints on Jupiter (*16*).

Time variability of the emissions is suggested by differences between the two clear-filter images from the first eclipse of orbit E15. Io dimmed noticeably as time elapsed after the start of the eclipse (Fig. 2C). Io's disk-integrated brightness was ~30% greater in the observation taken 11 min after entry into Jupiter's shadow than it was in the later observation taken 53 min after eclipse entry. Some of this darkening might be due to a decrease in the amount of light scattered by Jupiter's atmosphere as the satellite moved deeper into the planet's shadow, but the dimming is apparent even on the side of Io facing away from Jupiter. More surprisingly, the localized equatorial plume glows appeared to brighten by 37% over the same time interval. A similar reduction in Io's total radiance with elapsed time in Jupiter's shadow was seen during the second eclipse of orbit E15, but quantitative measurements cannot be derived from the noisy and badly smeared images. Dimming of UV emissions from atomic O and S in Io's atmosphere upon ingress into Jupiter's shadow has also been observed by HST (*17*).

To investigate how the emission morphology varies with jovian magnetic longitude, we compared the E15 clear-filter images to previous clear-filter observations (*18*). Jupiter's magnetic field is tilted with respect to the planet's rotation axis, so the equator of the jovian magnetic field and the center of Io's plasma torus oscillate above and below Io's orbital plane (*19*). We compared one of the E15 images to two earlier clear-filter eclipse images acquired with similar viewing geometries on orbits G7 and G8 (Fig. 2B) and found that the pole with the brightest limb emission alternated between the north and south. The G7 and G8 observations were made while Io was at System III magnetic longitudes of 165° and 261°, respectively. At these locations, the center of the plasma torus was to the south of Io, on the same side as the brighter polar limb glows. Similarly, the limb glow during E15 (magnetic longitude of 72°) is brighter in the north, the same side of Io as the plasma torus position. This correspondence between polar limb glow brightness and the location of the torus center appears to be true of the other available clear-filter eclipse images as well [see supplementary table (available at www.sciencemag.org/feature/data/1039991.shl)]. In each case, the limb glow was brightest on the pole that was closest to the equator of the jovian magnetic field at the time of the observation. Io's polar UV emissions (*4*) and optical O emission (*7*) have been noted to display similar behavior.

During orbits G7, G8, and E15, the brightest glows on the sub- and anti-Jupiter hemispheres were associated with fixed geographic locations

Table 1. Galileo SSI Io eclipse observations during the first of two eclipses in orbit 15. Image times are spacecraft event times, uncorrected for light travel time to Earth. The eclipse began at 1998:151:00:06:17.482 GMT (year:day:hours:minutes:seconds). The effective spatial resolution (Res.) is lower than the data listed, because the images are smeared over several pixels because of the long exposure times. λ_{III} refers to Io's position with respect to Jupiter's magnetic field. Lat., latitude; Long., longitude; deg., degrees.

Observation	Image number	Picture number	Filter	Lat. (deg.)	Long. (deg.)	Res. (km/pixel)	Image time (GMT)	λ_{III} long. (deg.)
CLR1	449843800	15I0004	Clear	−0.33	68.23	13.97	1998:151:00:17:07.511	53
GRN	449847102	15I0006	Green	−0.34	71.43	13.53	1998:151:00:50:41.389	68
RED	449847302	15I0007	Red	−0.34	71.63	13.50	1998:151:00:52:42.722	69
VIO	449847502	15I0008	Violet	−0.34	71.82	13.48	1998:151:00:54:44.056	70
CLR2	449847913	15I0022	Clear	−0.34	72.20	13.42	1998:151:00:58:43.510	72

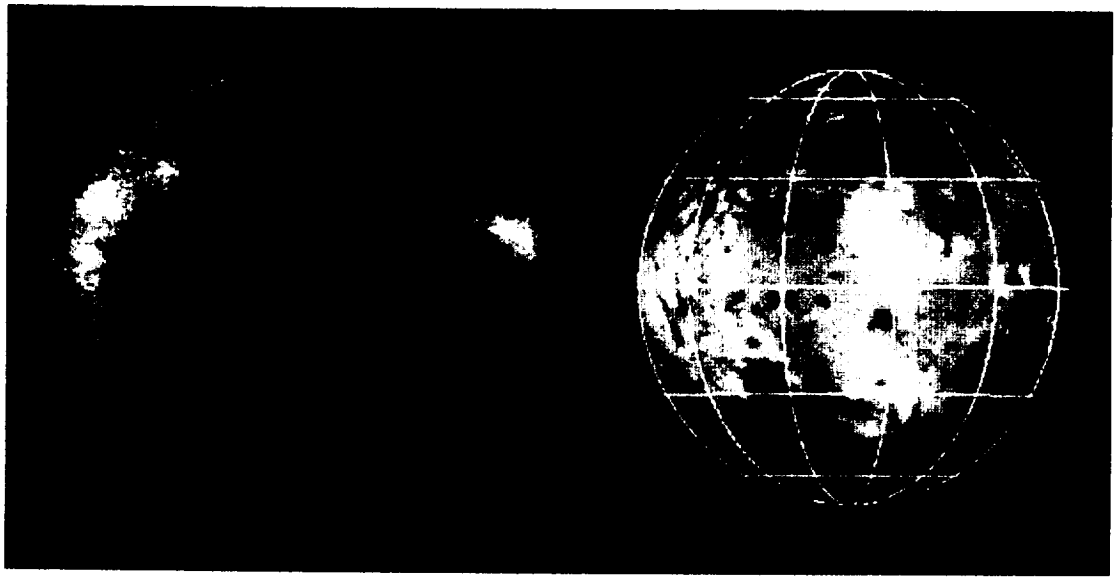

Fig. 1. Enhanced visible color (red, green, and violet) image of Io in eclipse (left) compared to a sunlit view of Io from a similar perspective (right). Three distinct components make up Io's visible aurorae. Bright blue glows emanate from volcanic plumes near the sub- and anti-Jupiter points (longitudes of 0° and 180°). Weaker red glows are seen along the polar limbs, brighter in the north than in the south. A faint green glow appears against the disk of Io, concentrated on the night side (longitudes of 90° and beyond). The red and green glows appear brighter than natural in this contrast-stretched picture.

on the surface and did not appear to change position as a function of the geometry of Jupiter's magnetosphere (Fig. 2B). In contrast to the UV equatorial emissions (*4*), the brighter visible equatorial glows were closely associated with known centers of volcanic activity on Io's surface, including Acala, Kanehekili, and Ra on the sub-Jupiter hemisphere and Prometheus, Culann, Zamama, and Amirani on the anti-Jupiter side. In many of the other eclipse observations, the equatorial glows fluctuated in latitude, in most cases correlated with the positions of the tangent points of the jovian magnetic field lines. SSI images from the earliest orbit (G1) showed differences on the sub-Jupiter hemisphere, because the Kanehekili and Acala plumes were inactive and the Ra plume was active (*18*).

To test the association of the blue equatorial glows with specific volcanic plumes, we simulated the appearance of Io in orbit E15, using a three-dimensional plume model with simple ballistic particle trajectories (*1, 20*). Test particles were launched from fixed surface locations corresponding to known plumes and hot spots, with randomly chosen initial speeds (constrained to be within a fixed range) and launch directions (constrained to lie within 45° of vertical). The trajectories were computed at 100-s intervals, and the positions of the particles at each time step were recorded for graphical rendering. The best match to the E15 eclipse observations (Fig. 3) was obtained with initial launch speeds between 500 and 1100 m s^{-1}, from the following plumes: Acala (11°N, 334°W), Culann (20°S, 160°W), Prometheus (2°S, 153°W), Zamama (18°N, 173°W), and Amirani (22°N, 114°W). The simulation adequately resembles the observations (compare Fig. 1) but fails to reproduce faint emissions from a cluster of small bright spots west of Acala.

The exact mechanisms that produce Io's colorful glows are not known. Electrons from several sources are available to excite the emissions. Field-aligned Birkeland currents, generated by the motion of the jovian magnetic field past Io, connect Jupiter to Io at the sub- and anti-Jupiter points near the sites of the equatorial plume glows (*21*). Concentrations of plasma torus electrons are also expected near the sub- and anti-Jupiter points as the plasma flows

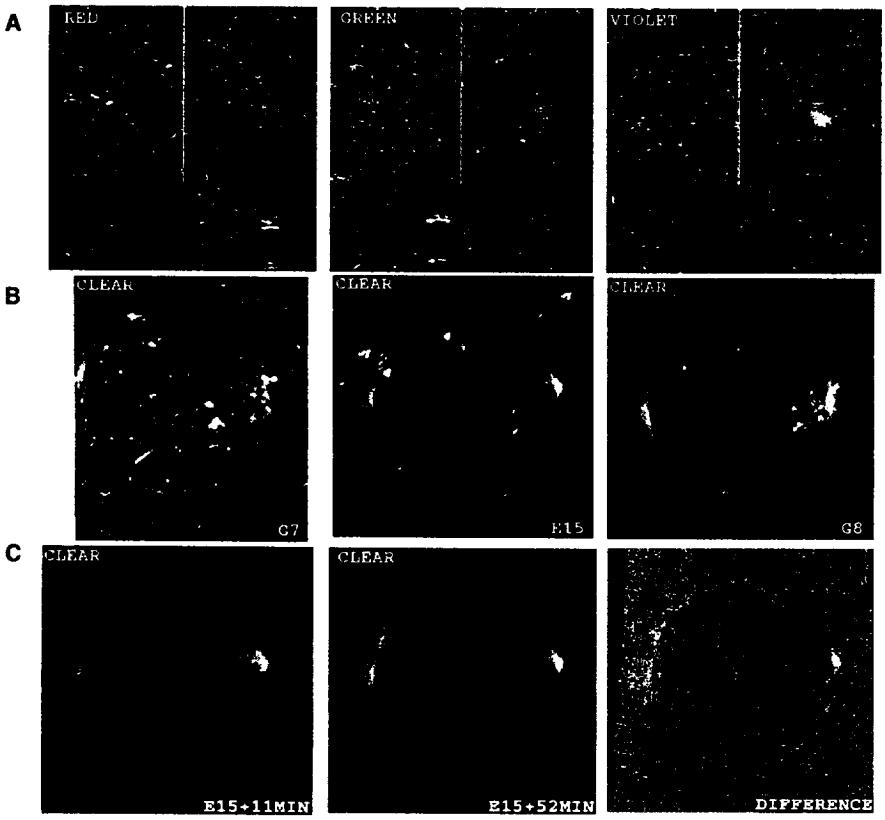

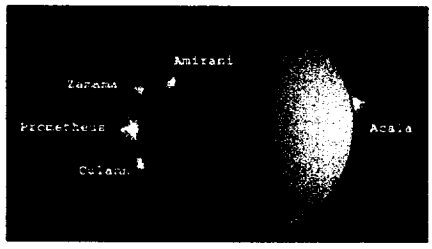

Fig. 2 (top). Raw SSI images of Io in eclipse. **(A)** Different diffuse emission morphologies can be seen in each of the separate E15 color frames. Two particularly bright volcanoes are visible as spots in the top left of the red-filter frame. **(B)** A comparison between the E15 clear-filter image (middle) and previous clear-filter pictures taken from slightly different perspectives during orbits G7 and G8. The brightest glow on the sub-Jupiter hemisphere is associated with a volcanic plume (Acala) at a fixed geographic location on the surface and does not appear to change position as a function of the geometry of Jupiter's magnetosphere. **(C)** Changes in the appearance of Io between 11 min after the start of eclipse (left) and 41 min later (middle). The difference between the two images (right) shows that Io's disk darkened as the eclipse progressed, while the plumes brightened. **Fig. 3 (bottom).** Plume model. Three-dimensional numerical simulation of ballistic trajectories from known volcanic sources on Io's surface. The size of a plume is controlled by the initial launch speeds of the particles (here, between 500 and 1100 m s^{-1}). At least five separate plumes are needed to account for the blue emissions seen in Fig. 1.

Table 2. Brightness and radiated power estimates of Io glows. These estimates are based on the average SSI system response to white light over the bandpasses of each filter, and they may underestimate line emission strengths because of the variation of the filter sensitivity with wavelength. Calculations assume emission at the following wavelengths: violet, 404 nm; green, 560 nm; red, 630 nm; and clear, 560 nm. Measurement uncertainty (standard deviation of the mean) is 25 to 50%. The detection limit in the SSI clear filter is estimated at 2 kR.

Observation	Brightness (nW cm^{-2} sr^{-1})	Brightness (kR)	Power (MW)
	Io disk average		
CLR1	1.57	55.4	2414
CLR2	1.21	39.7	1637
VIO	0.32	8.2	472
GRN	0.23	8.0	335
RED	0.17	6.8	254
	Acala maximum		
CLR1	8.63	305.2	61
CLR2	11.81	417.7	57
VIO	3.36	85.7	62
GRN	0.84	29.7	8
RED	0.46	18.4	12
	Prometheus maximum		
CLR1	5.05	178.6	99
CLR2	7.10	251.3	92
VIO	1.67	42.6	67
GRN	0.54	19.0	27
RED	0.41	16.1	22
	North polar limb		
CLR1	2.77	98.1	119
CLR2	2.51	88.7	72
VIO	0.70	17.9	13
GRN	0.48	17.1	20
RED	0.53	21.0	31
	Night-side disk		
CLR1	2.17	77.0	798
CLR2	1.54	54.6	597
VIO	0.34	8.7	81
GRN	0.55	19.5	164
RED	0.23	9.2	97

past Io (*22*). Plasma torus electrons are implicated by the red limb glows, which vary in brightness with the location of the plasma torus center. Photoelectrons from solar UV radiation might also contribute to the excitation of atmospheric emissions on Io, adding to the intensity of the disk glow early in eclipse. More likely, the post-ingress dimming of Io could indicate the partial collapse of an extended sublimation atmosphere superimposed on the presence of localized volcanic gases. The equatorial plume glows, in contrast, actually brighten with time as eclipses progress. Perhaps, as the atmospheric conductivity decreases during eclipse, a greater share of the current through Io is conducted by the volcanic plumes (*23*).

A major question is the identity of emitting species, which cannot be determined from the broadband SSI observations alone. Many of Io's atmospheric constituents have emission lines at visible wavelengths. Candidate atomic species for the red glow include the forbidden neutral O [O I] lines at 630 and 636 nm, H-α lines at 656 nm, and singly ionized S (S II) lines at 672 and 673 nm. Possible sources for the green glow are [O I] lines at 558 nm and Na I lines at 589 and 590 nm. Recent spectral observations of Io in eclipse from the Keck telescope (*9*) identified O lines at 630, 636, and 558 nm and found Na D lines at 589 and 590 nm to be brighter than the O green line. Atomic O and Na are thus considered to be the most likely candidates for the red and green glows, respectively. No identifiable emission lines (such as those from O I or O II) were seen from 420 to 445 nm, the portion of the SSI violet-filter bandpass covered by the ground-based observations.

Io's bright blue glows are probably due to molecular emission from SO_2, known to be abundant in volcanic plumes (*1, 24*). Laboratory spectra of UV-visible emission from SO_2 bombarded by electrons at various energies (*6, 25*) show molecular bands extending to visible wavelengths that are brighter in violet than in green wavelengths, just as seen in the SSI data. If SO_2 is the source of the blue glows, then Io's spectrum may allow us to constrain the temperature of the electrons exciting the emissions. The threshold energy for exciting the SO_2 (electron states of A − X and one-electron orbitals of a − X) molecular transitions responsible for the UV emission and its visible tail is ~4 eV (*6*). Sulfur dioxide begins to dissociate at electron energies of 5.6 eV and, for energies greater than ~10 eV, produces a bright spectral feature due to SO that can be seen in the laboratory at 256 nm (*6, 25*). The nondetection of 256-nm SO emission on Io by HST (*17*) seems to imply that the blue glows are excited by electrons with energies in the range of 4 to 10 eV. This range includes the mean electron temperature (~5 eV) inferred for the background plasma torus (*26*). However, these observations were made at different times (6 years apart), and the electron temperature may vary considerably with time.

If these emissions are due to electron impact excitation, we can estimate the electron densities and column abundances of the emitting species needed to produce the observed brightnesses (*27*). For electron impact excitation of atomic Na to match the maximum observed night-side disk brightness of 19.5 kR in the green filter, the electron density must be at least an order of magnitude larger than the nominal plasma torus density of 2000 electrons cm^{-3} (*28*), even if an optically thick column of Na (~10^{13} cm^{-2}) is assumed. Enhanced electron densities of ~20,000 to 40,000 cm^{-3} in the Io plasma wake (*29*), centered on the leading hemisphere at 90°, may thus be responsible for the broad green night-side emissions. Enhanced electron densities have also been suggested for the "ribbon" in the plasma torus (*30*). The brighter green emissions on Io's leading night side (Fig. 1, left) could be due to the electron shielding of Na by SO_2 in the thicker leading day-side atmosphere (longitudes of 268° to 88°W) (Fig. 1, right), consistent with the diurnal behavior predicted from atmospheric models (*31*). Such intense electron impact excitation of atomic O would produce the disk-averaged brightness of 6.8 kR and the maximum brightness at the north polar limb of 21 kR seen in the red filter for column densities of ~1×10^{14} cm^{-2} and >1×10^{14} cm^{-2}, respectively. This is near the maximum emission brightness of atomic O (at 630 and 636 nm) because it is limited by collisional quenching. Because of attenuation in Io's atmosphere, the population of magnetospheric electrons available at low altitudes to excite the more energetic SO_2 emissions (photons of ~4 to 5.6 eV) is substantially smaller than the population available to excite the less energetic O and Na emissions (~2 eV). If we assume an electron density of 2000 cm^{-3} for the SO_2 glows, then the violet-filter disk-averaged brightness of 8.2 kR and the maximum brightness at Acala of 85.7 kR imply approximate SO_2 column densities of ~10^{16} molecules cm^{-2} and 10^{17} molecules cm^{-2}, respectively. These are more than an order of magnitude larger than the atomic O columns estimated above, similar to model calculations for Io's atmosphere (*31*).

References and Notes

1. For a comprehensive review, see E. Lellouch, *Icarus* **124**, 1 (1996).
2. Recent observations by the UV spectrometer on Galileo are reported by A. R. Hendrix, C. A. Barth, and C. W. Hord [*J. Geophys. Res.* **104**, 11817 (1999)].
3. R. A. Brown, in *Exploration of the Planetary System, Proceedings of the Symposium, Torun, Poland, September 5–8, 1973*, A. Woszczyk and C. Iwaniszewska, Eds. (Reidel, Dordrecht, Netherlands, 1974), pp. 527–531; L. M. Trafton, *Nature* **258**, 690 (1975); J. T. Trauger *et al.*, *Bull. Am. Astron. Soc.* **8**, 468 (1976); R. A. Brown, *Astrophys. J.* **244**, 1072 (1981); S. T. Durrance, P. D. Feldman, H. A. Weaver, *Astrophys. J. Lett.* **267**, L125 (1983).
4. F. L. Roesler *et al.*, *Science* **283**, 353 (1999).
5. A. F. Cook *et al.*, *ibid.* **211**, 1419 (1981).
6. J. M. Ajello, G. K. James, I. Kanik, *J. Geophys. Res.* **97**, 10501 (1992).
7. J. T. Trauger, K. R. Stapelfeldt, G. E. Ballester, J. T. Clarke, WFPC2 Science Team, *Bull. Am. Astron. Soc.* **29**, 1002 (1997).
8. F. Scherb and W. H. Smyth, *J. Geophys. Res.* **98**, 18729 (1993).
9. M. E. Brown *et al.*, in preparation.
10. M. J. S. Belton *et al.*, *Science* **274**, 377 (1996).
11. A. S. McEwen *et al.*, *ibid.* **281**, 87 (1998).
12. Bandpasses listed are the wavelengths over which the system response to white light is at least 1% of the peak value for each filter, to 5-nm precision [H. Breneman and K. Klaasen, *Report D-5880* (Jet Propulsion Laboratory, Pasadena, CA, 1993)].
13. The E15 color data were recorded with exposure times (25.6 s) longer than those used in previous attempts and were telemetered with lossless compression. An earlier color sequence from orbit G7 was degraded by accidental multiple exposures.
14. K. P. Klaasen *et al.*, *Opt. Eng.* **36**, 3001 (1997). We have subtracted an empirically determined background component, which was calculated as the average brightness of the region surrounding Io's disk. Brightness estimates are based on the average system response to white light over the entire bandpass of each filter. Hence, line emissions may be underestimated if they occur at wavelengths near the limits of the filters' sensitivity.
15. Total optical power is defined as $4\pi JA$, where A is the area of the emission in square centimeters (in the image plane at the distance of the source) and J is the average measured radiance in watts per square centimeter per steradian. Power estimates assume emission at the following wavelengths: violet, 404 nm; green, 560 nm; red, 630 nm; and clear, 560 nm. Depending on the actual spectrum, the sum of the power emitted in the red, green, and violet filters may not necessarily equal that in the clear filter [see also (*14*)].
16. A. P. Ingersoll *et al.*, *Icarus* **135**, 251 (1998).
17. J. T. Clark, J. Ajello, J. Luhmann, N. Schneider, I. Kanik, *J. Geophys. Res.* **99**, 8387 (1994); G. E. Ballester *et al.*, *Bull. Am. Astron. Soc.* **29**, 980 (1997).
18. A. S. McEwen *et al.*, *Icarus* **135**, 181 (1998).
19. Jupiter is surrounded by a torus-shaped cloud of trapped charged particles that rotate with the planet's magnetic field. The plasma torus is mainly made up of S and O ions and electrons that are continually being replenished by Io. The centrifugal equator of the plasma torus is inclined by ~7° to Jupiter's equatorial plane, so the torus wobbles with respect to Io's position every 13 hours as Jupiter rotates. Io is at maximum north and south magnetic latitudes (that is, farthest from the plasma torus center) for System III magnetic longitudes of ~200° and 20°, respectively, and is in the magnetic equator (the densest part of the plasma torus) at ~110° and 290°, respectively. Embedded within the torus is a narrow vertical band of concentrated plasma known as the "ribbon." The origin of this curious feature is as yet poorly known.
20. See also R. G. Strom and N. M. Schneider, in *Satellites of Jupiter*, D. Morrison, Ed. (Univ. of Arizona Press, Tucson, AZ, 1982), chap. 16. More realistic hydrodynamic simulations [for example, J. V. Austin and D. B. Goldstein, *Bull. Am. Astron. Soc.* **30**, 1121 (1998)] produce plumes that are somewhat flatter than those shown here, owing to shock pressure and horizontal flow.
21. P. Goldreich and D. Lynden-Bell, *Astrophys. J.* **156**, 59 (1969).
22. J. Linker, K. Khurana, M. Kivelson, R. Walker, *J. Geophys. Res.* **103**, 19867 (1998); M. Combi, K. Kabin, T. Gombosi, D. Dezeeuw, K. Powell, *ibid.*, p. 9071; J. Saur, F. M. Neubauer, D. F. Strobel, M. E. Summers, *ibid.*, in press.
23. Possible effects of current flow through Io were described by T. Gold [*Science* **206**, 1071 (1979)] and A. Peratt and A. Dessler [*Astrophys. Space Sci.* **144**, 451 (1988)].
24. J. Pearl *et al.*, *Nature* **280**, 757 (1979); P. Sartoretti *et al.*, *Icarus* **122**, 273 (1996).
25. K. Miller and K. Becker, *Can. J. Phys.* **65**, 530 (1987).

26. E. C. Sittler and D. F. Strobel, *J. Geophys. Res.* **92**, 5741 (1987).
27. For electron impact excitation of Io's atmosphere in eclipse, column abundances were estimated by equating the measured brightnesses to the product of a gas-column density, an average electron density in the gas column, and an average emission rate (for the particular brightness) that depends on the effective electron temperature in the gas column. This linear relation is approximately valid if the gas column is optically thin (not true for Na optical emissions), so that created photons may escape freely without further absorption by the gas column, and if no collisional quenching occurs (not true for O optical emissions at lower altitudes). The determination of the electron temperature and density in the column is a complex problem not addressed here. Instead, we adopt a range of possible values for the electron temperature (to bound the emission rate) of 40,000 K (3.4 eV) to 60,000 K (5.2 eV) and adopt nominal plasma wake values for the electron densities of 20,000 cm^{-3} for Na and O; we also correct for the brightness for the optically thick Na column. On the basis of these temperatures, the emission rates assumed for Na were 5.4×10^{-7} to 6.8×10^{-7} photons cm^3 s^{-1} [R. Clark, N. Magee Jr., J. Mann, A. Merts, *Astrophys. J.* **254**, 412 (1982)], and the rates for O were 2.4×10^{-9} to 3.2×10^{-9} photons cm^3 s^{-1} (D. Shemansky, private communication). For SO_2 located deeper in the atmosphere, an electron temperature of 40,000 K was adopted along with an electron density of 2000 cm^{-3}. An approximate electron impact excitation rate of 1.7×10^{-10} photons cm^3 s^{-1} for the molecular band structures of SO_2 appropriate to the SSI violet filter was estimated from laboratory measurements (*6*, *25*), with guidance given by K. Becker (private communication).
28. Background plasma torus electron density as measured near Io's orbit in the plasma torus by the Voyager spacecraft is ~2000 cm^{-3} [F. Bagenal, *J. Geophys. Res.* **99**, 11043 (1994)].
29. Electron densities in the Io plasma wake as measured by the Galileo spacecraft are as high as 40,000 cm^{-3}, an order of magnitude larger than the value of ~4000 cm^{-3} measured in the plasma torus near Io [D. A. Gurnett, W. S. Kurth, A. Roux, S. J. Bolton, C. F. Kennel, *Science* **274**, 391 (1996); L. A. Frank *et al.*, *ibid.*, p. 394].
30. M. Volwerk, M. Brown, A. Dessler, B. Sandel, *Geophys. Res. Lett.* **24**, 1147 (1997).
31. M. C. Wong and W. H. Smyth, *Bull. Am. Astron. Soc.* **30**, 1117 (1998); in preparation.
32. We are grateful for informative discussions with many patient colleagues before and during the Madison, Wisconsin, meeting of the Division for Planetary Sciences of the American Astronomical Society. Particular thanks are due to C. Alexander, F. Bagenal, F. Crary, A. Dessler, F. Herbert, W. Hubbard, D. Hunten, K. Klaasen, L. Lane, M. McGrath, K. Rages, and N. Schneider.

12 March 1999; accepted 24 June 1999

Quantitative Assessment of Reactive Surface Area of Phlogopite During Acid Dissolution

Eric Rufe and Michael F. Hochella Jr.

The reactive surface area of a dissolving sheet silicate, phlogopite, was quantitatively assessed in experiments performed in the fluid cell of an atomic force microscope at room temperature and pH values of 2 and 5.7. Additional assessment was provided by surface chemical analysis and electron diffraction. Dissolution rates of phlogopite {*hk*0} edges are in the range of 10^{-10} moles per square meters per second, two orders of magnitude faster than bulk rates for this mineral. The basal {001} surfaces also show distinct reactivity, although it is short-lived before they become relatively inert. These basal surfaces are shown to leach, hydrate, and expand to an amorphous silica-enriched film.

Chemical weathering of silicate minerals exerts substantial influences on processes such as neutralization of anthropogenic acidic inputs, supplying and cycling of nutrients in natural systems, and long-term climate change by acting as a sink for atmospheric CO_2. Laboratory and field-based studies that determine dissolution rates rely on measurements of exposed mineral surface area, but unfortunately, surface area remains one of the most difficult parameters to characterize. Most often, laboratory rates are normalized to the initial surface area measured by a Brunaer-Emmett-Teller (BET) adsorption isotherm. For many silicates, no linear relation exists between rate and BET surface area (*1*), implying that not all of the measured surface area participates in the reaction at the same rate or by the same mechanism. The term "reactive surface area" is often used to distinguish the portions of the surface that dominantly contribute to measured fluxes from portions that do not. In the literature, the way in which reactive surface area is defined is variable (*2*).

To gain insight into the intricacies of mineral dissolution, others have used in situ atomic force microscopy (AFM) to examine reactions in real time on particular crystallographic faces or microtopographic features of several nonsilicate minerals (*3*). However, there are no published in situ AFM studies in which silicate dissolution rates were measured at room temperature (*4*). Our study combines in situ AFM observations of the dissolution of the mica phlogopite $[K_2Mg_6(Al_2Si_6O_{20})(OH,F)_4]$ at room temperature with x-ray photoelectron spectroscopy (XPS) and low-energy electron diffraction (LEED) analyses to quantitatively assess reactive surface area (*5*). Among silicates, micas are best suited for investigating the role of reactive surface area because mica dissolution has been well characterized by several solution studies (*6*–*9*) and because their sheetlike structure allows for the easy identification of surfaces with greatly different reactivity (*10*).

Freshly cleaved phlogopite {001} surfaces were etched in HF to produce crystallographically controlled etch pits (*11*) and then placed in an AFM fluid cell to which an aqueous solution was introduced (*12*). Dissolution proceeds by the removal of material from the etch pit walls (*13*) (Fig. 1). Etch pits retain the same morphology while dissolving, indicating that each etch pit wall retreats at essentially the same rate. Additionally, no new etch pits nucleate on {001} surfaces. We have imaged the same region of the surface at various times over the course of several days, and the volume of phlogopite removed from a particular etch pit is measured at each time interval (*14*). XPS analysis shows decreasing K/Si, Al/Si, Mg/Si, and F/Si atomic ratios within the first 24 hours of reaction. Because Mg, Al, and K are preferentially removed with respect to Si, the dissolution rates determined from these AFM observations are compared to dissolution rates calculated from Si release reported in solution studies. Dissolution rates were calculated as

$$\text{rate} = \frac{(\Delta V/V_m)}{\text{SA}(t)} \quad (\text{mol m}^{-2}\,\text{s}^{-1}) \qquad (1)$$

where ΔV is the volume of phlogopite removed from the etch pit, V_m is the molar volume of the phlogopite (based on a complete formula unit), t is the time interval, and SA is surface area. Dissolution rates of pit edges measured in this study were normalized to the initial SA of the {*hk*0} edges (*15*) (Fig. 2). However, dissolution rates of micas in the literature are normalized to the initial BET-measured SA of particles, which includes both {001} and {*hk*0} surfaces. To compare the rates calculated from an etch pit directly to the rates reported in the literature, it is necessary to construct an imaginary particle with the same edge surface area as that of the etch pit. This was achieved by treating each etch pit as a "negative" particle with the same lateral dimensions as follows. An etch pit Z nanometers deep of size $A_{initial}$ expands to size A_{final} during time t. Assume that this is equivalent to a particle Z nanometers thick of size A_{final} shrinking to size $A_{initial}$ during time t. The equivalent particle is constructed so that

Department of Geological Sciences, Virginia Polytechnic Institute and State University, Blacksburg, VA 24061–0420, USA.

Appendix F

Io's Oxygen Source: Determination from Ground-based Observations and Implications for the Plasma Torus

Io's Oxygen Source:

Determination from Ground-based Observations

and Implications for the Plasma Torus

W. H. Smyth[1]

and

M. L. Marconi[2]

Submitted to
Journal for Geophysical Research
August 20, 1999

Preprint Version

1. Atmospheric and Environmental Research, Inc., 840 Memorial Drive, Cambridge, MA 02139

2. Fresh Pond Research Institute, 64 Fairfield Street, Cambridge, MA 02140

ABSTRACT

From modeling analysis of two different ground-based observations for Io's neutral oxygen cloud in [O I] 6300 Å emission, new exobase atomic oxygen sources for incomplete collisional cascade have been determined to be 1.27 x 10^{28} atoms sec^{-1} and 1.47 x 10^{28} atoms sec^{-1}, ~4 times larger than earlier estimates. Implications for local heating and escaping energy rates of neutrals at Io and for the ion pickup energy-input rates to the plasma torus produced by this larger oxygen cascade source and also by other atomic oxygen and sulfur source processes (approximately scaled from the oxygen cascade source) are discussed. The estimated power to sustain these O and S neutral sources is 0.83 x 10^{12} W and is divided between 0.88 x 10^{11} W for atmospheric heating and 0.74 x 10^{12} W for neutral escape. The total ion pickup input power to the plasma torus is estimated to approach ~2 x 10^{12} W with an "outer source region" (above Io's exobase for the cascade source created neutral extended clouds) to "inner source region" (below Io's exobase produced by charge exchange) torus power input ratio in the range of 1:2 to 1:3. This physical picture provides a viable solution to the mass loading and energy crisis of the plasma torus. A "power ribbon" is produced by the "inner source region" and may provide a rationale for the observed ultraviolet "flashes and sparkles" of the S^{++} plasma torus ribbon and the chaotic time variability of [O I] 6300 Å emission at Io.

1. INTRODUCTION

Atomic oxygen from Io was first discovered in 1980 from ground-based observations by Brown (1981). In this discovery measurement, very dim 8 ± 4 Rayleigh [O I] 6300 Å emission was detected from Io's extended neutral clouds in a small slit located near (or at) the west ansa of the satellite's orbit and well removed from the orbital location of Io. This emission, which is thought to be excited by impact of plasma torus electrons, immediately indicated that a significant amount of atomic oxygen had escaped the gravitational grasps of the satellite [contained within Io's Lagrange radius of ~5.85 satellite radii (R_{Io})] and had populated circumplanetary orbits. This discovery indicated that atomic oxygen was also a constituent of Io's local atmosphere and corona and that the ionization of these oxygen atoms would likely provide a significant O^+ plasma source for the heavy ion (O^+, O^{++}, S^+, S^{++}, S^{+++}) Io plasma torus that had been documented in 1979 by the Voyager spacecraft mission. Rocket-based measurements in 1981 (Durrance et al., 1983; Skinner and Durrance, 1986) of ultraviolet emissions from the plasma torus region using a large 15 arc sec x 110 arc sec aperture that was well removed from Io discovered atomic sulfur in Io's neutral cloud in 1425 Å emission with an average brightness of 2.8 ± 1.3 Rayleighs. These measurements also confirmed the existence of atomic oxygen in the neutral cloud from a blend of 1304 Å emissions from atomic oxygen and sulfur with an average brightness of 4.2 ± 2 Rayleighs. In addition, in 1990 similar rocket measurements of the neutral sulfur cloud were also acquired in a large aperture using the Hopkins Ultraviolet Telescope (Durrance et al., 1995). More recently in 1993, Thomas (1996) acquired from ground-based observations at eastern elongation the only other [O I] 6300 Å emission measurement that has been made to date for atomic oxygen in Io's neutral cloud and reported a similar brightness to that obtained earlier by Brown (1981).

In addition to these very dim observations of atomic oxygen and sulfur in the neutral cloud remote from Io, an increasing number of observations have more recently been made for atomic oxygen and sulfur very near Io. These observations have been almost entirely restricted to distances from Io that are within the Lagrange sphere of the satellite and hence sample oxygen in Io's local atmosphere and bound corona. Until recently, these near-Io observations provided only aperture-average brightness values that were much brighter than the dim emissions observed in the more distant neutral cloud. These aperture-averaged observations have included ultraviolet emissions for atomic oxygen and sulfur obtained from the International Ultraviolet Explorer (IUE) in 1986-1994 (Ballester et al., 1987; Ballester, 1989; M.A. McGrath, personal communication, 1995) and from the Hubble Space Telescope (HST) in 1992-1994 (Clarke et al., 1994; Ballester et al., 1994; J.T. Clarke, personal communication, 1995; M.A. McGrath, personal

communication, 1995). In addition, near-Io observations of atomic oxygen in [O I] 6300 Å emission in an Io-centered 5.2 x 5.2 arc second aperture have been obtained by an ongoing ground-based program (Scherb and Smyth, 1993; Oliversen et al., 1998), which has now assembled a large systematic data set over the period from 1990-1998. In 1997, spectacular ultraviolet images of Io in a number of emission lines of atomic oxygen and sulfur were acquired with the new Space Telescope Imaging Spectrometer (STIS) aboard the HST and reported by Roesler et al. (1999) with more of these STIS images for Io obtained in 1998 (Wolven et al., 1999). In addition, two spectacular images of Io in atomic oxygen in [O I] 6300 Å emission were acquired from HST in 1997 when Io was eclipsed by Jupiter's shadow (Trauger et al., 1997). For Io in eclipse, the disk-average brightness for atomic oxygen in optical emission (6300 Å, 6363 Å) has also been measured in 1998 from ground-based observations (M.E. Brown, personal communication, 1998), and very high-resolution color eclipse images were acquired in 1998 by the SSI instrument aboard the Galileo spacecraft for which optical emission from atomic oxygen is the most likely candidate species for the observed brightness in the red (6150–7100 Å) filter (Geissler et al., 1999).

Only limited progress has been made in extracting the source rate for oxygen and sulfur at Io's exobase from the observed oxygen emission brightnesses noted above. The relationships between the neutral source rate and observed emission brightness involve a number of physical processes that are not fully understood. For Io's corona and neutral clouds, these processes include the nature of the oxygen and sulfur source mechanisms at Io's exobase, the space-time nature of the neutral lifetimes in the near-Io environment and plasma torus, and the nature of the excitation mechanism for atomic oxygen and sulfur and their spacetime dependence in the near-Io environment and plasma torus. For emission from the local atmosphere, the situation becomes even more complex and involves factors that include the location and activity of volcanic gas plumes, the dynamics of the combined volcanic and sublimation atmospheric gases heated by plasma processes, additional excitation produced by the Birkeland-current closure at Io, and atmospheric chemistry caused by solar photons, gas-phase collisions, and gas-plasma interactions.

For the dim oxygen neutral cloud, progress has nevertheless been made by drawing physical insight from studies for the spatial nature of the sodium cloud determined from ground-based observations of the bright D-lines (5890 Å, 5896 Å) which are at least two orders of magnitude brighter than optical emission for atomic oxygen (Smyth, 1992). An atomic oxygen source rate of 3.2×10^{27} atoms s^{-1} was reported by (Scherb and Smyth, 1993) for the observation of Brown (1981) by assuming (1) an isotropic and 2.6 km/s monoenergetic source at Io's

exobase, that had proven useful to characterize approximately the morphology of the neutral sodium cloud near Io's orbit, and (2) an electron impact excitation mechanism in the plasma torus. Since that time a complete source velocity distribution has been determined for sodium at Io's exobase from modeling of combined sodium observations on several different spatial scales (Smyth and Combi, 1997). The dominant source mechanism that populates the neutral cloud near Io's orbit was shown to be an incomplete collisional cascade (sputtering) source distribution that peaks at 0.5 km s^{-1}, well below the satellite escape speed, and extends in the tail of the distribution to many tens of km s^{-1}. With this new insight into the source velocity distribution for the neutral cloud for sodium, which is a trace species in Io's local atmosphere and corona, it is now possible to adopt this source velocity distribution as a first order description for atomic oxygen and proceed to analyze the neutral cloud observations for atomic oxygen acquired by both Brown (1981) and Thomas (1996) to determine more realistic oxygen source rates. This analysis is the objective of this paper.

The paper is organized as follows. The observations of Brown (1981) and Thomas (1996) are presented in section 2. In section 3, the neutral cloud model used in the analysis is described followed by its application to the observations. A discussion of the model results, their implications, and conclusions is given in section 4.

2. OBSERVATIONS

Ground-based observations reported by Brown (1981) and Thomas (1996) for Io's neutral oxygen cloud in the 6300 Å emission line were both acquired by a slit with a field of view that was well removed from Io's immediate location. The sky plane geometry for these two observations is presented in Figure 1 and shows the relative locations of the observing slits, Jupiter, Io, and Io's orbit. The observation of Thomas was acquired exactly 13 years to the day after the observation of Brown, which is close to an orbital period of Jupiter, causing the tilt angle for Io's orbit projected onto the sky plane to be very similar.

The observations of Brown were made on March 5, 1980 with a small slit that covered a 0.32 R_J x 0.05 R_J rectangle with the long side parallel to the satellite orbital plane. As illustrated in Figure 1, the observing slit of Brown was centered on the symmetry line of the projected sky plane ellipse of Io's orbit and was positioned at 5.0 R_J west (right) of Jupiter for two observations and at 5.9 R_J west (western elongation) of Jupiter for four observations. During these six measurements, the satellite was moving toward western elongation (270°) on its orbit and covered an Io geocentric phase angle interval of 181 to 215°. The small filled circles in Figure 1

to the right of Jupiter show the orbital locations of Io at the mid-point time of each of the six observations. During this time, Io also covered a System III longitude interval in the plasma torus from 105 to 215° so that the satellite quickly crossed the plasma torus centrifugal symmetry plane (110°) and then spent the remainder of its time north of that plane. The six observed brightnesses were properly Doppler-shifted and added by Brown to improve signal to noise and provided a slit average [O I] 6300 Å emission brightness of 8 ± 4 Rayleighs.

The primary [O I] 6300 Å emission observation (Number 199) reported by Thomas was acquired on March 5, 1993. At the midpoint of this observation, Io was approaching eastern elongation (90°) with a geocentric phase angle of 73° (small open circle left of Jupiter in Figure 1) and was south of the plasma torus centrifugal symmetry plane with a System III longitude of 339°. As illustrated in Figure 1, the observation was acquired using a slit of dimensions 7 R_J x 0.07 R_J with the long axis oriented perpendicular to Io's orbital plane and placed near the eastern elongation point of Io's orbit and ~0.5 Jupiter radius (~20 Io radii) from the center of the disk of Io. The slit is so located to measure Io's forward oxygen cloud. A reliable north-south brightness profile for the 6300 Å emission line along the slit was only obtained very close to the satellite plane as shown in Figure 2 with a peak brightness of 8.8 ± 1.7 Rayleighs. This peak brightness is similar to the 8 ± 4 Rayleighs 6300 Å average emission brightness measured by Brown (1981) for the forward oxygen cloud near the western elongation point of Io's orbit. A second but poorer [O I] 6300 Å emission observation (Number 212) acquired 2.5 hours later was also reported by Thomas for Io with a mid-point Io geocentric phase angle of 95° and an Io System III longitude of 51° (i.e., the satellite was still south of the plasma torus equator symmetry plane). For this measurement, a similar peak emission brightness of 9 ± 3 Rayleighs was obtained but was located 0.19 R_J (~7.5 Io radii) north of Io for a north-south oriented slit centered on the satellite. In this paper, modeling analysis of the Thomas [O I] 6300 Å emission observations will be limited to the better and more fully described observation (Number 199) shown in Figure 2.

3. ANALYSIS OF THE OBSERVATIONS

3.1 Model Description

The mathematical formulation and description of the neutral cloud model for atomic oxygen adopted here was developed by Smyth and Combi (1988a), and its application to the oxygen observations is similar in style and in treatment of the plasma torus to that adopted in the earlier application to the sodium neutral cloud (Smyth and Combi, 1988b). In short, atoms are ejected from the satellite exobase with velocities that describe a given source velocity

distribution, and their trajectories in space are determined by solving the circular restricted three-body equations of motion that include the gravity fields of Io and Jupiter. Along these trajectories, appropriate weights are calculated to determine in three-dimensions the space and time dependent gas density, volumetric emission rates, and ion production rates caused by the interaction of the gas and the oscillatory motion of the plasma torus relative to Io's orbital plane. The three-dimensional description of the electron and ion densities and temperatures in the plasma torus, adopted in the neutral cloud model, is based upon a tilted and off-set dipole planetary magnetic field, the plasma properties near western elongation for the 1979 Voyager spacecraft encounter, a nominal east-west electric field, and a System III longitude asymmetry in the active sector. Because of the east-west electric field, the plasma torus properties are also time varying in local time (see Smyth and Combi, 1988b).

The source velocity distribution adopted at the exobase for atomic oxygen is the isotropic incomplete collisional cascade distribution determined for sodium by Smyth and Combi (1997). For the incomplete collisional cascade process, this source distribution should also apply to atomic oxygen at least to first order, since sodium is a trace species. For sodium, this source speed distribution is responsible for the creation of the distribution of sodium in Io's corona as well as the forward sodium cloud and the trailing sodium cloud (excluding the higher-speed contributions by the directional feature source) near Io's orbit. The incomplete collisional cascade distribution peaks at 0.5 km/sec (well below the exobase escape speed of ~2 km/sec) and has a tail that extends to many 10's of km/sec. This source distribution provides a significant source of atoms with (1) ballistic trajectories (~62%) that populate only the corona of the satellite, (2) low-speed escape trajectories that have similar speeds to the monoenergetic 2.6 km/sec source adopted earlier by Scherb and Smyth (1993), and (3) higher-speed escape trajectories that quickly move away from Io's orbit and do not contribute significantly to the forward cloud. By adopting this more realistic incomplete collisional cascade source distribution at the exobase and requiring the same number of atoms to populate the forward cloud near Io's orbit, the oxygen source rate at the exobase will, necessarily, be larger than the value determined earlier by Scherb and Smyth (1993) for the observations of Brown (1981) when using only a simple 2.6 km/sec monoenergetic source.

The lifetime of oxygen atoms is determined by electron impact and charge exchange processes in the plasma torus which are both inherently space-time dependent and which for charge exchange is also velocity dependent due to the relative motion of the plasma torus and the atom trajectories. The charge exchange cross sections adopted in the neutral oxygen cloud model are those given by McGrath and Johnson (1989) with refinements provided by R.E.

Johnson (personal communication, 1989). The relative importance of the different lifetime processes at Io's orbit in the plasma torus symmetry plane at western elongation is summarized in Table 1. At this location, charge exchange is seen to dominate over electron impact ionization. The relative importance of the lifetime processes in Table 1 will, however, vary for different locations in the plasma torus. The minimum charge exchange lifetime, for example, is located near Io's orbit where the ion densities are largest. The minimum electron impact lifetime, however, occurs near 7 Jupiter radii because of the combined effects, with larger radial distances, of the increasing electron temperature and the decreasing electron density. The total lifetime of atomic oxygen in the plasma torus coordinate frame is shown in Figure 3 in a two-dimensional plane at eastern elongation for the time of the Thomas (1996) observation and at western elongation for the time of the Brown (1981) observation.

The [O I] 6300 Å emission for oxygen atoms along the atom trajectories is assumed to be excited by plasma torus electron impact and is, hence, also inherently space-time dependent. The electron impact [O I] 6300 Å volumetric emission rate adopted in the neutral cloud model is well established and its dependence upon the electron temperature is shown in Figure 4. This emission rate is calculated using the COREQ (COllisional and Radiative EQuilibrum) code with updated atomic data files developed by D.E. Shemansky (personal communication, 1992). The local emission photon rate per oxygen atom is obtained by multiplying this emission rate by the local electron density. The line of sight integration of the product of the neutral oxygen density, the electron density, the emission rate then determines the neutral cloud brightness on the sky plane of the observer.

3.2 Modeling Analysis

Model calculations for the two-dimensional [O I] 6300 Å emission brightness on the sky plane have been undertaken using the atomic oxygen neutral cloud model described above with the more realistic incomplete collisional cascade source distribution. The source rate at the satellite exobase for atomic oxygen is determined by matching the model calculated and measured brightness in the observing slit. For the March 5, 1980 observation of Brown (1981), the model calculation is shown in Figure 5 that corresponds to the mid-point location of Io for the six co-added observations. The model calculation matches the slit average [O I] 6300 Å emission brightness of 8 ± 4 Rayleighs for an isotropic oxygen exobase source of 1.27×10^{28} atoms sec^{-1}. For the March 5, 1993 observation of Thomas (1996), the oxygen model calculation is shown in Figure 6 for the midpoint of the observation. An isotropic exobase oxygen source of 1.47×10^{28} atoms sec^{-1} is required to match the average brightness of 5.7 Rayleighs in that portion of the observing slit in Figure 2 for which a measured signal was acquired. The model

calculated and measured north-south brightness profiles for the Thomas observation are shown in Figure 2 and compare reasonably within experimental error. There is an apparent discrepancy in the location of the peak intensity between the model and data. Given the substantial experimental error, however, we will leave an analysis of this for a future study of more recently obtained, but not yet available, data for atomic oxygen acquired by N. Thomas (personal communication, 1998).

4. DISCUSSION AND CONCLUSIONS

The atomic oxygen source rates of 1.27 x 10^{28} atoms sec^{-1} and 1.47 x 10^{28} atoms sec^{-1} determined from the two observations are surprisingly very similar despite the 13-year time interval between these measurements. Since only about 0.38 of the oxygen atoms escape Io for the incomplete collisional cascade source distribution adopted here, the source rates for the escaping fraction are 4.83 x 10^{27} atoms sec^{-1} and 5.59 x 10^{27} atoms sec^{-1}, respectively, for the Brown and Thomas measurements. The estimated escape rate of Scherb and Smyth (1993) for an analysis of Brown's observation, assuming a simpler monoenergetic 2.6 km s^{-1} initial velocity for the oxygen at Io's exobase, was 3.2 x 10^{27} atoms s^{-1}. Hence, the new oxygen escape rates are ~1.5 to 1.75 times larger, and the total oxygen exobase source rate (escaping and non-escaping) for the complete cascade source is ~4 times larger. For the incomplete collisional cascade source distribution, the new atomic oxygen escape rates are only ~5 to 21% larger than the escape rate of 4.6 x 10^{27} atoms sec^{-1} for incomplete collisional cascade estimated earlier by cross-section scaling arguments (Smyth, 1998). It is interesting to note that the new atomic oxygen incomplete collisional source rate is also similar to the inferred rate obtained by assuming two oxygen atoms per SO_2 molecule for the SO_2 source rates of 8.9 x 10^{27} molecules s^{-1} estimated by Scherb and Smyth (1993) based on near-Io [O I] 6300 Å emission measurements.

The new oxygen source rates for the incomplete collisional cascade distribution at Io's exobase have interesting implications. To explore them more concretely, the average oxygen exobase source rate for the two measurements of 1.37 x 10^{28} atoms sec^{-1} is adopted in Table 2. In addition, an incomplete collisional cascade rate for atomic sulfur is assumed for the same source velocity distribution but with an exobase source rate that is one-half of the average oxygen exobase source rate, as would be appropriate if SO_2 were the parent molecule. For the

incomplete collisional cascade, the corresponding exobase escape rates (38%) are also listed in Table 2 together with the "Neutral Energy Input Rate" (the rate that kinetic energy is supplied to neutrals by ions in the particular exobase source process at Io) and the "Torus Energy Input Rate" (the net rate that gyro-kinetic energy is supplied to new pickup ions in the plasma torus through ionization and/or charge exchange of neutrals from Io). The neutral energy input rate is determined by scaling the earlier incomplete collisional cascade energy rate of Smyth (1998) for the larger exobase source rate determined here, and the torus energy input rate is determined by scaling, for the O and S exobase escape rates given here, the earlier ion energy input rates for exospheric ejection of Smyth (1992, in Table 4). To complete estimates in Table 2 for the higher-velocity processes at Io's exobase of (1) low-velocity (~20 km s^{-1}) charge exchange (CE) and direct ejection and (2) full-velocity (nominally 56.8 km s^{-1}) charge exchange, the corresponding source and energy rates are also included. For these two higher-velocity sources, the exobase source and escape rates, which are the same, and the neutral energy input rates are determined by scaling the earlier corresponding values of Smyth (1998) with the new/old ratio (5.21/4.6 = 1.1326) of the exobase oxygen escape rate. The torus energy input rates are determined by scaling the earlier ion energy input rates for charge exchange of Smyth (1992) using the O and S exobase escape rates given here.

The combined O and S incomplete collisional cascade exobase source rate in Table 2 of ~2 x 10^{28} atoms sec^{-1} is produced primarily by multiple collisional processes deeper in Io's atmosphere and has essentially the same value as the total estimated escape rate of O and S from Io's exobase for all source processes. The power of 0.22 x 10^{11} W required to sustain the incomplete collisional cascade distribution is a significant fraction (33%) of the initial upstream ion corotational kinetic energy rate (0.67 x 10^{11} W) flowing through an Io disk area, but is small compared to the instantaneous new pickup ion net gyro-kinetic energy of 4.83 x 10^{11} W that it adds to the plasma torus energy budget. It should be noted that the power extracted from the corotating plasma to sustain this source is highly localized in Io's atmosphere whereas the instantaneous power input to the plasma torus created by this source is initially located in the spatially distributed volume of the extended neutral clouds so as to produce an "outer source region" for the Iogenic plasma (i.e., distributed outward from Io's exobase both ahead and behind Io and concentrated near Io's orbit) that is highly peaked about Io as described by Smyth and

Marconi (1999). The instantaneous power source of these pickup ions subsequently, of course, moves relative to Io with the plasma flow and provides a circumplanetary distributed energy source for the plasma torus. The power of 0.22 x 10^{11} W required to sustain the incomplete collisional cascade exobase source rate and hence this circumplanetary distributed energy source for the plasma torus, however, has been estimated to be only about 20% of the power extracted locally from the plasma flow by Io's atmosphere through elastic ion sputtering interaction processes (Pospieszalska and Johnson, 1996; Marconi et al., 1996). The remaining ~80% of the power (0.88 x 10^{11} W) is deposited as heat in Io's atmosphere, is important in raising Io's exobase altitude and altering the day-to night sublimation gas flow, and is primarily lost by radiation and heat conduction/convection to the surface. The total estimated ion sputtering power input to Io's atmosphere would then be ~1.1 x 10^{11} W and is very similar to values obtained in recent two-dimensional modeling of Io's atmospheres by Wong and Smyth (1999) and Monte Carlo ion sputtering studies for Io's atmosphere by Lisiecki et al. (1999).

For low-velocity charge exchange and direct ejection, the combined O and S exobase source rate in Table 2 of ~2.83 x 10^{27} atoms sec^{-1} is thought to be produced at higher altitudes in Io's atmosphere (and ionosphere) where ions and newly created atoms of intermediate speeds (~20 km s^{-1}) can more easily travel without sustaining multiple collisions. Although this exobase source rate is almost an order of magnitude smaller than the incomplete collisional source, the neutral power input of 0.38 x 10^{11} W required to sustain this smaller source is larger because of the increased (factor ~10-15) energy per atom. Whether or not the low-velocity charge exchange and direct collisional ejection source provides a small net gain or loss for the gyration energy of the involved ions in this "inner source region" of Io's atmosphere (i.e., the spatial region below the exobase) is difficult to assess, but the escaping neutrals will provide in the "outer source region" a significant rate for new pickup ions with an estimated instantaneous power input of 1.76 x 10^{11} W to the plasma torus budget that will be initially distributed (owing to their larger neutral velocities) over a much larger volume of the inner magnetosphere than that of the incomplete collisional cascade source primarily localized near Io's orbit. This larger spatially-distributed power source for the plasma torus may then be further enhanced by inward transport processes as described by Smith et al. (1988).

For full-velocity charge exchange, the combined O and S exobase source rate in Table 2 of 8.84 x 10^{27} atoms sec^{-1} is thought to be produced at high altitudes in Io's atmosphere near and below the exobase where the fast corotational ions and newly created atoms can easily travel and escape without sustaining a second collision. The neutrals rapidly escape the Jupiter system, producing O and S zenocoronae (Smyth and Combi, 1991). Because of their large speed, however, they will provide almost no spatially extended plasma power source for the "outer source region" in the inner magnetosphere. The power of 6.84 x 10^{11} W required to sustain the charge exchange neutral source is so large that it can only be supplied by the local planetary magnetic field energy that is partially converted to neutral kinetic energy by the ion pickup current that it creates. As discussed earlier by Smyth (1998), this ion pickup current is the likely cause of the remaining and unexplained ~400 nT reduction in the local planetary magnetic field measured near Io by the Galileo spacecraft (Kivelson et al., 1996a,b; Khurana et al., 1997). The charge exchange neutral source is accompanied by an instantaneous plasma torus net energy input rate of 5.10 x 10^{11} W that is highly localized in Io's "inner source region" and in effect provides a point energy source or for the plasma torus. Upon subsequently moving downstream of Io, this point source will form a thread that will rapidly change into a concentrated energy source ribbon (in magnetic latitude and System III longitude). The pickup-ion "power ribbon" will wander initially in a nonuniform manner within the L-shell volume of the plasma torus created by the pickup ion trajectories as determined by the combined effects of the corotational, east-west electric field, and System III longitude-offset motions (Smyth and Marconi, 1998) and will subsequently undergo radial plasma transport within and beyond this volume. If wave-particle interactions are not a dominant energy sink, the power ribbon should have an energy lifetime of ~few x 10^6 s, and, prior to significant radial transport, a height ~2R_J and a width of £0.05 R_J, which is 4 times thinner than the nominal 0.2 R_J width of the S^+ plasma torus ribbon (Schneider and Trauger, 1995). Such a concentrated and nonuniform volumetric distribution of the pickup ion power ribbon may play a significant role in producing the short-term temporal variability or time-dependent "flashes and sparkles" of the ultraviolet brightness of the torus S^{++} plasma ribbon observed in the Voyager UVS data (Sandel and Broadfoot, 1982; Volwerk et al., 1997) and also the short-term temporal (and apparently chaotic) variability of the [O I] 6300 Å emission brightness observed in a 5.2 x 5.2 arc second aperture centered on Io for nearly a decade from ground-based measurements (Scherb and Smyth, 1993; Scherb et al., 1999).

The total neutral (escape) energy input rate of 0.74 x 10^{12} W and the total torus energy input rate of 1.17 x 10^{12} W in Table 2 are similar to the earlier values, respectively, of 0.65 x 10^{12} W (Smyth, 1998) and of 1.0 x 10^{12} W (Smyth, 1992). The input power to sustain all neutral processes is estimated to be 0.83 x 10^{12} W if collisional cascade heating of Io's atmosphere is also included. The energy budget for the plasma torus, which is dominated by the UV energy radiated by the heavy sulfur ions, is estimated to be ~few x 10^{12} W (Hall et al., 1995) and is only about a factor of two or so larger than the estimated total torus energy input rate of 1.17 x 10^{12} W in Table 2. The contribution to this estimated total torus energy input rate by the incomplete collisional cascade source (41%) is reasonably firm being based directly upon the [O I] 6300 Å emission observations of Brown and Thomas. The contributions by the low-velocity CE and direct ejection source (15%) and the full-velocity charge exchange source (44%) are, however, determined from cross-section scaling arguments (Smyth and Combi, 1991; Smyth, 1992) applied to the incomplete collisional cascade escape source rates. The scaling arguments are only a first order means of estimating these two higher-velocity source rates upon which their torus energy input rates are based. The rates cannot be determined directly from the very dim [O I] 6300 Å emission brightness for these two higher-velocity source rates since they are well below current observational detection limits. A direct theoretical calculation of the two higher-velocity source rates would require the solution of the three-dimensional multi-species interaction problem for Io's atmosphere and the plasma torus with the proper inclusion of volcanic and surface sublimation gas sources, photochemistry, gas-phase chemistry, the plasma properties and their reaction chemistry, the Birkeland currents, the satellite ionosphere, and Io plasma wake, which is beyond current modeling capabilities. In addition to expected time dependence, the contribution to the torus energy input rate of the full-velocity charge exchange source for O and S alone in Table 2, however, could easily be double if the ion flux were assumed approximately constant but the assumed full pickup ion speed were increased from the nominally assumed value of 56.8 to ~80 km s^{-1} near Io, as suggested by the Galileo PLS observations (Frank et al., 1996). This would then provide an instantaneous 1.02 x 10^{12} W to the pickup ion power ribbon and a total torus energy input rate of ~1.68 x 10^{12} W. If the ion flux were also assumed to increase as the velocity, then the total estimated torus energy input rate would be 2.0 x 10^{12} W. Even these higher estimates for the total torus energy input rate can be

considered to be only a lower limit since other local ion sources from below the exobase (e.g., a leaky ionosphere) and from charge exchange and electron impact ionization of neutrals other than atomic oxygen and sulfur may also have significant plasma source rates. Indeed from recent MHD simulations for Io's interaction with the plasma torus (Combi et al., 1998; Linker et al., 1998; Combi et al., 1999), estimated net-mass and charge exchange loading rates are generally larger by a factor of about two and suggest that other such ion sources or a larger scaling factor are appropriate.

Hence with more refined future estimates and with the "outer source region" (neutral extended clouds) to "inner source region" (charge exchange processes below Io's exobase) torus power input ratio in the range of 1:2 to 1:3, it would seems possible that the total torus energy input rate introduced by neutrals from Io may be able to supply the energy budget for the plasma torus. Indeed, it is particularly important to note that such a local charge exchange pickup source at Io in the "inner source region" is the heterogeneous energy source favored by Shemansky (1988) to supply the additional energy input to the plasma torus that could not be supplied by the "neutral cloud theory" as approximately described in a one-box-model where both the nominal (and homogeneous) neutral gas densities and plasma torus properties were simultaneously required to be obtained as a steady-state solution of the coupled continuity and energy equations. In order to provide an appropriate increase in the electron temperature and a proper ratio for the S^{++} to S^{+} abundance ratio, Shemansky (1988) determined that an "outer source region" to the "inner source region" torus power input ratio of ~1:2 was generally needed. For MHD simulations of Io's interaction with the plasma torus for the December 1995 Galileo spacecraft encounter epoch (Combi et al., 1998; Linker et al., 1998; Combi et al., 1999), this power ratio has been more recently estimated to be in the range of ~1:2 to 1:3. Hence a viable solution to the mass loading and energy crisis (Shemansky, 1988; Smith et al., 1988) of the plasma torus is that the plasma torus mass is supplied by the extended neutral clouds and possibly some direct ion escape from Io and that the plasma torus energy is provided primarily by the pickup power ribbon created by localized charge exchange processes in Io's atmosphere.

Three future steps to improve the estimates of the important O and S source rates may be anticipated. First, the Voyager plasma torus description currently adopted in the neutral cloud

model needs to be updated to a Galileo plasma torus description when it becomes available. The Galileo electron and ion densities are about a factor of ~2 times larger (Frank et al., 1996; Gurnett et al., 1996) so that the greater oxygen destruction rate from Io will be somewhat balanced by the greater emission rate with the outcome largely dependent upon the electron temperature and the location of the emitting neutrals relative to Io's location. Second, the source velocity distributions at Io's exobase for O and S need to be independently determined in order to correct differences that may exist from the assumed sodium source velocity distribution. Third, the source rate for atomic sulfur needs to be independently determined so as to remove the assumption that it is one-half of the oxygen source rate. Careful modeling of the new HST/STIS simultaneous observations for the O and S extended emission data (Roesler et al., 1999; Wolven et al., 1999) and the neutral sulfur cloud measurements by Durrance et al. (1983, 1995), currently being pursued, may provide a first opportunity to address the latter two improvements.

ACKNOWLEDGMENTS

We wish to thank N. Thomas for helpful discussions regarding his ground-based oxygen observations for Io. This work was supported by the National Aeronautics and Space Administration through contract NASW-96020 from the Planetary Atmospheres Program.

REFERENCES

Ballester, G.E., J. Clarke, J. Trauger, K. Stapelfeldt, D. Crisp, D. Strobel, M.A. McGrath, N. Schneider, J. Ajello, and M. Combi, Ultraviolet observations of Io with HST: WFPC2 imaging and GHRS and FOS spectroscopy (abstract), *BAAS, 26*, 1136, 1994.

Ballester, G.E., Ultraviolet observations of the atmosphere of Io and the plasma torus, Ph.D. Thesis, The John Hopkins University, 1989.

Ballester, G.E., H.W. Moos, P.D. Feldman, D.F.Strobel, and M.E.Summers, Detection of neutral oxygen and sulfur emissions near Io using IUE, *Ap. J., 319*, L33- L38, 1987.

Brown, R.A., The Jupiter hot plasma torus: Observed electron temperature and energy flow, *Ap. J., 244*, 1072-1080, 1981.

Clarke, J.T., J. Ajello, J. Luhmann, N. Schneider, and I. Kanik, Hubble Space Telescope UV spectral observations of Io passing into eclipse, *J. Geophys. Res., 99*, 8387-8402, 1994.

Combi, M.R., K. Kabin, T.I. Gombosi, D.L. DeZeeuw, and K.G. Powell, Io's plasma environment during the Galileo flyby: Global three-dimensional MHD modeling with adaptive mesh refinement, *J. Geophys. Res., 103*, 9071-9081, 1998.

Combi, M.R., K. Kabin, T.I. Gombosi, D.L. DeZeeuw, and K.G. Powell, Interactions of Jupiter's plasma torus with the Galilean satellites: Io and Europa, paper presented at the "Magnetospheres of the Outer Planets Meeting", Paris, France, 9-14 August, 1999.

Durrance, S.T., P.D. Feldman, W.P. Blair, A.F. Davidsen, G.A. Kriss, J.W. Kruk, K.S. Long, and H.W. Moos, Neutral sulfur emission from the Io torus measured with the Hopkins Ultraviolet Telescope, *Ap. J., 447*, 408-415, 1995.

Durrance, S.T., P.D. Feldman, and H.A. Weaver, Rocket detection of ultraviolet emission from neutral oxygen and sulfur in the Io torus, *Ap. J. (Letters), 267*, L125-L129, 1983.

Frank, L.A., W.R. Paterson, K.L. Ackerson, V.M. Vasyliunas, F.V. Coroniti, and S.J. Bolton, Plasma observations at Io with the Galileo spacecraft, *Science, 274*, 394, 1996.

Geissler, P.E., A.S. McEwen, W. Ip, M.J.S. Belton, T.V. Johnson, W. Smyth, and A.P. Ingersoll, Galileo imaging of atmospheric emissions from Io, *Science, 285*, 870-874, 1999.

Gurnett, D.A., W.S. Kurth, A. Roux, S.J. Bolton, and C.F. Kennel, Galileo plasma wave observations in the Io plasma torus and near Io, *Science, 274*, 391-392, 1996.

Hall, D.T., G.R. Gladstone, F. Herbert, R. Lieu, and N. Thomas, Io torus EUV emission during the comet Shoemaker-Levy impact, Geophys. Res Letts., 22, 3441-3444, 1995.

Kivelson, M.G., K.K. Khurana, R.J. Walker, C.T. Russell, J.A. Linker, D.J. Southwood, and C. Polanskey, A magnetic signature at Io: Initial report from the Galileo magnetometer, *Science 273*, 337-340, 1996a.

Kivelson, M.G., K.K. Khurana, R.J. Walker, J. Warnecke, C.T. Russell, J.A. Linker, D.J. Southwood, and C. Polanskey, Io's interaction with the plasma torus: Galileo magnetometer report, *Science 274*, 396-398, 1996b.

Khurana, K.K., M.G. Kivelson, and C.T. Russell, Interaction of Io with its torus: Does Io have an internal magnetic field?, *Geophys. Res. Letts., 24*, 2391-2394, 1997.

Linker, J.A., K.K. Khurana, M.G. Kivelson, and R.J. Walker, MHD simulations of Io's interaction with the plasma torus, *J. Geophys. Res., 103*, 19867-19877, 1998.

Lisiecki, L., M.C. Wong, and W.H. Smyth, Io's magnetospheric interaction: Atmospheric heating and neutral escape (abstract), *Eos Trans. AGU, 80*, S200, 1999.

Marconi, M. L., L. Dagum, and W. H. Smyth, Hybrid fluid/kinetic approach to planetary atmospheres: An example of an immediate mass body, *Ap. J., 496*, 393-401, 1996.

McGrath, M.A., and R.E. Johnson, Charge exchange cross sections for the Io plasma torus, *J. Geophys. Res., 94*, 2677-2683, 1989.

Oliversen, R.J., F.Scherb, F.L. Roesler, J. Corliss, R.C. Woodward, M.E. Freed, O.L. Lupie, and W.H. Smyth, Io [O I] 6300 observations (abstract), *BAAS 30*, 1116, 1998.

Pospieszalska, M. K., and R. E. Johnson, Monte Carlo calculations of plasma ion-induced sputtering of an atmosphere: SO_2 ejected from Io, *J. Geophys. Res., 101*, 7565-7573, 1996.

Roesler, H.W. Moos, R.J. Oliversen, R.C. Woodward Jr., K.D. Retherford, F. Scherb, M.A. McGrath, W.H. Smyth, P.D. Feldman, and D.F. Strobel, Far-ultraviolet imaging spectroscopy of Io's atmosphere with HST/STIS, *Science, 283*, 353, 1999.

Sandel, B.R., and A.L. Broadfoot, Io's hot plasma torus-a synoptic view from Voyager, *J. Geophys. Res., 87*, 212-218, 1982.

Scherb, F., R.J. Oliversen, M.E. Freed, W.H. Smyth, J. Corliss, R.C. Woodward, P. Morgenthaler, and O.L. Lupie, Ground-based observations of [O I] 6300 Angstrom emission from Io, Paper presented at the "Magnetospheres of the Outer Planets Meeting", Paris, France, 9-14 August, 1999.

Scherb, F., and W.H. Smyth, Variability of [O I] 6300-Å emission near Io, *J. Geophys. Res., 98*, 18729-18736, 1993.

Schneider, N.M. and J.T. Trauger, The stucture of the Io torus, *Ap. J., 450*, 450-462, 1995.

Shemansky, D.E., Energy branching in the Io plasma torus: The failure of the neutral cloud theory, *J. Geophys. Res., 93*, 1773-1784, 1988.

Skinner, T.E., and S.T. Durrance, Neutral oxygen and sulfur densities in the Io torus, *Ap. J., 310*, 966-971, 1986.

Smith, R.A., F. Bagenal, A.F. Cheng, and D.F. Strobel, On the energy crisis in the plasma torus, *Geophys. Res. Letts., 15*, 545-548, 1988.

Smyth, W.H., Neutral cloud distribution in the Jovian system, *Adv. Space Res., 12*, 337-346, 1992.

Smyth, W.H., Energy escape rate of neutrals from Io and the implications for local magnetospheric interactions, *J. Geophys. Res., 103*, 11941-11950, 1998.

Smyth, W.H., and M.R. Combi, Io's sodium exosphere and spatially extended cloud: A consistent flux speed distribution, *Icarus, 126*, 58-77, 1997.

Smyth, W.H., and M.R. Combi, The sodium zenocorona, *J. Geophys. Res., 96*, 22711-22727, 1991.

Smyth, W.H., and M.R. Combi, A general model for Io's neutral gas cloud. I. Mathematical description, *Ap. J. Supp. 66*, 397-411, 1988a.

Smyth, W.H., and M.R. Combi, A general model for Io's neutral gas cloud. ii. Application to the sodium cloud, *Ap. J., 328*, 888-918, 1988b.

Smyth, W.H., and M.L. Marconi, The spatial nature of the Iogenic plasma source (abstract), *Eos Trans. AGU, 80*, S200, 1999.

Smyth, W.H., and M.L. Marconi, An explanation for the east-west asymmetry of the Io plasma torus, *J. Geophys. Res., 103*, 9091-9100, 1998.

Thomas, N., High resolution spectra of Io's neutral potassium and oxygen clouds, *Astron. Astrophys., 313*, 306-314, 1996.

Trauger, J.T., K.R. Stapelfeldt, G.E. Ballester, J.T. Clarke, and WFPC2 Science Team, HST Observations of [O I] emission from Io in eclipse (abstract), *BAAS, 29*, 1002, 1997.

Volwerk, M., M.E. Brown, A.J. Dessler, and B.R. Sandel, Evidence for short cooling time in the Io plasma torus, *Geophys. Res Letts., 24*, 1147-1150, 1997.

Wolven, B.C. P.D Feldman, H.W. Moos, K.D. Retherford, D.F. Strobel, and F.L. Roesler, Emission profiles of neutral oxygen and sulfur in Io's exospheric corona (abstract), *Eos Trans. AGU, 80*, S201, 1999.

Wong, M.C., and W.H. Smyth, Model calculations for Io's atmosphere at eastern and western elongations, Icarus, submitted, 1999.

Table 1

O Loss Processes in the Plasma Torus Near Io

		Relative Rate (%)	Lifetime (hr)
1.	$O + e \rightarrow O^+ + 2e$	21.77	80
2.	$O + O^+ \rightarrow O^+ + O$	67.75	26
3.	$O + O^{++} \rightarrow O + O^{++}$	0.45	3900
	$O^+ + O^+$	0.04	40000
4.	$O + S^+ \rightarrow O^+ + S$	0.09	19000
5.	$O + S^{++} \rightarrow O^+ + S^+$	5.04	350
6.	$O + S^{+++} \rightarrow (O^+)^* + (S^{++})^*$	4.84	360
7.	$O + h\nu \rightarrow O^+ + e$	0.02	38000
		100.00	

Table 2. Summary of Source and Energy Input Rates

Collisional Process	Exobase Source Rate Oxygen (atoms s^{-1})	Exobase Source Rate Sulfur (atoms s^{-1})	Exobase Escape Rate Oxygen (atoms s^{-1})	Exobase Escape Rate Sulfur (atoms s^{-1})	Neutral Energy Input Rate (W)	Torus Energy Input Rate (W)
Incomplete collisional cascade[a]	1.37×10^{28}	6.85×10^{27}	5.21×10^{27}	2.60×10^{27}	0.22×10^{11}	4.83×10^{11}
Low-velocity CE and direct ejection[b]	0.192×10^{28}	0.91×10^{27}	1.92×10^{27}	0.91×10^{27}	0.38×10^{11}	1.76×10^{11}
Full-velocity charge exchange[b]	0.679×10^{28}	2.04×10^{27}	6.79×10^{27}	2.04×10^{27}	6.84×10^{11}	5.10×10^{11}
Total	2.24×10^{28}	0.98×10^{28}	1.39×10^{28}	0.56×10^{28}	0.74×10^{12}	1.17×10^{12}

[a]The oxygen exobase source rate is the average of 1.27×10^{28} atoms s^{-1} and 1.47×10^{28} atoms s^{-1}; the sulfur exobase source rate is one-half the oxygen exobase source rate; exobase escape rates are 38% of the exobase rates; the neutral cloud energy input rates are determined using the source distribution average-speeds given by Smyth (1998); the plasma torus energy input rates are scaled from values of Smyth (1992).

[b]Source rates and neutral energy input rates are scaled from values of Smyth (1998) using the ratio 5.21/4.6 for the oxygen escape source rate; torus energy input rates are scaled using the exobase source rate from the charge exchange energy rates of Smyth (1992).

FIGURE CAPTIONS

Figure 1. Geometry for the [O I] 6300 Å Observations near Io's Orbit. The March 5, 1980 observations of Brown were made with a 0.32 RJ x 0.05 R_J slit (small rectangles with the long side parallel to the orbital plane) located for two observations at 5.0 RJ west (right) of Jupiter (circle at the center) and for four observations at 5.9 RJ west of Jupiter so as to be centered on the elongation point of the satellite's orbit. Io's orbit projected onto the sky plane is shown by the thin ellipse. The positions of Io at the mid-point of the six observations of Brown are shown by the small filled circles. The March 5, 1993 observation of Thomas was obtained with a vertically oriented slit (rectangle on the left side of Jupiter) of effective dimensions 7 RJ x 0.07 RJ that was located close to the position of Io (indicated by the small open circle).

Figure 2. [O I] 6300 Å Observational Profile of Thomas and Comparison with Model Calculation. The observed north-south spatial profile for the [O I] 6300 Å brightness distribution is shown by the asterisks with vertical-line error bars included. The negative numbers are south of the orbital plane. The model calculated brightness profile is shown by the solid line.

Figure 3. Lifetime of Atomic Oxygen in the Plasma Torus. The total (electron impact plus charge exchange) lifetime in units of hours for atomic oxygen is shown in the coordinate frame of the plasma torus in (a) at eastern elongation for the observation of Thomas that corresponds to an east ansa System III longitude of 316° and in (b) at western elongation for the mid-point of Brown's observation that corresponds to an west ansa System III longitude of 88°. The plasmacentric coordinate frame, used earlier by Smyth and Combi (1988b), includes the ~7° tilt of the magnetic dipole field with respect to the orbital plane of Io, a dipole off-set of the magnetic field relative to the center of Jupiter, and the presence of an east-west electric field of ~2.8 mV m^{-1} as seen in the Io frame. At the two elongation points, the locus of Io's position in the plasma torus coordinate frame is shown by the light gray oval-like closed line on which the oxygen lifetime varies periodically as a function of System III magnetic longitude of the satellite.

Figure 4. Electron Impact Emission Rate for the [O I] 6300 Å Line. The electron impact emission rate for the [O I] 6300 Å line as a function of electron temperature is shown as determined from the COREQ (COllisional and Radiative EQuilibrum) code developed by D.E. Shemansky (personal communication, 1992).

Figure 5. Model Calculation for Brown's Observation of the Sky Plane Brightness of the [O I] 6300 Å Emission. Contour plot of sky plane [O I] 6300 Å brightness. Brown's observations were modeled with a single model calculation with Io at the mid-point of the six observations with a satellite phase angle of 198° and an Io System III longitude of 161°. Atomic oxygen was assumed to be ejected isotropically from Io's exobase (radius assumed to be at 2600 km) with the modified sputtering flux velocity characterized by a Thomas-Fermi cross section (α = 7/3) with a most probable speed of 0.5 km/sec as determined by Smyth and Combi (1997) for atomic sodium at Io's exobase. The contour levels are, from outside to inside, 1.0, 2.0, 5.0, 10.0, and 20.0 Rayleighs. The total oxygen flux in the model was normalized so as to give the brightness of 8 Rayleighs reported by Brown. Also shown are the locations of Jupiter, Io's orbit, and Brown's observing slit (small rectangles).

Figure 6. Model Calculation for Thomas's Observation of the Sky Plane Brightness of the [O I] 6300 Å Emission. Same as Figure 5 except that the model corresponds to the geometry of Thomas's observation Number 199 with an Io phase angle of 73° and an Io System III longitude of 339° at the midpoint of the observation. The model flux was normalized so as to reproduce the average brightness of 5.7 Rayleighs in that portion of the slit included in Figure 2.

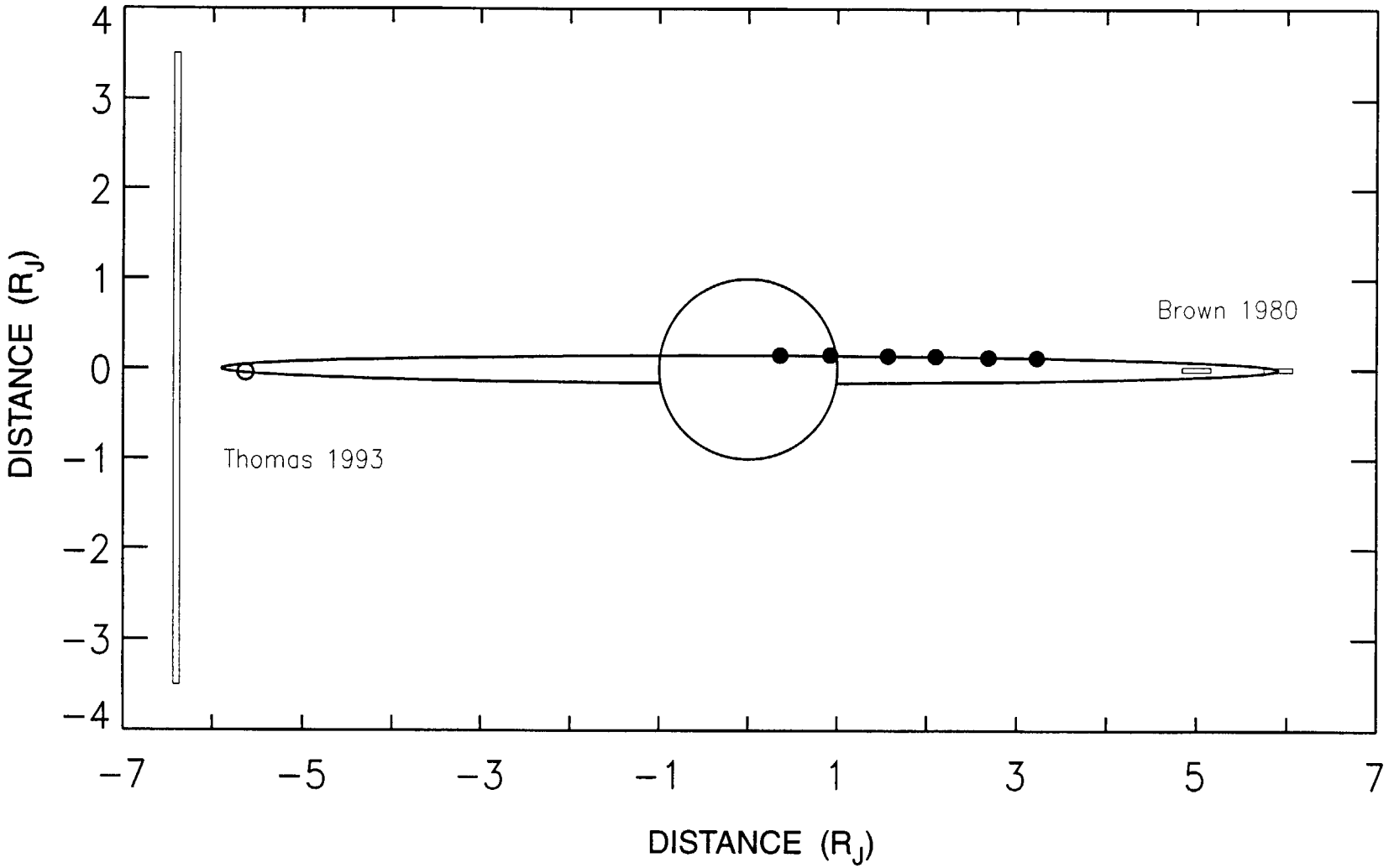
4
3
2
1
0
−1
−2
−3
−4
DISTANCE (R_J)
−7
−5
−3
−1
1
3
5
7
DISTANCE (R_J)
Brown 1980
Thomas 1993

Figure 1

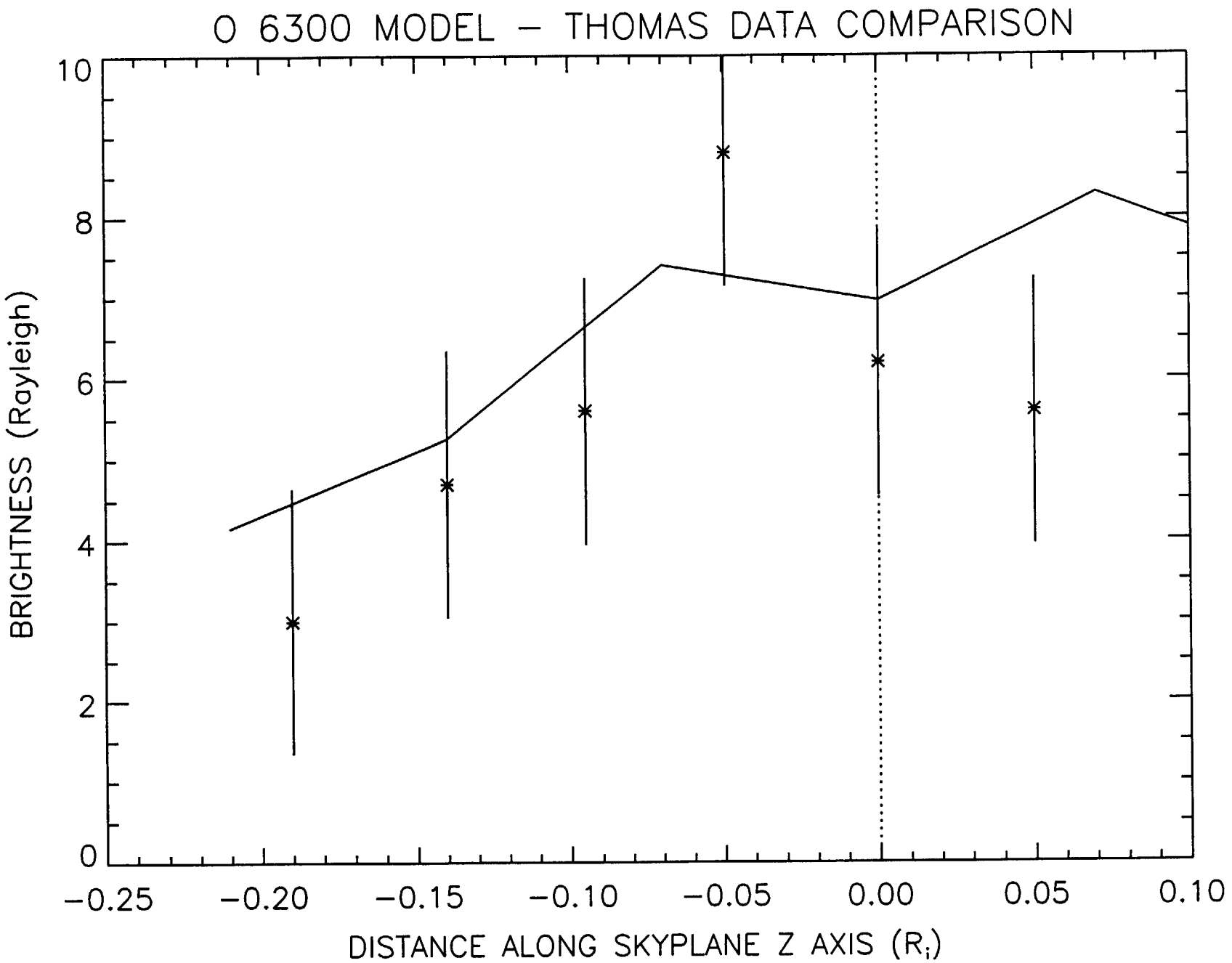
O 6300 MODEL – THOMAS DATA COMPARISON
BRIGHTNESS (Rayleigh)
10
8
6
4
2
0
−0.25
−0.20
−0.15
−0.10
−0.05
0.00
0.05
0.10
DISTANCE ALONG SKYPLANE Z AXIS (R$_i$)

Figure 2

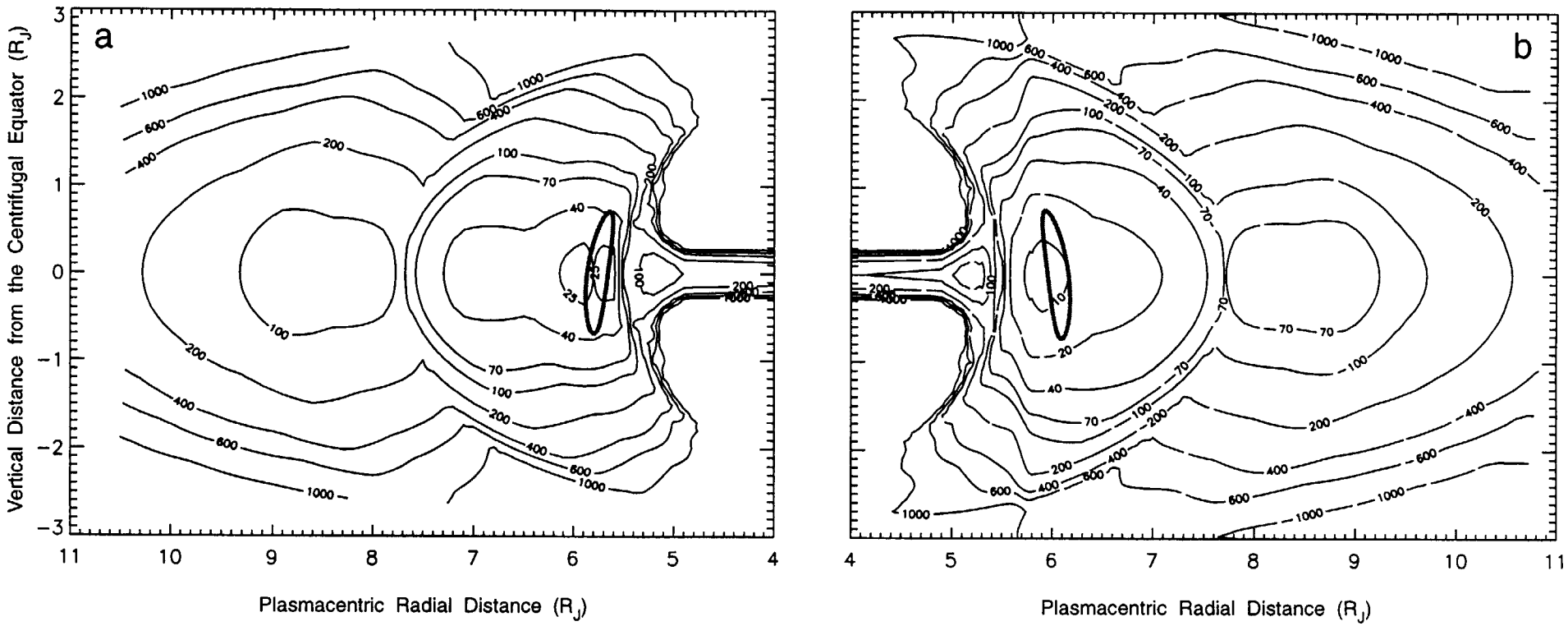
a
b
Vertical Distance from the Centrifugal Equator (R_J)
Plasmacentric Radial Distance (R_J)
Plasmacentric Radial Distance (R_J)

Figure 3

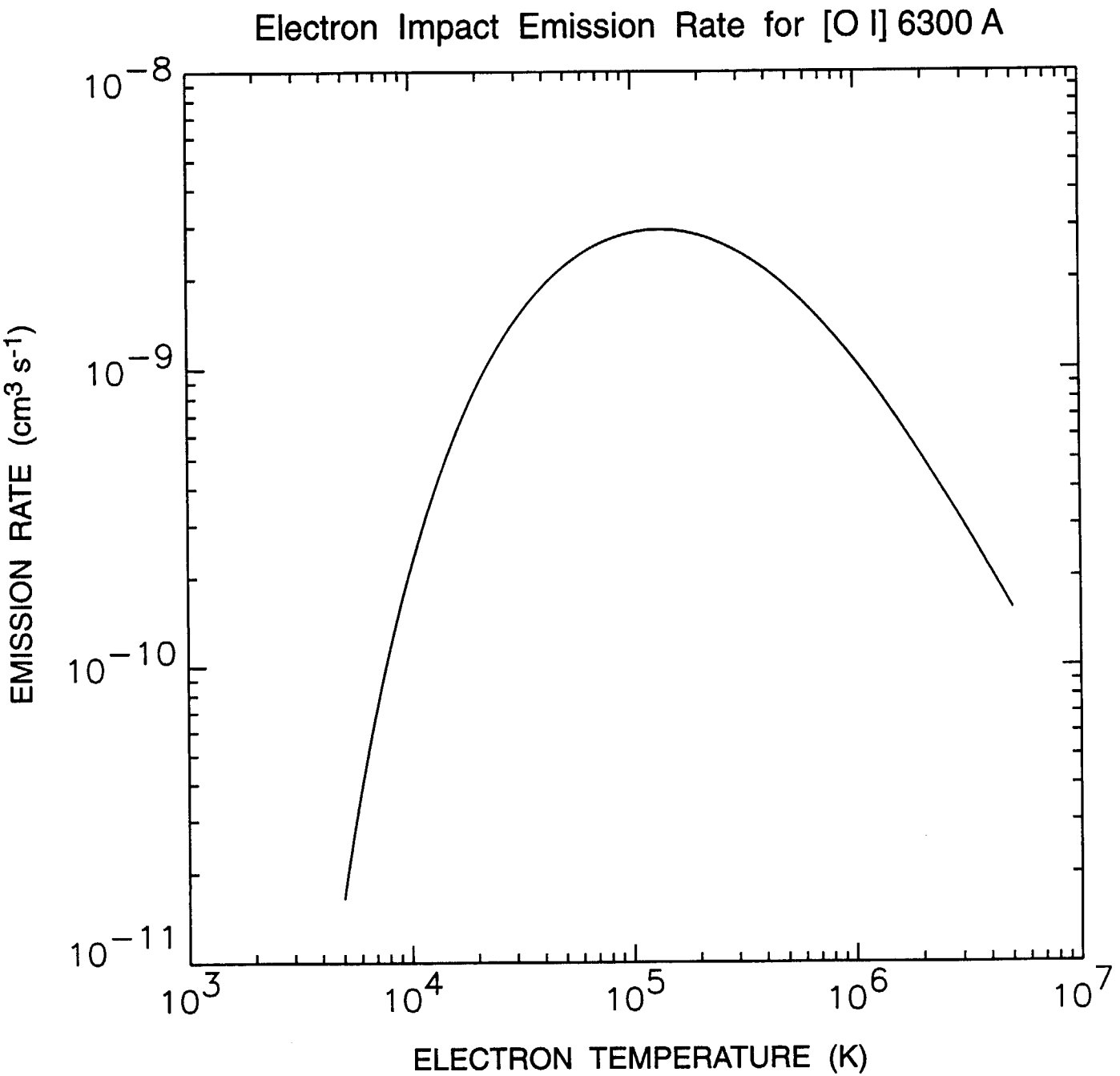
Electron Impact Emission Rate for [O I] 6300 A
EMISSION RATE (cm3 s-1)
10-8
10-9
10-10
10-11
10^3
10^4
10^5
10^6
10^7
ELECTRON TEMPERATURE (K)

Figure 4

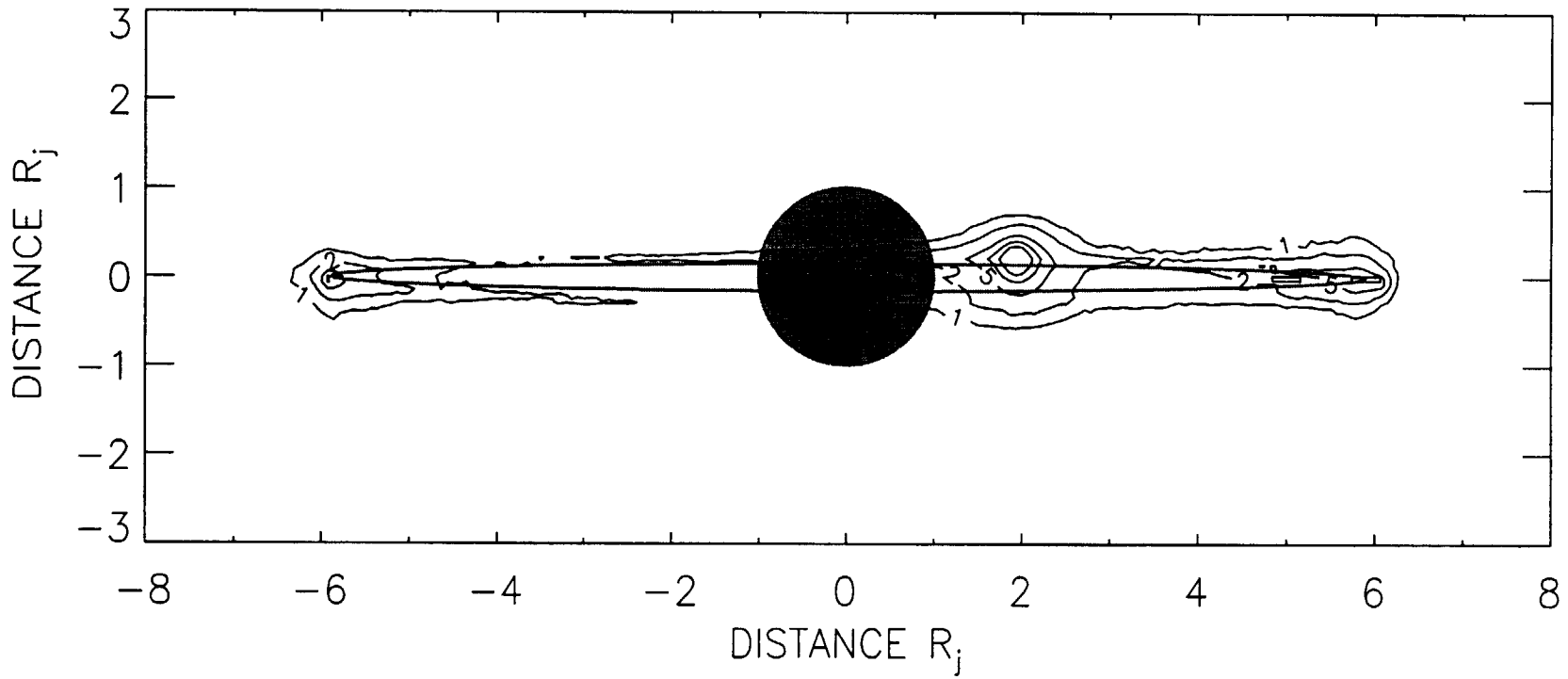

Figure 5

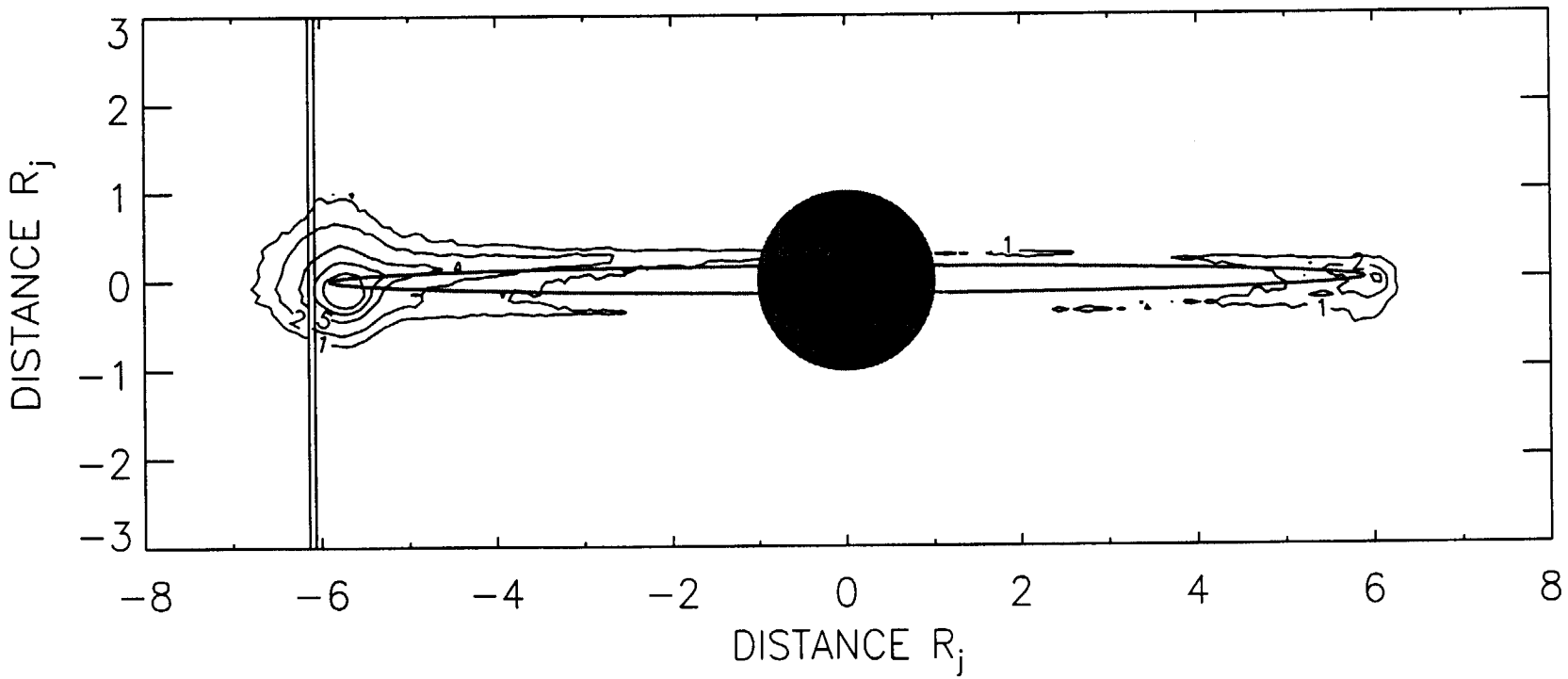

Figure 6